ÉCOLE POLYTECHNIQUE
FÉDÉRALE DE LAUSANNE

Development of a Beam Condition Monitor System for the Experimental Areas of the LHC Using CVD Diamond

Thèse
présentée à la Faculté des Sciences de Base
Institut de Physique de l'Energie et des Particules
Section de Physique

pour l'obtention du grade de Docteur ès Sciences

par
Juan Luis Fernández-Hernando
Ingénieur-industriel
Universitat Politècnica de Catalunya
Espagne

Jury
M. le Prof. H. Brune, président
M. le Dr M.T. Trân, directeur de thèse
M. le Prof. A. Fasoli, rapporteur interne
M. le Dr E. Tsesmelis, rapporteur externe et superviseur
M. le Dr J. Wenninger, rapporteur externe

Lausanne, EPFL
2004

To my mother

Abstract

The CERN Large Hadron Collider (LHC) will store 2808 bunches per colliding beam, each bunch consisting of 10^{11} protons at an energy of 7 TeV. If there is a failure in an element of the accelerator, the resulting beam losses could cause damages not only to the machine but also to the experiments. A Beam Condition Monitor (BCM) is foreseen to monitor fast increments of particle fluxes near the interaction point and, if necessary, to generate an abort signal to the LHC accelerator control to dump the beams. The system is being developed initially for the CMS experiment but is sufficiently general to find potential applications elsewhere.

Due to its high radiation hardness, CVD diamond has been studied for use as the BCM sensor. Various samples of CVD diamond have been characterized extensively with a ^{90}Sr source and high intensity test beams in order to assess the capabilities of such sensors and to study whether this detector technology is suitable for a BCM system. The results from these investigations are presented in this dissertation.

Le futur collisionneur du CERN, le "Large Hadron Collider" (LHC), stockera 2808 paquet de protons par faisceau, avec chaque paquet comprenant de 10^{11} protons à une énergie de 7 TeV. Si un élément de l'accélérateur venait à présenter des faiblesses ou à tomber en panne, les pertes de faisceau résultant pourraient endommager non seulement à la machine mais également les équipements des expériences. Un moniteur de l'état des faisceaux (BCM) est prévu pour surveiller des augmentations rapides des flux de particules près du point d'interaction et, au besoin, pour produire d'un signal d'arrêt à envoyer à la salle de contrôle de l'accélérateur afin d'éjecter les faisceaux. Le système est développé tout d'abord pour l'expérience de CMS, mais il est suffisamment général pour trouver des applications potentielles ailleurs.

En raison de sa résistance élevée auprès des radiations, le diamant CVD a été choisi comme sonde pour le BCM. Divers échantillons de diamant de CVD ont été caractérisés intensivement avec une source ^{90}Sr et dans des faisceaux d'intensité élevée afin d'évaluer les caractéristiques de telles sondes au diamant et d'étudier si cette technologie de détecteur convient à un système de BCM. Les résultats de ces investigations sont présentés en ce mémoire de thèse.

Contents

Introduction

The verification of theories whose aim is to explain how the world in which we all live is formed pushes Particle Physics toward new technological challenges. At CERN (European Organization for Nuclear Research) thousands of scientists, engineers and technicians have been working through the years building accelerators and experiments to discover new subnuclear particles and to verify the models of the interactions of these particles.

The SPS and the LEP (Super Proton Synchrotron and Large Electron Positron) colliders, at CERN, and other accelerators around the world have allowed to discover a whole set of particles that were predicted by the Standard Model (SM), making a big leap toward its verification. However, some questions still remain open and not all the particles that were predicted have appeared. In particular, the Higgs boson, a key particle in the SM, was not detected, as well as other massive particles that the top energy reached in LEP collisions was not enough to allow them to appear.

The next step is the construction and commissioning of the Large Hadron Collider (LHC). The LHC machine will be the most complex accelerator ever built and it will reach the energies necessary for the Higgs boson and other particles to show up. Four experiments surrounding the collision points will detect these particles and will be the witnesses of the completion of a theory and/or of the birth of "New Physics".

The LHC and its experiments are not only complex because of the technology that is necessary in order to perform their task, but also because of the protection and safety systems that must ensure their reliability and survival in case of accidents that, in such a complex machine, are more than probable to happen.

One of those systems is the Beam Condition Monitor (BCM), which is presented in this dissertation. The BCM is intended to work close to the interaction points and the beam pipe. Its aim is to protect the pixel detectors, which are the closest detectors to the interaction point, of the experiments from beam instabilities or beam losses which result from magnet or equipment failures. The BCM will also be a part of a Radiation Monitoring System for the experiments.

A system operating close to the interaction points must be able to withstand a hostile radiation environment. The sensors of the BCM will be the most exposed part of the system to radiation therefore they must be radiation hard. The type of material investigated in this thesis to be used as BCM sensor is the Chemical Vapour Deposition (CVD) diamond.

CVD diamond presents a large spectrum of advantages, being the most crucial of all its high radiation hardness. In this thesis, several CVD diamond sensor samples have been characterized, irradiated and tested in dedicated test beams in the irradiation facilities of the Proton Synchrotron at CERN and at the CERN test beam areas. The results, the data analysis and the conclusions extracted, are presented in this work.

Chapter 1 serves as introduction to the LHC and the four experiments: ATLAS, CMS, LHCb and ALICE. Chapter 2 describes the radiation environment which will prevail in the regions where the BCM sensors will eventually be placed and the subdetector systems that it must protect. Chapter 3 will emphasize the accident scenarios that could happen in the LHC and its impact on CMS for which the BCM is originally developed for.

The simulation of radiation background in the case of beam accidents shows that a radiation hard sensor able to withstand this harsh environment is needed. In chapter 6, after a brief overview on particle detection (chapter 5), CVD diamond is presented as the BCM sensor candidate. Then, as it has been already said, the results of the various tests performed on CVD diamond sensor samples are presented. At the end of this dissertation, an appendix will be devoted to a Radiation Monitoring System based on field effect devices.

Chapter 1

The LHC and its experiments

1.1 Physics overview

During the 1930s it was thought that neutrons, protons and electrons composed the building blocks of all matter. But there were still some questions: What holds together the protons and the neutrons in the nucleus? And which forces are involved in the radioactive decays of nuclei? Particle accelerators would become the tool that will provide the answers by producing particles with high momentum (p) and thus with short wavelength (λ), λ being inversely proportional to p of the particle, following the expression $\lambda = h/p$ where h is the Planck's constant. With shorter wavelengths smaller distances could be probed.
Accelerator experiments revealed a new set of particles, some being similar to the neutron and the proton and called *baryons*, and a whole new family of particles called *mesons*. In 1964, physicists Murray Gell-Mann and George Zweig introduced the idea of *quarks* and *anti-quarks*. Mesons are intermediate mass particles that are made up of a quark-antiquark pair; baryons are massive particles, which are made up of three quarks. Baryons and mesons are included in the overall class known as hadrons (the particles that interact with the *strong force*).

Thirty years later the quark idea was confirmed and it forms part of the *Standard Model of Fundamental Particles and Interactions*. Experiments showed that there are six types of quarks grouped in three doublets: *up, down, strange, charm, bottom* and *top*, in order of increasing mass; and also that there are six types of particles, called *leptons*, that include the electron. Figure 1.1 shows a diagram of the fundamental particles that form the Standard Model. The leptons are divided into charged leptons: *electron, muon* and *tau*; and neutral leptons, called *neutrinos*. For each of the six leptons there is an *antilepton* with equal mass and opposite charge.

The Standard Model also accounts for the forces and interactions of the particles. There exist four known types of interactions: *gravitational, electromagnetic, strong* and *weak*. Gravity is not included in the Standard Model because its effects are negligible in particle processes. Electromagnetic forces are responsible for binding the electrons to the nucleus. Atoms combine to form molecules due to the electromagnetic interactions. The strong force holds together the quarks to form hadrons, leptons have no strong interactions. Weak interactions are responsible for a type of quark or lepton to change into another type of quark or lepton.

In particle processes the forces are described as particles, thus for each type of force there is an associated carrier particle. For the electromagnetic force this particle is the *photon*, for the strong force these particles are called *gluons*, and for the weak force there are two associated carrier particles called the W and the Z *bosons.*

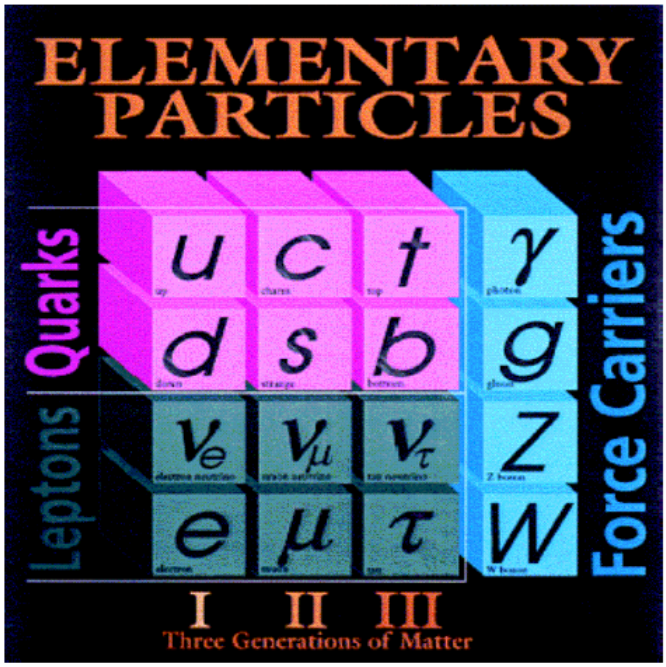

Fig. 1.1: Table of fundamental particles and force carriers included in the Standard Model.

A lot of issues about the structure and stability of matter are answered thanks to the Standard Model with its six types of quarks, leptons and the three forces, but there are unanswered questions like: Why are there three types of quarks and leptons of each charge? Is there some pattern to their masses? Are more types of particles and forces to be discovered? Are quarks and leptons really fundamental particles or do they have a substructure? What is the dark matter of the universe? How can the gravitational interactions be included in the Standard Model? And, why do the fundamental particles have mass?

The Standard Model proposes a field called the *Higgs field*, and particles by interacting with this field acquire their masses. The *Higgs boson* is the particle associated with this field. It is hoped that the LHC and the ALAS and CMS experiments will give the hints to answer some of those questions.

Supersymmetry links the matter particles (the quarks and the leptons) with the force-carrying particles (the gauge bosons: photon, graviton, gluons, W, Z plus the Higgs), every fundamental matter particle should have a massive "shadow" force carrier particle and every force carrier should have a massive "shadow" matter particle. These shadow-particles have not been seen, as they are very massive, but the lightest shadow-particles should be only around ten times heavier than the heaviest particles studied so far. This puts them in range of the LHC. It is thought that one of the supersymmetric particles, the *neutralino*, might compose the cold dark matter of the universe.

1.2 The Large Hadron Collider

The Large Hadron Collider (LHC) machine is a proton-proton collider that will be installed in the 26.6 km circumference tunnel previously used by the LEP electron-positron collider at CERN [1][2]. Superconducting dipole magnets with a field of 8.7 Tesla, operated at 1.9 K, will allow a beam energy of 7 TeV to be achieved. The beams intersect at four points where

experiments are placed. Two of these are high luminosity regions and house the ATLAS [3][4] and CMS [5][6] detectors. Two other regions house the ALICE detector [7][8], to be used for the study of heavy ion collisions, and LHCb [9][10], a detector optimized for the study of B-mesons, particles in which exists a bottom and an anti-bottom quark, and B-baryons. B-baryons are combinations of three quarks, one of them being a bottom quark.

The proton bunches of the LHC cross every 25 ns and the nominal luminosity is 10^{34} cm^{-2} sec^{-1} at which there is an average of around 20 *pp* interactions per bunch crossing. The machine will also be able to accelerate heavy ions resulting in the possibility of Pb-Pb collisions at 1150 TeV at the center of mass and luminosity up to 10^{27} cm^{-2} sec^{-1}.

The main goals are [11]:

- Discover or exclude the Standard Model Higgs and/or the multiple Higgs of supersymmetry.
- Discover or exclude supersymmetry over the entire theoretically allowed mass range.
- Discover or exclude new dynamics at the electroweak scale.

The energy range opened up by the LHC gives the opportunity to search for other objects:

- Discover or exclude any new electroweak gauge bosons with masses below several TeV.
- Discover or exclude any new quarks or leptons that are kinematically accessible.

Finally there is the possibility of exploiting the enormous production rates for certain Standard Model particles to conduct the following studies:

- The decay properties of the top quark, limits on exotic decays such as $t \rightarrow cZ$ or $t \rightarrow bH^{+}$.
- B-physics, particularly that of B-baryons, B_s mesons and rare decays of B mesons.

1.2.1 LHC layout

The LHC is composed of eight different octants, thus eight arc sections, where the beams are bend thanks to the main dipoles, and eight long straight sections. The two counter-rotating proton beams will circulate in separate beam pipes installed in the same magnet. At the experimental regions the beams will cross.

Each arc has a length of 2465 m and consists of 23 identical cells. Each cell is formed by six dipole magnets, whose length is of 15 m, and two quadrupole magnets. Dipole magnets deflect the beam whereas quadrupole magnets focus the beam in one transverse direction while defocusing in the other one, therefore, to obtain a full focus, two quadrupole magnets are needed. A section of a quadrupole magnet is shown in Figure 1.4. Small dipole, sextupole, octupole and decapole corrector magnets are installed to keep the particles on stable trajectories. All those different magnets form a Short Straight Section (SSS); a diagram is shown in Figure 1.3.

The four experiments are located in the middle of straight sections formed by the dispersion suppressors and the insertion magnets. The insertion magnets join both beams into a same beam pipe volume where they are focused by the inner triplet magnets in order to get a low betatron oscillation. The other insertions will be used by systems such as the beam dump,

the collimation or beam cleaning, RF-cavities to accelerate the particles and injection from the SPS [12] at an energy of 450 GeV. Figure1.2 shows an scheme of the LHC layout.

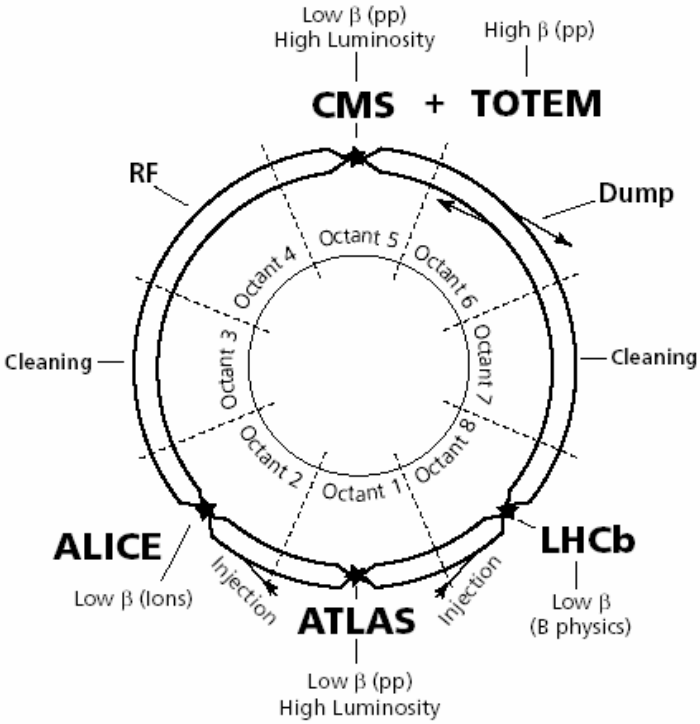

Fig. 1.2: Layout of the Large Hadron Collider.

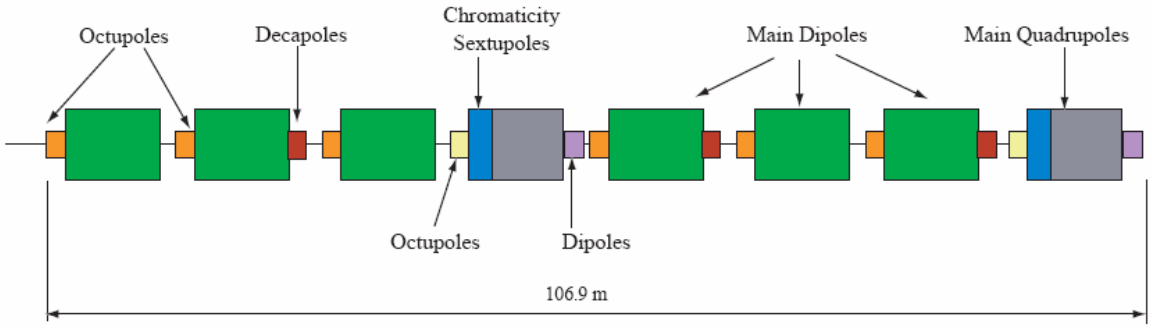

Fig. 1.3: LHC cell layout.

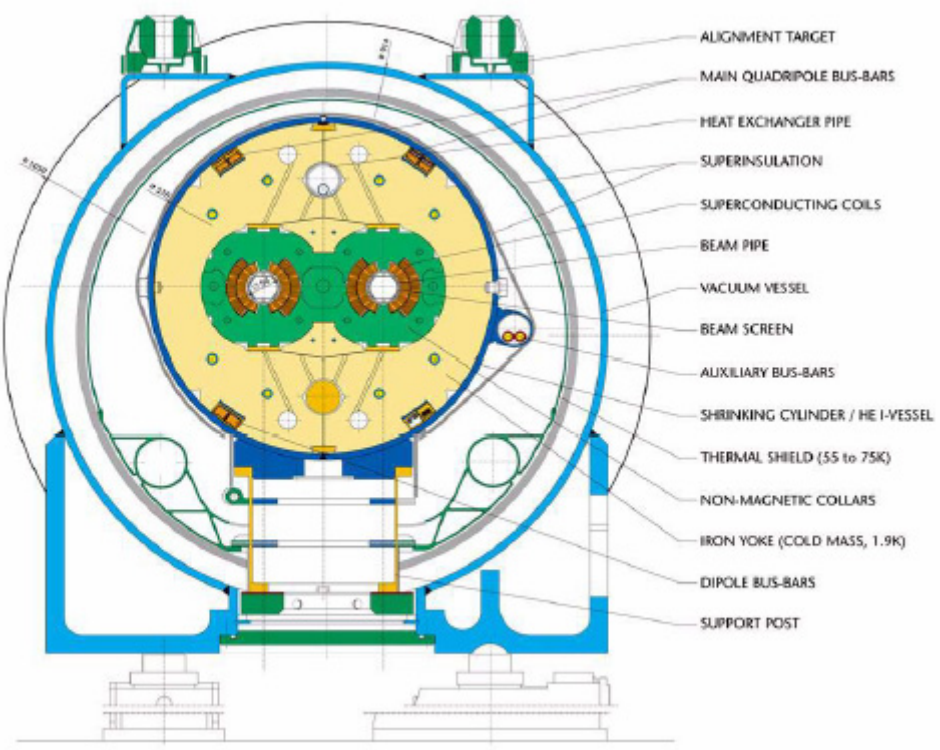

Fig. 1.4: Section of a LHC dipole. The two beam pipes for the counter-rotating beams are shown.

1.3 Detectors for High Energy Physics Experiments

Two important parameters to measure for a particle are their charge and their momentum. In collider experiments the innermost parts of the detector, the tracking device, are in a strong magnetic field. It must measure at least three points in order to determine the radius. The transverse momentum, p_t, of a particle with charge q is measured from its bending radius r:

$$p_t = q \cdot r \cdot \left|\vec{B}\right| \qquad \rightarrow \qquad r[m] \approx \frac{10}{3} \frac{p_t[GeV/c]}{\left|\vec{B}\right|[T]} \tag{1.1}$$

Detectors are made up of different components. Each component is specialised in detecting a set of properties of definite particles. Figure 1.5 shows the interaction of different types of particles in the different components of the detector.

Charged particles are detected in the tracking chamber and also in the electromagnetic calorimeter. Photons are detected by the electromagnetic calorimeter. The neutrons are seen by the energy they deposit in the hadron calorimeter. If a charged particle traverses large amounts of absorber with minor energy losses and small angular displacement such a particle is considered as a muon. Muons are identified in the muon chambers, after having penetrated through all the detector systems.

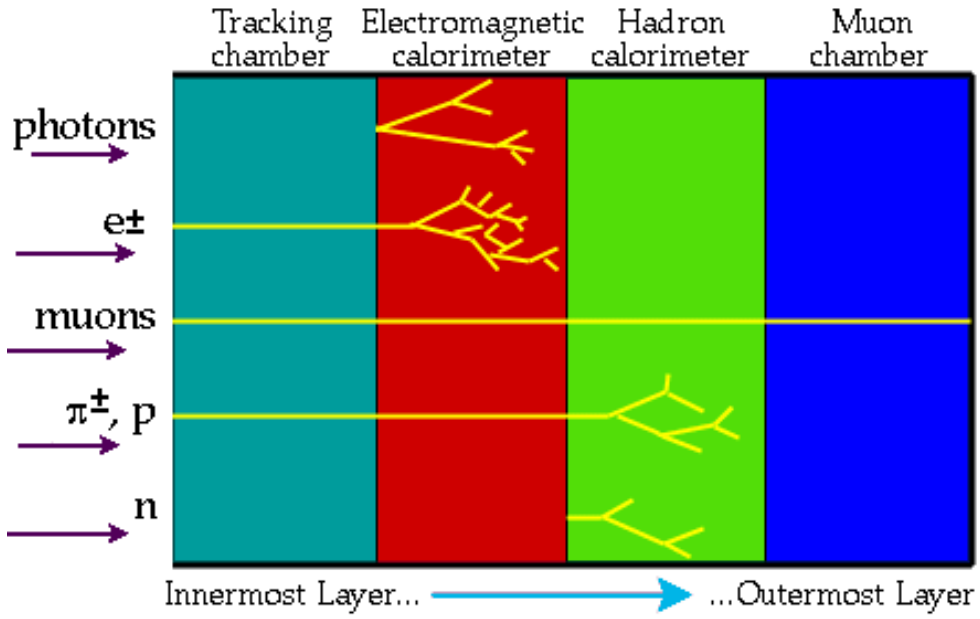

Fig. 1.5: Interaction of particles with the different components of a detector. Neutrinos are not shown because they rarely interact with matter, and can be only detected by missing matter and energy. π (pion) is a charged meson.

In the following sections the four main experiments at the LHC are described together with their pixel systems and inner trackers, which are the subdetectors most exposed to the radiation generated by the hadron collisions in the Interaction Point (IP) and to possible beam losses of the proton beams. The Beam Condition Monitor developed in this thesis aims to protect these subsystems and is going to be placed close to them and also close to the beam pipe.

1.4 The Compact Muon Solenoid

The Compact Muon Solenoid (CMS) is one of the two general purpose detectors at the LHC, with emphasis on muon identification and muon momentum measurement, precise photon and electron identification and calorimetry and central tracking for momentum measurement and vertex finding of charged particles. CMS is designed to run at the highest LHC luminosity of the LHC. Figure 1.6 shows an open view of CMS and its different components.

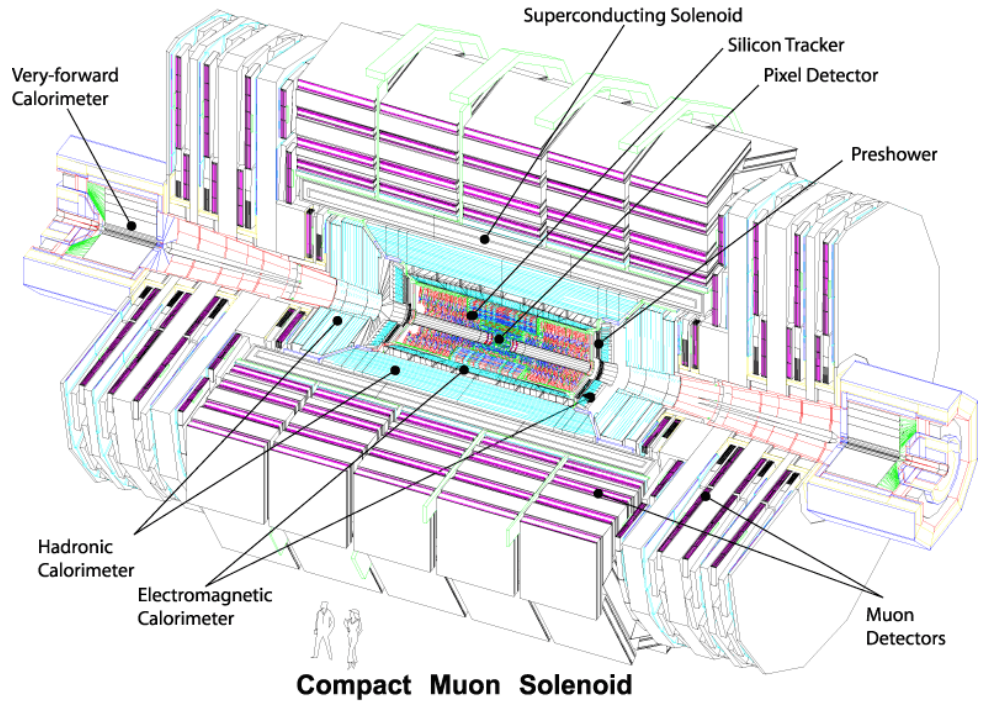

Fig. 1.6: Open view of CMS.

1.4.1 The CMS Silicon Strip Tracker

The CMS Silicon Strip Tracker (SST) consists of five barrel layers of silicon microstrip detectors located from an innermost radius of 22 cm to an outermost radius of 60 cm, three silicon disks and ten end-cap disks are located on either side of the interaction point. The SST is based on microstrip silicon sensors of 320 or 500 μm thick, covering a total area of around 70 m^2. It has a length of 5.6 m. Isolated tracks are expected to be reconstructed with an efficiency greater than 98%.

Figure 1.7 shows a detector module that consists of three elements: a set of silicon strip detectors, a readout hybrid and a carbon fibre support.

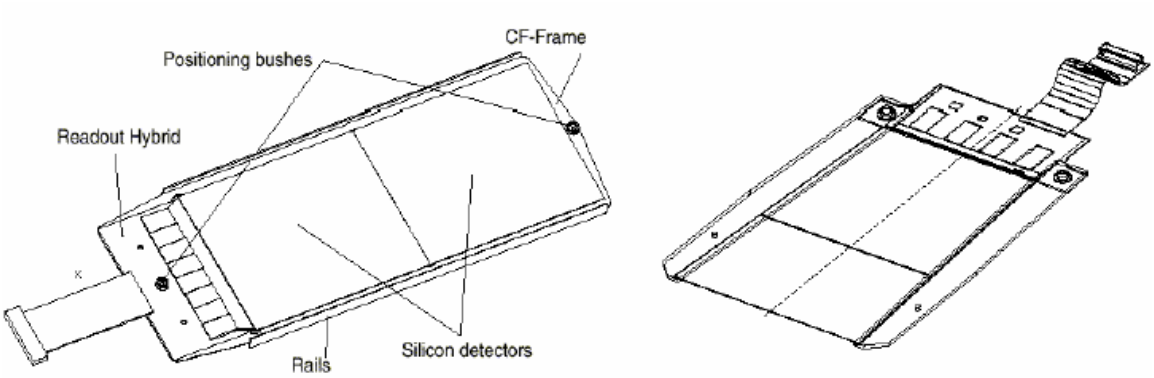

Fig. 1.7: Perspective view of a microstrip silicon tracker from the barrel, left, and from a disk endcap module, right. Its length ranges from 10 to 20 cm.

1.4.2 The CMS Pixel System

The purpose of the CMS Pixel System is the determination of the vertex and the rejection of background from jets and beam-beam interaction. Pixels will allow extrapolating track candidates from the outer layers to the vertex. The electronics must be fast and have the lowest possible noise. Both detectors and readout electronics must be radiation hard. The innermost layer of the system will need to be changed at least once during the experiment lifetime.

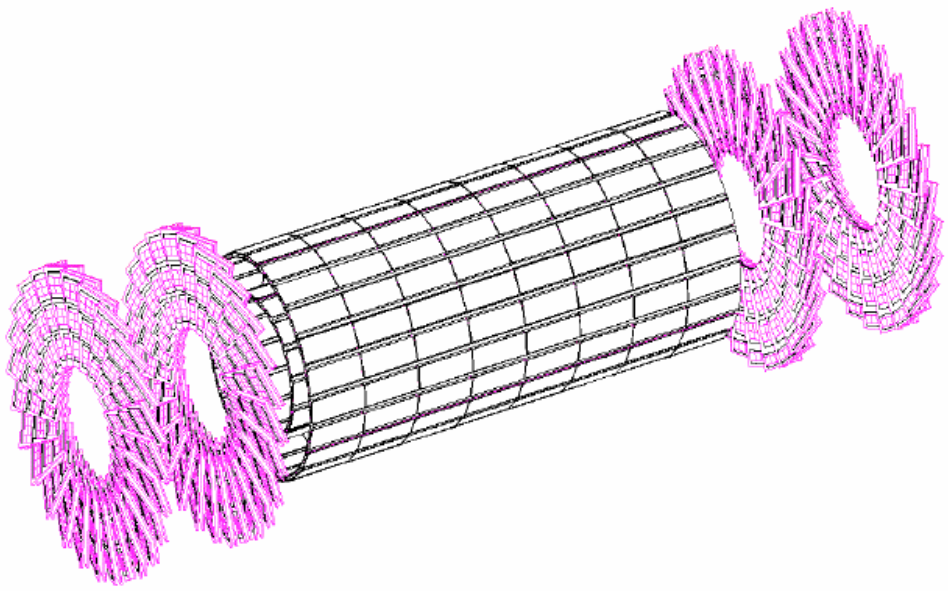

Fig. 1.8: View of the CMS Pixel System [13].

The CMS Pixel System will be composed of three barrel layers and two disk layers on each side of the barrel, as can be seen in Figure 1.8. The innermost radius of the barrel system will be located at around 4 cm from the beam axis, and the outermost at 11.5 cm [14].

1.5 The ATLAS Spectrometer

The ATLAS detector (acronym for *A Toroidal LHC ApparatuS*) contains different subdetector components for calorimetry, particle identification and particle tracking. A spectrometer measures momentum and energy. The particle energy is measured in the calorimeters, while the momentum is measured from the bending radius in the magnetic field generated by the super conducting solenoid, which magnitude is of 2 T.

The inner detector consists of a transition radiation tracker (TRT), then in its interior there is the semi-conductor tracker (SCT), and finally the inner pixel detector. An overall open view of ATLAS is shown in Figure 1.9. The overall detector has a length of 50 m, a diameter of 25 m and a weight of 7000 tons.

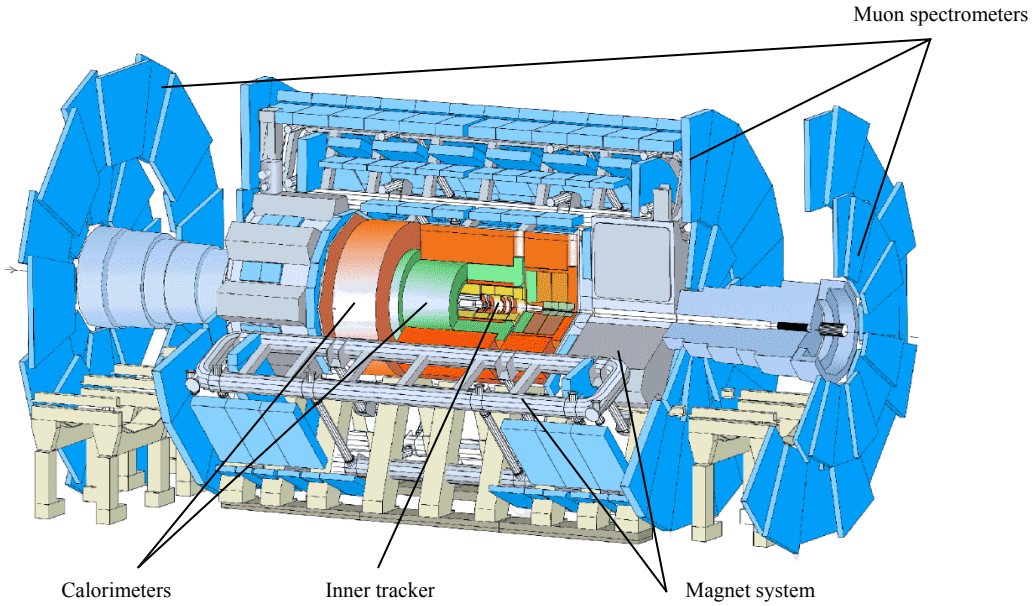

Fig. 1.9: Open view of ATLAS. There can be seen: The muon spectrometers to identify and measure muons, the calorimeters that measure the energies carried by the particles, the inner tracker and the magnet system.

1.5.1 ATLAS Semi-Conductor Tracker

The ATLAS Semi-Conductor Tracker (SCT) will have to reconstruct isolated lepton tracks with $p_t > 5$ *GeV/c* with an efficiency better than 95%

The SCT consists of four silicon barrels, with a total area of 34.4 m^2, and nine end-cap wheels on each side with a total area of 26.7 m^2. The barrel layers will have a radial spacing of 10 cm with the innermost layer at a radius of 30 cm from the beam axis. It will use a strip pitch of 80 µm that will allow a spatial resolution of 16 µm in the radial coordinate, and around 580 µm in the z-coordinate [15]. The total number of readout channels will be of $6.2 \cdot 10^6$. Figure 1.10 shows a drawing of the ATLAS inner tracker with its different subsystems.

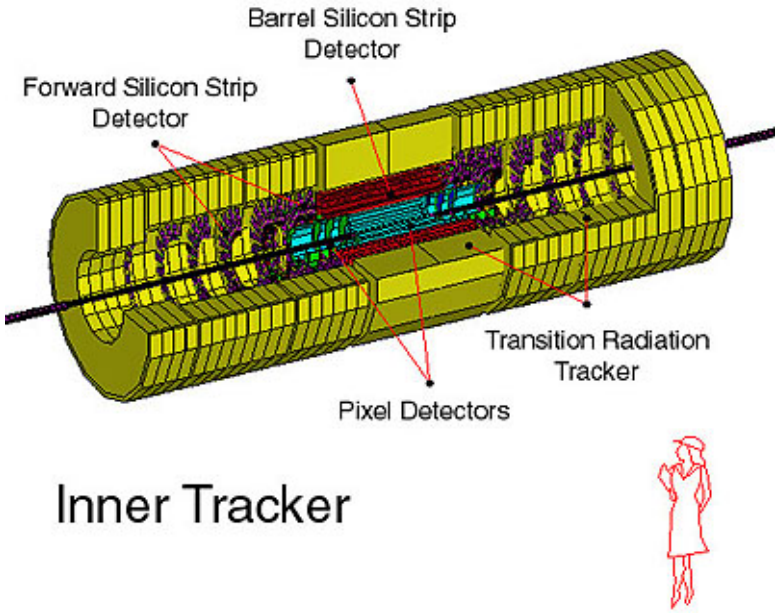

Fig. 1.10: ATLAS Inner Tracker detector.

1.5.2 ATLAS Pixel System

The ATLAS Pixel System will be composed of three barrel layers and eight disk layers, four in each side of the barrel. The barrel layers will be located from an innermost radius of 4.15 cm (limited by the beam pipe radius) from the beam axis, to a radius of 13.75 cm. The disks will be located from z = 49 cm to z = 103.5 cm. The total number of readout channels will be of $140 \cdot 10^6$. The spatial resolution in the radial direction will be of 12 μm, and in the z-coordinate it will be of 66 μm. Figure 1.11 shows a drawing of the ATLAS Pixel System.

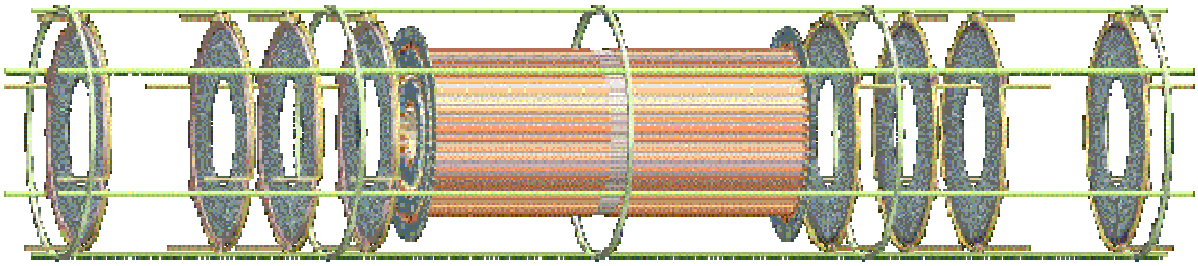

Fig. 1.11: ATLAS Pixel System detector.

1.6 *B* Physics and the LHCb Experiment

To fully exploit the physics potential offered by the large *b*-quark production cross-section at the LHC (10^{12} $b\bar{b}$ pairs produced per year), a dedicated experiment for *b*-physics is foreseen, called LHCb.

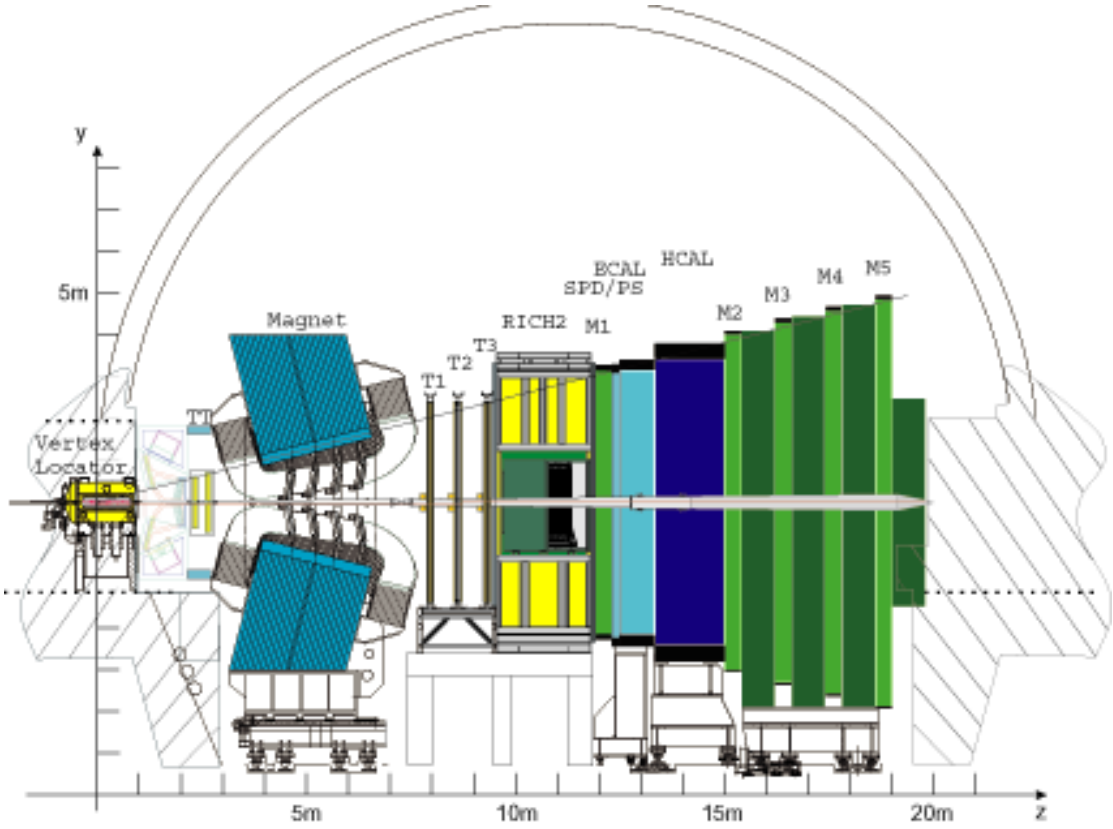

Fig. 1.12: The LHCb detector seen from above (cut in the bending plane).

LHCb will use a forward geometry, see Figure 1.12, which exploits the Lorentz boost of the $b\bar{b}$ system while sacrificing little acceptance as the quark pair tends to lie close in rapidity. The detector includes particle-identification capabilities and has excellent mass resolution.

1.6.1 The LHCb Tracking System

The main task of the tracking system is to provide efficient reconstruction of charged particle tracks and precise measurements of their momenta. It consists of four tracking stations: one located between RICH1 (see Figure 1.12) and the LHCb dipole magnet, and three stations located between the magnet and RICH2.

The Outer Tracker [16] uses straw-tube drift chambers with 5 mm cell diameter and covers the largest fraction of the detector sensitive area. The largest station will cover a

sensitive area of 720 cm x 600 cm. The Inner Tracker uses silicon microstrip placed in three stations at low angles and at the same locations as the Outer Tracker.

The Silicon Trigger Tracker (TT) [17] uses silicon microstrip detectors with a strip pitch of around 200 μm. Its sensitive area is around 11 m^2. Figure 1.13 shows a drawing of the Silicon Trigger Tracker.

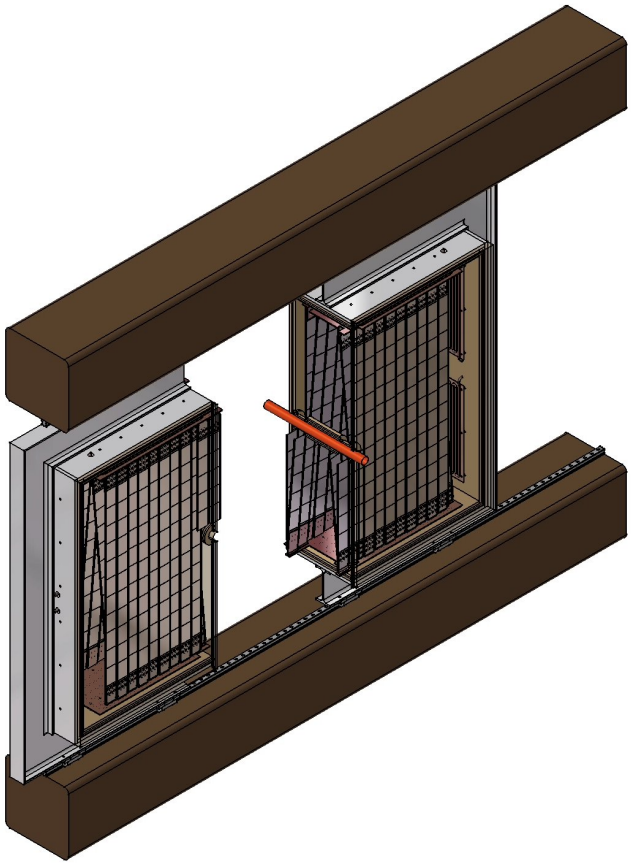

Fig. 1.13: Drawing of the Silicon Trigger Tracker.

1.7 ALICE

ALICE (A Large Ion Collider Experiment) is a dedicated heavy-ion detector that will exploit the unique physics potential of nucleus-nucleus interactions at LHC energies. Its objective is to study the physics of strongly interacting matter at extreme energy densities, where the formation of a new phase of matter, the quark-gluon plasma, is expected. Figure 1.14 shows an open view of the ALICE subsystems.

1.7.1 ALICE Inner Tracking System

The Inner Tracking System (ITS) will be made from six cylindrical layers of silicon wafers like the one shown in Figure 1.15. They will surround the collision point and measure the

properties of particles emerging from collisions. The ITS will look for particles containing strange and charm quarks by identifying the points at which they decay.

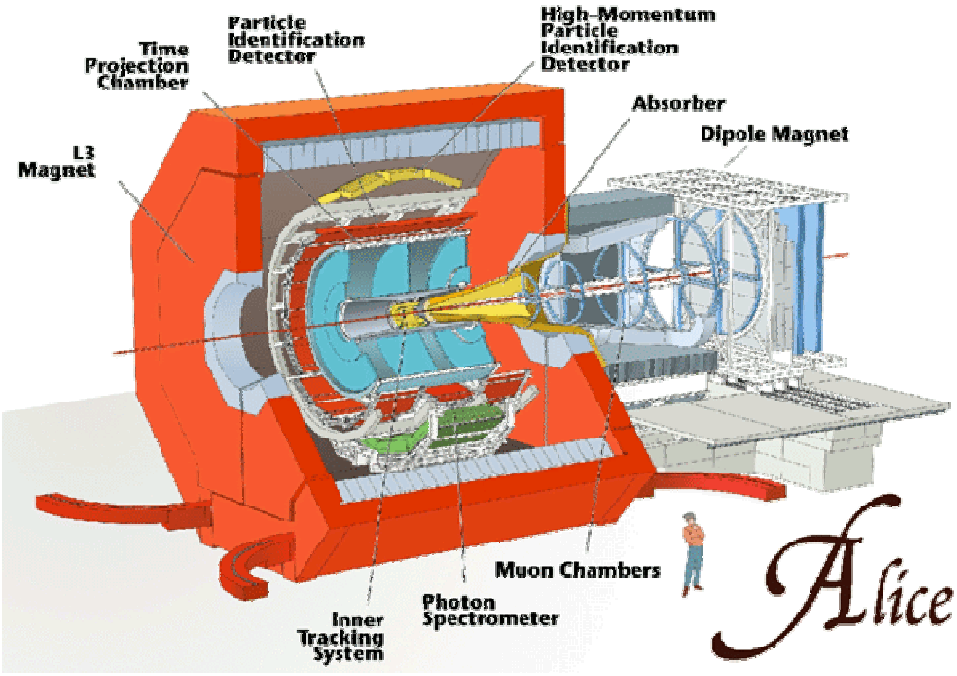

Fig. 1.14: Open view of the ALICE detector.

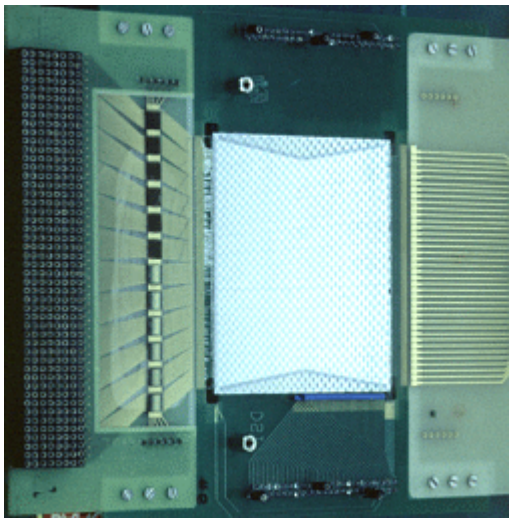

Fig. 1.15: Silicon sensor of the ALICE detector ITS.

Chapter 2

Radiation environment in CMS and ATLAS

The radiation environment close to the Interaction Points (IP), with the LHC producing around $8 \cdot 10^8$ *pp* inelastic events per second, at a luminosity of 10^{34} $cm^{-2}s^{-1}$ and for a total cross section of 80 mb, is going to be extremely hostile. The major radiation sources at LHC are:

- The particle production from proton interaction.
- Local beam losses.
- Beam-gas interaction.

In normal operating conditions beam losses should not exceed 10^7 protons/s [18]. Beam gas interactions are estimated to be around 10^2 $m^{-1}s^{-1}$ [18]. The main source of radiation is, during normal operating condition, the secondary particle generation from the proton collisions of the LHC beam (around 10^9 s^{-1}).

Those secondary particles will degrade the detector material, activate different components and damage semiconductor components of the readout electronics.

2.1 Radiation environment in CMS

The proton-proton collisions in the IP will generate a high amount of secondary particles and collision products that will deposit their energy in the material surrounding the interaction point (ionization) or will damage it by generating damage in the material bulks [19].

FLUKA [20] simulations allows to calculate the absorbed dose due to the energy deposition by particle ionization, and the particle fluence (in particles per units of area) which is an integration of the particle flux over a time period. The fluence gives an indication of the bulk damage induced in the materials. Table 2.1 gives the particle fluence for a year of normal operation, at the different sub-detector systems of the CMS. Note that the fluence and dose can vary by various orders of magnitude when moving along the radial component, while in the z direction those values remain almost constant.

	Neutron fluence [neutrons/cm^2] per year		Charged hadron fluence [particles/cm^2] per year		Dose [Gy] per year	
	Neutrons	**Position**	**Hadrons**	**Position**	**Dose**	**Position**
Tracker	10^{13}	In all r (independent of z)	$2.5 \cdot 10^{14}$	Low values of r (independent of z)	$\sim 10^5$	Low values of r (independent of z)
			10^{12}	High values of r (independent of z)	$\sim 10^3$	High values of r (independent of z)
ECAL	$< 4 \cdot 10^{12}$	Barrel	Contribution negligible		10^3	Barrel
	$2 \cdot 10^{13}$	Endcap for low r values	Contribution negligible		$3 \cdot 10^4$	Endcap
	$< 10^{12}$	Endcap for high r values	Contribution negligible			
HCAL	Negligible	Barrel	Less than 10% of the neutron flux		Contribution negligible	
	10^{14}	Endcap for low r values	Less than 10% of the neutron flux		$2 \cdot 10^4$	Endcap
	$\sim 10^{13}$	Endcap for high r values	Less than 10% of the neutron flux			
HF	$>10^{14}$	Inside	Contribution negligible		$5 \cdot 10^5$	Maximum dose in the inside
Muon chambers	$\sim 10^{11}$	Inside chamber	$\sim 10^9$	Inside chamber	10	Inside chamber
	$\sim 10^{10}$	Outside chamber	$\sim 10^8$	Outside chamber	1	Outside chamber

Table 2.1: Values of fluence and dose in various locations of CMS.

Figure 2.1 shows the particle fluence over a period of 10 years of LHC operation inside CMS depending on the radial position and at different z coordinates. The plot shows the strong radial dependence of the particle fluence in comparison with almost no dependence along the beam axis. 10 years is the expected lifetime for LHC operation. BCM sensors will be placed very near to the beampipe, i.e. in a very low radial position. They must resist all the fluence they will receive during 10 years and still be operational.

The next table (table 2.2) [21] shows the particle composition of the radiation field. The particles consist mainly of charged and neutral pions.

Type of particle	Percentage in the composition of the radiation field
Proton	3.2
Neutrons	3.2
Charged pions	49.6
Neutral pions	27.8
Electrons-gamma	4.1
Others	12.1

Table 2.2: Different types of particles that compose the radiation field in CMS.

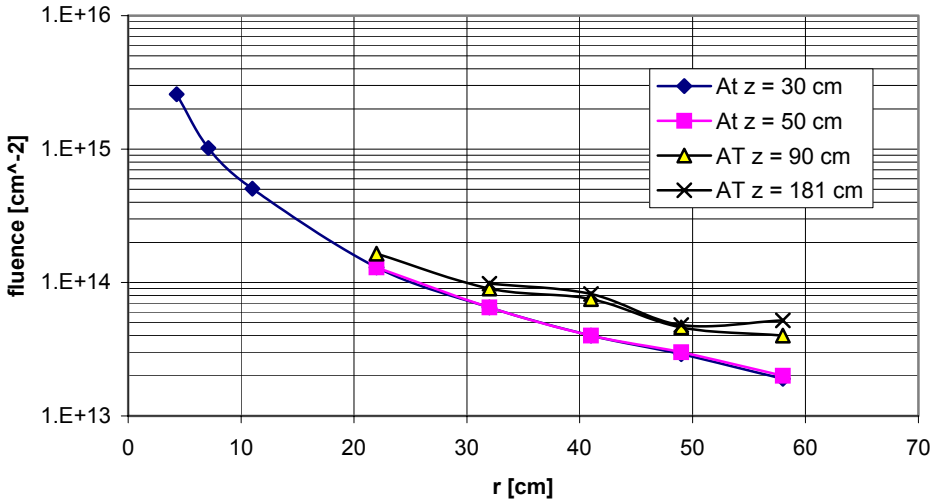

Fig. 2.1: Radial position at the IP5 against 10 years fluence, in normal operation conditions. Each line represents a different position on the z axis (direction of the beam). Data based on M. Huhtinen simulations.

2.1.1 Fluence and dose in the CMS inner pixel system

The particle fluxes and doses on the CMS inner pixel system region are very similar to those that the BCM sensors and readout electronics will encounter once placed in their positions in CMS.

Figure 2.2 shows the hadron fluence, the neutron fluence and the absorbed dose after 10 years of LHC operation in the pixel region: radial distances range from 4 to 11 cm, and z-coordinate ranges from 0 (the IP) to 30 cm.

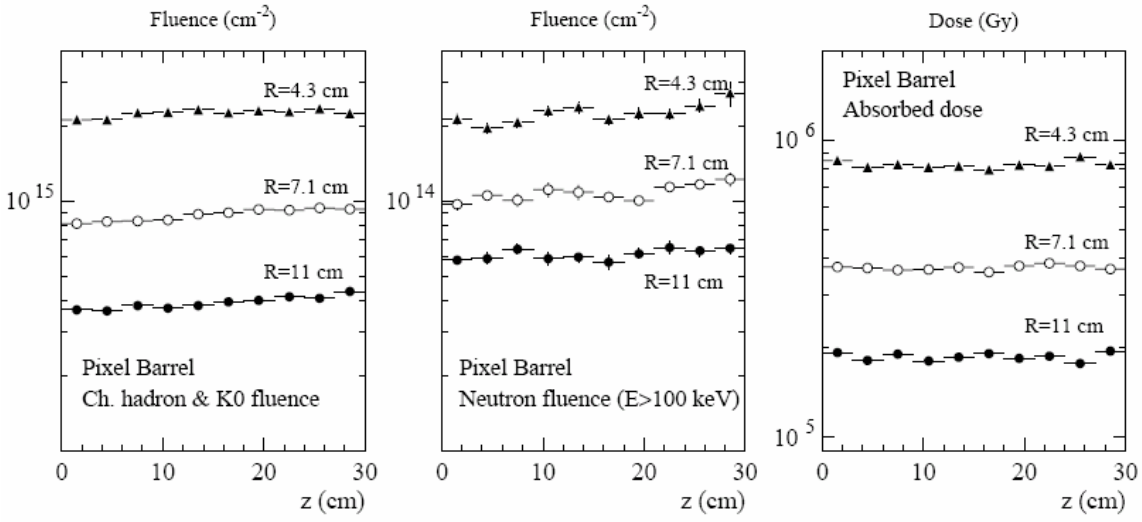

Fig. 2.2: Hadron fluence, neutron fluence and absorved dose after 10 years of LHC operation in the CMS pixel region.

2.1.2 Particle fluxes in the Tracker

In this zone there are two main contributions to the particle fluence, one comes from the charged hadrons generated by the bunch collisions, and the other comes from neutrons that are generated from the interactions between those above mentioned charged hadrons with the heavy materials ($PbWO_4$) which ECAL is made of.

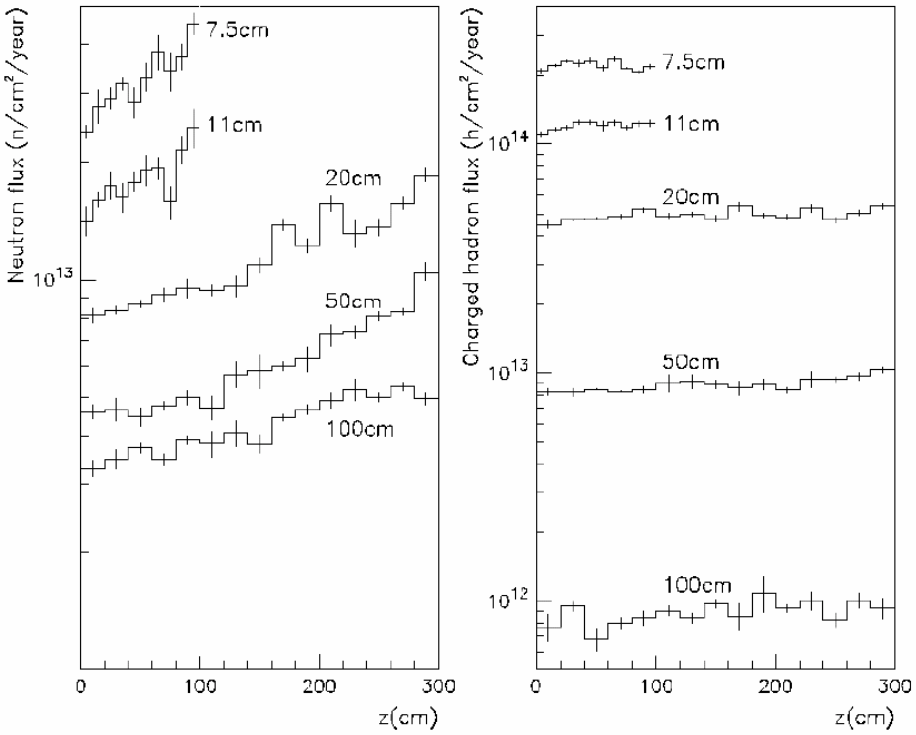

Fig. 2.3: Neutron flux (left) and charged hadron flux (right) in different regions of the CMS Tracker.

The neutrons are back scattered towards the tracking region. Simulation results plotted in Figure 2.3 show that the hadron flux is uniform along the beam axis but varies rapidly with the radial distances, because of the intense magnetic field present inside the experiment. The neutron flux varies with z by around a factor 2 from z = 0 to z ~300 cm. It is envisaged a flux of 10^{13} neutrons/(cm^2year) and 10^{14} hadrons/(cm^2year) for radial distances below 20 cm from the IP [21].

Figure 2.4 shows the deposited dose in the Tracker. The doses are uniform along the beam axis. Below 10 cm of radial distance the dose per year is around 100 kGy [22]. The contribution of high energy neutrons to the dose is negligible [23].

The interaction of particles with the silicon Tracker during the years of LHC operation will result in a decrease of the tracking and detection efficiencies. Neutrons damage the silicon lattice and generate dislocations leading to an increase of the depletion voltage and to a decrease of charge collection efficiency. Protons and charged hadrons generate the same effects on the silicon [24][25][26]. Energy deposition from ionization can create surface damage in semiconductors, affecting the readout systems and electronics.

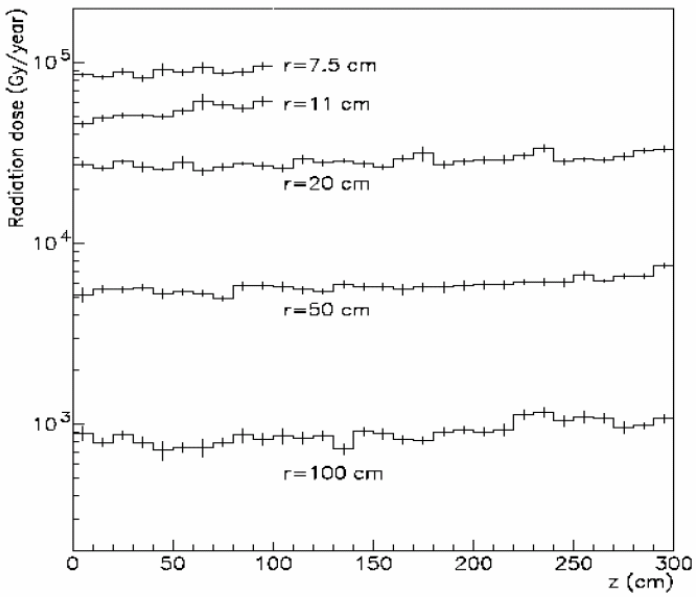

Fig. 2.4: Dose inside the CMS Tracker at different radial positions.

2.1.3 Particles fluxes and doses in the Forward Calorimeter (HF)

The position of this calorimeter is very close to the beam pipe. Due to this position the amount of energy absorbed in this forward calorimeter (HF) from the hadronic collisions is five times larger than the energy absorbed by the calorimeters in the central region of the experiment.

The interactions between the hadrons and the heavy materials composing the calorimeter generate a flux of neutrons larger than 10^{14} neutrons/(cm^{2}year), and a maximum dose of 500 kGy, as shown in Figure 2.5. The left plot of Figure 2.5 shows that the neutron fluxes at the back of the HF range from 10^6 neutrons/(cm^{2}s) to more than 10^7 neutrons/(cm^{2}s). On the external surface, those fluxes are of the order of 10^6 neutrons/(cm^{2}s).

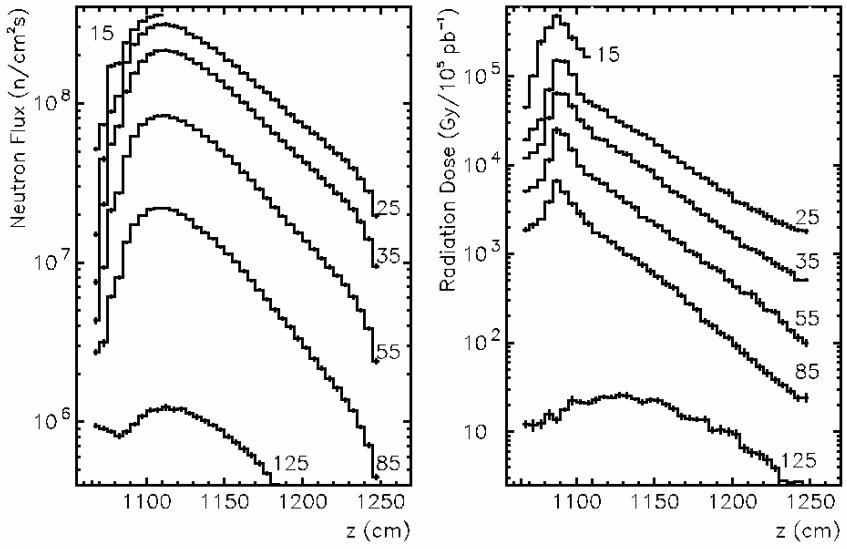

Fig. 2.5: Neutron flux (left) and dose (right) in the CMS forward calorimeter (HF) at different radial positions depending of the z coordinate.

2.2 Radiation environment in ATLAS

Table 2.3, shows the maximum doses and particle fluence per year in different ATLAS components [18].

The inner detector (containing silicon detectors) is exposed to intense particle fluence from charged hadrons, coming from the bunch interaction, and neutrons backscattered from the calorimeter.

Detector component	Dose [kGy/year]	Neutron fluence [cm^{-2}/year]	Total fluence [cm^{-2}/year]
Pixel	34	$1.6 \cdot 10^{13}$	$5.9 \cdot 10^{13}$
SCT (barrel)	15	$1.0 \cdot 10^{13}$	$2.7 \cdot 10^{13}$
SCT (forward)	10	$1.6 \cdot 10^{13}$	$2.2 \cdot 10^{13}$
GaAs	16	----	$1.3 \cdot 10^{13}$
MSGC	7.2	----	$2.0 \cdot 10^{13}$
Barrel TRT	2.5	----	$6.3 \cdot 10^{13}$
End-cap TRT	4.7	----	$1.3 \cdot 10^{13}$
Barrel em calor	0.6	----	$1.5 \cdot 10^{13}$
Barrel tile calor	0.02	----	$1.6 \cdot 10^{12}$
Barrel/EB crack	0.036	----	$2.0 \cdot 10^{12}$
End-cap em calor	53	----	$4.1 \cdot 10^{14}$
End-cap had calor	12	----	$6.1 \cdot 10^{14}$
Forward calor	2300	----	$1.0 \cdot 10^{16}$

Table 2.3: Maximal values per year for dose and fluence in ATLAS components.

Chapter 3

Accident scenarios

The LHC, with about 8000 magnets powered in 1700 electrical circuits, can suffer several different kinds of accidents or malfunctions that could lead to beam losses if any of those systems fails. Other accidents can be due to aperture restrictions provoked by beam screens, interconnections, vacuum valves or collimator jaws, more than 100, which can obstruct the beam passage.

Those beam losses can happen either in a single turn, with a sudden beam loss, or in progressive losses during numerous turns. One turn failures are called ultra-fast losses. Multi-turn failures can be divided between very-fast losses, those who happens in less than 5 ms, fast losses, which happen in more than 5 ms and steady losses, where the beam is lost in one second or more.

3.1 One turn failures

One turn failures can be provoked by an injection failure or by a failure during a beam dump [27].

For the injection the beam is accelerated in the SPS to 450 GeV and transferred to the LHC through a 2.8 km long transfer line [28]. During the extraction from the SPS the beam could damage septum magnets [29] or kicker magnets [29]. A failure of those magnets would steer the beam onto a wrong trajectory. A wrong current value in one of the magnets, or in case of an aperture restriction, i.e. a closed vacuum valve, the beam will be lost. The worse case during injection would be that a corrector magnet close to one of the experiments is set to maximum current, in that case the beam will go directly into it. The damage produced by the beam at 450 GeV is proportional to 10-20 bunches of the beam at nominal intensity [27].

A possible scenario for a extraction failure is the pre-firing of one of the 15 kicker magnets of the beam dump system. In that case the other 14 kickers will be immediately triggered, dumping the beam, but deflecting part of it not to the dumping line. Other similar possibility would be an unsynchronized beam abort, on which the dump kicker does not hit the abort gap. In both accidents some of those deflected bunches will still run through the accelerator and collide with collimators, equipment or even experiments. These kinds of accidents are considered to be the worse case in reference of particle fluence and are studied more deeply in section 3.3.

In order to extract the beam properly a gap of 3 μs in the beam is set to be free of particles. The beam dump kicker system must be synchronized with this abort gap in order no wrong deflection of particles is produced. Debunching caused by RF noise or intrabeam scattering populates the beam abort gap [30].

For this type of losses, ultra-fast losses, no prevention of the accident is possible. All the protection will rely on collimators and beam absorbers.

3.2 Multi-turn failures

These kind of losses can be provoked by quenches of superconducting magnets [27] or power failures in single or several magnets. The current decay on a superconducting quenching magnet is approximately Gaussian [31], with the maximum corresponding to the initial current, down to the zero current. The magnetic field decays following the expression:

$$\frac{\Delta B}{B_0} = 1 - e^{-\frac{t^2}{2\sigma^2}} \tag{3.1}$$

where B is the magnetic field value, B_0 the initial magnetic field, and σ the decay time constant for a quench, that has a typical value of 0.2 seconds [32].

Other hardware failures, power converter failures, have an exponential decay of the magnetic field in the magnet

$$\frac{\Delta B}{B_0} = 1 - e^{-\frac{t}{\tau}} \tag{3.2}$$

with τ_d the decay time constant that is calculated dividing the inductance L by the resistance R, $\tau_d = L/R$. Table 3.1 lists the fastest beam losses after equipment failure.

Magnet System	Operation Mode	ΔT
D1 warm	Collision	5 turns
Damper	Injection	6 turns
Warm quadrupoles	Any	18 turns
Dump septum	Any	35 turns
Warm orbit corrector	Collision	55 turns

Table 3.1: Top 5 of the fastest losses after equipment failure. The second column specifies the operation mode for which the losses can occur (injection versus collision optics). The third column gives the maximum time interval before beam loss will happen. [33]

The shortest time interval is only 5 turns, and corresponds to the warm dipole D1 magnets. Taking into account that a particle in the beam makes a turn in 89 μs, that time interval is about 425 μs. This time sets in a way the response time of the BCM system.

A failure in a dipole magnet will distort the beams. The deflection angle caused by the variation in the magnetic field is

$$\Theta = \frac{e}{p} \cdot l \cdot \Delta B \tag{3.3}$$

where l is the magnet length and p the particle momentum.

The D1 magnets are single aperture separating dipoles, both beams are held in the same aperture, ready to be put separated into two beam pipes. They will be installed next to the quadrupole magnets close to the interaction point. A scheme of the positions is given in figure 3.1.

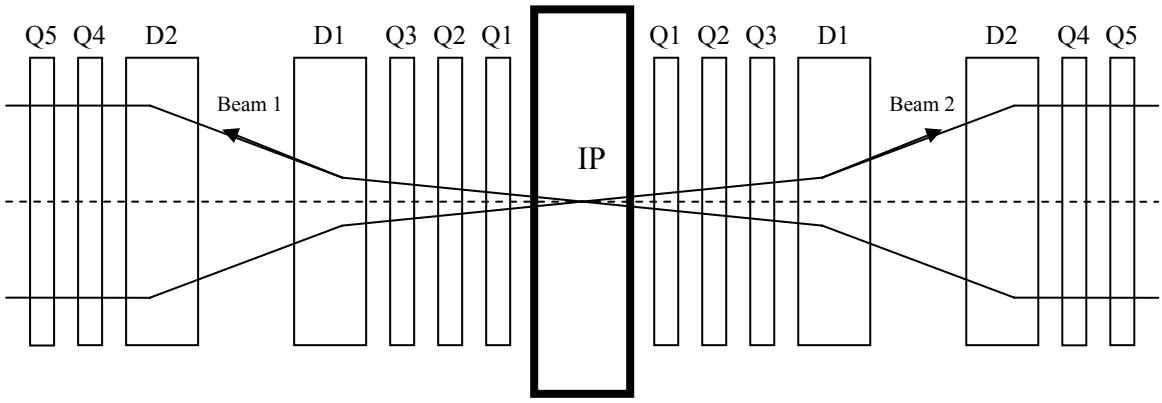

Fig. 3.1: Scheme of the magnet locations around the interaction point. Q refers to quadrupole while D refers to dipole. Q3, Q2 and Q1 form the inner triplet.

There are only warm D1 magnets at IP5, CMS, and IP1, ATLAS. At IP2, Alice, and IP8, LHCb, superconducting (cold) magnets will be used, one on each side of the IP. The warm D1 magnets consist of a succession of 6 magnets on each side of the IP, their length being 3.4 m and their nominal magnetic field 1.38 T. The whole 12 magnets are connected in series to one power converter.

3.3 Worse case scenario

As previously said, the worse case scenario that an experiment, such as CMS, can face would be a beam deflection generated by the beam dump magnets. Two different scenarios have been envisaged [34]:

- Single module pre-fire: Where accidentally one of the 15 kicker magnets from the beam dump system fires. The rest modules will be immediately triggered. This is an unlikely scenario. The accident duration is of 86 μs and $4 \cdot 10^{13}$ protons will be lost in IP5.

- Unsynchronized beam abort: This happens when the dump kicker does not hit the abort gap. The bunches are swept out for 3 μs until the kicker reaches its nominal magnetic field (full strength). Some of the deviated bunches will continue to run in the machine and they will hit the next limiting aperture. The accident duration is of 260 ns and 10^{12} protons will be lost in IP5.

Beam abort malfunctions will mainly affect the CMS, located in IP5, since it is the experiment which is closer to the dump insertion in IP6. A Fluka simulation showing a mapping of the dose generated in the CMS due to an unsynchronized beam abort can be seen in figure 3.2.

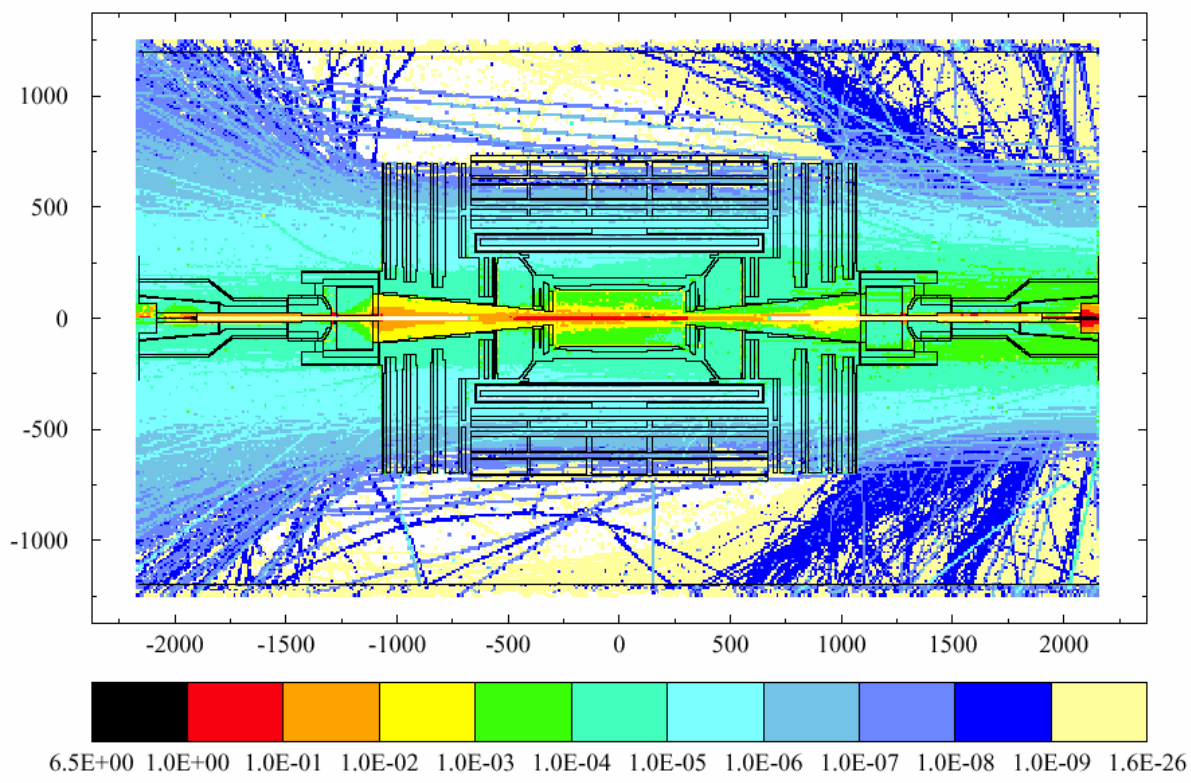

Fig. 3.2: Simulation showing a mapping of the dose in Gy due to a pre-fire accident of the kicker magnets. The dose is integrated during 260 ns. Source of the picture: M. Huhtinen.

For the positions where the BCM sensors are planned to be located this accidents represents an increment of dose rate of 10^8. Figure 3.3 shows a detail of the inner part of the experiment, closer to the IP. The dose rate for a position at 4.3 cm from the beam line is about $3.8 \cdot 10^4$ Gy/s while in normal condition this dose rate would be of $2.6 \cdot 10^{-3}$ Gy/s. The particle flux during this beam accident is expected to increase by a factor of up to 10^9 compared to normal running conditions. The flux during normal operation near the interaction point is 50 to 60 MIPs/(cm^2μs) [35].

A test beam to simulate the particle fluxes involved in that kind of accident was dedicated for testing the response of the BCM sensors to it. This test beam and its results are explained in detail on chapter 9.

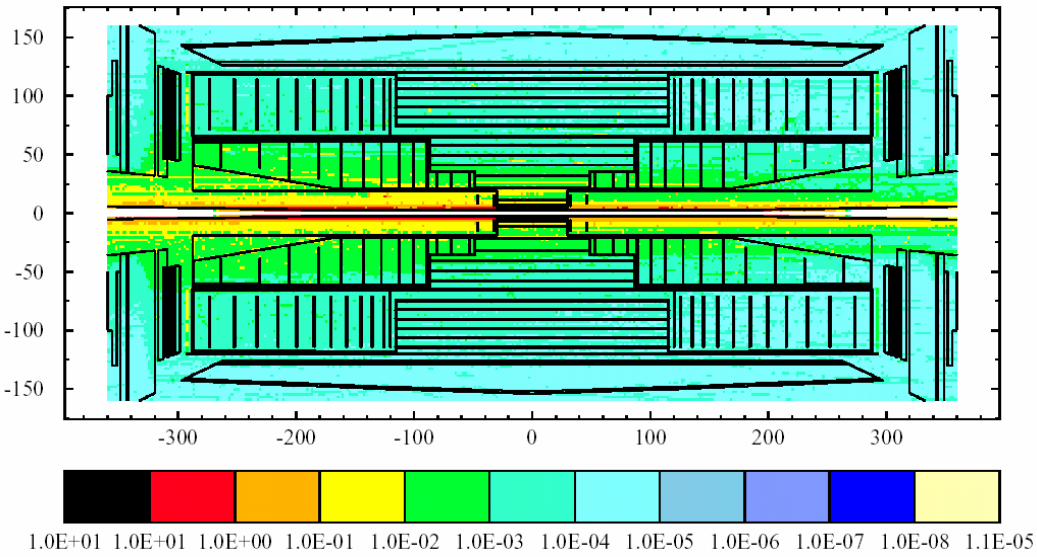

Fig. 3.3: Simulation showing a mapping of the dose in Gy due to a pre-fire accident of the kicker magnets. The dose is integrated during 260 ns. Source of the picture: M. Huhtinen.

Chapter 4

A Beam Condition Monitor proposal for the experiments of the LHC

4.1 Beam Condition Monitor purpose

The purpose of the Beam Condition Monitor (BCM) is to provide real-time radiation monitoring within CMS and ATLAS, to detect and initiate protection procedures for detector subsystems at the onset of beam instabilities and accidents. In order to do so the BCM has to be able to detect abnormal particle fluxes and send a signal to the beam interlock in order to dump the beams.

The BCM will be the central part of the radiation monitoring system for the safety of the equipment (see Appendix). The goal is to provide the monitoring information in the time scale of the LHC beam structure of 25ns. Another issue for the BCM is to provide a fast feedback to the machine for the optimization of the beam conditions.

The BCM should work together with the LHC machine protection system and will interact with the other safety systems from the experiments, such as the Detector Safety System (DSS) [36], and from the machine, such as the machine interlock system or the Beam Loss Monitors (BLM) [37].

The DSS also requires an input to the interlock system to dump the beams. This last system only accepts one input per experiment, this means that the DSS and the BCM will have to share the experiment input to the interlock system. The DSS will also record the BCM sensor readings for online and post mortem evaluation.

In the case where the beam is dumped, either by an alert signal from the BLM or the BCM, the readings from the sensors of both systems will be analyzed. In order that these readings could be compared, the BCM readout has to assign a time flag to every reading or group of readings.

4.2 The Detector Safety System

The role of the DSS is to safeguard the experimental equipment. It acts to prevent damages from any detected faulty situations such as: too high temperature, water leaks, etc, either inside or outside the detector.

The DSS will automatically detect a faulty situation. The action is then initiated by a Detector Safety Unit (DSU). These actions will generally disrupt the process of data taking.

The DSS front-end comprises a number of sensors and a set of Programmable Logic Controller (PLC) based DSUs interconnected via a reliable network. The DSS Back-end is based on PVSS [38] and it readouts the DSUs actions.

The front-end accepts inputs from its dedicated analogue and digital sensors and signals directly from the sub-detectors. A scheme of the interaction of the DSS with other systems, like the Detector Control System (DCS) and the CERN Safety System (CSS), and the connections with the DSUs and the experiment, is shown in Figure 4.1.

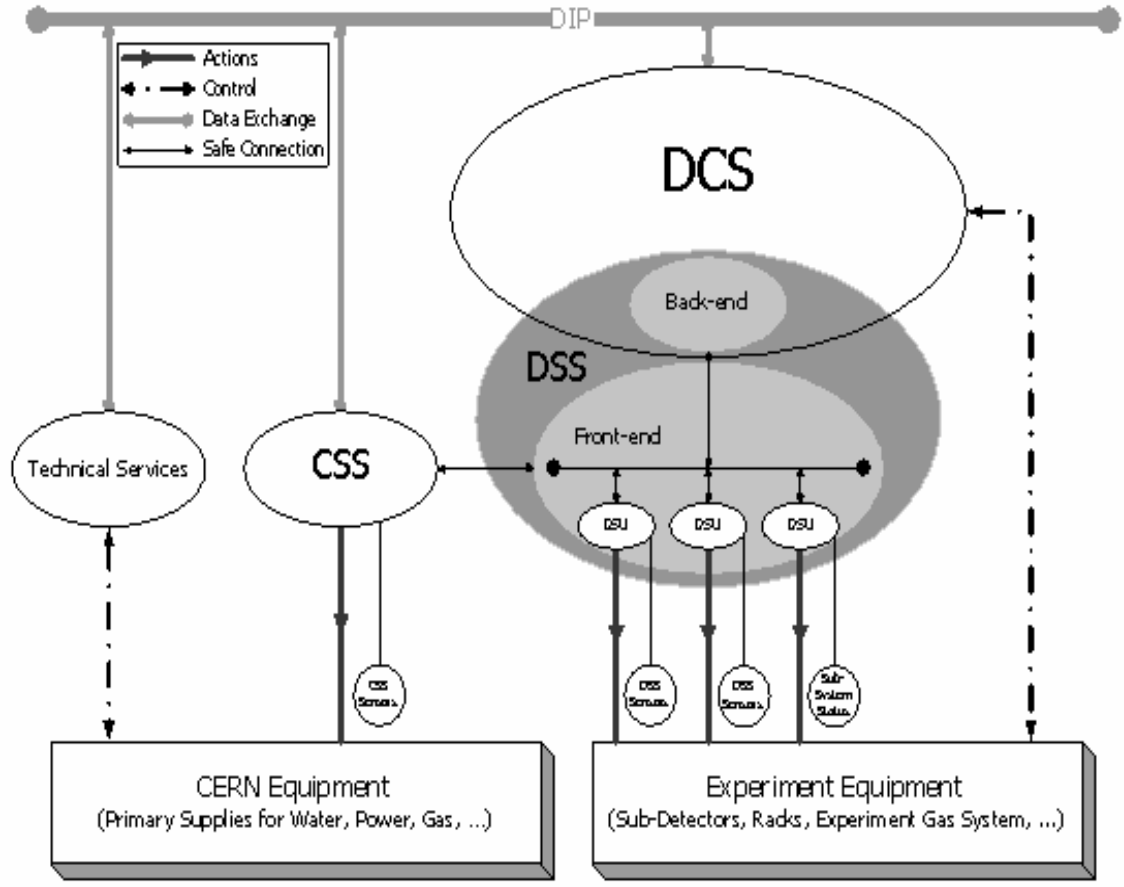

Fig. 4.1: Context diagram of the DSS system respect to the CSS the DCS and the Technical Services.

4.3 The Beam Loss Monitoring system

The BLM system of the LHC is one of the most critical elements for the machine protection. It must prevent the super conducting magnets to quench [39][40] as a result of energy deposited by lost protons, an equivalent energy of 10^6 protons at 7 TeV/m for a loss duration of 1 turn (10^9 protons/m at 450 GeV for a loss duration of 1 turn) is enough to quench the magnet [41], and the machine components from damages caused these same beam losses. It will help in the evaluation and identification of the loss mechanism.

The system will generate a beam dump trigger when the beam losses exceed the designated thresholds.

The required time resolution for the monitors depends in their location [37]. The time resolution, the time in between of each measurement, for the monitors has to be 89 μs (1 turn). The 1 turn resolution allows to extract the beam with a delay of maximum 3 turns.

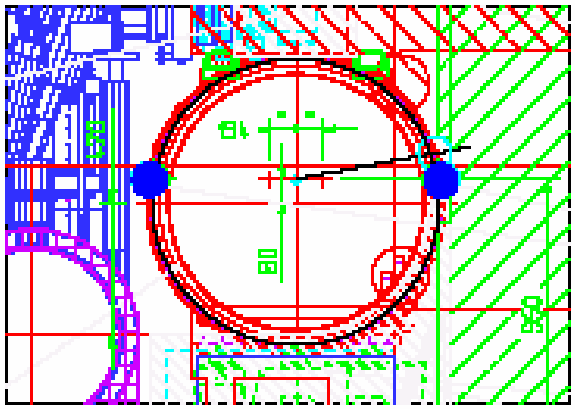

Fig. 4.2: Cross section drawing of the LHC tunnel with the cryo line (lower left corner) and the cryostat of a quadrupole magnet. The beam loss detectors are indicated by the two blue circles.

The measurement principle is based on the energy deposition detection of secondary shower particles using ionization chambers [40] and on secondary emission monitors located outside of the magnet cryostats. The beam loss monitors are placed on either side of the magnets in the horizontal plane defined by the beam vacuum tubes in order to obtain the maximum signal and to be able to distinguish between each beam of the LHC. In Figure 4.2 one can see the locations of the monitors. At this position, the secondary particle fluence is the highest and the losses from the two beams can be distinguished by time of flight as the separation of the monitors is the largest possible.

4.4 The machine interlock system

The different protection systems mentioned above work independently from the others. However, they must be coordinated and linked in a common structure. The machine interlock system is in charge of receiving the output information from the different protection systems and, together with other machine systems and experiments, has to generate the proper actions to ensure safety.

The architecture of the machine interlock system is divided in two separate systems: the Powering Interlock system and the Beam Interlock system. These systems are independent although the Powering Interlock will send a signal to the Beam Interlock in case of a power fault.

The Powering Interlock system allows to power the magnets when some specific conditions are met and causes a safe discharge of the energy stored in the magnet system in case of a quench or other failures.

The Beam Interlock system will allow the injection of the beam to the machine if a number of safety conditions are met. It will request a beam dump by the Beam Dump system if any unsafe situation is detected. Figure 4.3 shows the layout of the Beam Interlock system,

and it can be seen that a Beam Interlock Controller (BIC) will be installed in either side of each IP.

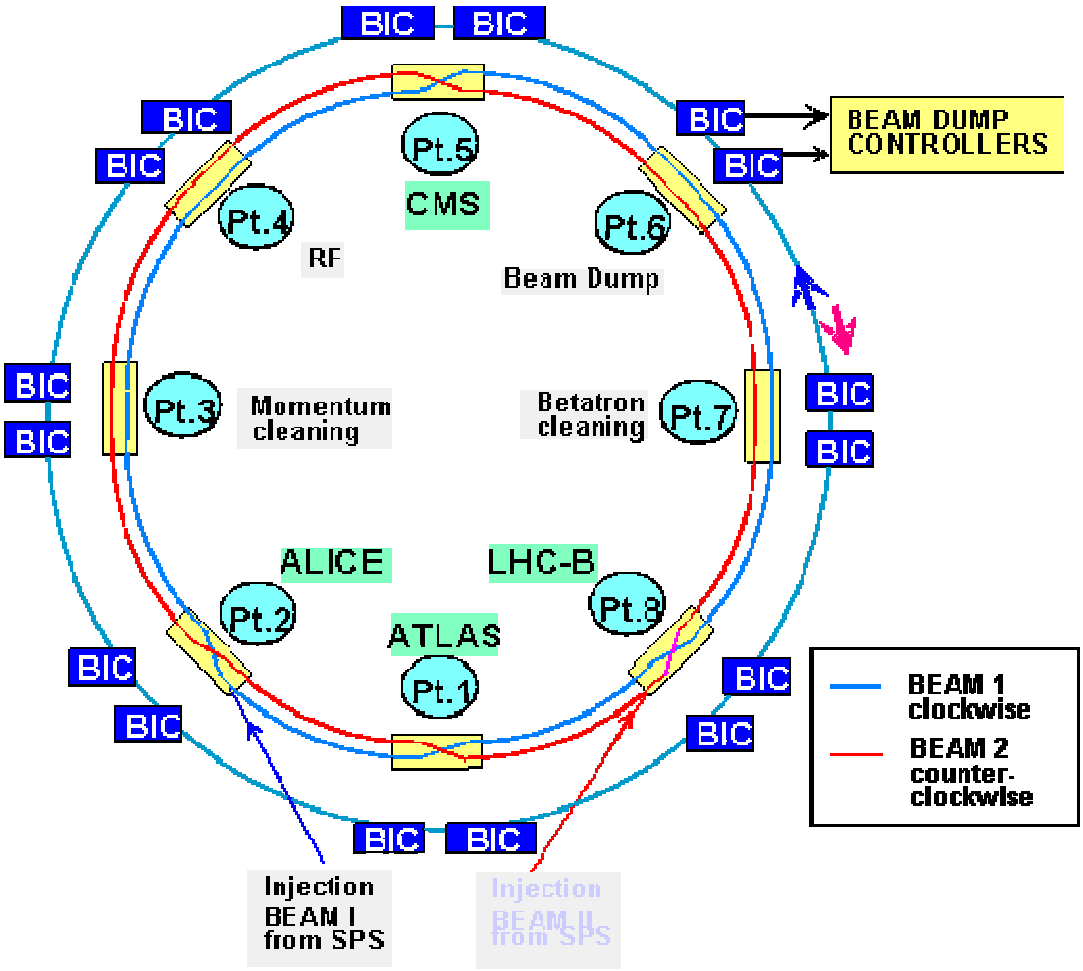

Fig. 4.3: General layout of the Beam Interlock system.

The BIC are connected to two fast links, the Beam Permit Loops (BPL). When the loops are broken, the beams are extracted into the beam dump blocks by the Beam Dump system. These loops will check the state of every BIC at a frequency of 10 MHz. In addition, a computer connection to the BIC is required in order to monitor, test and do a post mortem analysis of the fault causes. Figure 4.4 shows a scheme of the diverse inputs to a BIC: the Quench Protection System (QPS), the experiments (CMS, LHCb, etc.), the BLM. In the case where some or a group of inputs send an abort signal, the switch that the BPL controls will close the circuit and a beam dump will be triggered.

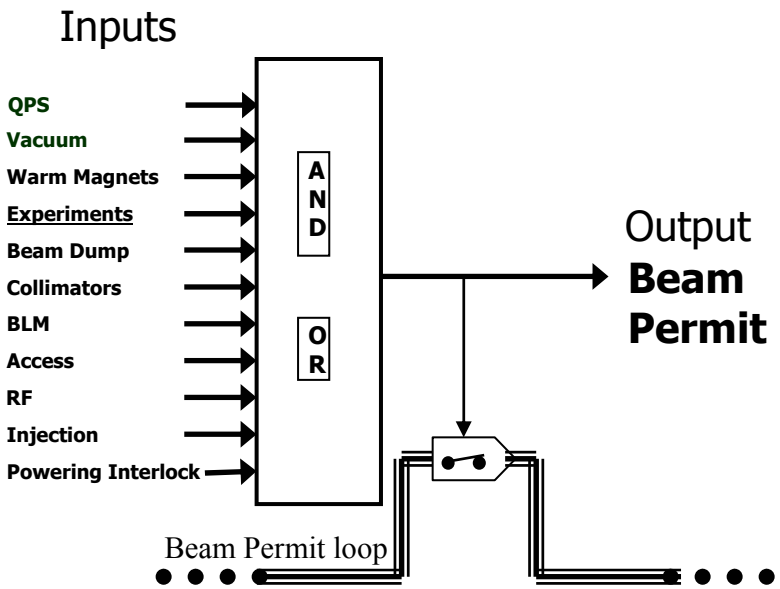

Fig. 4.4: Input signals on a BIC. The output will close the BPL triggering a beam dump.

4.5 Location of sensors and restrictions

BCM sensors will be located close to the beam pipe (see Figure 4.5). Fast electronics will be placed either inside or outside the main volume of the experiment and will process the signal from the sensors.

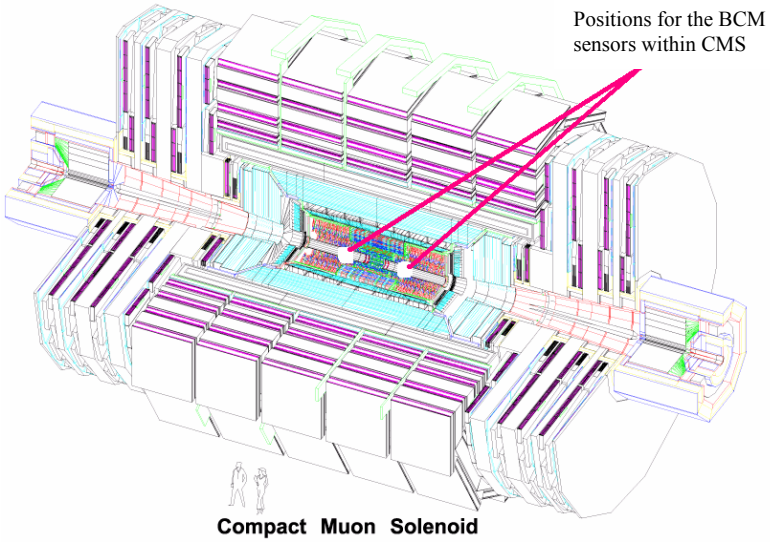

Fig. 4.5: View of the CMS experiment with possible locations for the BCM sensors.

Due to spatial restrictions and the high levels of particle fluence (see Chapter 2) in the positions where the sensors have to be placed, the BCM detector has to be small and radiation hard. CVD diamond was chosen for this application because it meets both requirements of

being small and of being able to withstand high level of particle fluence. Moreover, it requires minimal services (it does not need cooling), presents low leakage currents (less than 1 nA), and has a fast signal response (~1 ns).

The sensors will be readout by a coaxial cable whose length will be around 16 meters. A cable of this length will add a level of electronic noise equivalent to the electrons generated by a MIP. In order to detect single MIP events, fast current amplifiers will have to be positioned close to the sensors (from 15 to 30 cm away), and must be also radiation hard and small. A short description of the amplifiers will be given below. Figure 4.6 shows the possible location of one sensor, close to the beam pipe, and the path that the cable should follow to drive the signal to the readout electronics.

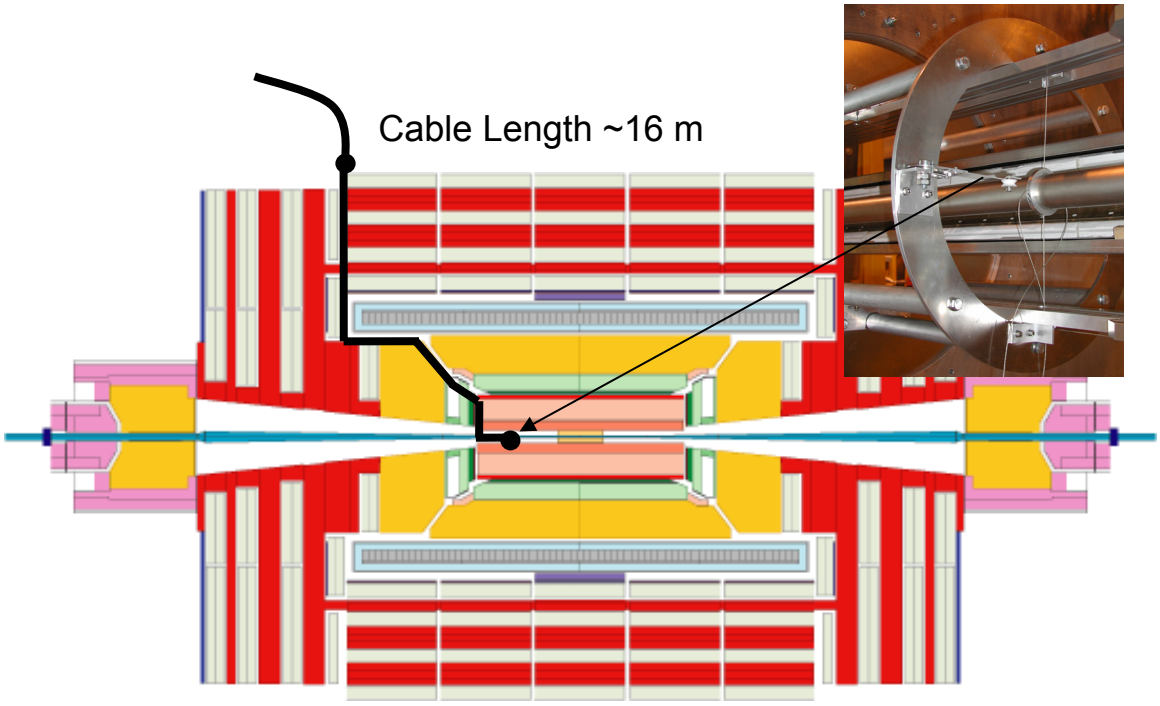

Fig. 4.6: Position of one of the BCM sensors close to the beam pipe and path of the cable that sends the readings to the readout electronics in CMS.

There will be a set of minimum four sensors on each side of the IP, approximately 3 m away from it in the beam axis direction (12.5 ns from the IP). The four sensors of each group will be located very close to the beam pipe, at a radial distance from the beam axis of around 4.5 cm, surrounding the pipe as shown in Figure 4.7. With this disposition the sensors must be able of detecting lost protons from the beam, or the collision products from lost protons which travel along the beam. Also if the beam goes of axis being close to the beam pipe will allow a better recognition of deterioration of the beam condition.

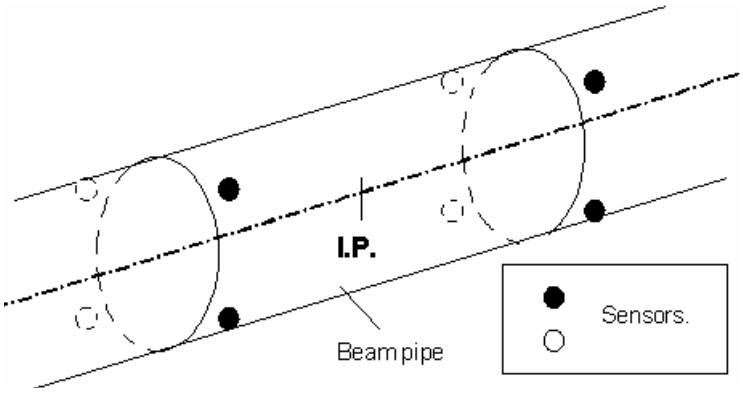

Fig. 4.7: Scheme of the sensor disposition around the beam pipe.

The sensors should be able to detect the beam halo when the beam is moving off axis, following a distortion of the orbit caused by some dipole failure, or an "explosion" of the emittance caused by some quadrupole failure. The signals will be read, amplified and sent to a FPGA (Field-Programmable Gate Array) that will process the signals. The logic will then decide whether it is appropriate or not to send a dump signal to the BIC.

4.6 Readout system

The readout of the BCM sensors will be done in this way: the generated signal in the detectors will be amplified by low-noise fast current or voltage amplifiers, and then the amplified signal will be sent outside the CMS volume through a coaxial cable. The current will be then transformed to a light signal by an opto-hybrid that will send this light towards the control room where it will be transformed to current again. The signal analysis will be done by FPGAs in which a logic which will decide whether the beam conditions are good or not has been implemented.

FPGAs are programmable digital logic chips. They can be programmed to do almost any digital function. An FPGA is similar to a Programmable Logic Device (PLD), but whereas PLDs are generally limited to hundreds of gates, FPGAs support thousands of gates.

4.6.1 Amplifiers

The amplifier for the BCM will be a fast, low noise, current amplifier. Its source will be the BCM sensor and its charge the readout electronics that will follow.

To detect a single MIP the amplifier must be close to the sensor, therefore inside the experiment volume. The noise that generates the cable used to drive the signal out from the experimental volume is of the same order of magnitude that the number of electrons generated by a MIP in the sensor (around 7000 e^- in diamond and 15000 e^- in silicon). Therefore the amplifier must be low noise. It must also be radiation hard in order to resist the doses that will be at a distance of 15 to 20 cm from where the sensors sit.

Different amplifiers have been studied and more are still under study. Some of them are not radiation hard, thus, with them it will not be possible to detect single MIPs from the bunch crossing during normal operating conditions, but it will be possible to detect adverse beam conditions and the development of an accident.

In LHC the bunch crossing is produced every 25 ns. The amplifier must have a fall time shorter than this time.

A possible option to be used is a *differential amplifier*. This type of device amplifies the difference between two input signals (-) and (+). A differential amplifier which presents a great gain is called *operational amplifier*. Operational amplifiers are made as integrated circuits. One of its greatest advantages is its miniaturization. The dimensions of an operational amplifier can be of the order of the mm^2.

4.7 Similar beam monitors

4.7.1 Radiation monitoring and abort system in BaBar

The BaBar detector [42] consists of a silicon vertex detector, a drift chamber, a Cherenkov based particle identification system, a CsI electromagnetic calorimeter, and a magnet with an instrumented flux return, their muon detector.

Three of the BaBar subdetector systems, the Silicon Vertex Tracker (SVT) [43], the Drift Chambers (DCH) [44] and the Electromagnetic Calorimeter (EMC) [45] use PIN diodes and CVD diamond detectors to monitor backgrounds and, in case of failures, send abort signals to the PEP-II accelerator [46].

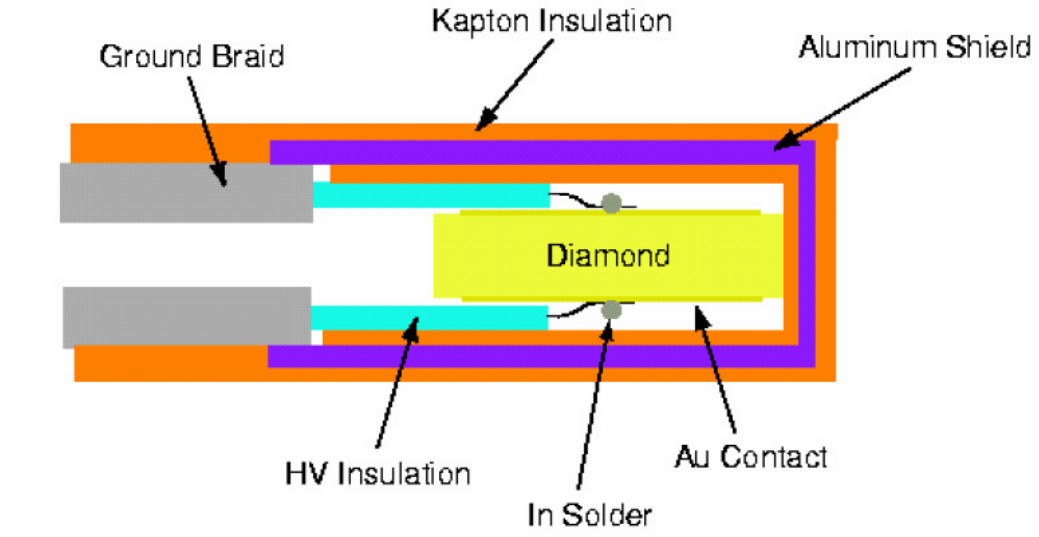

Fig. 4.8: CVD diamond sensor setup.

Figure 4.8 shows the diamond sensor setup located near the interaction region close to the beam pipe (see Figure 4.9). Figure 4.10 shows a picture of the diamond sensor itself with its gold metallization and cable connections.

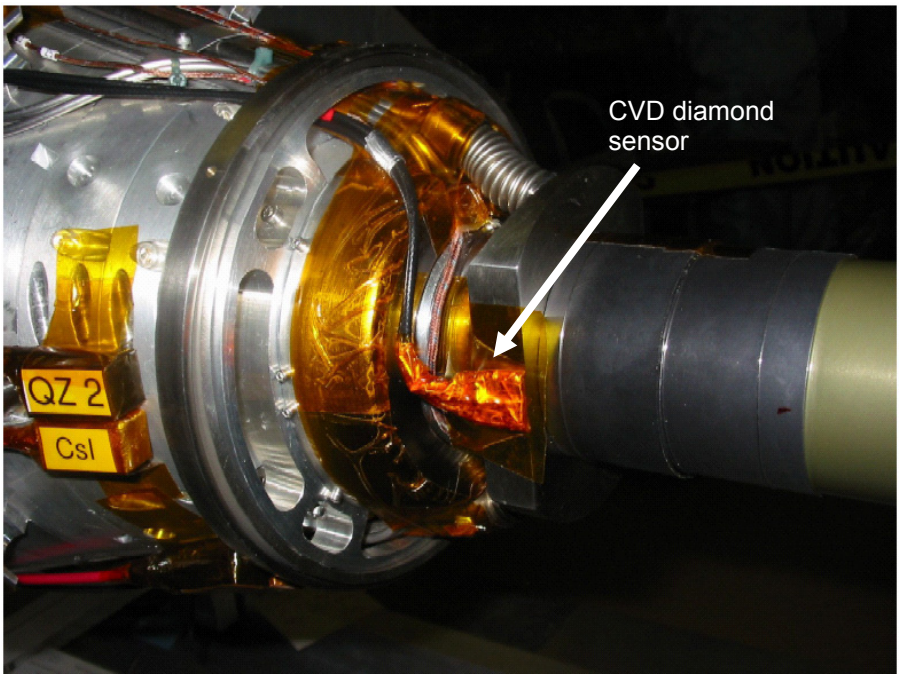

Fig. 4.9: CVD diamond sensor setup in its location at BaBar.

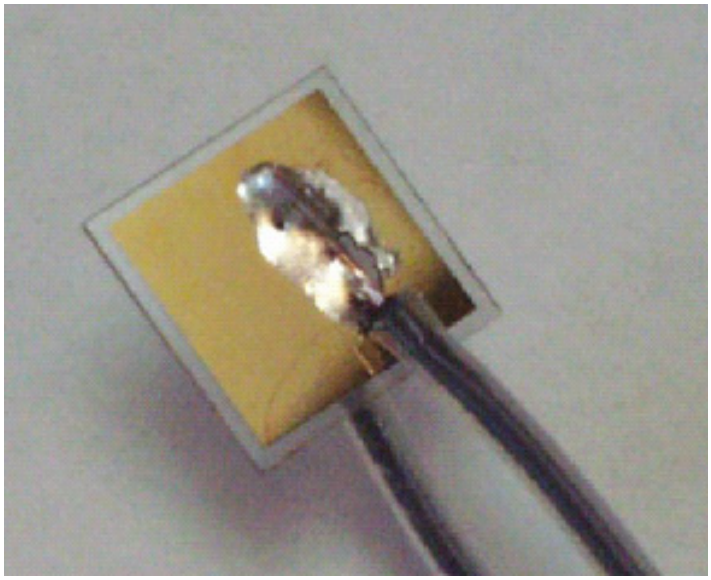

Fig. 4.10: CVD diamond sensor used at BaBar.

The diamond sensors and the silicon diodes detect the particles generated at each bunch crossing. Figure 4.11 shows the currents from both sets of sensors and it can be seen how they follow each other. These signals are also compared to the beam current of the LER (Low Energy Ring). Again, the currents of both sensors follow the LER current. The diamond detectors are observed to be less noisy than the diodes.

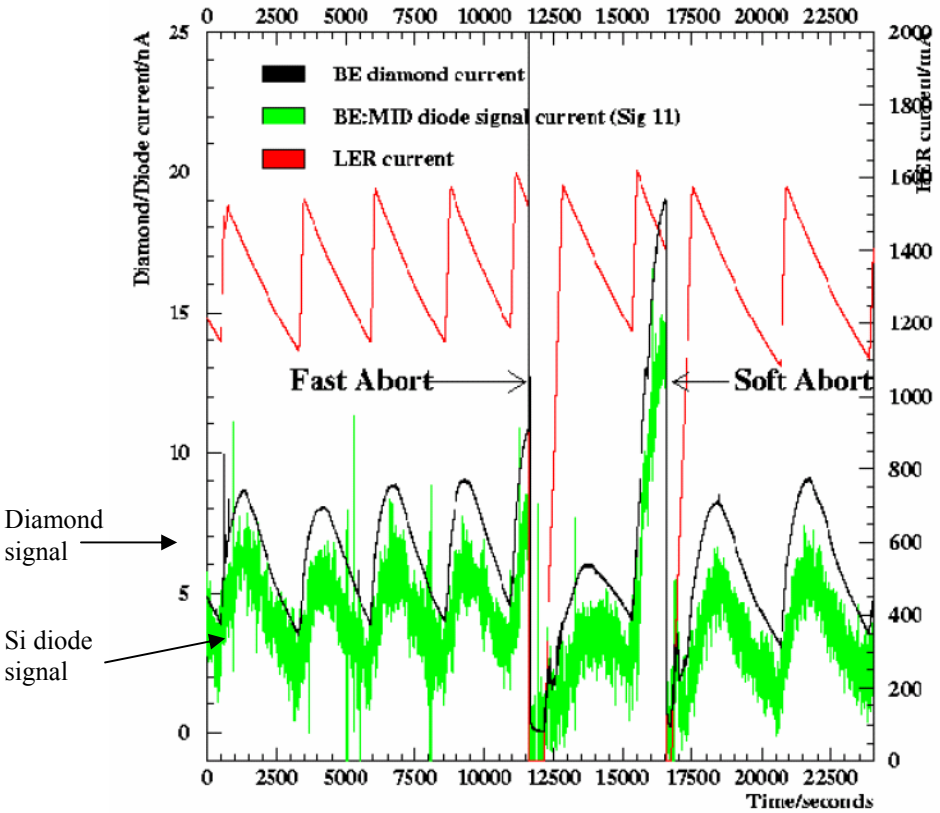

Fig. 4.11: Signal from the diodes and the diamond. The diamond follows closely the diode signal.

In BaBar, the nominal radiation doses in the horizontal plane are 30-40 mRad/s during injection and 15-25 mRad/s during stable colliding beams are. These dose rates are primarily due to degraded energy electrons and positrons generated nearby by beam gas bremsstrahlung and to scattered beam particles from distant Coulomb interactions. Synchrotron radiation does not add any significant contribution.

The readout is located a few tens of meters from the sensors. Each sensor is used either to monitor the dose rate or as an input to the protection circuitry for a beam-abort interlock system. Typical dose rate thresholds for the protection system are 150 mRad/s. The fastest response time for the protection circuit is about 500 μs.

4.7.2 BELLE diamond beam monitor

Belle [47] is an experiment at the KEK B-factory [48]. Its goal is to study B-physics at the Γ(4S). The system used is very similar to the one in BaBar. Figure 4.12 shows a diamond sensor close to the interaction region.

Beam background is one of the most important issues in the KEKB/BELLE operation, since the BELLE detector has a micro vertex detector surrounding the collision point where this background is at its highest level. The electronics used there is based on CMOS technology which is not radiation hard. The dose tolerance of the electronics used in the BELLE vertex detector is as low as 200 kRad.

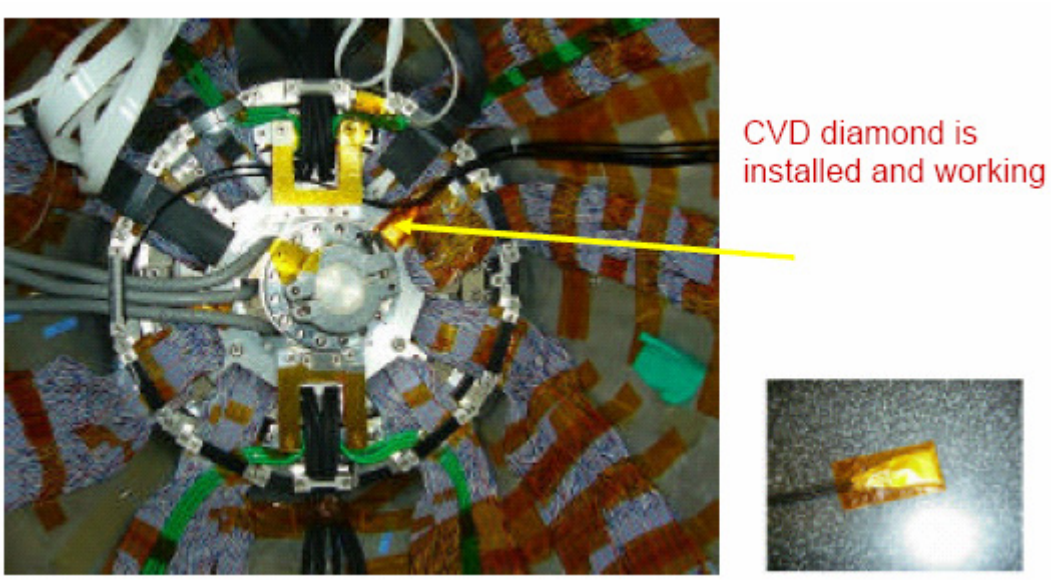

Fig. 4.12: CVD diamond sensor setup in its location at Belle. Left: Diamond sensor.

Several kind of radiation monitors are installed in the BELLE detector. PIN photodiodes and CVD diamond sensors are placed inside the vertex detector system to monitor instantaneous dose rate. Accumulated dose is also checked regularly by radiation field effect transistors (RadFET), which are sensitive to the accumulated surface damage from ionizing radiation. The integrated dose is obtained from the change in threshold voltage of the RadFET devices.

4.7.3 Radiation Monitor for the ZEUS detector at HERA

A radiation monitoring and automatic beam dump system has been installed in the interaction region of the ZEUS experiment [49] during the last upgrade of the electron-proton collider HERA [50]. It is used to prevent the ZEUS Silicon Microvertex Detector (MVD) [51] from beam background induced radiation damage during HERA operation. The dose rate measurement is based on the readout signals from silicon PIN diodes. A precise temperature measurement allows to correct for the temperature induced changes in the offset leakage current of the diodes. The online dose rate measurement is complemented by a system of RadFETs. In addition, thermo-luminescence dosimeters (TLDs) measuring the integrated dose of photon and neutron irradiation are used to control and calibrate the online dose measurements. The radiation monitoring system has been designed to measure the dose on a time scale from milliseconds up to the experiment lifetime of several years. It provides online informations on the actual level of background radiation to both the HERA and ZEUS shift crews and triggers an automatic dump of the lepton beam in case of excessively high instantaneous dose rates.

The layout of the radiation monitor system is sketched in Figure 4.13. There are 16 reversed biased silicon PIN diodes, grouped in 8 modules and mounted close to the ZEUS interaction point in the vicinity of the MVD. Each module consists of two diodes of 1 cm^2 mounted individually on printed circuit boards.

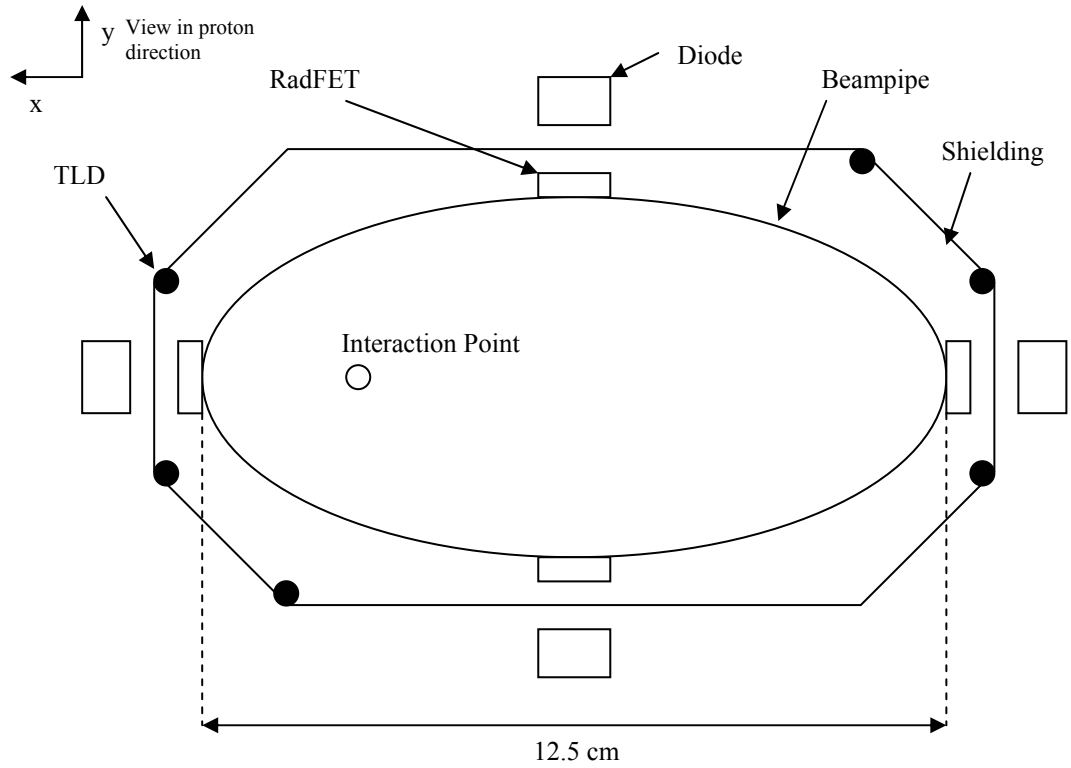

Fig. 4.13: Position of the monitors in the x-y plane.

Chapter 5

Particle detection

5.1 Interaction of charged particles with matter

Charged particles lose part, or all their energy, while traversing matter due to electromagnetic interactions with the atoms from the material being traversed. This energy can be lost in different ways: ionization, Bremsstrahlung radiation, Cherenkov radiation or transition radiation.

Charged particles lose energy primarily by ionizing the atoms from the media they are traversing. The mean rate of energy loss or stopping power for particles other than electrons is given by the Bethe-Bloch formula [52]

$$-\frac{dE}{dx} = 4\pi N_A r_e^2 m_e c^2 z_p^2 \frac{Z}{A}\frac{1}{\beta^2}\left[\frac{1}{2}\ln\frac{2m_e c^2\beta^2\gamma^2 T_{\max}}{I_p^2} - \beta^2 - \frac{\delta_p}{2}\right] \tag{5.1}$$

where m_e and r_e is the mass and the classical electron radius, z_p is the charge of the incoming particle in electron units, β its velocity ($\beta=v/c$), γ is the gamma factor of the incoming particle; Z, A, and I_p are media properties: charge and atomic number of media atoms, and average ionization potential for the media ($I_p \sim 16\cdot Z^{0.9}$ eV for $Z>1$); δ_p is a small correction due to media polarization; c is the speed of light, N_A the Avogadro number; and T_{max} is the maximum kinetic energy which can be transferred to a free electron in a single collision.

Equation (5.1) is composed of a decreasing part and a rising part with the particle velocity. The decreasing part ($1/\beta^2$) is produced by the Rutherford cross-section

$$\sigma_R(E) = \frac{2\pi Z^2 e^4}{m_e v_p^2 E^2} \tag{5.2}$$

where E is the energy loss of a particle with charge Ze (e is the elementary charge) and velocity v_p. This decrease dominates for low particle speeds. As can be seen from Equation (5.2) the cross section rises with the inverse of the square of the particle velocity. The rise at relativistic particle velocities is caused by the transverse excitation term:

$$\frac{1}{2}\ln\frac{2m_e c^2\beta^2\gamma^2 T_{\max}}{I_p^2} - \beta^2 \tag{5.3}$$

Here T_{max} is the maximum energy that an incoming particle of mass M and momentum $M\beta\gamma c$ can transfer to a stationary free electron. T_{max} is given by:

$$T_{\max} = \frac{2m_e c^2 \beta^2 \gamma^2}{1 + \frac{2\gamma m_e}{M} + \frac{m_e^2}{M^2}} \tag{5.4}$$

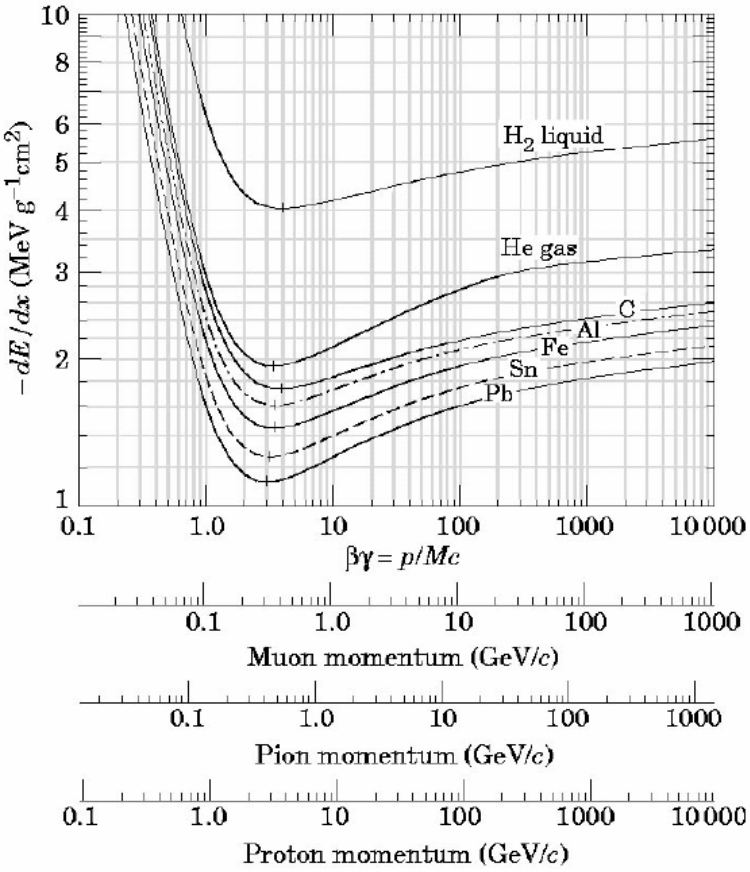

Fig. 5.1: Energy loss rate in liquid (bubble chamber) hydrogen, gaseous helium, carbon, aluminium, tin and lead.

From Equation (5.1) one can see that energy losses depend on the charge of the incoming particle (as z_p^2), and decrease with the particle speed ($1/\beta^2$), meaning that slow moving particles lose more energy. With the increase of the momentum, and as the velocity saturates at the speed of light, this leads to flattening out of dE/dx. Figure 5.1 shows the actual density-normalized energy loss curves for a few materials. The rise after the minimum is very slow and hardly exceeds 50%. The particles with velocities corresponding to $\beta\gamma>3$ are usually called minimum ionizing particles (MIP).

5.2 Landau fluctuations

The quantity $(dE/dx)\delta x$ is the mean energy loss via interaction with electrons in a layer of medium with thickness δx. For finite δx, there are fluctuations in the actual energy loss. The

distribution will look like a distorted Gaussian tending towards high values, the Landau tail [53][54]. Only for a thick layer [(dE/dx)] δx >> T_{max}] is the distribution nearly Gaussian because the number of scattering events is high.

Landau fluctuations correspond to large energy transfers from the incident particle to atomic electrons. Such electrons are called δ-electrons. They typically cause additional ionization.

The Bethe-Bloch formula gives the average energy losses for ionization and excitation. The fluctuations around the most probable value can be parameterized by the Landau distribution:

$$L(\lambda_d) = \frac{1}{\sqrt{2\pi}} \exp\left[-\frac{1}{2}\left(\lambda_d + e^{-\lambda}\right)\right] \tag{5.5}$$

where λ_d is the deviation from most probable energy losses and is given by

$$\lambda_d = \frac{\Delta E - \Delta E^W}{\xi} \tag{5.6}$$

where ΔE is the average energy losses in a layer with a determined thickness, ΔE^W is the most probable energy losses, and ξ is a parameter characterizing the width of the distribution.

Knowing the average of energy losses ΔE for a particle in a media it is possible to estimate the average number of electrons released as $\Delta E/W$, where W is the average energy spent per electron release. In the diamond this is 13 eV.

5.3 Restricted energy loss rates for relativistic ionizing particles

The restricted energy loss refers to the energy deposited in the medium, is the energy measured by the detector and is not the same as the energy lost by the particle. Secondary particles (electrons and photons) generated by the incoming particle, could escape from the active volume leading to a decrease of deposited energy with respect to the energy lost by the particle. The restricted energy loss is given by:

$$-\left(\frac{dE}{dx}\right)_{T<T_{cut}} = 4\pi N_A r_e^2 m_e c^2 z_p^2 \frac{Z}{A}\frac{1}{\beta^2}\left[\frac{1}{2}\ln\left(\frac{2m_e c^2 \gamma^2 \beta^2 T_{upper}}{I^2}\right) - \frac{\beta^2}{2}\left(1 + \frac{T_{upper}}{T_{\max}}\right) - \frac{\delta}{2}\right] \tag{5.7}$$

where T_{upper} is the minimal value between T_{cut} and T_{max}.

5.4 Corrections on the mean energy loss rate

The exact mean energy loss rate should take into account all the corrections including: the density effect [52] and energy loss at low energies or shell correction [55]. Therefore the value for the energy loss is often given by tables or graphs, like the one in Figure 5.2, which shows the energy losses of diverse charged particles.

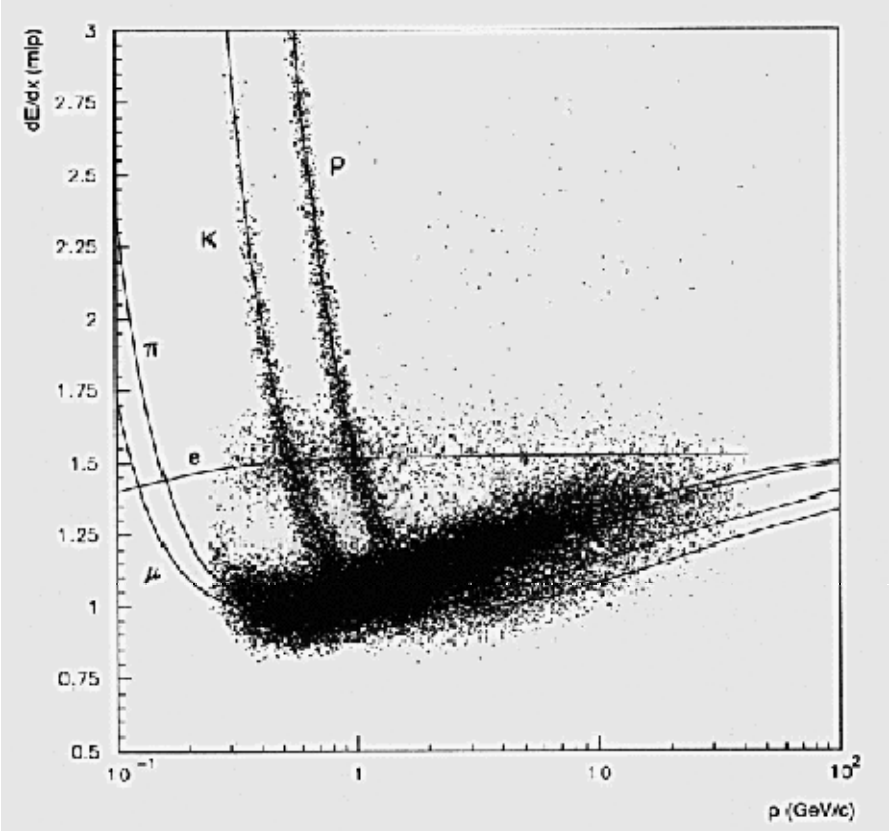

Fig. 5.2: Energy loss at different energies for μ, π, K, protons and electrons.

5.5 Multiple scattering of charged particles

A charged particle that traverses a medium is deflected by several small-angle scatters. Those deflections will result in the fact that this direction of the particles will have a Gaussian distribution, whose average is zero and the width is given as follows [56]:

$$\theta_0 = \frac{13.6MeV}{\beta cp} z_p \sqrt{x/X_0}\left[1 + 0.038 \ln\left(x/X_0\right)\right] \tag{5.8}$$

where p, βc and z_p are the momentum, velocity, and charge number of the incident particle, x is the thickness of the scattering medium and X_0 is the radiation length, which is described in the next section. Figure 5.3 shows a scheme describing the quantities used to describe the multiple scattering. θ_{plane} is the deflection angle, projected into a two dimensional plane. θ_0 is the rms of the distribution of θ_{plane} values.

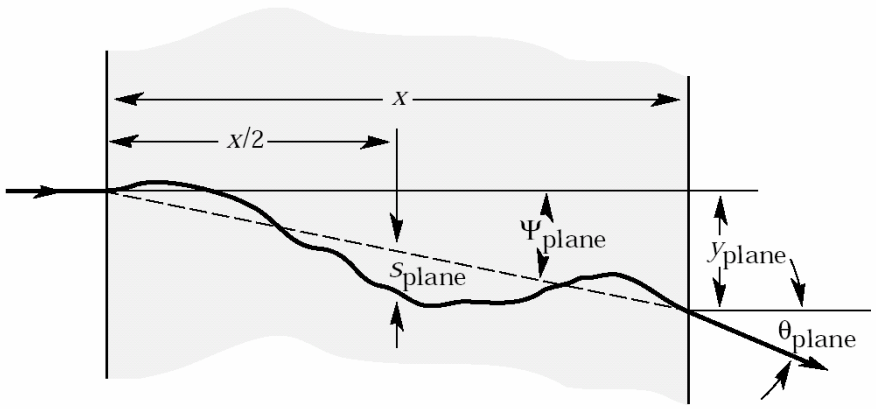

Fig. 5.3: Quantities used to describe multiple scattering. The particle is incident to the plane of the figure.

5.6 Radiation length

The radiation length, X_0, is a characteristic of the medium, and is defined as the mean distance over which a high energy electron will lose about *1/e* of its energy by bremsstrahlung. X_0 can be calculated as [52]:

$$X_0 = \frac{716.4 g/cm^2 A}{Z(Z+1)\ln\left(287/\sqrt{Z}\right)\rho} \tag{5.9}$$

with ρ being the density of the medium. The radiation length for a diamond is 12.2 cm, while for silicon is 9.36 cm.

5.7 Electron interactions with matter

Electrons (and positrons) at low energies lose primarily their energy by ionization, although other processes contribute, as shown in Figure 5.4.

The ionization loss by electrons and positrons is different from that of heavy particles due to the kinematics, the spin, and the identity of the incident electron with the electrons of the target.

For electrons or positrons of high energy the main mechanism of energy loss is by Bremsstrahlung. The emission of Bremsstrahlung occurs when the charged particle is decelerated inside the medium. The energy loss is proportional to the incoming particle energy, E, and inversely proportional to the radiation length, X_0, of the incoming particle in the medium. The mean energy loss due to Bremsstrahlung follows the expression:

$$-\left(\frac{dE}{dx}\right)_{Brems} = \frac{E}{X_0} \tag{5.10}$$

The energy at which the energy loss rate due to Bremsstrahlung and the one due to ionization become equal is called critical energy, E_C [57]. An approximation of this energy is given by [57]:

$$E_C = \frac{800MeV}{Z+1.2} \tag{5.11}$$

In the next Figure a plot showing the different ways for an electron or a positron to lose a fraction of its energy inside lead as a function of its energy. The E_C is the cross point of the Bremsstrahlung line with the Ionization line.

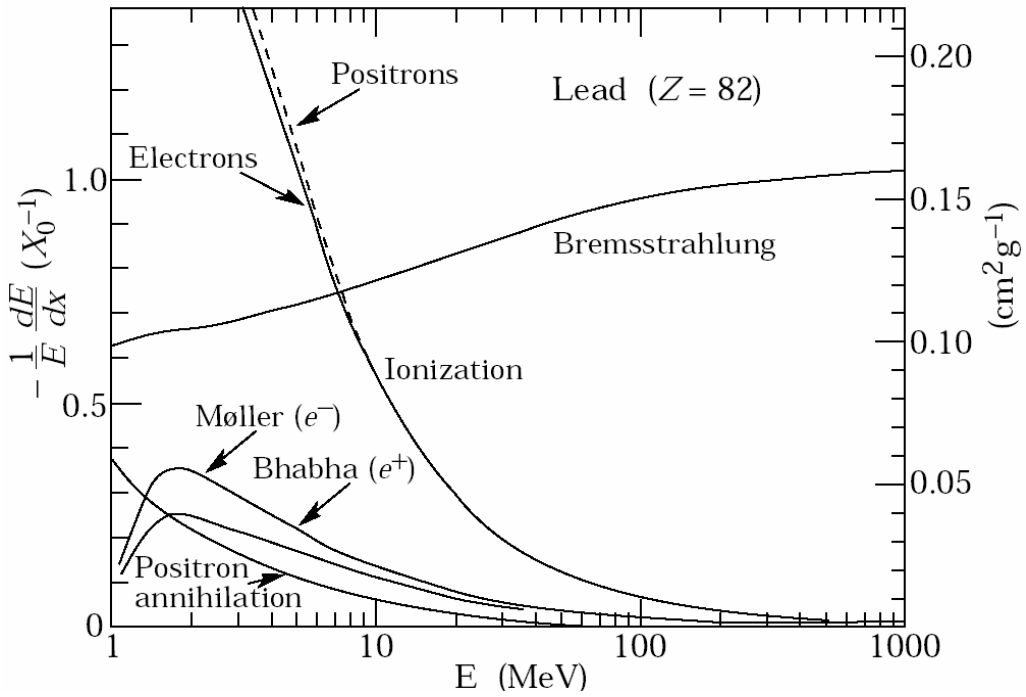

Fig. 5.4: Fractional energy loss per radiation length in lead as a function of electron or positron energy.

5.8 Solid state detectors

Solids can be classified by the energy difference between their valence band and their conduction band. The valence and conduction bands are separated by the band gap. A conductor has an overlap of its bands. The insulator has a large band gap energy, E_g, of several electron volts and its conduction band is empty. In the semi-conductor electrons from the valence band, consequently, occupy levels in the conduction band, leaving vacancies or holes in the valence band. Figure 5.6 illustrates these differences.

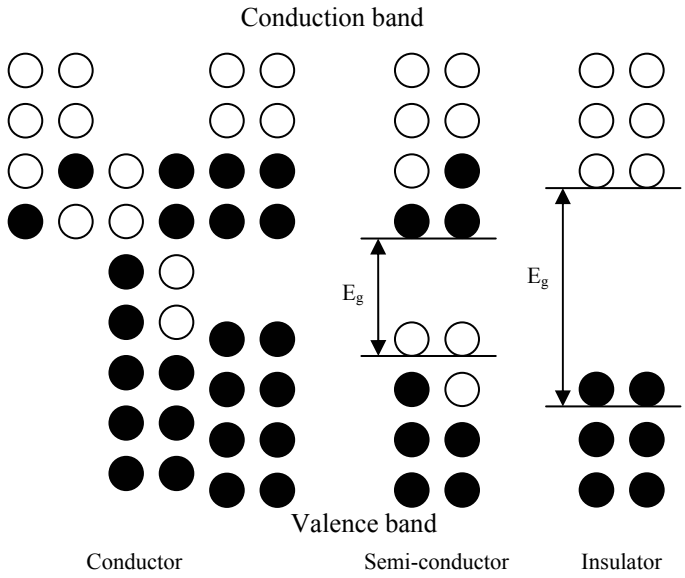

Fig. 5.6: Scheme of the energy levels on different types of solids. Black rounds are electrons, white are vacancies.

In diamond and silicon a transition of an electron into the lowest energy of the conduction band is only possible if the electron gets the necessary amount of energy to do so. The minimum amount of energy required is given by the E_g.

There are several different materials that can be used in a semiconductor solid state detector. The most common are: silicon, germanium and gallium arsenide.

The main advantages of silicon are its high availability, its low cost and that the charge collection is practically complete. Moreover it can be run at room temperature and its technology is well known, i.e. there is a very good understanding of the material.

The advantage of germanium is that more charges are produced than in silicon for a given amount of deposited energy. This allows a more precise determination of energy or track position. Germanium is often used for spectroscopic studies. The main disadvantage is that it must be cooled in order to be operative.

Gallium arsenide has a high atomic number which makes it interesting for medical applications as X-rays detectors. Its radiation resistance to neutrons is superior to that of silicon [Oh-15], however, it suffers more than silicon from charged hadronic radiation, making its applicability to the field of particle accelerator experiments impractical. Another disadvantage is its high cost.

Diamond material is considered to be the future of tracking detectors in high luminosity experiments. The stronger points in diamond are its radiation hardness, superior to silicon, and that diamond can work at a wider range of temperatures. The weak points would be its cost and, that for the same deposited energy, less charges are created in diamond in comparison with silicon.

Solid state detectors work on the same principle as ionization chambers: they collect the charge generated by ionizing radiation in a solid. Solid state detectors are made of semi-conducting material. A voltage is applied on this material, via electrode contacts, to separate and collect the electron hole pairs generated by the intrusion of a charged particle. The applied voltage generates a depletion layer, in the case of silicon, where any charge created inside is collected at an electrode. In the case of diamond, the sensitive volume is essentially given by the geometry of the applied field, which depends on the shape of the electrodes. The generated charge drifts toward the electrodes. The change of the charge distribution induces an image charge on the electrodes which is compensated by the flow of charge in the external circuit to balance the potential difference. The resulting current in the external circuit is then integrated by a charge amplifier and the signal is detected. Figure 5.5 illustrates the whole process. The amount of charge created by a charged particle is a characteristic of the material. The collected charge on the electrodes is proportional to the energy deposited in the sensor.

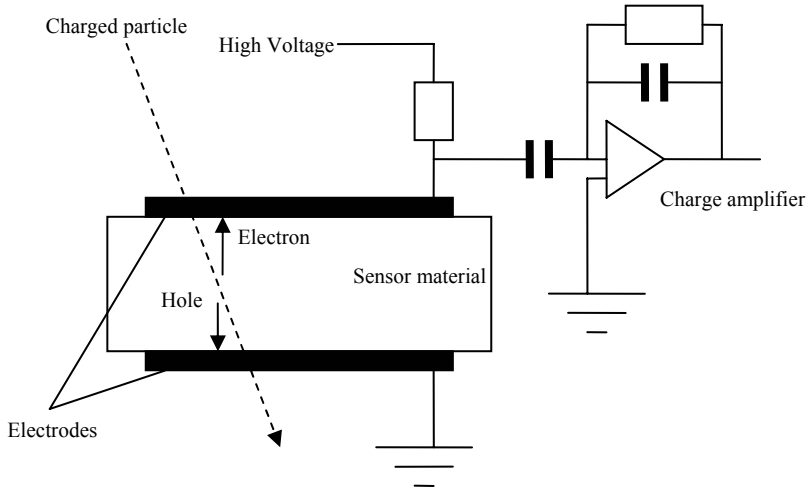

Fig. 5.5: Principle of operation of a solid state particle detector.

Chapter 6

CVD diamond

6.1 Diamonds

Diamond is an isometric (cubic) form of crystalline carbon as opposed to the hexagonal form, the graphite. They are the high-pressure polymorph of carbon which is metastable at room temperature.

Diamond exhibits close packing of the carbon atoms with a lattice spacing of 1.54 Å, such that each is surrounded by four others in a tetrahedral array, as shown in Figure 6.1. Diamond displays extreme covalence bonds between atoms, the whole crystal being in effect one molecule. Any breakdown of the structure involves the breaking of strong covalent bonds and this gives diamond both its chemical stability and extreme hardness. These bonds also have an ionic character and are at the origin of properties of the crystal like its exceptional hardness and its heat conductivity, which is four times bigger than copper. Table 6.1 lists the principal properties of diamond. The band gap of diamond is 5.45 eV [58] at room temperature, which is relatively high compared to the one of silicon, 1.1 eV, and germanium, 0.76 eV [59]. The direct transition requires an energy of 7.3 eV.

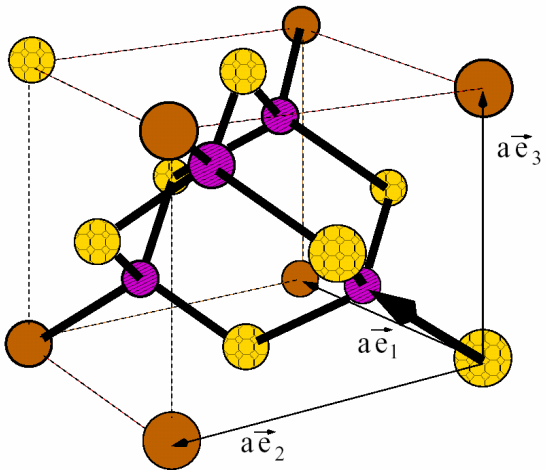

Fig. 6.1: Face centered cubic (fcc) diamond lattice.

The large band gap makes pure diamond an insulator at room temperature with a resistivity ranging from 10^{13} to 10^{16} Ω·cm. Nevertheless, if impurities are added on the diamond structure it can behave as a semiconductor.

The electron and hole mobility of diamond, at room temperature and electric fields smaller than 1000 V/cm^2, is higher than the one of Si [60]. The saturation velocity of electrons was calculated to be $2.3 \cdot 10^7$ cm/s [61] at fields higher than 30 kV/cm^2.

Property	Value	Units
Hardness	10,000	Kg/mm^2
Strength, tensile	>1.2	GPa
Strength, compressive	>110	GPa
Density	3.52	g/cm^3
Young's modulus	1.22	GPa
Poisson's ratio	0.2	Dimensionless
Thermal expansion coeff.	0.0000011	K^{-1}
Thermal conductivity	20.0	W/(cm·K)
Thermal shock parameter	30,000,000	W/m
Debye temperature	2,200	K
Dielectric constant	5.7	Dimensionless
Dielectric strength	10,000,000	V/cm
Electron mobility	2,200	cm^2/(V·s)
Hole mobility	1,600	cm^2/(V·s)
Electron saturated velocity	23,000,000	cm/s
Hole saturated velocity	10,000,000	cm/s
Bandgap	5.45	eV
Resistivity	10^{13}-10^{16}	Ω·cm

Table 6.1: Principal physical properties of diamond.

The required energy to generate an electron hole pair in diamond is $E_{eh} \cong 13$ eV. This value is larger than in Si (3.6 eV). This means that less charge carriers are generated per deposited energy and the signal from an ionizing particle is smaller in diamond than in Si. The theoretical value of E_{eh} has been calculated to be 13.6 eV [62] and has been determined experimentally to be 13.19 eV [63]. Table 6.2 shows a comparison of some important properties of diamond and Si.

Property	Diamond	Si
Atomic number	6	14
Atomic weight	12.0	28.1
Energy to create e-h pair [ev]	13	3.6
Average dE/dx for a MIP [MeV/(g·cm^2)]	1.75	1.66
Radiation length [cm]	18.8	9.4
Average ionization density for a MIP [e-h/μm]	36	110

Table 6.2: Comparison between diamond and Si.

6.2 Synthetic CVD diamond

CVD is an abbreviation for Chemical Vapour Deposition which is a crystal growth process used not only for diamond but also for a range of different semiconductor and other crystalline materials such as silicon or gallium arsenide. The technique generally involves the growth of a solid material from the gas phase using a reactive gas mixture which supplies the necessary active species (carbon in the case of diamond) onto a controlled surface (or substrate). Figure 6.2 shows a scheme of this technique. In contrast to high pressure/high temperature (HPHT) synthesis, the CVD technique is generally performed below atmospheric pressure. Because CVD can use very high purity reagents, the technique is capable of synthesizing crystals in which the purity is closely controlled.

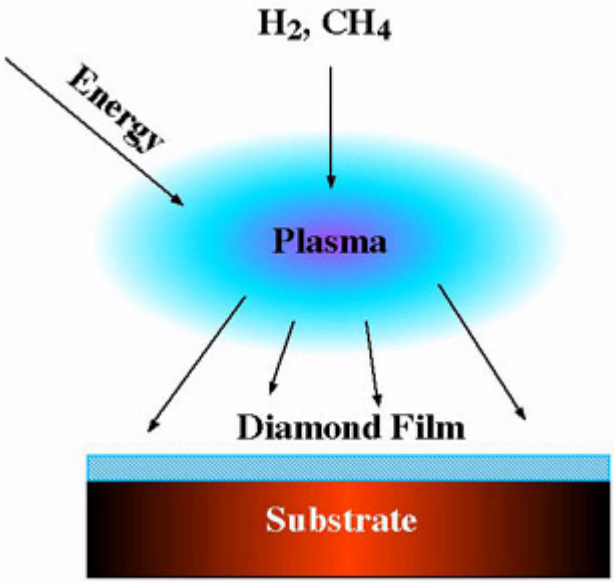

Fig. 6.2: Scheme of the process technique to grow CVD diamond.

CVD diamond is usually produced by energizing mixtures of hydrogen and hydrocarbon gases with heat or electrical energy in a deposition reactor. A region of ionized gas (plasma) drives the complex chemistry which causes diamond coatings to grow on objects placed in the reactor. Particular aspects of the chemistry ensure that diamond forms under conditions which would otherwise promote graphite growth. Some CVD diamond properties may be tailored during deposition. For example, electrically conducting diamond can be made be adding boron to the growth gases during deposition. When the diamond layer has reached its target thickness, the reactor is shut down and the diamond-coated substrates are unloaded.

Energy can be supplied to the growth gas mix by use of electrically heated tungsten filaments (hot filament technology), by microwave plasma discharge, or by heating the gas mix with a high-intensity DC arc discharge. CVD diamond can also be produced by controlled combustion of acetylene and oxygen. Each technology variant presents its particular set of tradeoffs for manufacture of different types of CVD diamond products.

Figure 6.3 illustrates two of the most common methods to fabricate CVD diamonds. Even if the methods are different, both share common features: the growth of diamond requires that the precursor gas, usually CH_4, is diluted in excess of hydrogen, in a mixing ratio

of 1%vol. CH_4; also the temperature of the substrate is usually greater than 700 °C to ensure the formation of diamond rather than amorphous carbon.

Hot filament CVD (HFCVD), Figure 6.3 a), uses a vacuum chamber continuously pumped using a rotary pump, while the process gases are inserted at a controlled rate. The pressure is kept at typically 20-30 Torr. The substrate heater is at a temperature of around 700 °C to 900 °C. The substrate to be coated sits on the heater a few millimeters from a filament electrically heated to temperatures up to 2200 °C. This method produces polycrystalline diamond films of a reasonable quality at a rate of 1-10 μm/h. The main problem of this method is the difficulty to avoid contamination of the diamond film by the filament material, which might not a problem for diamond to be used in mechanical applications but is not acceptable for electronic applications.

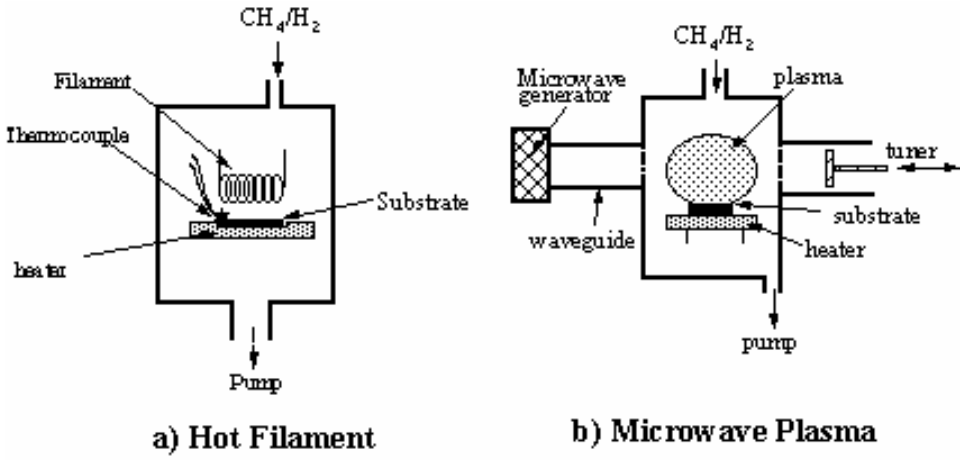

Fig. 6.3: Samples of two of the most common types of low pressure CVD reactor. (a) Hot filament reactor, (b) Microwave Plasma Enhanced Reactor.

Microvawe plasma CVD (MWCVD) reactor, Figure 6.3 b), uses similar conditions as HF reactors. Microwave power is coupled into the chamber via a dielectric window, usually made of quartz, in order to make a discharge; it couples energy into gas phase electrons that transfer their energy to the gas and heats it. The heat dissociates the gas molecules, forms active species and deposits the diamond onto the active surface immersed in the plasma. In this kind of reactor there is no filament involved. This makes MWCVD the system to be chosen for electronic application.

The growth of diamond on the substrate layer starts at the same time as the nucleation of single carbon atoms begins, initiating a sp^3 tetrahedral lattice. Figure 6.4 shows the initial stages of nucleation, with individual diamond crystallites growing in scratches on a Ni surface.

Atomic hydrogen drives the diamond generation process. In a HF system the atomic hydrogen is produced by thermal dissociation of the molecular hydrogen on the hot filament surface. In the plasma system, H is created by electron impact dissociation of H_2. Figure 6.5 shows the process of CVD diamond generation. During growth, the diamond surface is nearly fully saturated with hydrogen thus limiting the number of sites where hydrocarbon species (usually CH_3) can be added. Atomic H forms H_2 with a surface H leaving a reactive surface site. Then two reactions can happen: (i) the free site reacts with another nearby H atom, returning the surface to its previous situation; (ii) occasionally a CH_3 radical from the gas mixture can react with the surface site adding in this way carbon to the lattice. The same procedure is then repeated in adjacent sites making the diamond grow.

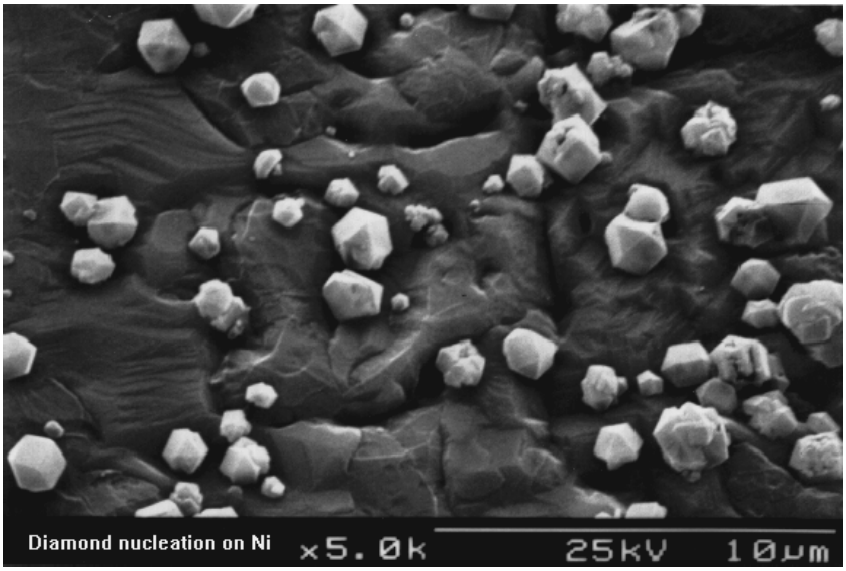

Fig. 6.4: Beginning of the nucleation process. Several microcrystals of diamond start to grow on a Ni substrate layer.

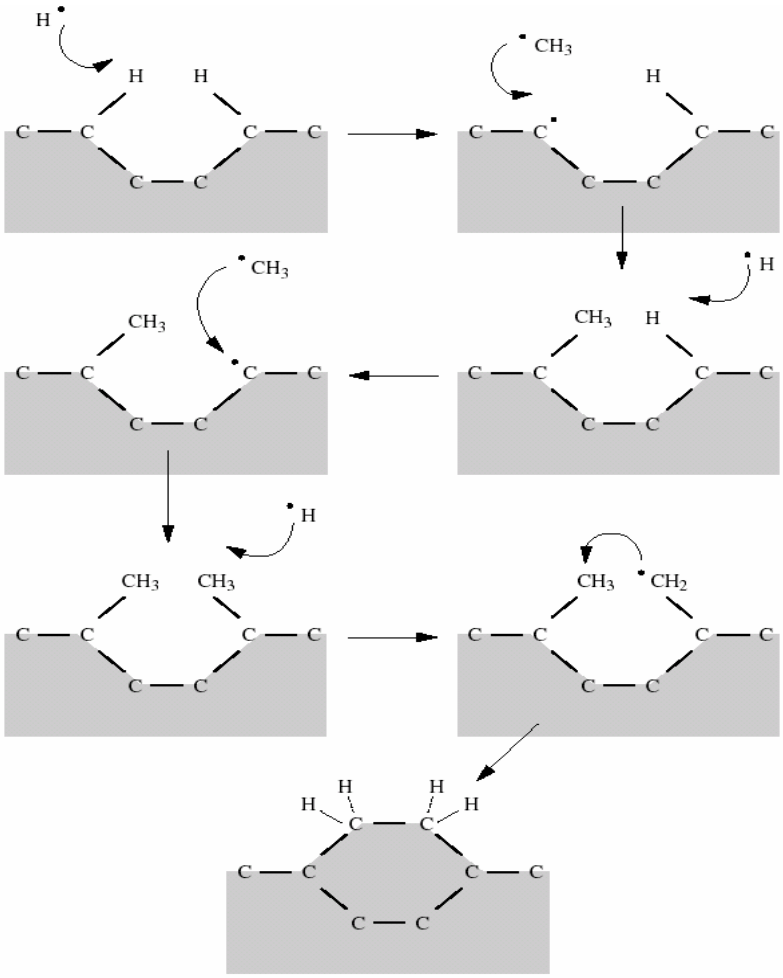

Fig. 6.5: Scheme of the reaction process that leads to diamond growth.

The grown diamond will look like the ones shown in Figure 6.6. Figure 6.6 left shows a scanning Electron Microscope picture of the cross-section of a 2.3mm thick optical grade CVD diamond layer. Figure 6.6 right shows a scanning Electron Microscope picture of the grown surface of a CVD diamond layer.

Fig. 6.6: Scanning Electron Microscope pictures of the cross section (left) and the grown surface (right) of a polycrystalline CVD diamond.

6.3 Signal generation

Considering the electric field across the diamond being that of an ideal plate capacitor and the metallic contacts cover all the diamond surface, then $E=U/d$, with E being the electric field, U the voltage difference between the contacts and d the diamond thickness. The direction of the electric field is perpendicular to the diamond surface. The electrons will drift towards the anode; this charge displacement causes a change of the potential on the electrodes. A current

$$I = \frac{e \cdot v_e}{d} \tag{6.1}$$

flows in the circuit [64]. Where v_e is the electron drift velocity and e the electron charge. Integrating the current over time the induced charge is obtained. The time during which an electron can drift is limited by the lifetime, τ, or the distance to the anode. For an ideal crystal, τ is infinite, but not for real crystals where impurity atoms, dislocations and grain boundaries distort the band structure and introduce additional levels in the forbidden band. Those additional levels act as recombination or trapping centers, thus limiting the carrier lifetime. τ depends on the material and not on the electric field.

Knowing τ, and using the condition that $\tau \leq z/v_e$, where z is the distance to the anode, the induced charge for one electron is:

$$Q_C = \frac{e}{d}\int_0^{\tau} v_e \cdot dt = \frac{e}{d} \cdot v_e \cdot \tau \tag{6.2}$$

The product of drift velocity and lifetime gives the distance between the point of creation of the charge and its stop point. This distance is called the drift length, δ, also called

Schubweg [65]. The drift velocity of the charge carrier, v, is calculated by the product of the E and the carrier mobility, μ, which depends on E. Thus δ can be expressed as:

$$\delta = v \cdot \tau = \mu(E) \cdot E \cdot \tau \tag{6.3}$$

Figure 6.7 describes the main parameters used in the equations.

For a distribution of n_0 electrons Equation (6.2) must be modified due to the fact that the capture of the electrons by the crystal is a statistical process and τ is a characteristic lifetime. This group of electrons is at a given initial time, t_0, at a distance z from the electrode, the number of free electrons after some time, Δt, will be:

$$n(\Delta t) = n_0 \cdot e^{\frac{-\Delta t}{\tau}} \tag{6.4}$$

Applying (6.3) and the drift distance Δz to (6.4) we obtain the expression:

$$n(\Delta z) = n_0 \cdot e^{\frac{-\Delta z}{\delta}} \tag{6.5}$$

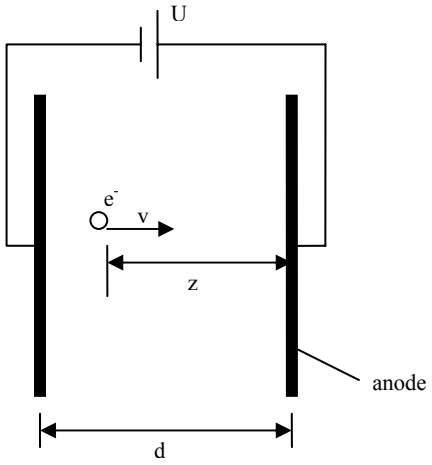

Fig. 6.7 Description of the main parameters used in the calculation of induced charge on the anode.

To calculate the induced charge generated from a group of n_0 electrons expression (6.4) must be added to equation (6.2) and instead of limiting the time interval to the lifetime, the total time will be z/v, which is the total time for an electron to reach the anode. The new expression is therefore:

$$Q_C = \frac{e}{d}\int_0^{\frac{z}{v}} v \cdot n(t) \cdot dt = \frac{e}{d} \cdot n_0 \cdot v \cdot \tau \cdot \left(1 - e^{\frac{-z/v}{\tau}}\right) = n_0 \cdot e \cdot \frac{\delta}{d} \cdot \left(1 - e^{\frac{-z}{\delta}}\right) \tag{6.6}$$

For $z >> \delta$ the following approximation can be made:

$$Q_C \approx n_0 \cdot e \cdot \frac{\delta}{d} \tag{6.7}$$

where

$$n_0 \cdot e = Q_G \tag{6.8}$$

is the induced charge originally generated by an ionizing particle in the diamond. The charge that induces the signal in the contacts is but a fraction of Q_G, being the ratio between δ and d. Therefore Q_C can be rewritten as:

$$Q_C \approx Q_G \cdot \frac{\delta}{d} \tag{6.9}$$

Similar expressions can be deducted for the charge generated by the holes. The total induced signal is the sum of the hole and the electron contribution

$$Q_C = Q_e + Q_h \approx Q_G \frac{\delta_e + \delta_h}{d} \equiv Q_G \frac{\delta_Q}{d} \tag{6.10}$$

where δ_e is the drift distance for electrons, δ_h the drift distance for holes and δ_Q the collection distance [66], making the assumption that the density of electrons and holes in the diamond is equal and constant in all the diamond volume, which is true for ionization processes. If free charge carriers are generated in a thin surface layer only one carrier type will contribute to the signal because the drift length will be zero for the other type. Therefore, the van Hecht relation [65] applies to approximate the drift length to the collection distance $\delta \cong \delta_Q$.

To measure the collection distance in CVD diamond Q_G and Q_C need to be known. A minimum ionizing particle (MIP) traversing a CVD sensor will generate 36 electron-hole pairs per μm [60]. This yields Q_G for all the detector thickness, d. Measuring the charge on the electrodes will give Q_C. The collection efficiency of a sensor can be defined as

$$\varepsilon_Q = \frac{Q_C}{Q_G} \approx \frac{\delta}{d} \tag{6.11}$$

Chapter 7

Diamond characterization

In order to understand the different characteristics and to check the quality of the samples at our disposal, see one of the samples in Figure 7.1, several tests and measurements were performed. First, a measurement on the current characteristics of the diamond was done in order to know the voltage range that could be applied to it. Then the collection distance for MIPs was measured in a stand using a ^{90}Sr source at different electric fields: this allows the understanding of the sensor response to charged particles. Some of the diamond samples were irradiated and then the above mentioned measurements were performed again. Another part of the characterisation process was to put the available samples in a test beam of protons, in order to simulate the environment inside the LHC experiments. These test beams are explained in great details in chapters 9 and 10.

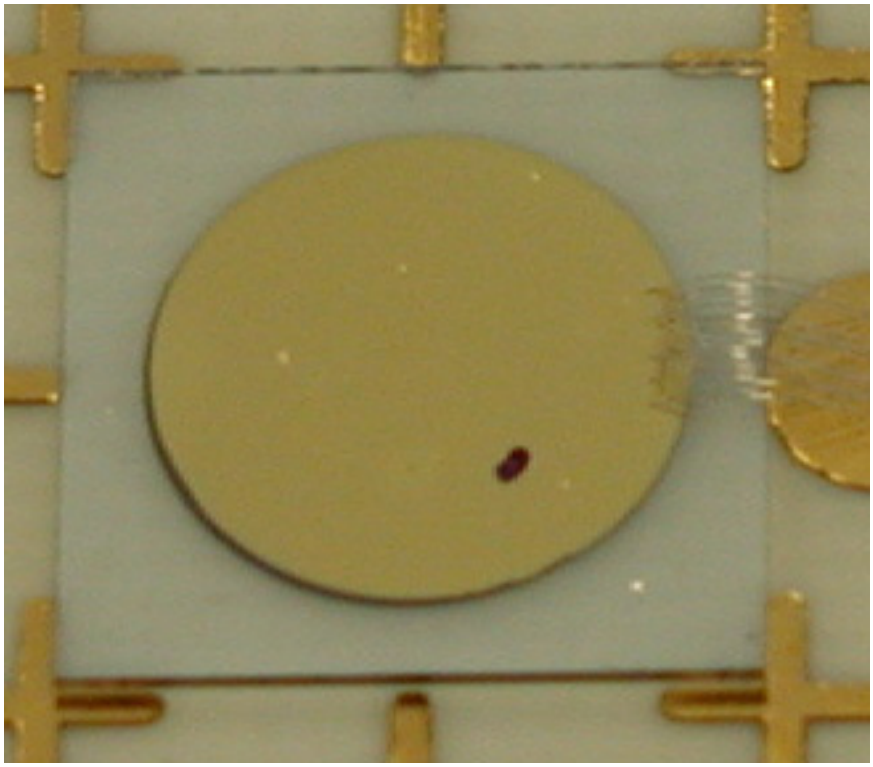

Fig. 7.1: CVD diamond of 1 cm^2 with round metallization.

7.1 I-V characteristics

The I-V characteristics define the bias range of the diamond. This measurement is also used to check the quality of the samples and its contact metallization.

To perform this measurement, diamond samples were biased at different voltages, from -1000 V to +1000 V, with a Keithley 237 [67] voltage source. To stabilize the leakage current in order to obtain a reproducible and reliable reading, the current was measured after a settling time of 20 seconds. The diamond was inside an aluminium box and is electrically shielded; the box is light tight to avoid any increase of the noise current due to transition of electrons across the band gap. A scheme of this setup is shown in Figure 7.2.

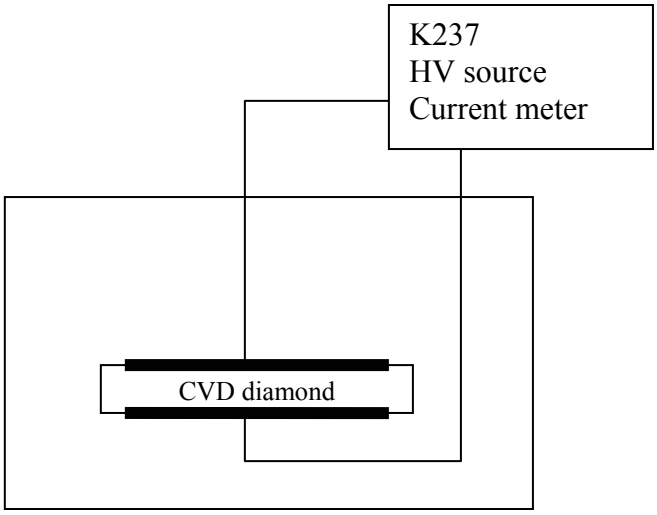

Fig. 7.2: Scheme of the setup for the I-V measurement. The diamond is inside a light tight box.

The contacts form a plate capacitor with the diamond in the middle. The electrical field between the contacts depends on the diamond thickness, *d*, and the bias voltage applied, *V*, following the expression:

$$\left|\vec{E}\right| = \frac{V}{d} \tag{7.1}$$

The Ohm's law defines the ohmic characteristics of the diamond:

$$\vec{j} = \frac{\vec{E}}{\rho_r} \tag{7.2}$$

where $\vec{j}$ is the current density, and ρ_r the resistivity. The measurement of other electrical properties, such as the charge collection efficiency, is only possible if the resistance of the sample is above ~1 GΩ. For smaller resistances the noise introduced by the leakage current prevents any meaningful measurement.

Different polycrystalline and monocrystalline, which is a CVD diamond whose structure is composed by just a single crystal, CVD diamond samples were measured reporting I-V curves like the one shown in Figure 7.3 for a 300 μm thick polycrystalline

diamond. The diamond presents a linear, ohmic, behaviour inside a range from -2.33 V/µm to 3 V/µm. Figure 7.4 shows the I-V curve of a 500 µm thick polycrystalline diamond. In this case no breakthrough is observed, as the electric field was never beyond 2 V/µm. The next two plots (Figure 7.5) show the I-V curve of another 500 µm thick polycrystalline diamond. Beyond an electric field of 1.6 V/µm, i.e. for voltages larger than 800 V, there is a breakthrough. Figure 7.5 right shows the curves in a logarithmic scale. These curves might indicate that the diamond was not properly metallized. Figure 7.6 shows the I-V characteristics for a 440 µm thick monocrystalline diamond, e6-sc-01. Unexpected low break-down field, ~0.25 V/µm, has been observed for the single-crystal detector compared to the poly-crystal one.

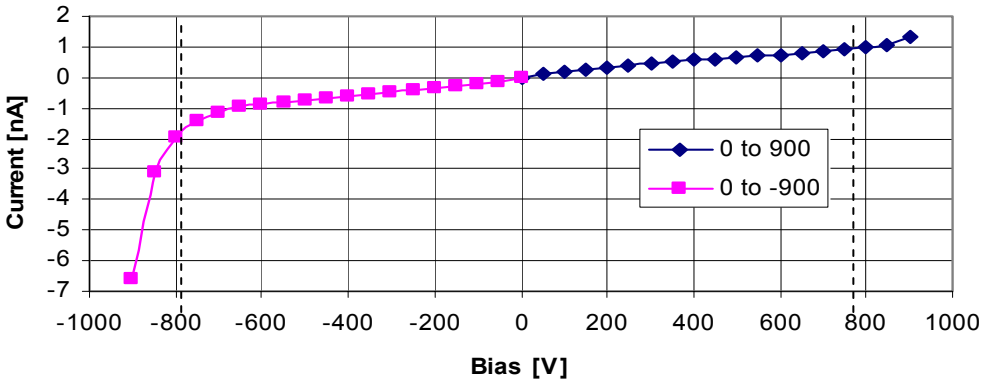

Fig. 7.3: I-V characteristics for a 300 µm thick polycrystalline CVD diamond.

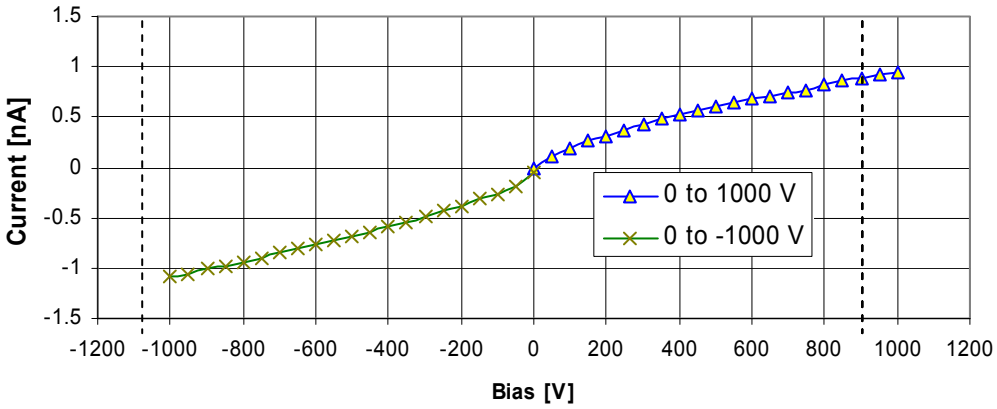

Fig. 7.4: I-V characteristics for a 500 µm thick polycrystalline CVD diamond.

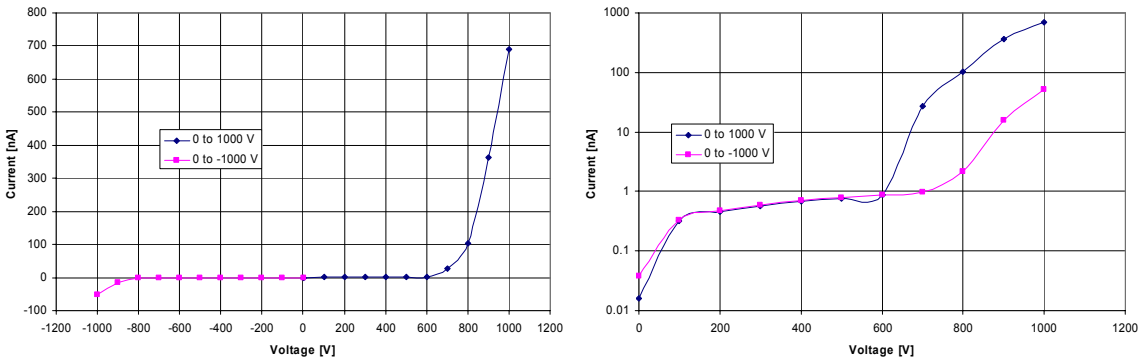

Fig. 7.5: I-V characteristics for a 500 µm thick polycrystalline CVD diamond. Left:linear scale for the current, right: logarithmic scale for the current.

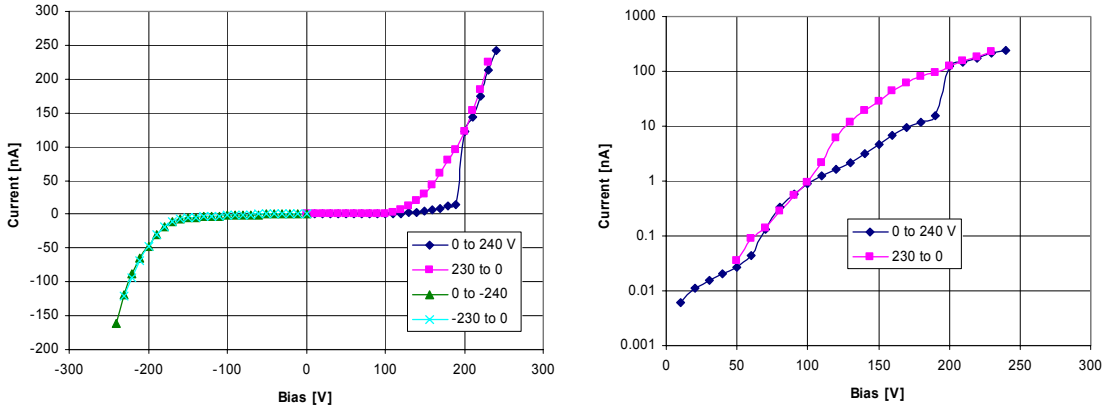

Fig. 7.6: I-V characteristics for a 440 µm thick monocrystalline CVD diamond. Left: linear scale for the current, right: logarithmic scale for the current.

The excellent symmetry of the mono-crystal data with respect to the bias polarity and the lack of a hysteresis behaviour indicate a low concentration of fixed space charge in the diamond bulk and a homogenous distribution of electron and hole traps. Figure 7.6 right shows in a logarithmic scale, the evolution of the current versus the bias for the mono-crystal diamond.

The contacts for the diamond whose I-V characteristics are shown in Figure 7.5, the polycrystalline, have an area of 0.44 cm^2. The typical resistivity of the polycrystalline diamond of Figure 7.5 is about 10^{13} Ωcm, which, in the linear region, is a typical value for the diamond. The monocrystal contact area is about 0.03 cm^2 and its resistivity prior to current breakthrough is also around 10^{13} Ωcm.

Figure. 7.7 shows the I-V curves for another monocrystal diamond, CDS134. In this case, the diamond presents a wider range in voltage before the breakthrough, which is beyond 250 V for both polarities. In one of the polarities, the breakthrough starts rising exponentially, after 340 V. One observes however a good symmetry in the curves for both polarities in the ohmic region.

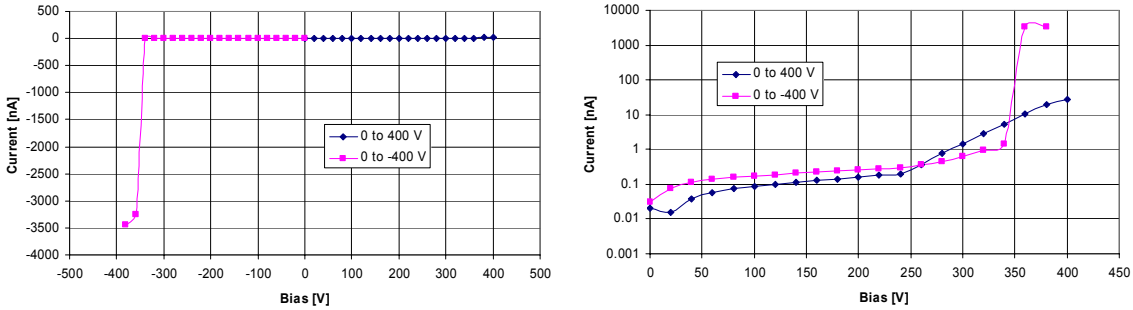

Fig. 7.7: I-V characteristics for a 490 µm thick monocrystalline CVD diamond. Left: linear scale for the current, right: logarithmic scale for the current.

7.1.1 Conclusions

The I-V characteristics were measured for all the diamond samples at our disposal. The measurements showed a good behaviour for most of the diamond samples, with current breakthroughs beyond 2 V/μm, for the polycrystalline, and similar curves in both polarities (symmetrical I-V curve), indicating that the metallizations were acceptable in most of the cases. Only one polycrystalline diamond had a breakthrough below what is considered it would be normal. The I-V characteristic curve was also not symmetric, indicating a possible defect in the metallized contacts.

The monocrystalline diamond shows a very symmetric behaviour, although its current breakthrough levels were low. This limits the bias range for this kind of diamond.

7.2 Charge collection distance measurements

The charge collection properties of all the samples were characterised with beta particles from a ^{90}Sr source; the emitted electrons have a maximum energy of 2.28 MeV. The characteristic energy-loss of the beta particles in the diamond is approximately that of minimum ionizing particles (MIPs). A MIP in diamond will generate on average 36 electron-hole pairs per µm. The collection distance δ is a measure of the efficiency of collecting the generated charge in the bulk:

$$\delta = \frac{Q_C}{Q_G} \cdot d \tag{7.3}$$

where Q_C is the collected charge, Q_G the primary ionization charge produced by the particle and d the detector thickness. In the case of small efficiencies, the collection distance corresponds to the sum of the average drift distance of electrons and holes.

The characterisation set-up consists of an aluminum box with a ^{90}Sr source. Inside the box the diamond sensor is placed on a pedestal with a small hole to allow the beta particles to arrive to the sensor through a collimator. The pedestal is at a certain voltage, given by a high voltage source, a Keithley 237. A removable needle over the diamond is being used as the ground, thus, biasing the sensor. A scintillator detector provides the trigger. This signal goes into a discriminator and if the signal is above a certain level, it triggers the digital scope to read the signal coming from the diamond sensor through a charge amplifier and a shaper.

The voltage source and the digital scope are controlled and read out via GPIB by a LabVIEW [68] program. The program substracts an average value of the base line to the maximum value from the signal. Those values are averaged over the number of pulses collected during 5 minutes; this average is then used to compute the collection distance value. The program also makes a histogram from each top value of each signal coming from the sensor. Figure 7.8 shows an scheme of the set-up.

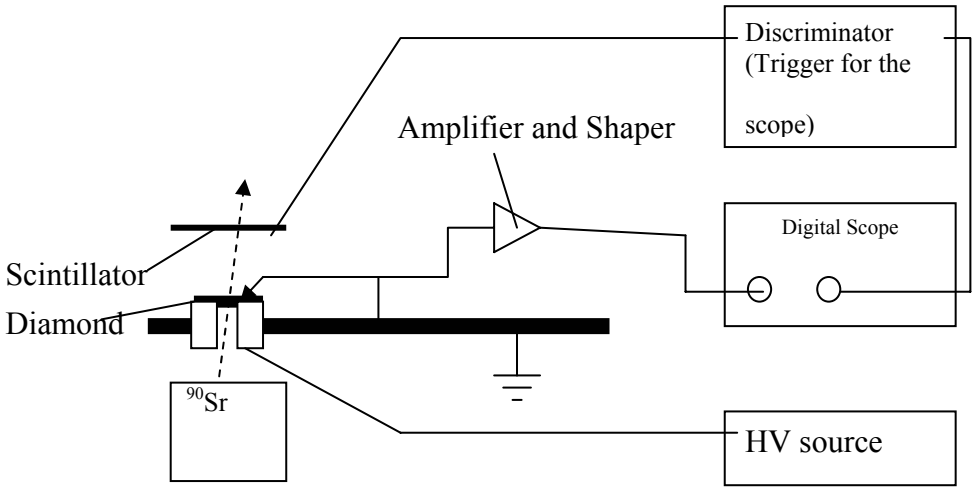

Fig. 7.8: Scheme of the characterization set-up.

7.2.1 Calibration of the system

To calibrate the system, the output signal from a Silicon sensor of 365 μm thickness biased at 80 V was measured. At 80 V the sensor is fully depleted.

The radioactive source was Am-241. This source provides 59.5 keV gammas with an intensity of 36% of the source activity, and 14 keV gammas with an intensity of 43%, though the latter have a so small energy that few, if any, can penetrate the detector housing. All the energy of the photons is deposited into the sensor volume via photoelectric effect. The expected number of electrons is therefore in the Si ~16500, number obtained from the ratio of the photon energy, 59500 eV, and the energy needed to create an e-h pair in Si, 3.6 eV. This number corresponds to the most probable signal from the sensor, i.e. the maximum of the peaks in the histogram (see Figure 7.9).

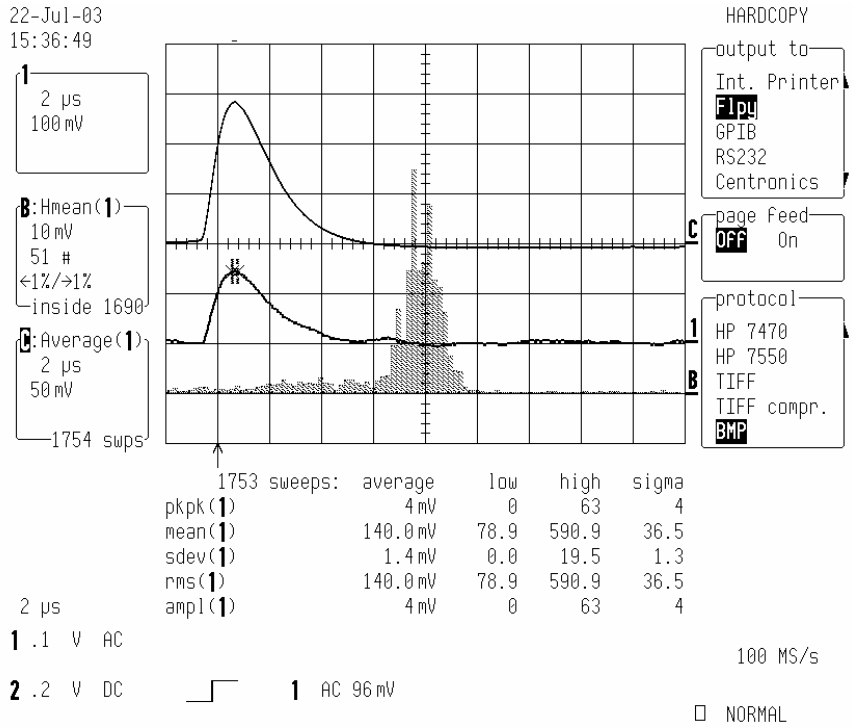

Fig. 7.9: Screen dump from the digital scope. Line C is the average of 1753 readings. The histogram gives information about the frequencies of the top values of the different readings (line 1).

From Figure 7.9, one can extract the most probable signal at 138 mV and fit the conversion factor of 16500 e^-/138 mV = 120 e^-/mV.

7.2.2 Samples characterized

Nine different diamond samples are considered in this study, seven of them were polycrystalline: CDS126 and CDS124 with thickness of ~ 300 μm, CDS154 and CDS155 (~360 μm thick), CDS113, CDS115 and CDS116 (~500μm thick), and two were mono-crystalline: CDS134 and e6-CD-01 (~440 μm thick).

For the measurement of the collection distance four different configurations, with a different diamond orientation and polarization of the electric field, have been used. These are graphically described in Figure 7.10.

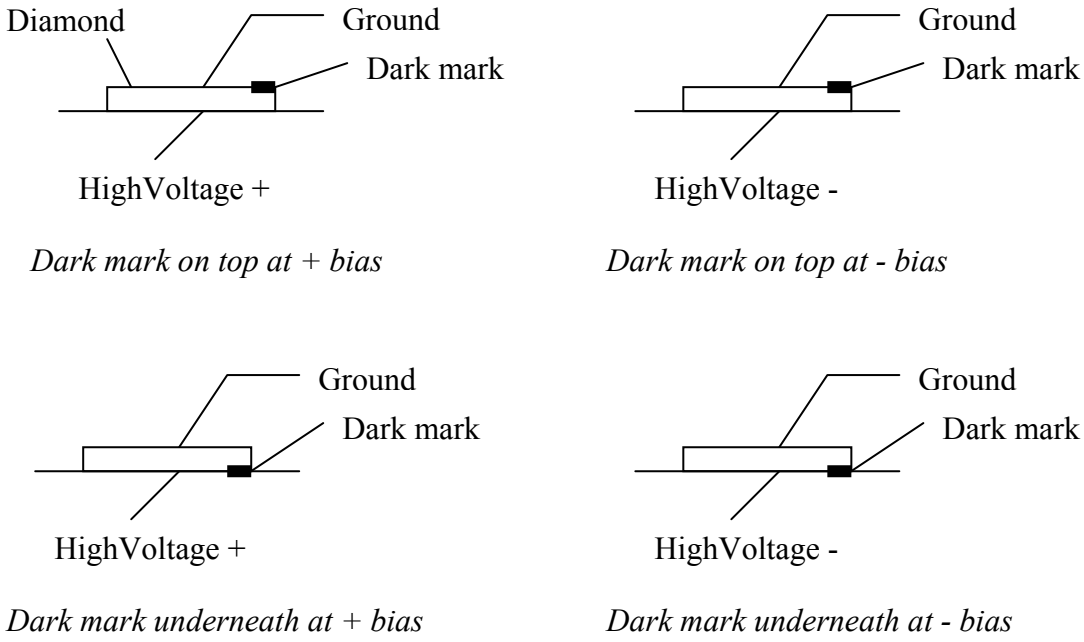

Fig. 7.10: Different measuring configurations for the diamonds.

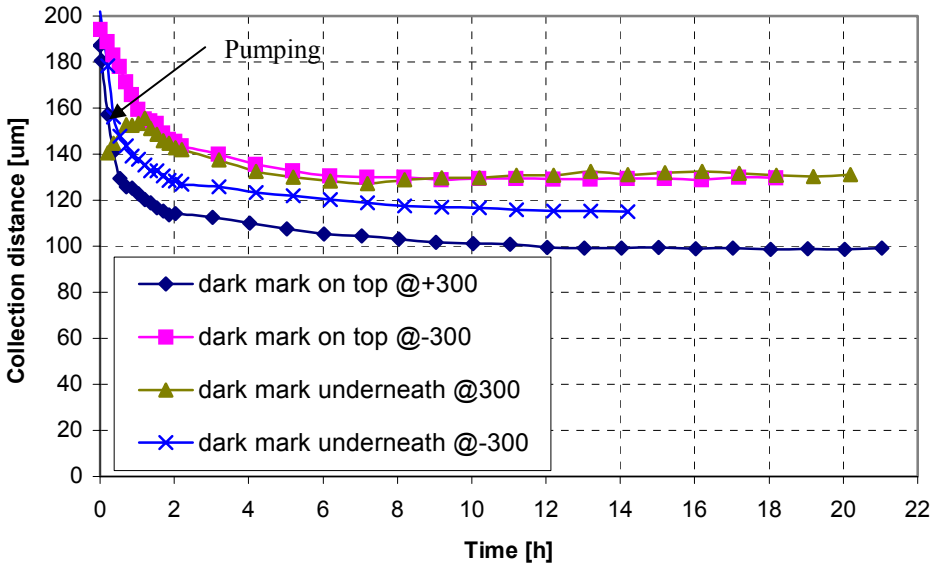

Fig. 7.11: Evolution of the collection distance over time of CDS126 at 4 different configurations.

The plots in Figure 7.11 show the evolution of the collection distance in each of the four configurations for CDS126 under a field of 1 V/µm. The curve “dark mark underneath at 300 V” shows the “pumping” (see section 7.2.3) of the diamond. After this pump the signal

drops due to strong polarisation. The rest of the curves show the evolution of the polarisation in the diamond.

The differences in collection distance between the four configurations are at maximum a 20%. Table 7.1 shows a summary of the collection distances measured at 1 V/µm for different diamonds in different configurations.

	CDS126	CDS116
Dark mark on top at +1 V/µm	100 µm	205 µm
Dark mark on top at -1 V/µm	130 µm	175 µm
Dark mark underneath +1V/µm	130 µm	200 µm
Dark mark underneath -1V/µm	118 µm	185 µm

Table 7.1: Collection distance for CDS126 and CDS116 in 4 different configurations.

Dark mark on top at positive polarisation should be equivalent to dark mark underneath at negative, and dark mark on top at negative polarisation should be equivalent to dark mark underneath at positive polarisation.

7.2.3 The priming or pumping effect

Traps inside the bulk limit the lifetime of charge carriers and the collection distance. Traps can be filled by capturing charge carriers generated by ionization, thus decreasing the effective trap density and increasing the collection distance. This effect is termed *priming* or *pumping* of the diamond [69]. An example of this can be seen in Figures 7.12 a and b.

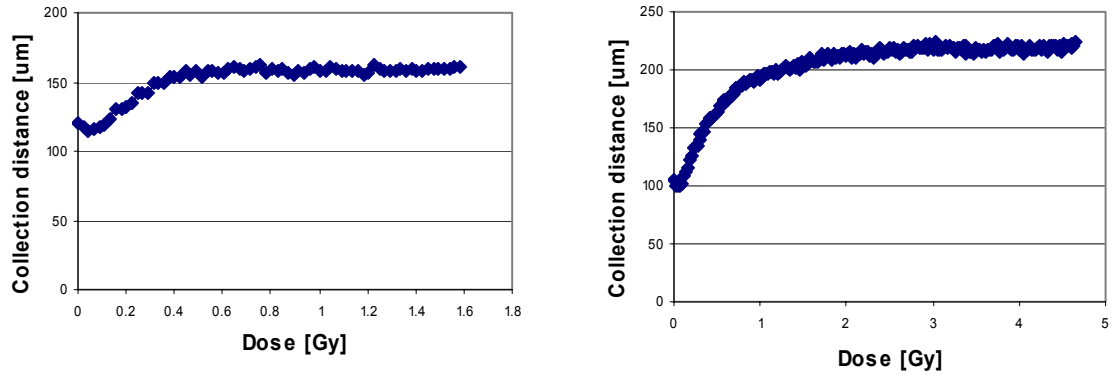

Fig. 7.12: Left: Pumping for a 360 µm thick polycrystalline CVD diamond at 1V/µm. Right: Pumping for a 500 µm thick polycrystalline CVD diamond at 1V/µm. Pumping performed with a collimated ^{90}Sr β-source.

Some diamond samples need a larger irradiation than the others to fill all their traps. As shown in Figure 7.12, CDS113, of 500 µm thickness, needs doses up to 3 Gy, whereas CDS154 needs only 0.5 Gy. The necessary dose for pumping a diamond does not depend only on its volume but also on how the diamond was fabricated and the levels of impurities or lattice deformations.

The trapping of charge happens in energy levels located in the forbidden band gap; these levels are caused by impurities or defects in the diamond. The defects can be displaced carbon atoms on the diamond lattice or impurities, usually O and N atoms [70] which forms point defects.

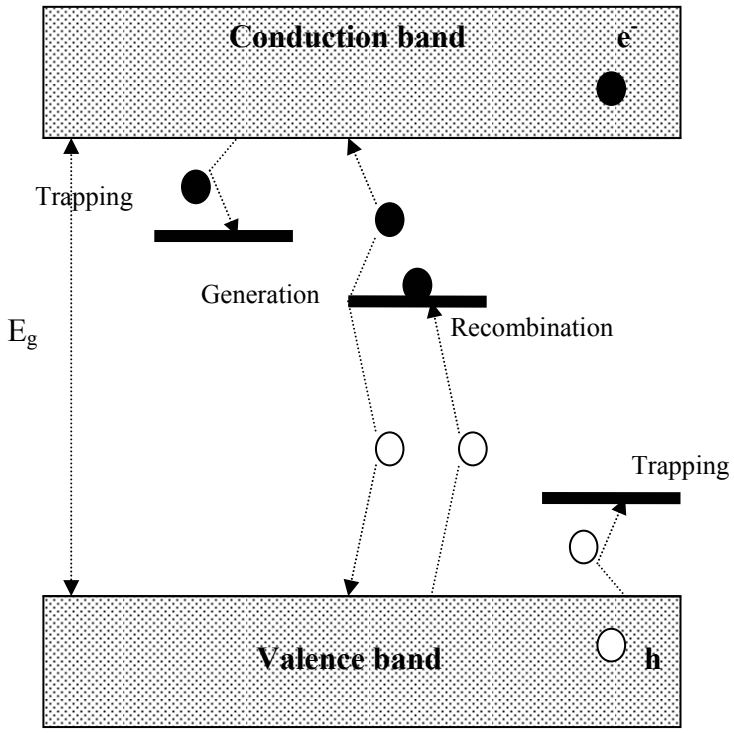

Fig. 7.13: Mechanism of charge trapping with energy levels between the valence and conduction band that act as traps, or generation and recombination sites.

As Figure 7.13 shows, charge traps can act in different ways:

- Trapping a charge carrier, an electron from the conduction band or a hole from the valence band;
- recombination of an electron with a hole;
- generation of a couple of charge carriers from the inserted energy level.

Pumping has been not observed in the monocrystal. Figure 7.14 shows how the collection distance of e6-sc-01 remains practically constant along the whole duration of the irradiation with the beta source. One possible explanation is that, as the whole sensor is just a single crystal structure, there are no defects on the lattice due to the stress produced by the contact of different crystal structures. Nevertheless, impurities, or a bad metallization, can be the origin of charge traps. This has not been observed for e6-sc-01, thus demonstrating that the diamond is very pure.

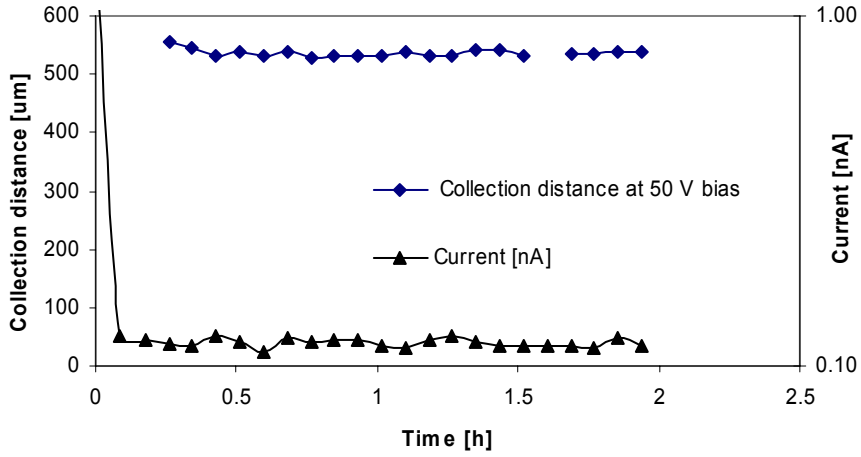

Fig. 7.14: Signal to a MIP from e6-sc-01, a monocrystal diamond.

7.2.4 Polarisation and charge collection distance

When applying a bias to a diamond we observe a transient polarization effect that reduces the effective electric field inside the bulk, causing a decrease in the signal. This effect is clearly visible in pumped diamonds, and in diamonds that are being pumped while being biased; this effect is noticeable during the first minutes of the measurement. The trapped charges inside the diamond create an internal electric field that counteracts the external bias. This polarisation field lowers the effective field strength in the sensor, thus decreasing the signal.

This effect depends on the applied bias voltage, and has been observed to stabilize about 2 hours after the change of bias. For every bias change, another stabilization period appears, as can be seen in Figure 7.15 and Figure 7.16. The plots show the values of the collection distance δ at different bias voltages as a function of time as the bias is increased (Figure 7.15) and decreased (Figure 7.16). The nominal collection distance δ is defined as the measurement after the collection distance signal has stabilized. This effect has not been observed in the monocrystal e6-sc-01, and corroborates the conclusion that it does not contain any trap that generates the polarization field.

Figure 7.15 shows that the stabilized collection distance increases with the bias voltage on the diamond. For CDS124 at 500 V the collection distance is around 160 µm while at 300 V, the nominal bias for this diamond 300 µm thick, it is around 120 µm. The increase of the signal is smaller for higher voltages. Between 100 V and 200 V an increase of almost 40 µm is observed while the increase between 400 V and 500 V is less than 20 µm: the higher electrical fields are indeed closer to the saturation field where the drift velocity of the charge carriers saturates. The signal from the diamond will be unchanged at fields beyond this saturation level.

The depolarisation curves, shown in Figure 7.16, present a faster stabilization period than the one observed for the polarisation curves. The signal stabilizes at the same level, the same collection distance values, than after the polarisation periods. This condition is not observed for irradiated samples, as will be shown in Chapter 8.

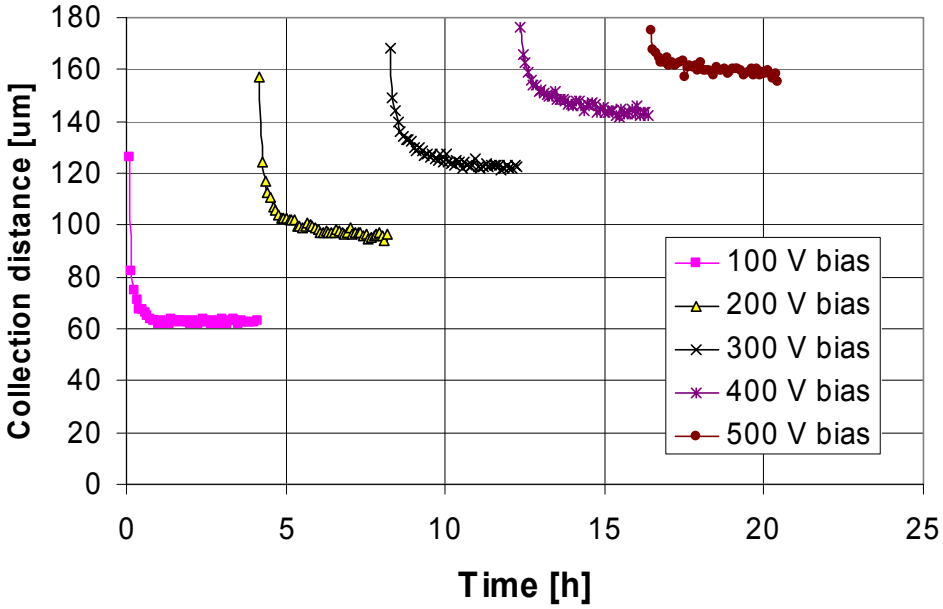

Fig. 7.15: δ versus time curves showing a polarization period each time the bias is increased for CDS124, a 300µm thick polycrystalline CVD diamond. Each point corresponds to the signal averaged over 5 minutes of exposure to the collimated β-source.

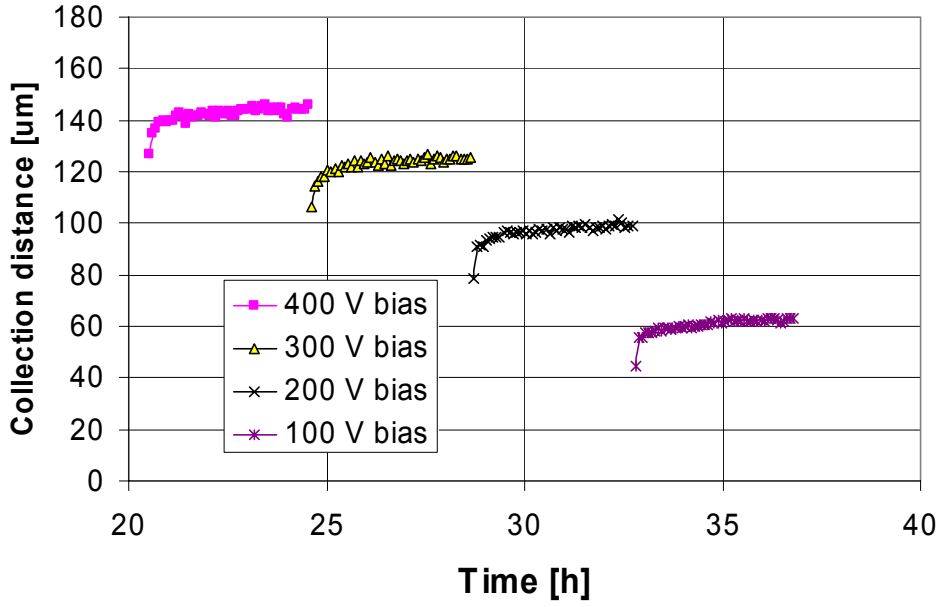

Fig. 7.16: δ versus time curves showing a depolarization period each time the bias is decreased for CDS124, a 300µm thick polycrystalline CVD diamond. Each point corresponds to the signal averaged over 5 minutes of exposure to the collimated β-source.

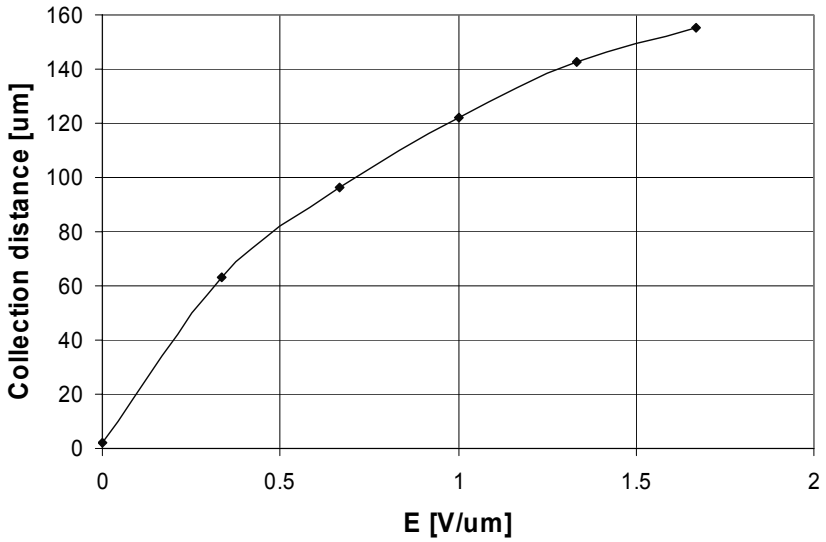

Fig. 7.17: δ versus electrical field for a 300μm thick diamond fully pumped with the betas from the ^{90}Sr. Each point represents the signal from the diamond to a MIP after a stabilization period of 4 hours to avoid any polarization effect.

The last point for each step of bias from the measurement showed in Figures 7.15 and 7.16 is used to generate the graph shown in Figure 7.17. This plot gives the collection distance in a range of electric field for the diamond sample. Once this diamond has been irradiated in a test beam, the signal read from it will be proportional to the number of MIPs traversing the sensor. This number will be known thanks to this kind of characterisation.

Other measurements done that allow a characterisation of the sensor properties are shown in Figures 7.18 for a polycrystalline diamond and Figure 7.19 for a monocrystalline one.

These plots show the detector response to a MIP after 20 minutes of applying the new bias. The measurement cycle starts at 0 V and scans the full range between +500 V and -500 V in steps of 100 V for the polycrystal and between 150 V and -150 V in irregular steps for the monocrystal.

The hysteresis observed in the polycrystal case, Figure 7.18, is due to polarization and depolarization effects as 20 minutes is not enough time for the stabilization of the signal (see Figures 7.15 and 7.16). This diamond shows a nice symmetry in both bias polarities. The signal is not fully saturated, but the saturation seems to start at a field value above 1.5 V/μm.

The monocrystal sensor, Figure 7.19, shows a very different behaviour. Polarisation is not observed (see also Figure 7.14). Very low saturation fields of 0.05 V/μm and a complete saturated plateau, which is never observed in the polycrystal case, have been measured. However, the high charge collection distance which is higher than the thickness of the detector is not understood yet for this measurement. After a heating process (see section 7.4, Figure 7.29) the collection distance saturates first at the expected value, almost equal, or less than the detector thickness.

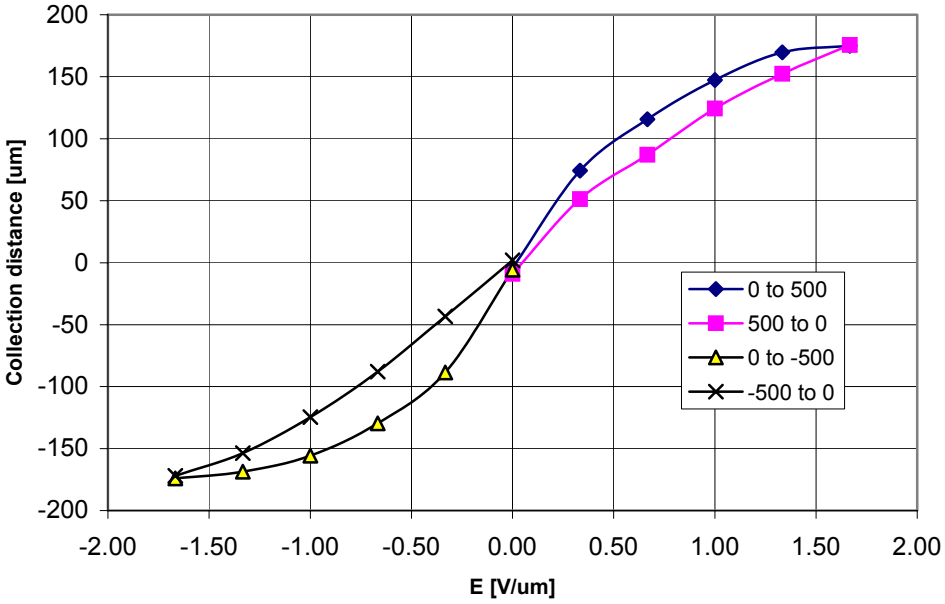

Fig. 7.18: Collection distance against bias measurement done for CDS124 with the configuration dark mark underneath. Each point is the signal after 20 minutes.

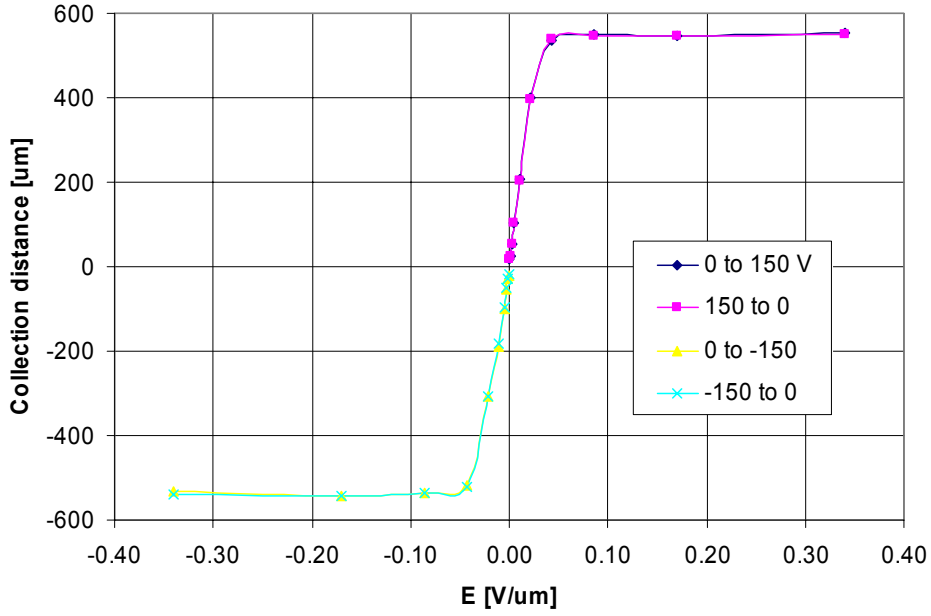

Fig. 7.19: δ versus electrical field for e6-sc-01.

7.2.5 Conclusions

The collection distance on CVD diamond depends on the bias polarity. Collection distances can vary by a 20%. Some diamond samples present quite good signal symmetry in both polarities, as seen in the graphs of the collection distance versus different electrical fields.

There are charge traps and defects on the diamond lattice which affect the diamond collection distance. With polycrystalline diamond a pumping period during which these charges are filled has been observed. The amount of radiation necessary to fill the traps until a constant signal is achieved is usually less than 1 Gy, but it has been observed that for some diamond samples this dose can be three times larger. This effect does not represent an issue for the BCM as the amount of radiation traversing the sensors will always keep the diamond pumped. The monocrystalline diamond sample that was measured does not present a pumping period.

Polarisation effects on diamond are generated by traps and imperfections on the diamond lattice. A further study is described in the next section.

7.3 Study of the polarisation

The polarisation effect seen on polycrystalline diamond samples (shown in Figures 7.15 and 7.16) is bias dependent. Figure 7.20 shows two polarisation curves for CDS124, a 300 µm thick diamond. The points from one of the curves have been obtained with the diamond irradiated with the beta particles from the Sr source during the whole measurement. The points from the other curve have been obtained without the source: the diamond was only exposed to the radiation during the 5 minutes necessary to obtain the collection distance value.

It can be seen that both curves match, demonstrating that the polarisation depends on the bias and that it decreases with time from the moment this bias is applied. It does not depend on the radiation or on the activity of the source.

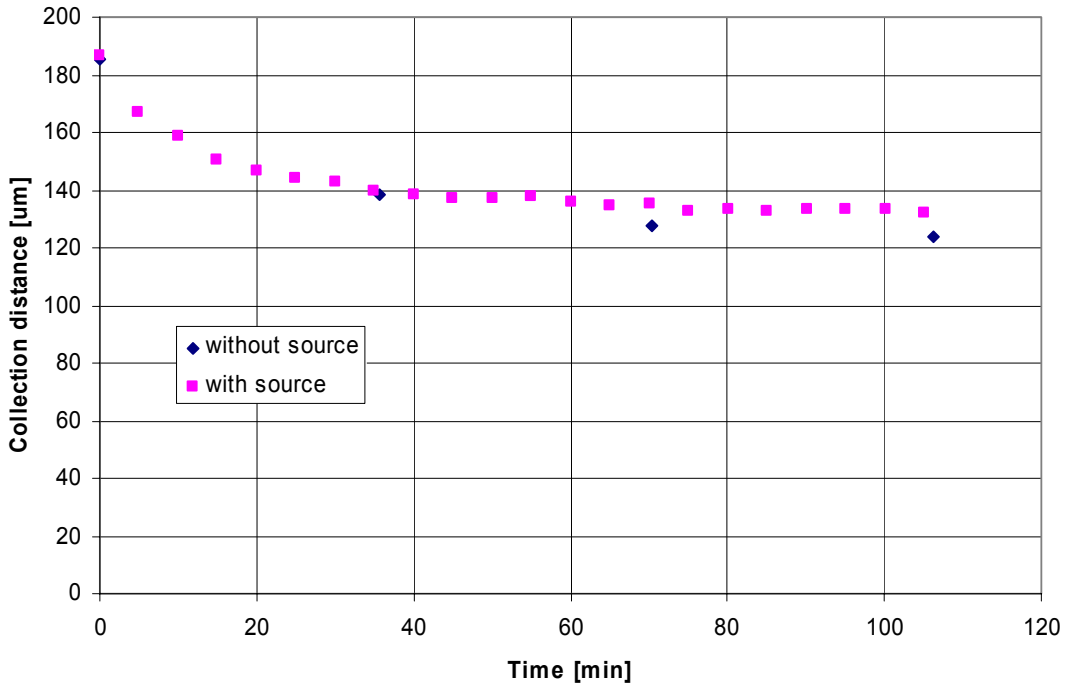

Fig. 7.20: Collection distance of a polycrystalline diamond versus time taken in two different ways: with the source and without it.

Polarisation curves follow a double exponential expression:

$$A_0 + A_1 \cdot e^{-\frac{t}{\tau_1}} + A_2 \cdot e^{-\frac{t}{\tau_2}} \tag{7.4}$$

where t is the time since the bias has been applied. A_0 , A_1 , A_2 depend on the charge collection properties of the diamond at a given bias, and their units are collection distance units [µm]; τ_1, τ_2 supposedly depend only on the electrical field applied and represent the time constant for each exponential, the have time units. The unit used here is hours. Figure 7.21 shows the fits, in blue, to the polarization curves from Figure 7.15.

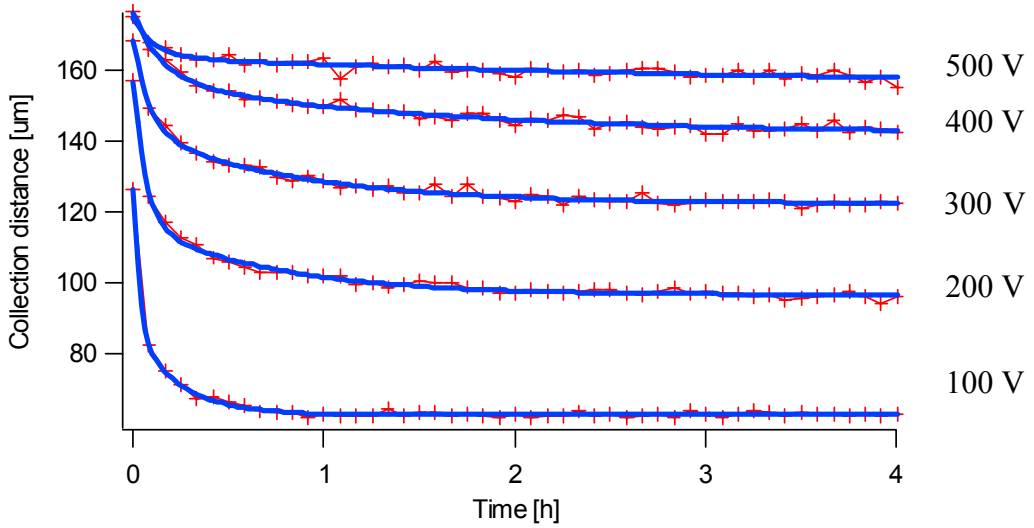

Fig. 7.21: Polarisation curves of a polycrystalline diamond at different bias.

In Figure 7.22 left a positive correlation of A_0 with the electric field is demonstrated. Two different curves can be differentiated depending on the diamond thickness: diamond with a thickness of 500 µm follow a curve with larger amplitude than those of 300 µm.

A_1 and A_2, Figure 7.22 b, seem to follow a negative correlation with respect to the electric field completely independent from the diamond thickness.

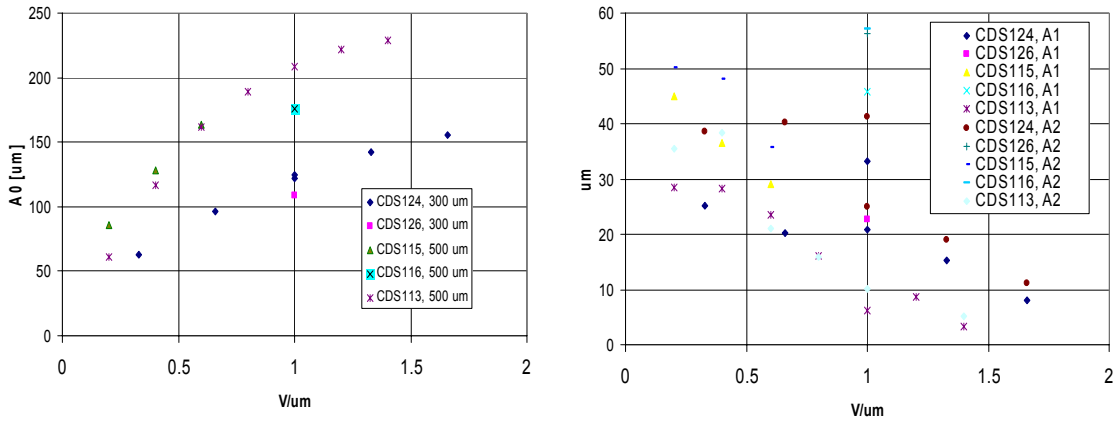

Fig. 7.22: Left: A_0 versus the electric field for different polycrystalline diamonds. Right: A_1 and A_2 versus the electric field for different polycrystalline diamonds.

The plots in Figure 7.23 show no correlation between the electric field across the diamond or the diamond thickness and variables τ_1 and τ_2. On average, and discarding the eccentric points, τ_1 seems to be over 10 times larger than τ_2. The time constants for the slow exponential, τ_1, have values usually around 2 hours. The values for the fast exponential, τ_2, have values around 6 minutes.

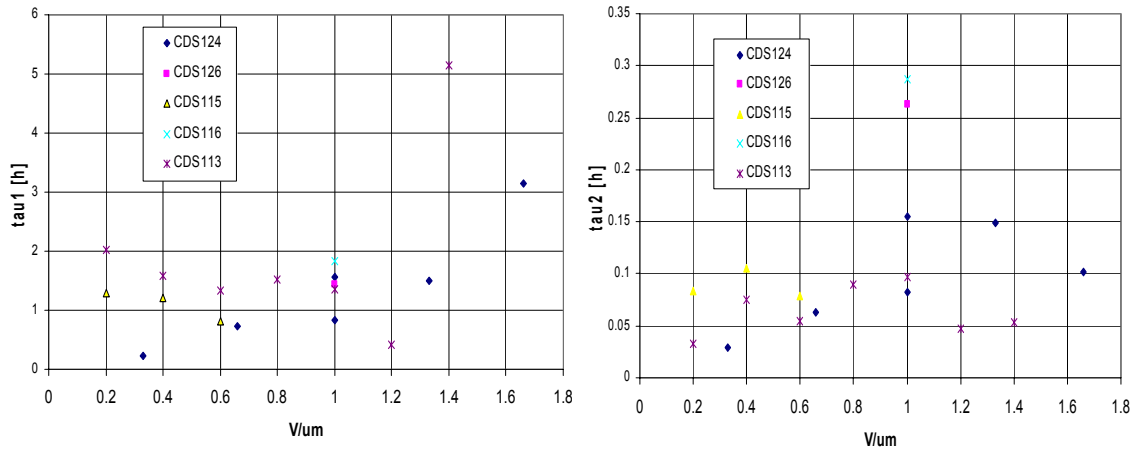

Fig. 7.23: Left: τ_1 versus the electric field for different polycrystalline diamonds. Right: τ_2 versus the electric field for different polycrystalline diamonds.

7.3.1 Conclusions

Polarization is bias dependent. At higher biases the difference on the initial and final signals, decreases. The magnitude of these differences also depends on the diamond thickness, or its volume.

The polarization curve, i.e. the collection distance against time, can be fitted as a double exponential expression. The time constants of the exponential terms are generally homogeneous and did not show bias or thickness dependence.

Diamond showed the same polarization behaviour whether it was the presence of a particle source or not. Nevertheless, the depolarization at 0 V showed a clear dependence on the source, not fully depolarizing without the presence of radiation. An explanation to this effect can be that the internal electric field generated by the charge traps cannot be dismantled without the presence of ionizing radiation.

7.4 Thermally Stimulated Currents

In order to free all the filled traps inside the sensor volume after exposure to ionization radiation, either with the betas from ^{90}Sr source or the 24 GeV protons from the CERN Proton-Synchrotron (PS) beam, a Thermally Stimulated Current (TSC) measurement on the diamond will show the current increase generated by the freed charges.

The objective of this measurement is to see the thermo-stimulated current peak that ensures that the diamond has been depumped. Another thing would be to record the current during the cooling when the peak has appeared. The integral of the peak gives the number of freed charges, while the temperature where this peak occurs gives the energy of the band gap of the diamond.

The diamond is placed on to a metallic surface, which corresponds to the ground, and a cramp holds it in place. This cramp is at a voltage for biasing the diamond during the heating process. Temperature and current are monitored via GPIB by LabVIEW software. A scheme of the set-up can be seen in Figure 7.24.

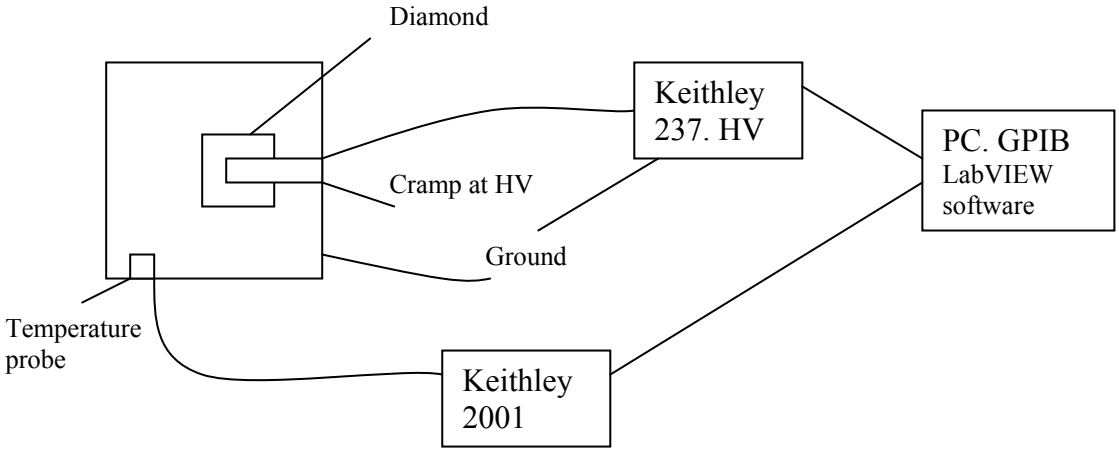

Fig. 7.24: Set-up for the depumping process with heat. The support sits onto a heater. The temperature probe is isolated from the ground.

Figure 7.25 shows the evolution of the temperature during the heating up of the diamond in the measurement. The reproducibility of this heating rate is very high. The temperature of all diamond samples that were measured was increased following the same procedure.

Figure 7.26 shows the measurement for CDS126 after an irradiation of $5 \cdot 10^{14}$ protons/cm^2 (see chapter 8). This diamond has the peak at 250 Celsius degrees. The amount of charges collected is of the order of $5 \cdot 10^{13}$ electrons. With the sensor volume being 30 mm^3 the concentration of charge inside the diamond is of the order of 10^{12} e$^-$/mm^3.

Figure 7.27 shows the TSC measurement performed on CDS115, a 500 μm thick diamond. This sensor was irradiated only with the betas from the ^{90}Sr during a few hours, the time necessary to pump the diamond. The difference from the proton irradiation is, apart that the betas do not produce bulk damage, that the irradiated volume is reduced by the source collimator whereas with the PS protons the whole diamond volume was affected. The current achieved is one order of magnitude below the maximum current achieved with the proton

irradiation. The peak for CDS115 is located at a temperature of 226 ºC, lower than the one for CDS126 (250 ºC).

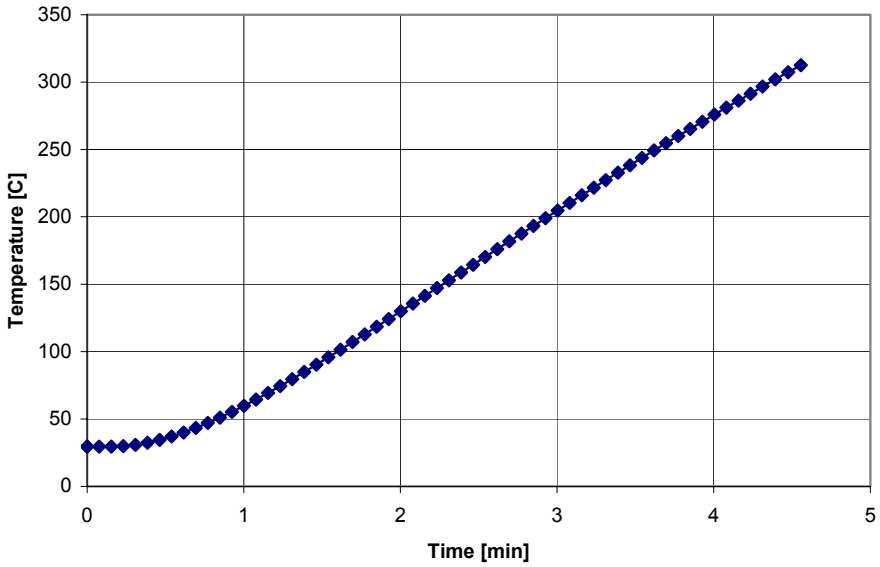

Fig. 7.25: Temperature against Time for the heater used in the set-up. The line can be approximated to a linear expression beyond a temperature of 50 degrees.

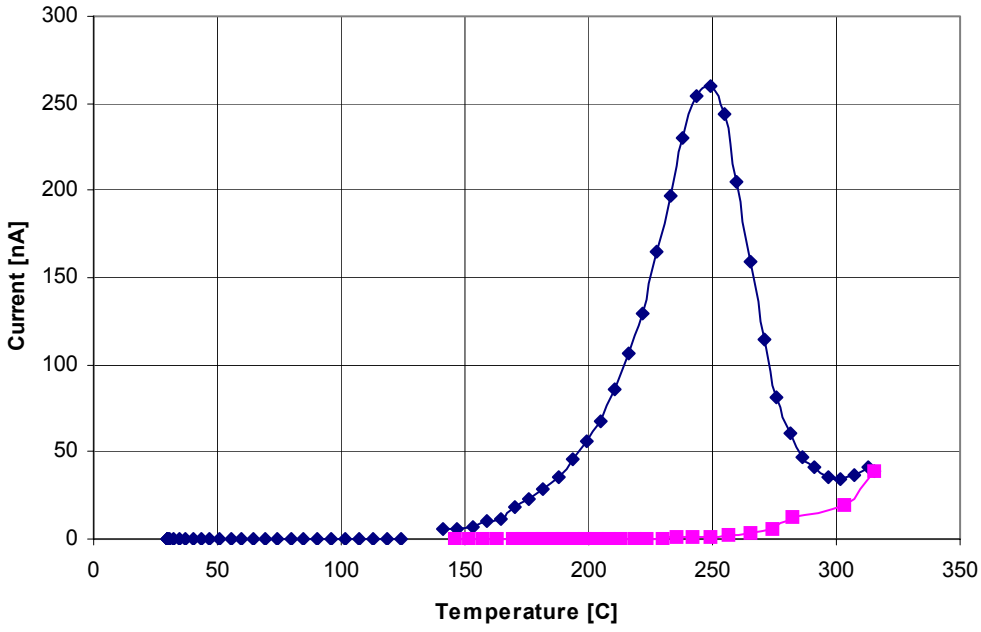

Fig. 7.26: Current against Temperature for CDS126. The peak is located at 250 Celsius and the current reached arrives to 260 nA. The pink curve is the “cooling down” curve that happens just after the second increase of current just started. The area of the peak gives us the number of charge traps into the diamond.

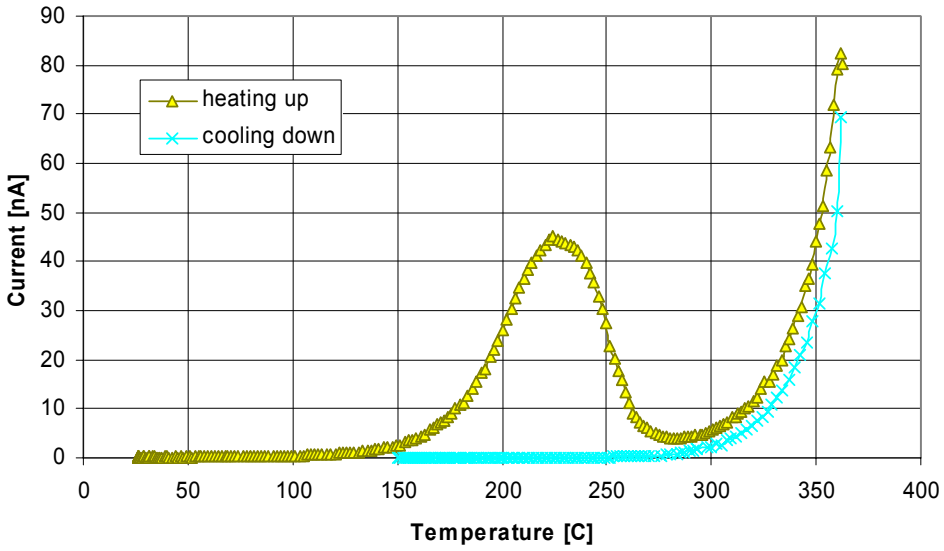

Fig. 7.27: Current against Temperature for CDS115. The peak is located at 225 Celsius and the current reached arrives to 45 nA. The cyan curve is the "cooling down".

Figure 7.28 shows the TSC measurement for the monocrystal diamond after few hours under irradiation by the ^{90}Sr betas. The current peak is a factor 5 smaller than in the case of CDS115, a polycrystalline diamond. This is expected for monocrystal structures, as they lodge much less traps than the polycrystalline structure. The temperature where this peak appears is 241 ºC.

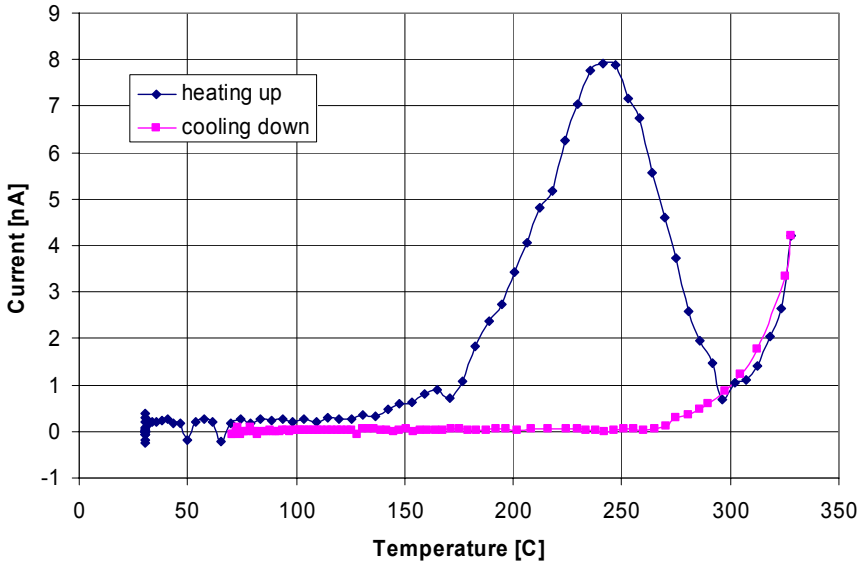

Fig. 7.28: Current against Temperature for e6-sc-01. The peak is located at 245 Celsius and the current reached arrives to 8 nA. The pink curve is the "cooling down".

After the depumping process the diamond samples have been measured again. First of all, a collection distance vs. time measurement where the pumping could be observed again.

The pumping measurement was done with the same ^{90}Sr source. Once the pumping is over, the measurement of the collection distance against the electric field was performed in a hysteretic way.

Diamond samples that were not irradiated by the 24 GeV protons did not show any change in their characteristics. The results on the proton irradiated diamond after the TSC procedure are shown on chapter 8. Changes on its collection distance were observed for the single crystal, see Figure 7.29. The collection distance dropped to a value coherent with the diamond thickness, see also Figure 7.14.

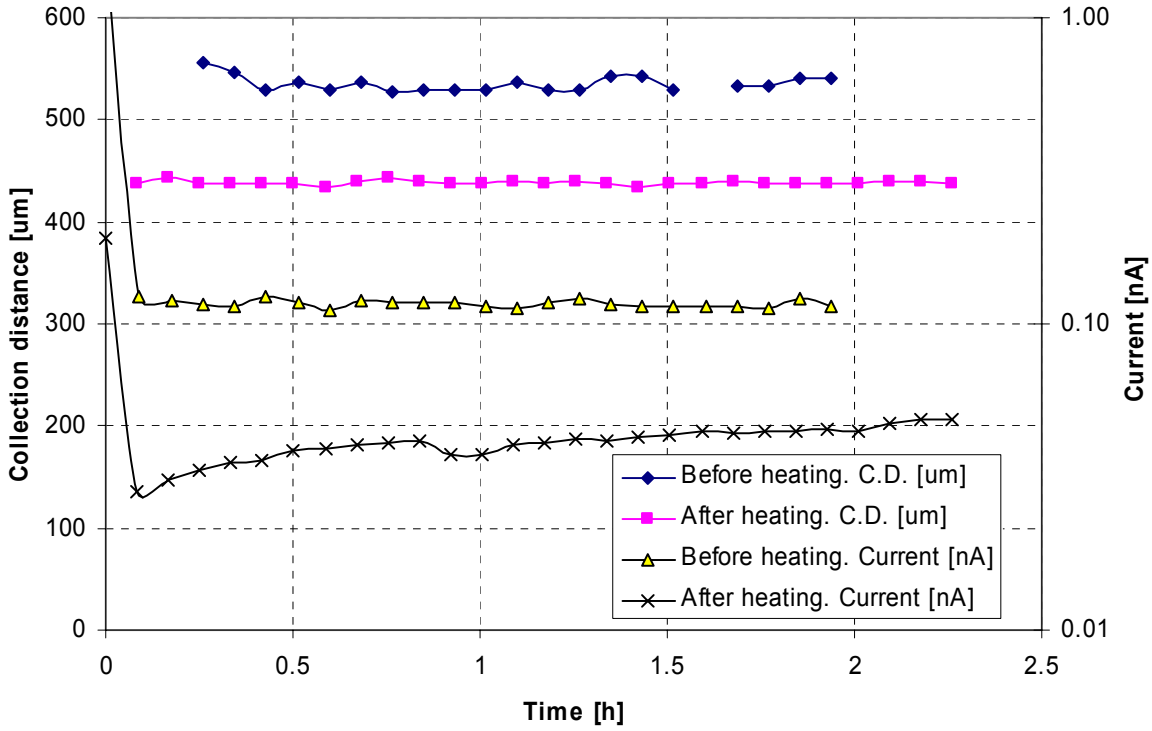

Fig. 7.29: Signal to a MIP from e6-sc-01 biased at 50 V versus time, before and after heating, the leakage current is also shown.

7.4.1 Conclusions

The temperatures at where the TSC peaks were produced, in the diamonds measured, indicate that the charge traps in these diamond samples are in similar energy levels. That could indicate that the type of impurities is the same for all samples. The two polycrystalline diamonds measured were made from the same wafer, therefore this is expected. The monocrystal, instead, did not show any hint about charge traps during the collection distance measurements, it did not pump nor it polarized, yet a TSC peak is observed, also in a similar temperature range. That confirms the presence of traps, from impurities, in the crystal lattice. Impurities that may be similar to the polycrystalline ones. Nevertheless, the level of current achieved by the monocrystal is much less important than the ones achieved from the polycrystalline ones.

Chapter 8

Radiation tolerance

BCM sensors must work properly during all the LHC lifetime of 10 or more years. The amount of particle fluence that these sensors will be exposed to during all that time in the positions described in chapter 4 is about $2.8 \cdot 10^{15}$protons/cm^2.

Even if diamond is very radiation hard the damage generated by radiation can affect its electrical properties. The amount of radiation a diamond sensor can withstand without a significant loss of its functionality will determine its radiation tolerance. Most of the particles that will generate radiation damage at the IP areas of the LHC experiments will be charged hadrons from the proton-proton collisions. Therefore, to study the radiation damage on diamond from hadrons, the samples were irradiated at the Proton Synchrotron [71] facility at CERN that delivers 24 GeV protons.

8.1 Radiation effects

Diamond is affected in two ways by radiation: generation of electron-hole pairs by ionizing particles and production of defects in the crystalline structure or lattice due to hadronic radiation.

In the first case the created pairs can be separated by an applied electric field and either leave the diamond or get trapped in charge traps (see section 7). Ionization causes surface defects that do not alter the crystal lattice.

In the second case irradiation generates defects on the diamond bulk, modifying its lattice structure. Figure 8.1 illustrates this effect. The incident particles transfer their energy to the lattice atoms, knocking them from their site, and if they have energy enough, generating a vacancy. These displaced atoms are called “primary knock on atom” (PKA). They may transfer their kinetic energy to other lattice atoms which may cause “secondary knock on atoms” (SKA). The PKA and SKA will eventually stop at a free lattice site or in an interstitial lattice site, forming point defects. Figure 8.2 shows different types of point defects in diamond. These point defects introduce energy levels in the band gap, and alter the lifetime of the charge carriers. The carrier lifetime is related therefore to the concentration of point defects [72].

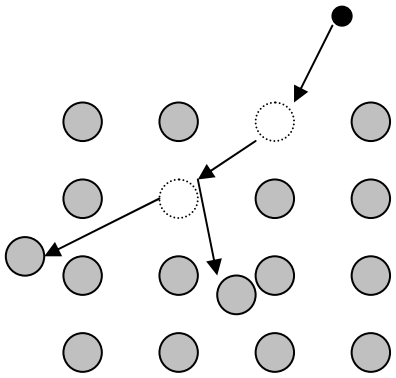

Fig. 8.1: A hadron knocks an atom from the lattice and displaces it: this gives a PKA. This atom can knock another lattice atom creating a SKA. This results in generating lattice defects.

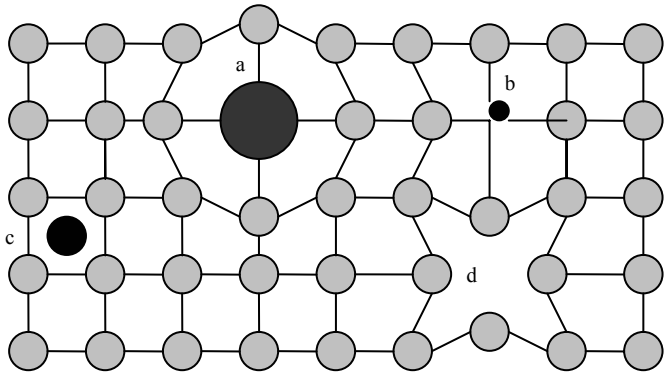

Fig. 8.2: Scheme of different types of point defects in the diamond lattice: a) and b) foreign substitutional atoms, c) foreign interstitial atom, d) vacancy.

8.2 The CERN Proton Synchrotron (PS)

The primary 24 GeV/c proton beam is directed towards the upstream iron shielding wall, using the BZH01 horizontal bending magnet as shown in Figure 8.3. The maximal beam intensity is $2\text{-}4\cdot10^{11}$ protons/spill. A quadrupole system, together with a frequency program, spreads the beam out in order to produce a uniform proton irradiation over a surface of several square centimetres. The expected flux is $2\cdot10^{9}$ protons/(cm^2s), in one spill per PS supercycle.

The sensors to be irradiated are placed in a container on a remote controlled shuttle (Figure 8.4) that moves on a rail inside an iron pipe with a section of 40 x 25 cm^2 and a length of about 15 meters. This pipe is inserted in the protection shielding and has three chicanes to avoid secondary particles to come out from the beam zone.

A luminescent screen with a camera is used to display and optimize the beam profile. A secondary emission chamber (SEC) provides a measurement of the proton beam intensity. The fluence is measured by activation of aluminium foils placed after the irradiated sensors.

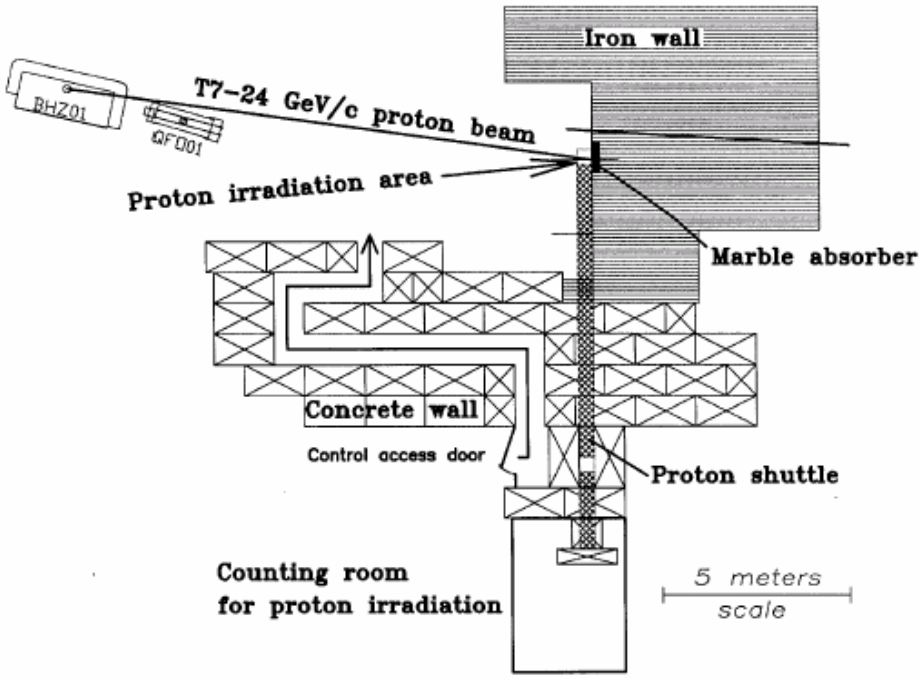

Fig. 8.3: Lay-out of the proton irradiation zone at the CERN PS.

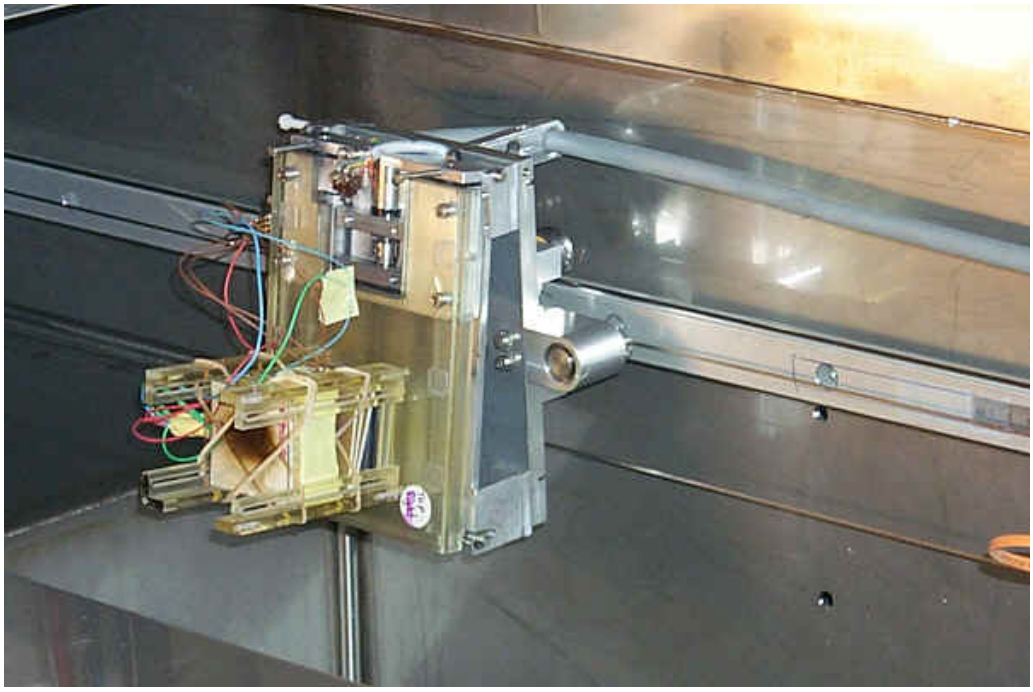

Fig. 8.4: Remote controlled shuttle were the diamonds to be irradiated are placed.

The radiation tolerance was tested with protons up to a fluence of $2.8 \cdot 10^{15}$ protons/cm^2 which is equivalent to the fluence expected after 10 years of normal operating conditions in the LHC near the CMS interaction point. Two diamond samples with thicknesses of 500 µm (CDS116) and 300 µm (CDS126) were used for this investigation.

8.3 First irradiation

In a first step CDS116 was irradiated up to a fluence of 10^{15} protons/cm^2 and CDS126 up to $5 \cdot 10^{14}$ protons/cm^2. Then their charge collection distance and current characteristics were measured. Figure 8.5 shows the signal from CDS116 (left) and CDS126 (right) during the polarization after this first irradiation step. The diamond samples were measured just after the proton irradiation and they were fully pumped by the protons. The collection distance for CDS116 is around 150 µm at 1 V/µm, which is clearly below the collection distance prior to the irradiation (200 µm). For CDS126 the observed phenomenon after the irradiation is reversed: its collection distance increases from 130 µm to 150 µm.

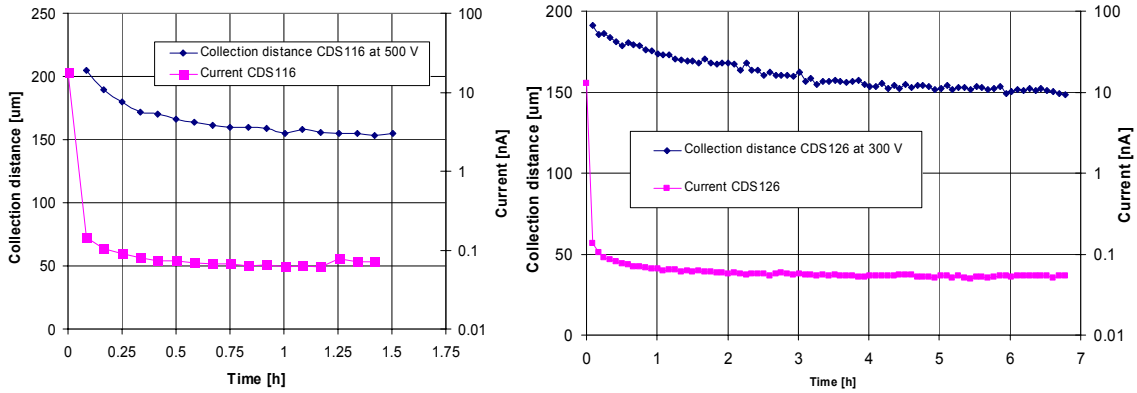

Fig. 8.5: Left: Signal from CDS116 at 1 V/µm after an irradiation of 10^{15} protons/cm^2; Right: signal from CDS126 at 1 V/µm after an irradiation of $5 \cdot 10^{14}$ protons/cm^2.

Figure 8.6 shows the collection distance versus electric field (left) and the dark current during the irradiation with the ^{90}Sr source (right) for CDS116. Figure 8.7 shows the same plots for CDS126. The cycle started at 0 V and scanned the full range between +1000 V and -1000 V in steps of 200 V for CDS116, and from +500 V to -500 V in steps of 100 V for CDS126. The difference of signal in the curves where the bias is increasing and in the curves where it is decreasing is due to polarization and depolarization effects. Each point on the graph represents the signal from the diamond measured after the new bias has been applied for only 20 minutes. The polarization has not yet reached the value at which the collection distance stabilizes (more than 20 minutes, see Figure 8.5). Figure 8.6 left shows the high reproducibility of the measurement even after the irradiation, for CDS116 the measurement was done 2 times consecutively.

The symmetry with respect for the polarities for both diamond samples is very good. CDS116 was measured up to a field of 2 V/µm, reaching a collection distance of 200 µm (Figure 8.6 left). The leakage current behaviour was also very good, being lower than 1 nA (Figure 8.6 right). For CDS126 a saturation of the collection signal is observed at an electrical field of 1.33 V/µm (Figure 8.7 left); the collection distance value is then almost 200 µm, but without enough time for the signal to polarize. The current behaviour (Figure 8.7 right) is not as clean as for CDS116. An increase of the current beyond 1 nA is observed for fields higher than 1 V/µm.

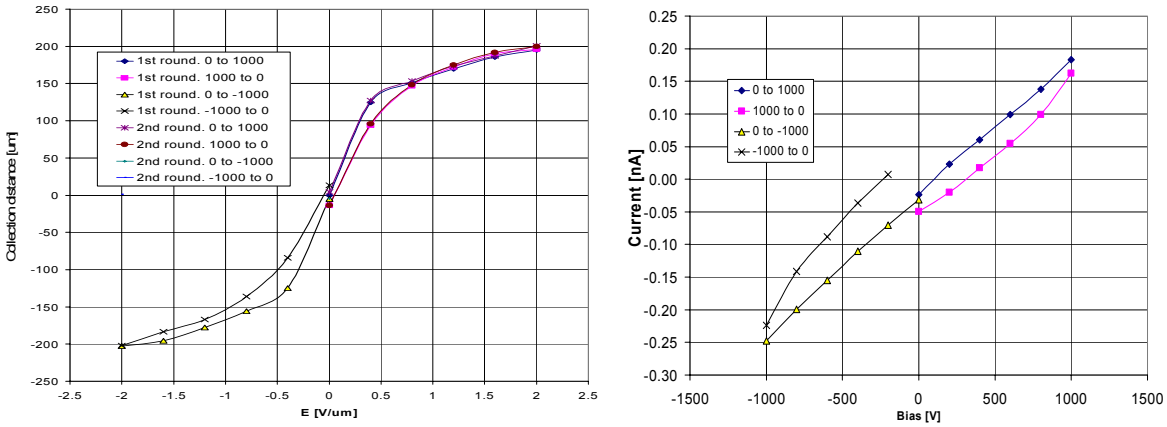

Fig. 8.6: Left: δ versus electrical field curves for CDS116 after a first irradiation of 10^{15} protons/cm^2. The measurement is done twice to test the reproducibility. Right: Leakage current during the measurement.

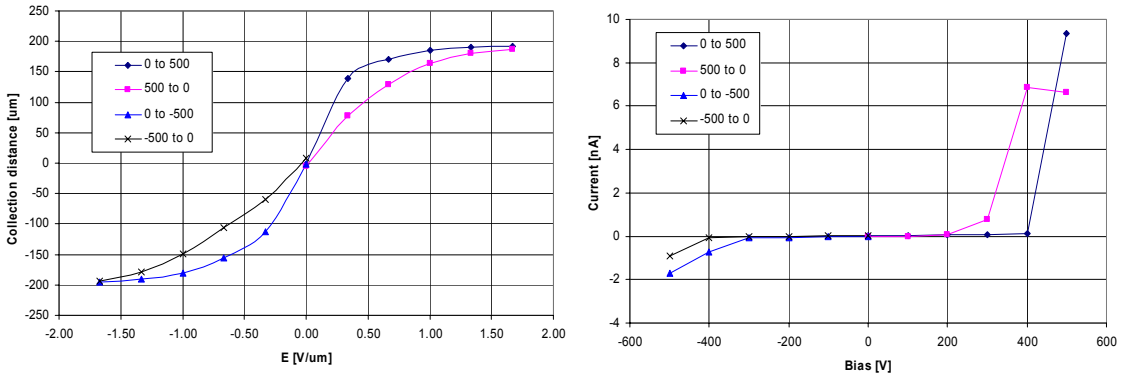

Fig. 8.7: Left: δ versus electrical field curves for CDS126 after a first irradiation of $5{\cdot}10^{14}$ protons/cm^2. Right: Leakage current during the measurement.

After measuring the collection distance characteristics of the samples both diamonds were heated following a TSC measurement procedure (see chapter 7, section 7.4). Figure 7.26 shows the results for CDS126. This procedure fully depumped the samples. The diamonds were pumped again with the beta source and again their characteristics were measured. Figure 8.8 shows the collection distance against the dose delivered by the ^{90}Sr for CDS116 (left) and CDS126 (right). CDS116 showed a longer pumping period. The collection distance reaches a value of 190 µm, but presumably, if the measurement had been longer in time, the signal would have arrived to 200 µm. CDS126 did not show the same pumping behaviour, with a signal after pumping around 145 µm.

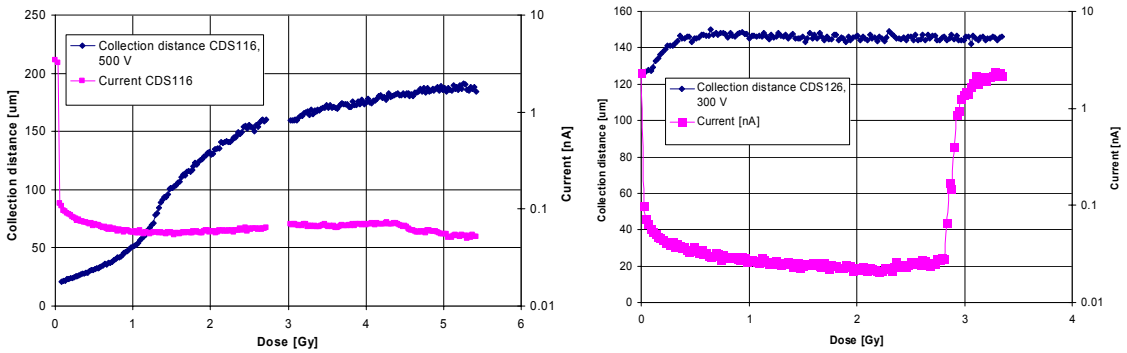

Fig. 8.8: Left: Signal from CDS116 at 1 V/µm after an irradiation of 10^{15} protons/cm^2 and after a TSC process that fully the depumped the diamond; right: signal from CDS126 at 1 V/µm after an irradiation of $5{\cdot}10^{14}$ protons/cm^2 and after a TSC process that fully the depumped the diamond.

The observations that can be made from Figure 8.8 are that the collection distance of the diamond seems to have been restored to their original values prior to irradiation. The pumping behaviour for both diamond samples is different after the irradiation and heating process. For CDS126, after the pumping there is still a remaining polarisation effect (see Figure 7.11) while after the irradiation and heating, i.e. after the sensor is pumped, the signal remains stable. CDS116 shows a strange pumping curve where the collection distance at the beginning of the irradiation with the beta source is almost negligible. It needed more dose to fill in the charge traps and achieve a stable collection distance. The explanation of that could be that the proton irradiation generated new charge traps in the diamond bulk that were emptied after the TSC measurement.

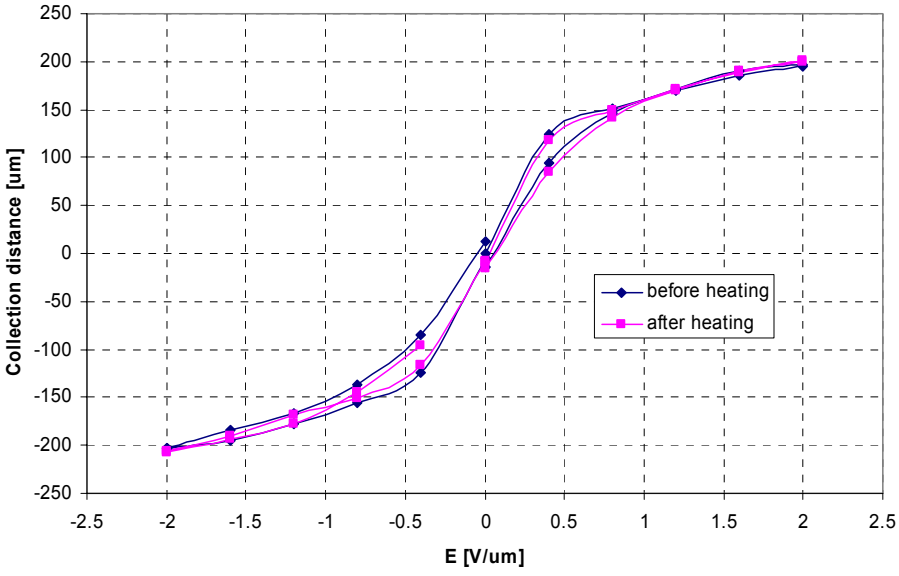

Fig. 8.9: δ versus electrical field curves for CDS116 after a first irradiation of 10^{15} protons/cm^2 and after a TSC procedure. Both curves are similar.

The hysteresis measurements of the collection distance for the diamond changing the bias every 20 minutes, taken after the heating and the pumping of the diamonds, did not change significantly, see Figure 8.9, and they look almost the same as the shown in Figures 8.6 for CDS116 and in Figure 8.7 for CDS126. An equivalent measurement but waiting 1 hour instead of 20 minutes is shown in Figure 8.10. It shows that the signal is bigger after depolarisation than after polarisation. That effect has appeared after the irradiation of the diamond. Figures 7.15 and 7.16 of section 7.2 show that the signals after polarisation and depolarisation, for an un-irradiated diamond, coincide. The curves show also an increase (Figure 8.10 left) after the polarisation period that is unexplained. It is possible that allowing more time for the measurement the final collection distance from the measurement while increasing bias, and the measurement while decreasing match.

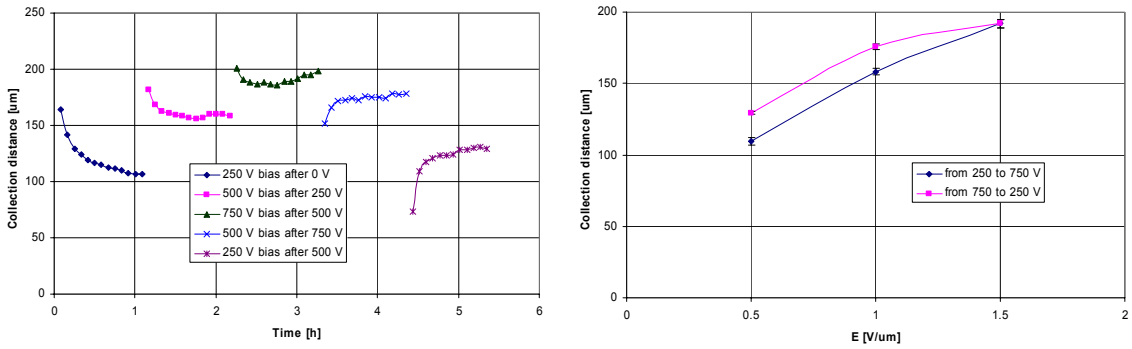

Fig. 8.10: Left: Evolution of the signal from CDS116 after the first irradiation at different voltages. Right: δ versus electrical field curves, one correspond to the increase of bias, the other when decreasing.

8.4 Second irradiation

These two samples were irradiated a second time with protons in the PS area; the fluence was this time $1.8 \cdot 10^{15}$ protons/cm^2 for both samples. The total integrated fluence for CDS116 is $2.8 \cdot 10^{15}$ protons/cm^2 and for CDS126 $2.3 \cdot 10^{15}$ protons/cm^2. After the irradiation a characterisation of collection distance was done and the results are showed in Figure 8.11.

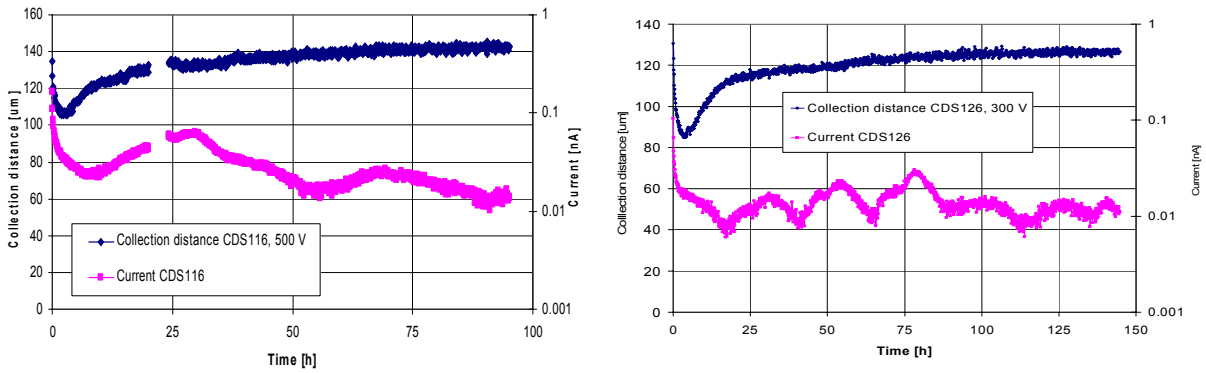

Fig. 8.11: Left: Signal from CDS116 at 1 V/µm after an irradiation of $2.8 \cdot 10^{15}$ protons/cm^2; right: signal from CDS126 at 1 V/µm after an irradiation of $1.8 \cdot 10^{15}$ protons/cm^2.

Both diamond samples present similar curves. After a pronounced polarisation effect at the beginning of the measurement the collection distance increases from the minimum up to after 50 hours of measurement a 22% for CDS116 and a 28% for CDS126. This increase might be due to the extra traps generated during the irradiation that are not stable enough for keeping the charge trapped and, therefore, they had released it allowing these traps to be filled again by the ^{90}Sr. The dark current level is smaller compared to the levels before and after the first irradiation, indicating that the noise has been reduced after irradiation. The evolution of the collection distance for an electric field of 1 V/µm is shown in Table 8.1.

	CDS126	**CDS116**
Before irradiation	~130 µm	~175 µm (470 V bias)
After irradiation	~150 µm	~155 µm
After heating	~145 µm	~180 µm
After second irradiation	~125 µm	~143 µm

Table 8.1: Collection distance values at 1 V/µm of both diamonds before and after each irradiation, as well as after the TSC process.

Hysteretic measurements of the collection distance of the diamond, after 20 minutes of having applied the bias, against the electric field are measured again after the second irradiation. Figure 8.12 shows the results for CDS126 and Figure 8.13 for CDS116. The measurement was done twice to observe the reproducibility of the measurement. The reproducibility is not as perfect as it was after the first irradiation, indicating that after this irradiation the damage taken by the diamond is clearly bigger. The leakage current breakthroughs of CDS126 (Figure 8.12 right) have also changed with respect to the first irradiation, where the diamond remained almost undamaged, now there is a breakthrough after 200 V, that is for a field lower than 1 V/µm and it has changed polarity (before, the quick breakthrough happened in the opposed polarity). The leakage currents for CDS116 (Figure 8.13 right) have diminished with respect to the first irradiation. After the first irradiation the maximum leakage current attained was of 0.25 nA. After the second one the maximum leakage current is about 0.1 nA.

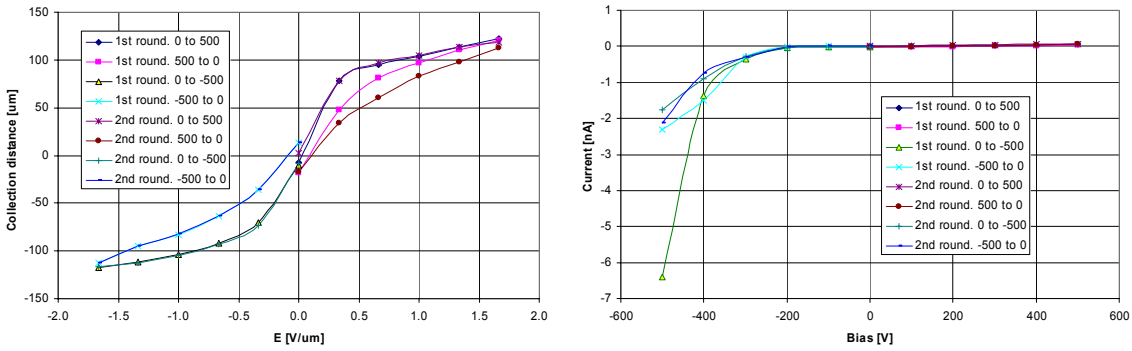

Fig. 8.12: Left: δ versus electrical field curves for CDS126 after a second irradiation of $1.8 10^{15}$protons/cm^2. Right: Leakage current during the measurement.

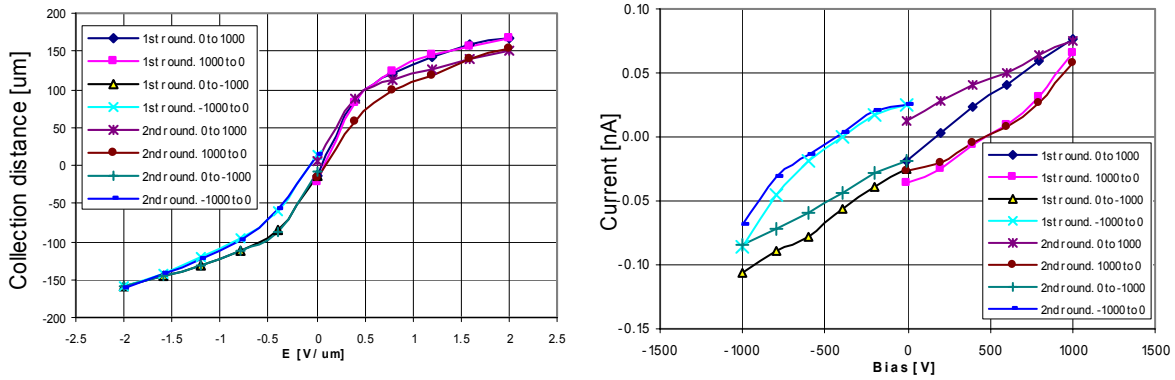

Fig. 8.13: Left: δ versus electrical field curves for CDS116 after a second irradiation of $2.8 \cdot 10^{15}$protons/cm^2. The measurement is done twice to test the reproducibility. Right: Leakage current during the measurement.

From the hysteretic plots we observe a degradation of the collection distance at 1 V/ µm of 37% for CDS116 and a 42% for CDS126 after the fluence equivalent to 10 years of LHC operation near the IP (see Figure 8.14).

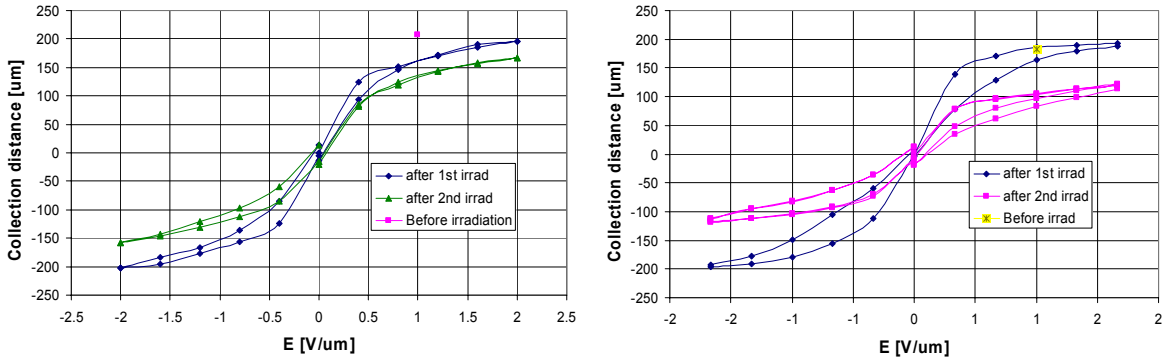

Fig. 8.14: Left: δ versus electrical field curves of CDS116 after a first irradiation of 10^{15}protons/cm^2 and after second irradiation of $2.8 \cdot 10^{15}$protons/cm^2, to the same 500µm thick polycrystalline CVD diamond. The value of δ before irradiation at 1V/µm is also given. Right: δ versus electrical field curves of CDS126 after a first irradiation of $5 \cdot 10^{14}$protons/cm^2 and after second irradiation of $1.8 \cdot 10^{15}$protons/cm^2, to the same 300µm thick polycrystalline CVD diamond. The value of δ before irradiation at 1V/µm is also given.

Measurements of the evolution of the collection distance versus time at different electric fields were also performed. Results are shown in Figure 8.15 for CDS126 and Figure 8.16 for CDS116. The evolution of the dark current in the diamond is also given. For CDS126 the collection distance was measured during 4 hours and for CDS116 during half this time, at constant bias. After this period of time, the bias was increased or decreased. The leakage current is unstable for CDS126 at bias bigger than 500 V, more than 1.67 V/µm (Figure 8.15 left). The current scale is logarithmic. For CDS116, the current scale is not logarithmic and the leakage current is very low even at fields bigger than 2 V/µm. The negative collection distance observed when the diamond was biased at 0 volts is due to the fact that the during the

depolarisation period the internal field in the diamond is negative, therefore the signal is read as if the bias has a different polarisation and plotted as negative.

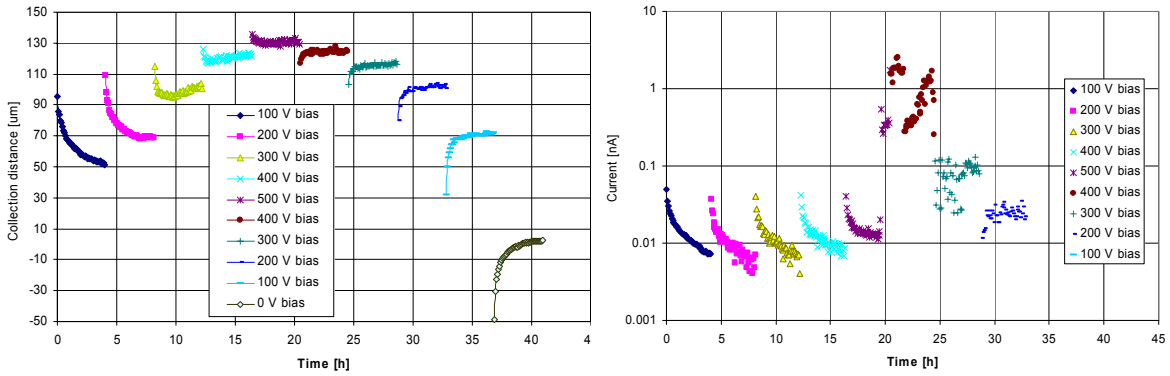

Fig. 8.15: Left: Evolution of the signal from CDS126 after the second irradiation at different electric fields. Right: Evolution of the leakage current at different electric fields.

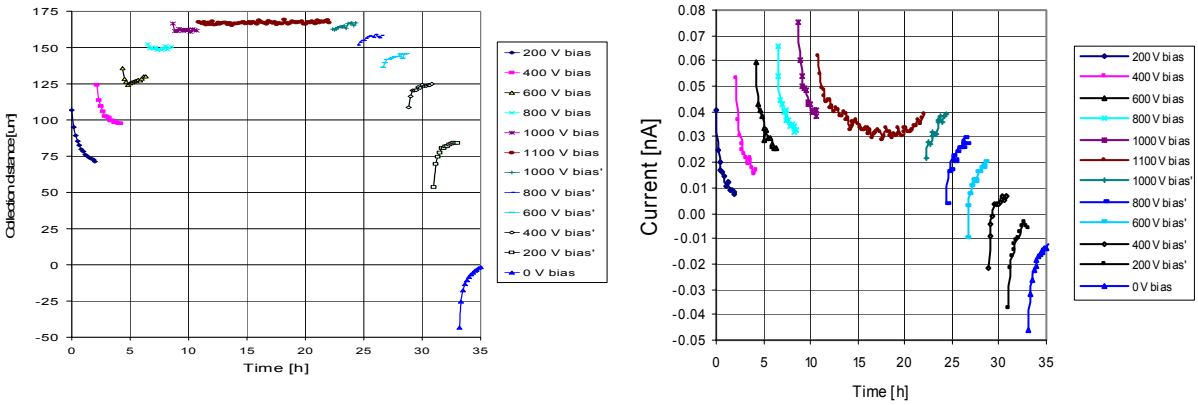

Fig. 8.16: Left: Evolution of the signal from CDS116 after the second irradiation at different electric fields. Right: Evolution of the leakage current at different electric fields.

The last points of each curve in Figures 8.15 left and 8.16 left are plotted in the graphs of collection distance against electric field shown in Figure 8.17. Notice the strange shape, seen in both diamonds, of the increasing bias curve. Again, with decreasing bias curve, the collection distance is higher than the one obtained with increasing voltage. This last effect has already been seen after the first irradiation and it is shown in Figure 8.10. The collection distance for CDS116 (Figure 8.17 left) appears to be saturated beyond electric fields of 2 V/µm (1000 V), corresponding to a saturated collection distance around 165 µm. For CDS126 (Figure 8.17 right) the saturation field is not completely reached, nevertheless the collection distance at an electric field of 1.66 V/µm (500 V) is almost 130 µm.

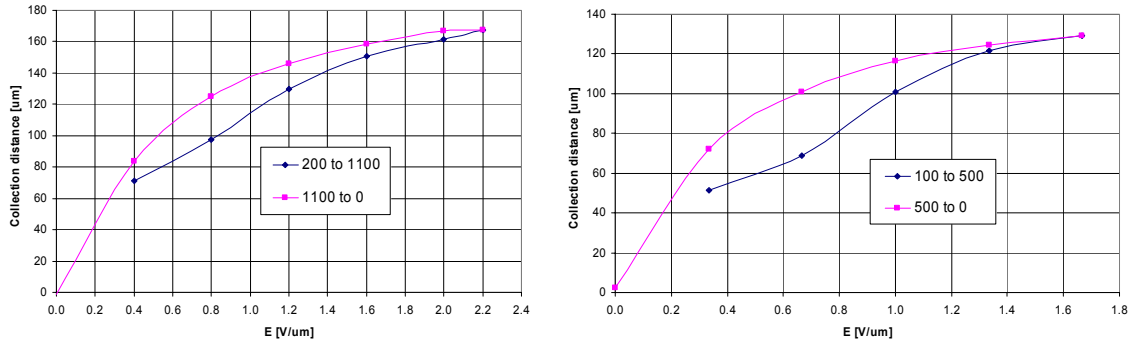

Fig. 8.17: Left: δ versus electrical field curves after an irradiation of $2.8 \cdot 10^{15}$protons/cm^2 for CDS116. Right: δ versus electrical field curves after an irradiation of $2.8 \cdot 10^{15}$protons/cm^2 for CDS126.

8.5 Conclusions

Diamond shows a signal degradation of 42% due to radiation damage after a proton fluence equivalent to 10 years of normal operation of the LHC in the design positions for BCM sensors in CMS. Therefore the diamonds prove that they can be used for this application as they still produce signal after being irradiated at a fluence of more than $2 \cdot 10^{15}$ protons/cm^2. Nevertheless corrections on the BCM readout system should be performed in order to adjust this decrease on collection distance.

The leakage current from the diamond samples decreased down to 60% from its original value prior to irradiations.

The most important effect of radiation damage on diamond is the creation of charge traps in its bulk. Due to this effect, pumping periods increase considerably. The number of generated traps can be so important that in case where the diamond is depumped these traps can act as a dwell which catches the electron hole pairs generated by a passing particle and masks the signal completely.

After performing a TSC, the diamond samples showed to have recovered the original collection distance values. New traps have been created, but once they are filled, they do not interfere with the signal: the damages that made a decrease on the signal seem to have disappeared.

Chapter 9

Simulation of the worst accident scenario with a test beam

To test the response of the sensors to a flux equivalent to the "worst case" beam accident scenario, the sensors were placed in a dedicated high intensity 24 GeV proton beam from the Proton Synchrotron (PS) facility at CERN.

This worst case scenario is assumed to be that of an unsynchronized beam abort accident [10], [11]. From simulation it has been estimated that ~10^{12} protons may then be lost at the CMS region, and at the location of the BCM, the fluence being ~10^{9} protons/cm^2 delivered in ~250 ns.

9.1 Cable requirements

Readout electronics were located in a distant control room. Therefore the cable that will be used to drive the signals to the electronic equipment was of a quality that ensures the integrity of the original signal value. This requirement also applies for the final BCM cabling, as BCM sensors will be located inside the experiments but the readout electronics will be placed in a less radioactive area, outside the experiment. The distance from the BCM sensors to these readout devices will be around 15 meters. Thus, the cable used for this test beam must have an equivalent length.

Different signal cables were tested by comparing the input signal from a signal generator to the cable with the output signal from the cable. Some results are shown below.

Figure 9.1 shows the signal output for 3 different high voltage cables R02232 type whose length was 20 meters. The input pulse is 400 mV during 5 ns. The signal response has a value of 260 mV, a width of 4.63 ns with a rise time of 2.80 ns and a fall time of 3.52 ns. The signal delay is of 123.52 ns.

For the case shown in Figure 9.2, the response to the same input signal for a co-axial cable RG58 [73] of 16 meters length has a value of 340 mV, with a width very close to the original 5 ns. The rise and the fall times are much shorter than for the previous sample.

Another cable tested is a SUHNER [74] of 50 Ohms. Its response for an input signal of 400 mV and 5 ns width is shown in Figure 9.3. It has an output of 280 mV. Again, the rise and fall times are long and similar to those of cable R02232 (see Figure 9.1).

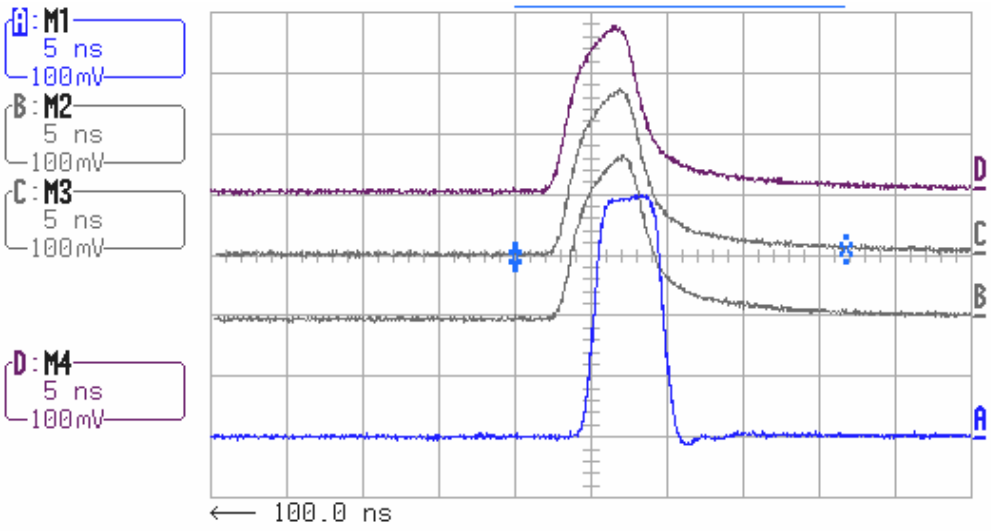

Fig. 9.1: Signal outputs from three high voltage cables R02232 of 20 m length. The cables were connected with male and female LEMO connectors. Trace A is the incoming pulse.

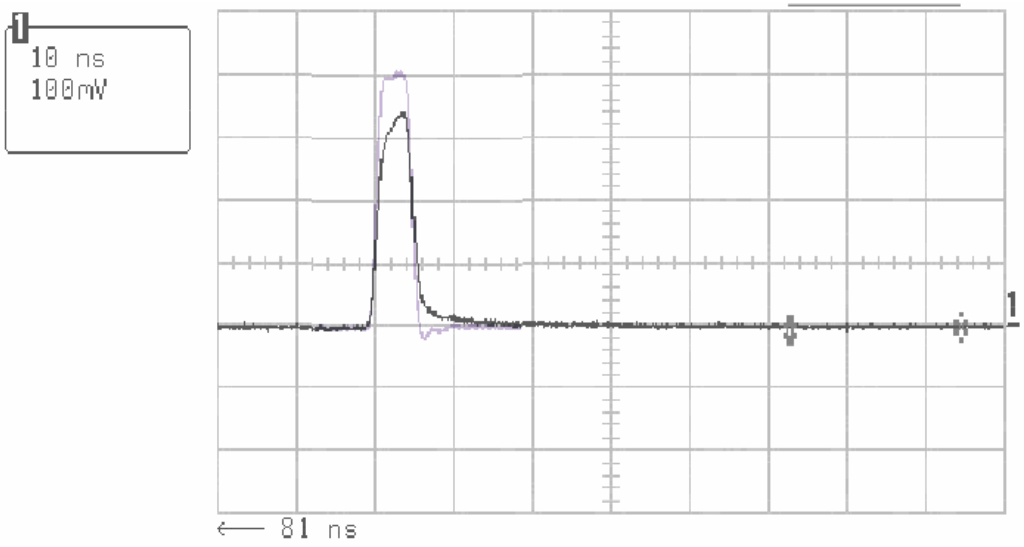

Fig. 9.2: Signal output from co-axial cable RG58 of 16 m length. Incoming pulse in grey.

In Figure 9.4 the responses to an input signal of 700 mV and 200 ns width for an unshielded (Figure 9.4 left) and shielded (Figure 9.4 right) cables of 10 meters length are shown. The output signal amplitude is below 30 mV. The distortion is more important in the unshielded case.

After having compared all results, the cables chosen for the test beam were the co-axial RG58 of 16 m length. Moreover, the 16 m is approximately the length of the cable that should connect the diamond inside the experiments to the readout electronics.

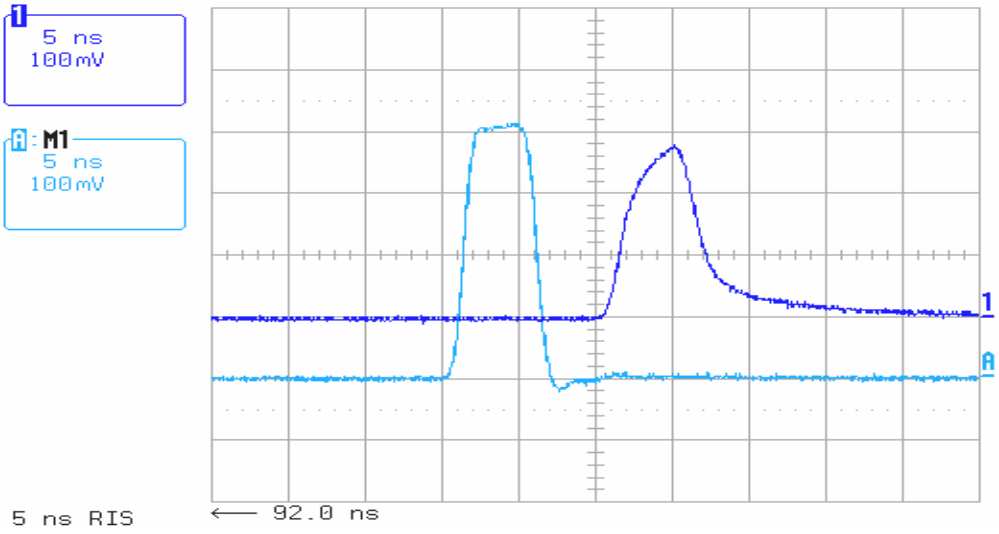

Fig. 9.3: Signal output from SUHNER 50 Ohms. Male and female are LEMO connectors. A: Incoming pulse; 1: Output from cable.

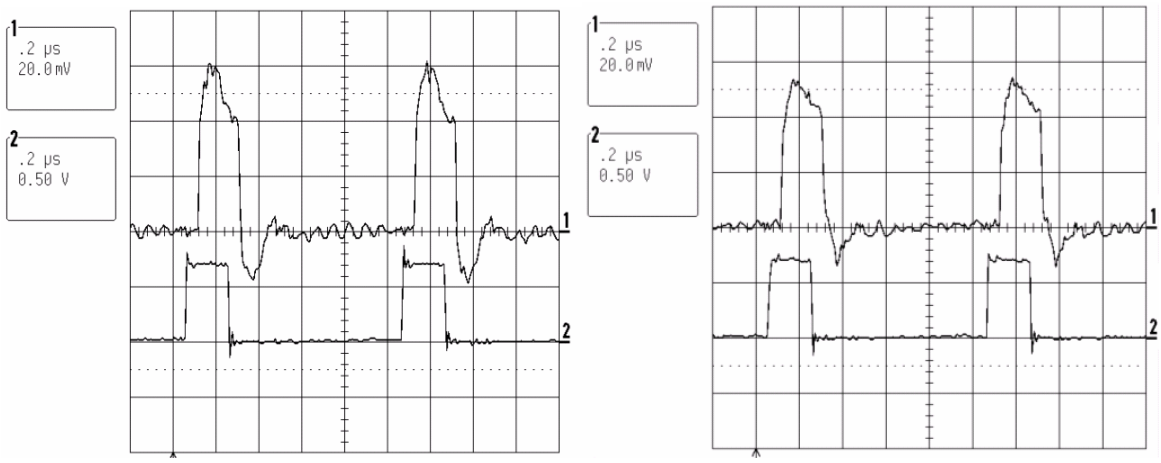

Fig. 9.4: Signal output, line 1, from thick cable unshielded (left), and shielded (right). 10 m length. 2: Incoming pulse; 1: Output from cable.

9.2 Beam characteristics and dosimetry

In order to approximate an unsynchronized beam abort the beam spill was composed of one bunch up to a maximum of eight bunches, each containing ~10^{11} 24 GeV protons (MIPs). The 1σ width of the bunch was 10.5 ns, and the inter-bunch spacing was 262 ns.

The beam spot had an oval shape of 9 cm by 3 cm. The beam profile was determined by using ^{24}Na dosimetry in aluminium film (see Figure 9.5). The bunch intensity varied by a factor ~53 from the highest intensity area ($1.5 \cdot 10^{10}$protons/cm^2 ±30%) near the centre (position A) to the periphery of the beam (position B). These were the 2 different locations in the beam spot where the sensors could be positioned.

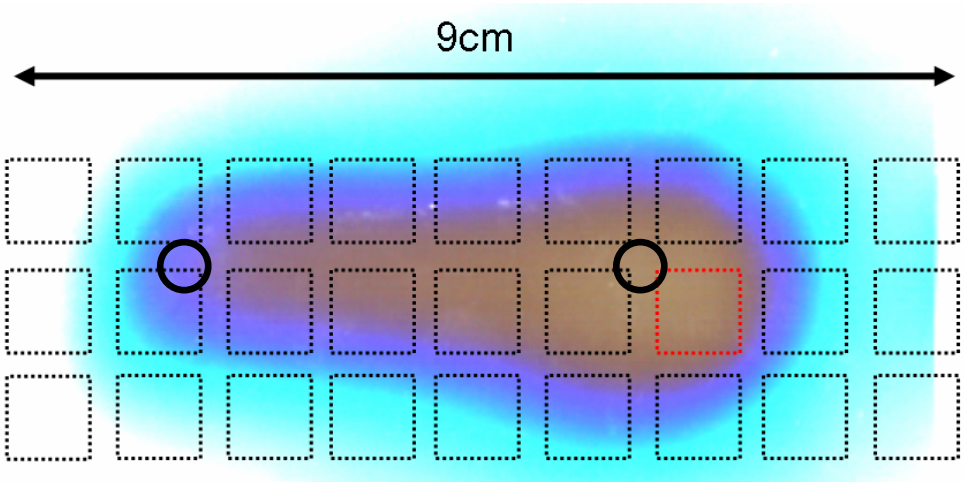

Fig. 9.5: Aluminum dosimetry. The circles show the positions for the sensor assembly.

9.3 Sensor assembly

Two irradiated diamond samples and two non-irradiated diamond samples were used for this test beam. Figure 9.6 shows a diamond sample mounted in a test box, and the complete assembly, and Figure 9.7 the bias circuit as used in the test beam.

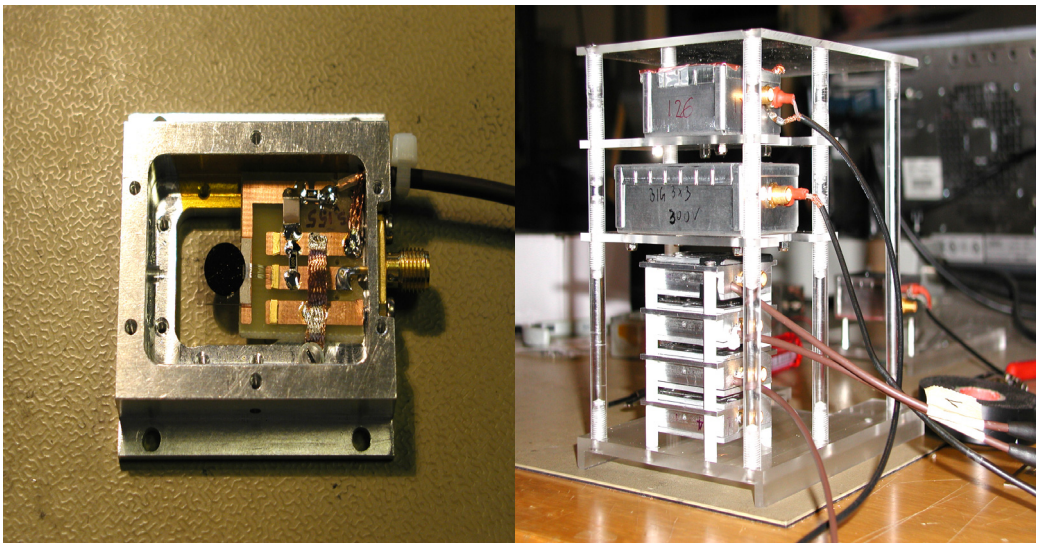

Fig. 9.6: Left: box containing a diamond sensor with the bias circuit connected to it. Right: assembly of several boxes containing diamonds and a silicon sensor.

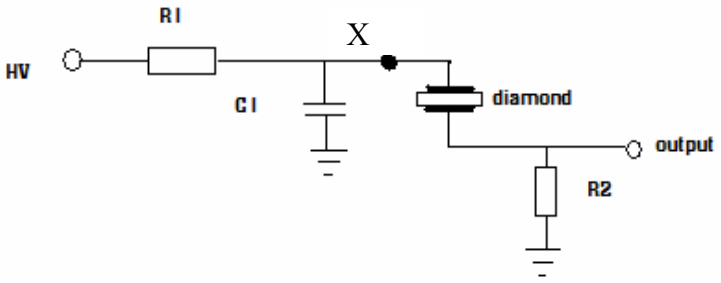

Fig. 9.7: Schematic of the bias circuit for the sensors. C1 acts as reservoir capacitor. R1 and R2 values are 1 M Ω. X: PSpice simulation probe, see text.

9.4 Results

The sensor was connected via a 16m long 50Ω coaxial cable, terminated by a matched resistance. A LeCroy LC564A 1GHz bandwidth digital oscilloscope was used to record the signals.

Figure 9.8 shows the response for a single bunch from diamonds CDS116 (500µm thick sample-irradiated) and CDS126 (300µm thick sample-irradiated), at position B, where the aluminium dosimetry measured around $3 \cdot 10^8$protons/cm^2. The leading edge of the signal has been fitted with a Gaussian and compared to the PS machine data (see Figure 9.9).

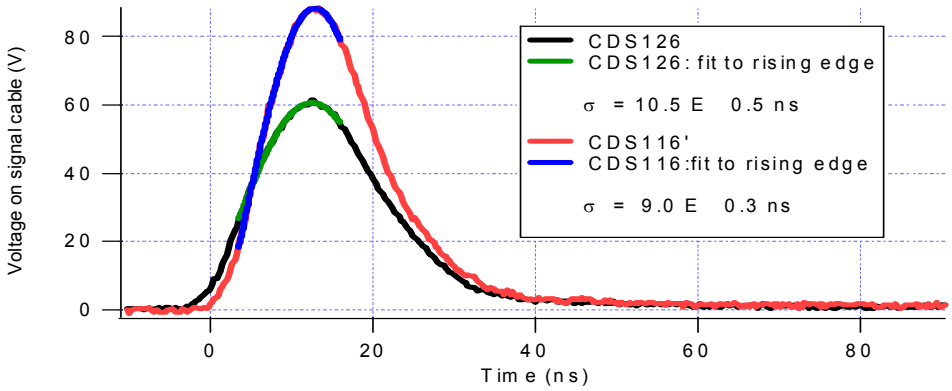

Fig. 9.8: Signal response from two different diamonds for a single bunch in position B. The signal structure can be compared with the bunch structure from the PS machine (see Figure 9.9).

To determine the fluence the following expression is used:

$$Fluence = \frac{P.Area}{R_c \cdot q_e \cdot \rho_e \cdot \delta} \tag{9.1}$$

where *P.Area* is the peak area, R_c is the cable resistance (50 Ω), q_e is the electron charge, ρ_e is the number of electrons per μm that a MIP generates in diamond and δ is the diamond collection distance.

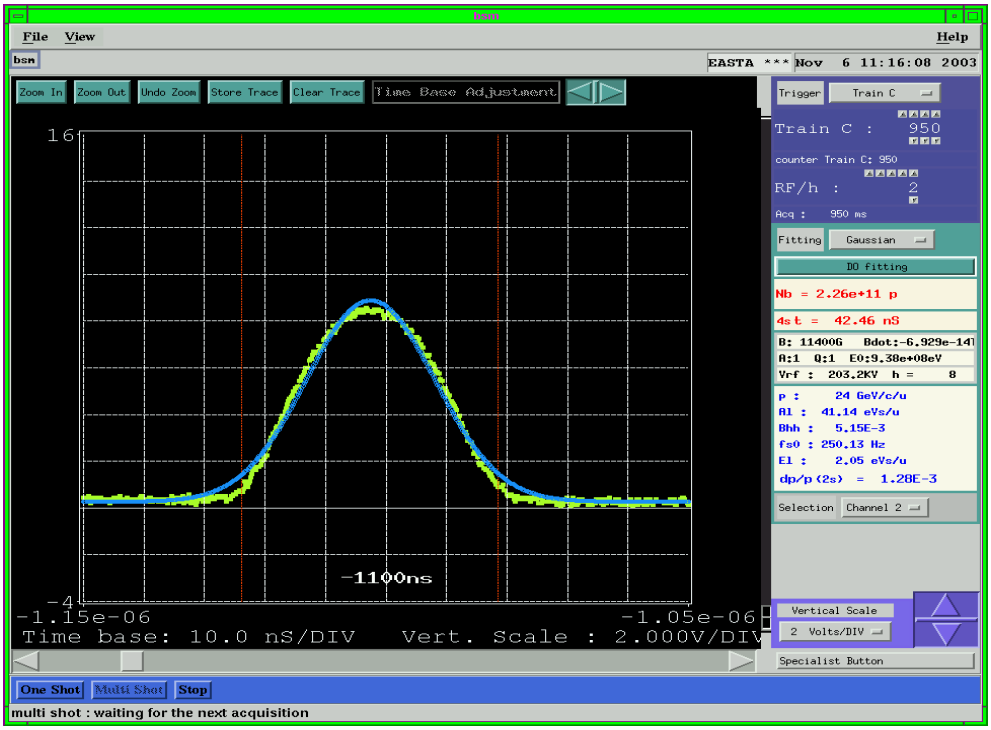

Fig. 9.9: Bunch structure given by the PS machine.

For CDS126 we obtain σ = 10.5 ns and for CDS116 σ = 9.0 ns. The values are comparable to the PS bunch structure, whose σ was 10.5ns. The trailing edge of the signal exhibits a non-Gaussian tail. The reason for the tail is not understood.

Integrating these pulses and taking into account the δ for each diamond at the corresponding bias and the area of the metallization, we obtain the number of protons per cm^2 and per pulse that traversed the sensors. The value found for CDS126 is $8.7 \cdot 10^7$ protons/cm^2, and for CDS116 it is $9.8 \cdot 10^7$ protons/cm^2, showing a reasonable agreement between the two samples. The difference from the dosimetry value is about a factor three. The uncertainties on the dosimetry are of the same order of magnitude, due to bunch to bunch variation and the position uncertainty within the beam.

Another aspect that can be observed from Figure 9.8 is the large amplitude of the signals. The maximum signal voltage for CDS126, biased at 300 V, is 61 V which represents 1.22 Amperes. For CDS116, biased at 500 V, the maximum signal voltage is even larger, namely 88 V, due to a larger δ. This represents a current of 1.76 Amperes through the diamond.

The signal from a shot with 8 bunches is shown in Figure 9.10 for the two diamond samples CDS126 and CDS116. The bunch structure is clearly visible with the interbunch spacing of 262 ns, consistent with the PS machine data.

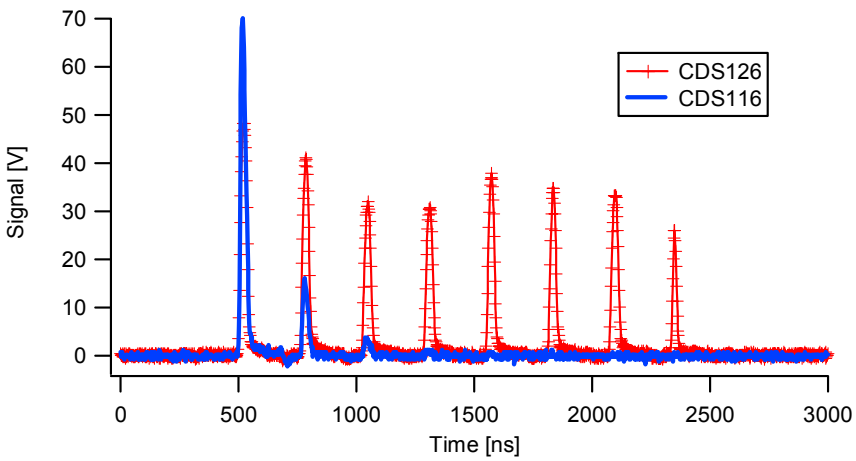

Fig. 9.10: Response signal of CDS126, biased at 300V, and CDS116, biased at 500V, to an 8 bunch shot. In the case of CDS116 the reservoir capacitor is not big enough to maintain the bias across the diamond.

The bias circuit (Figure 9.7) had a reservoir capacitance, C1, used to maintain the bias voltage on the samples. For CDS116, C1 had a value of 100 pF that was found to be insufficient to maintain the bias on the sample. The capacitor is fully discharged after the third bunch, thus the 5 last bunches are not seen by the diamond. In comparison CDS126 had a C1 of 15 nF that was sufficient to maintain the bias voltage for eight consecutive bunches.

A PSpice simulation [75] was used to determine how the voltage at point X of Figure 9.7 changes after each bunch. The results of this calculation are shown in Figure 9.11 for CDS126 and for CDS116. For CDS126 this voltage decreases 12 V over a bias of 300 V. For CDS116 the voltage drops to almost 0 V starting at a bias of 500 V.

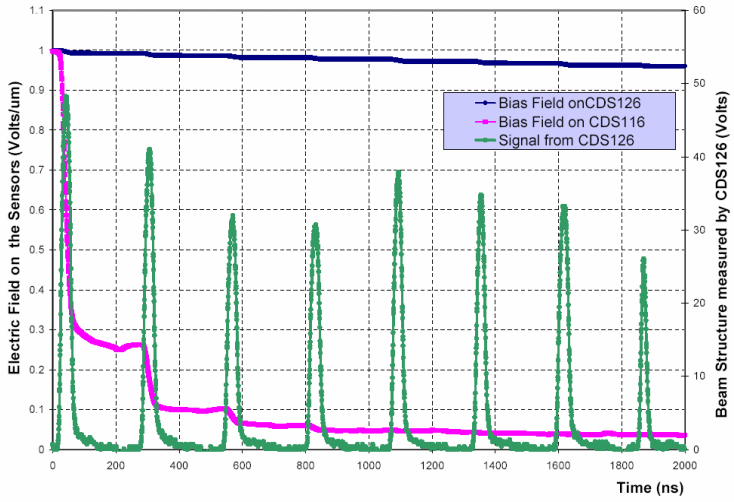

Fig. 9.11: PSpice simulation showing the decrease of the electric field across CDS126 and CDS116 due to the discharge of the capacitor after each bunch of the shot. Also shown is the signal, in volts, from CDS126.

After several shots at position B in the beam profile, the assembly was moved into position A, the most intense position in the beam. The results obtained for CDS126 are shown in Figure 9.12.

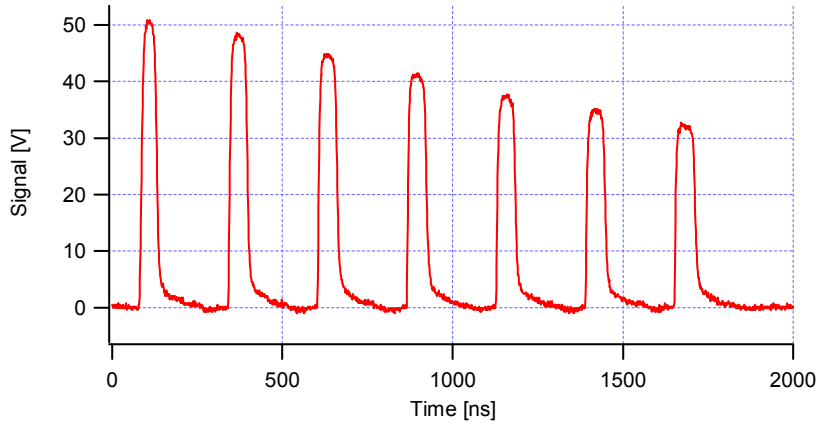

Fig. 9.12: Response signal of CDS126 to a 7 bunch shot in the beam spot position of maximum fluence (position A). The diamond was biased at 60V.

CDS126 was biased at 60 V and the signal reaches 50.8 V for the first bunch. For the following bunches the value decreases proportional to the discharge of the capacitor, decreasing the bias voltage on the diamond. A measurement with the bias voltage at 30 V is shown in Figure 9.13. Again the amplitude of the signal for the first bunch is close to the bias voltage. Also shown in Figure 9.13 is the voltage at point X (see Figure 9.7) during the seven bunch shot. The diamond acts as a quasi conductor due to the high ionization density during each bunch and discharges the reservoir capacitance C1.

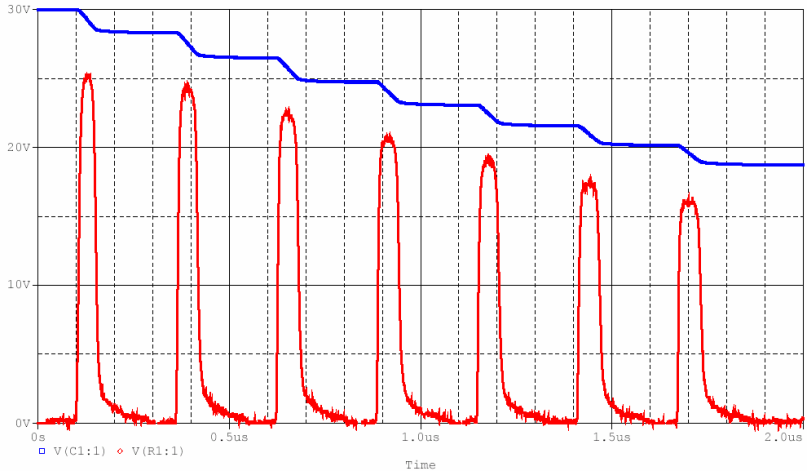

Fig. 9.13: Response signal of CDS126 to a 7 bunch shot in the beam spot position of maximum fluence. The diamond was biased at 30V. The upper curve shows the evolution of the bias voltage at point X of Fig. 9.7.

Figure 9.14 compares signals from a bunch at position A and from a bunch at position B. It is observed that for the signals seen in position A the capacitor C1 for CDS116 diamond is too small and discharges too quickly.

For CDS126 a clear difference in shape is observed between the saturated signals in position A and the signals at position B. The signal at position A has a plateau at a value near the bias voltage. It indicates that the amount of charge created in the diamond is sufficiently large to maintain a current in the bias circuit over an extended period of time.

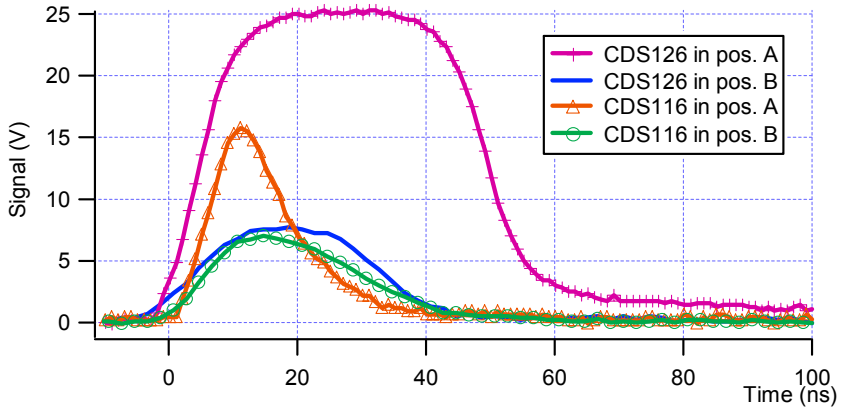

Fig. 9.14: Response signal of CDS126 and CDS116 to the 1st bunch at position A and at position B.

After the measurement in position A, no change of the response was observed when measuring again in position B, indicating no damage of the sensors.

9.5 Conclusions

CVD diamond is able to withstand intense beams. They have been exposed to particle fluxes similar to an unsynchronized beam abort within the CMS experiment. Under such conditions, the diamond samples are found to respond and recover from consecutive high intensity beam bunches.

The observed high currents generated in the diamond from conditions similar to an unsynchronized beam abort require that a protection system for the BCM readout electronics be implemented.

Chapter 10

Fast and slow extraction test beam

Several diamond sensors were tested under various beam conditions at the T7 irradiation facility of the PS. The composition and particle energy of the beam depended on the target and the magnet settings that were used. Energies ranged from 3 to 5 GeV. The beam could be extracted fastly and slowly.

For the fast extraction the particle bunch had a 4 σ width of 42 ns. Several bunches could be extracted, with a separation of 262 ns between them. The diamond samples were placed in an assembly located at the focal point of the beam transport system. The intensity of the fast extracted bunches varied following a Gaussian distribution. The maximum fluence was about $3 \cdot 10^6$ particles/cm^2.

The bunch of the slow extraction had a width of 400 ms and was used to test the capabilities of the diamond sensor and the readout electronics, to detect single MIPs.

The purpose of this test was to study the resolution of the diamond sensors and their readout to fluences ranging from single MIP per cm^2 to more than 10^6 particles/cm^2. These fluence values are the typical values that the BCM sensors will encounter during normal operating conditions and also during an accident build-up.

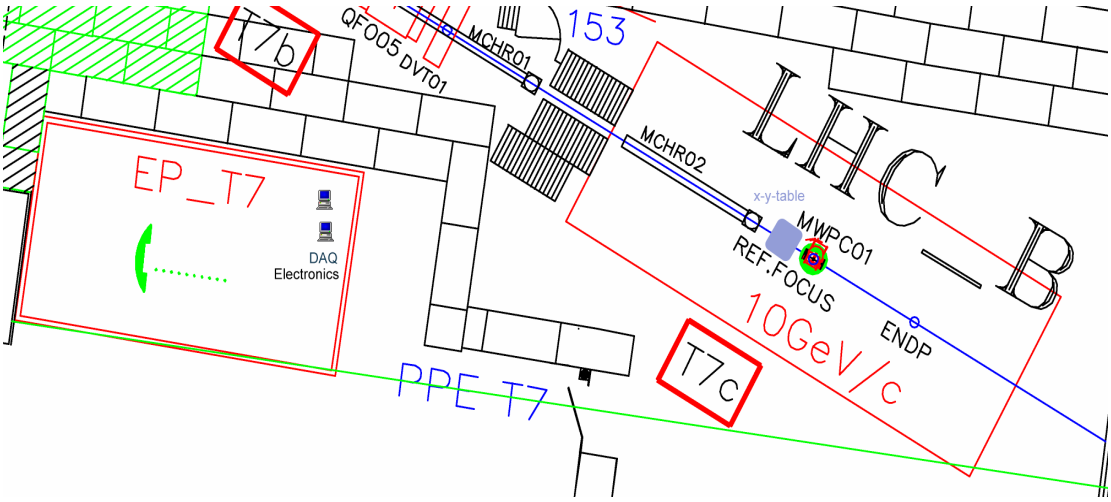

Fig. 10.1: Layout of the T7 beam line.

Since the uncertainties on the fluence to be monitored by the BCM are quite large, it must be demonstrated that the BCM device is capable to monitor the fluence over a large range of fluences. The test beam allows to cover a range from a few particles/cm^2/spill to about 10^5 particles/cm^2/spill.

The test beam period consisted of two days of slow extraction (10^{th}-11^{th} May 2004) and two days of fast extraction mode (12^{th}-13^{th} May 2004). Characteristics of the slow and fast extraction modes are given in the table below.

	Slow extraction	Fast extraction
Spill length	400ms	40ns < T < 8*256ns
Spill mini bunches	N>10^6	1 < N < 8
Particles per bunch	O(1)	O(10^6)
Beam diameter	~1cm x ~2cm	~1cm x ~2cm

Table 10.1: Characteristics of the beam at slow and fast extraction.

10.1 Diamond samples and assembly

Four diamond samples were used for this test beam: CDS116, CDS126, CDS154 and CDS155. The outputs of the two last diamonds are summed as shown on Figure 10.2. A list of the diamond sensors used and their properties can be found in Table 10.2.

Diamonds CDS116 and CDS126 have been irradiated previously to fluences of $2.8 \cdot 10^{15}$ protons/cm^2 and $1.5 \cdot 10^{15}$ protons/cm^2 respectively. CDS154 and CDS155 are un-irradiated diamonds. Their collection distances at different electrical fields can be seen in chapter 7.

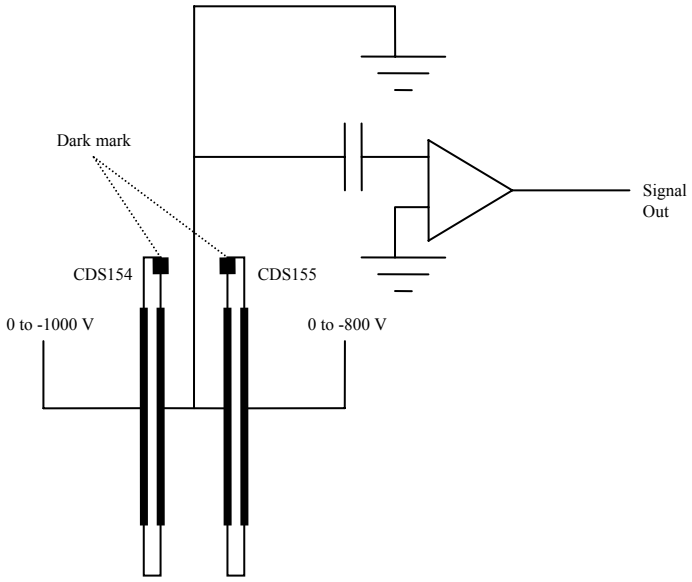

Fig. 10.2: Scheme of the set-up used for diamonds CDS154 and CDS155.

Name	Irradiated [p/cm^2]	Thickness [μm]	Metallization (Shape, Area)	Collection distance at 1V/μm [μm]
CDS116	2.8 10^{15}	500	Dot 0.44cm^2	120
CDS126	2.3 10^{15}	300	Dot 0.44cm^2	110
CDS154	0	360	Dot 0.44cm^2	164
CDS155	0	360	Dot 0.44cm^2	174

Table 10.2: Characteristics of the beam at slow and fast extraction.

The diamonds were placed in separate cartridges which can be mounted on a structure also containing the scintillators used for trigger and fluence measurement. The assembly is shown in Figure 10.3 and Figure 10.4. The structure was mounted on the base plate of an x-y table.

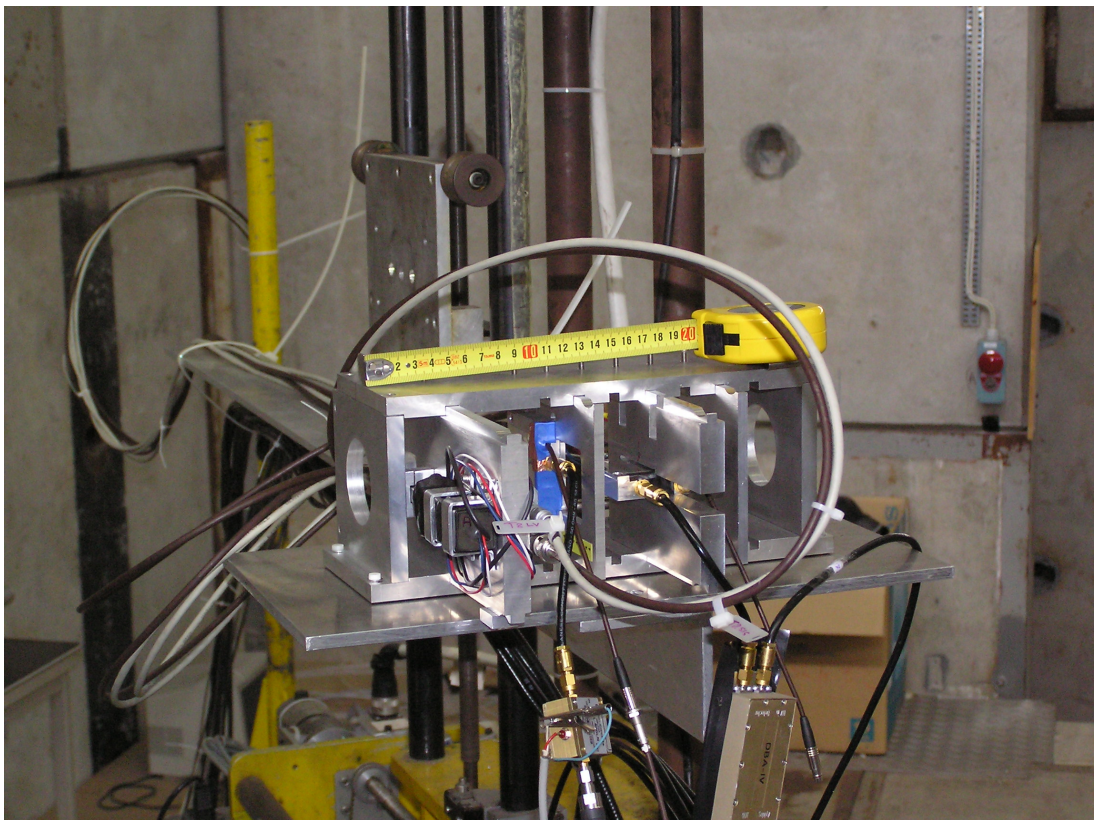

Fig. 10.3: The sensor assembly mounted on the base plate of the x-y table in the T7 area.

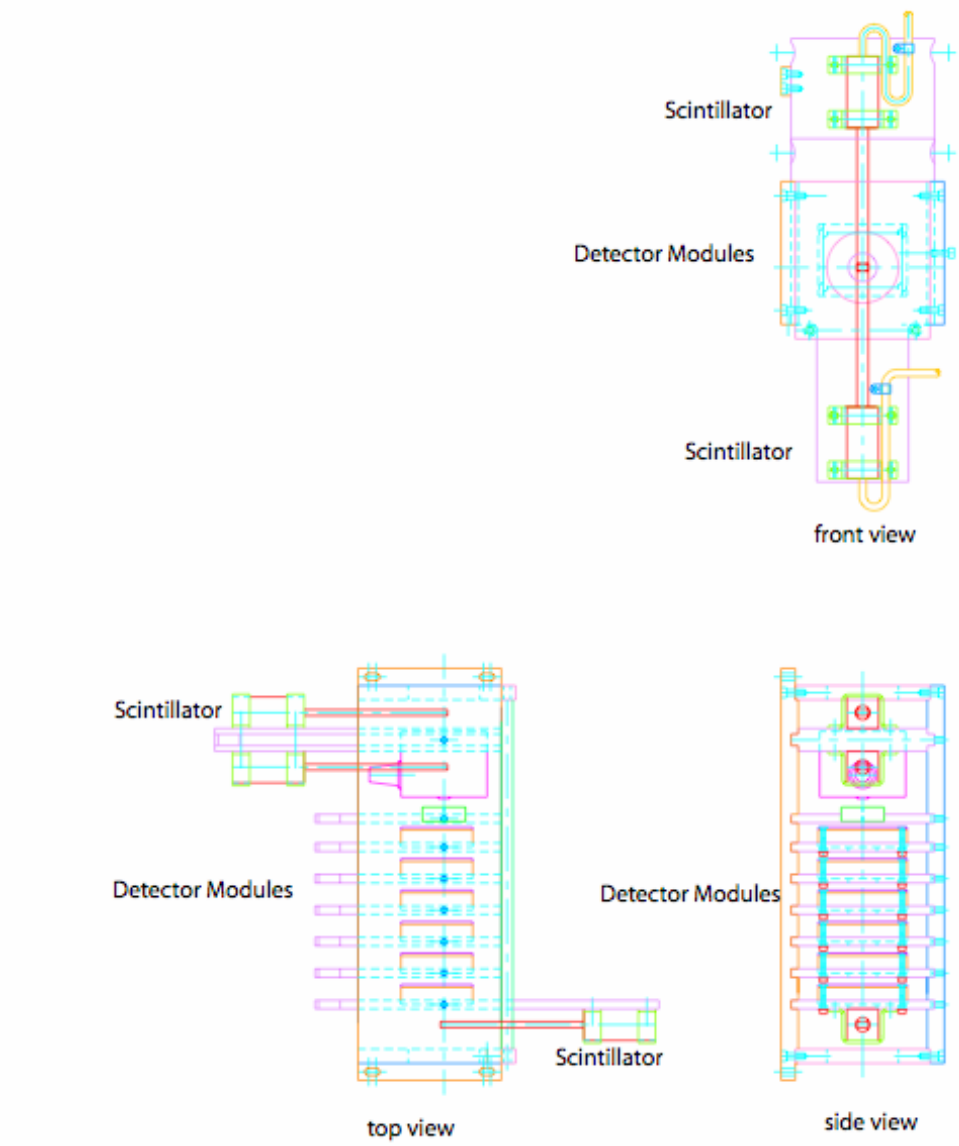

Fig. 10.4: Different views of the sensor assembly.

The Layout of the T7 beam-line is shown in Figure 10.1. The path of the DAQ/Electronics room EP/T7 to the x-y table near the focal point (blue square) is approximately 15 m.

10.2 Beam profile

A scan of the beam with the diamond was done with a fast extraction beam but with low intensity. Figure 10.5 shows the readings from diamond sensors CDS116 and CDS126. The horizontal position was fixed in the focal point (X=-4.2) and the assembly was moved on the vertical direction (Y).

Figure 10.5 shows the fluence readings from both sensors at all the different Y positions, from the position that showed the maximum fluence to the exterior of the beam spot.

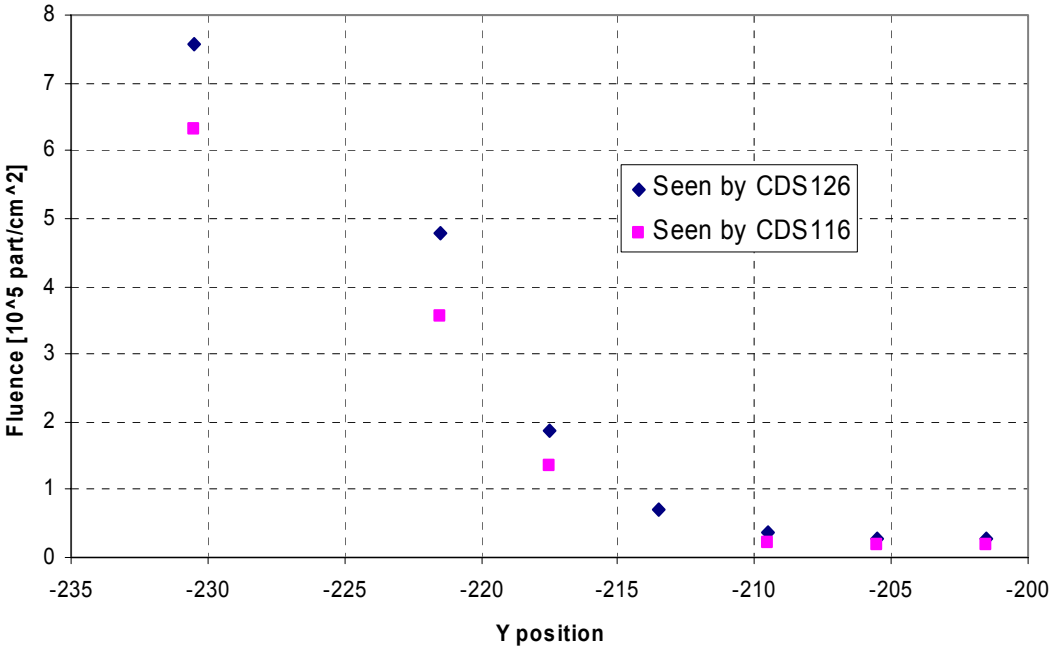

Fig. 10.5: Beam profile given by CDS116 and CDS126. Right figure, zoom of the most relevant zone.

The profile shows the position where the fluence is the highest and how the fluence changes with the vertical position. The assembly was fixed in the horizontal position, exactly in the focal point of the beam.

The profile of the beam measured by the diamond sensors is compared to the one measured by two sets of scintillators, named “cern 5x5” and “berlin 5x5” because their dimensions were of 5x5 mm^2 and one set was own by our group (cern) and the other was owned by another group that was working parasitically in the test beam area (berlin), in Figure 10.6. The values are normalized to 1 at their maximum. The profile given by the diamond sensors follows approximately the same curves measured by the two sets of scintillators. The measurement with the scintillators was done in slow extraction, but the beam profile is the same as during fast extractions, as Figure 10.6 demonstrates.

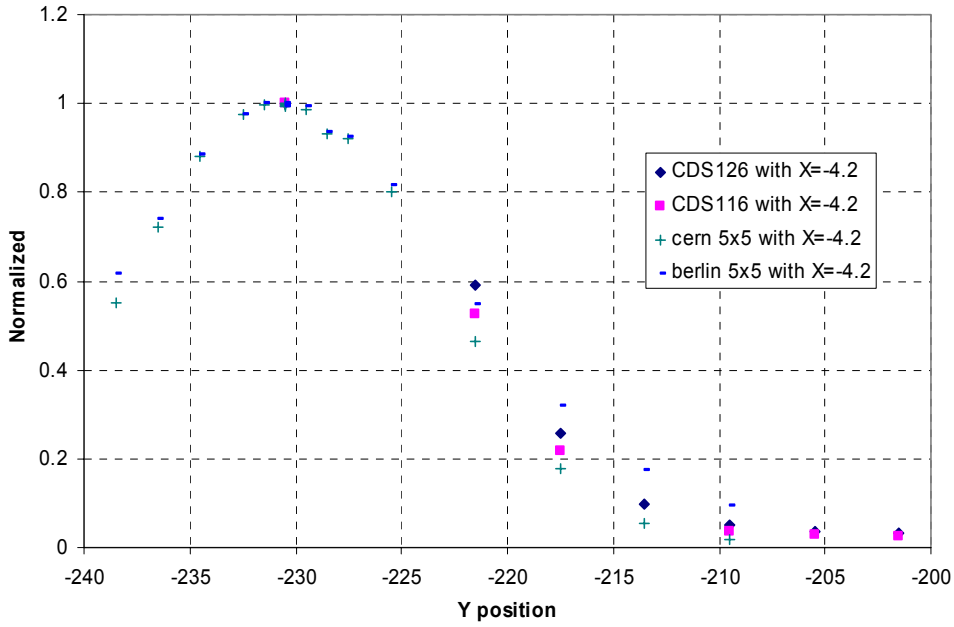

Fig. 10.6: Normalized beam profiles measured by CDS116, CDS126 and two different sets of scintilllators.

A beam profile and dosimetry was performed using OSL dosimeters. Figure 10.7 shows the relative beam profile measured by the OSL.

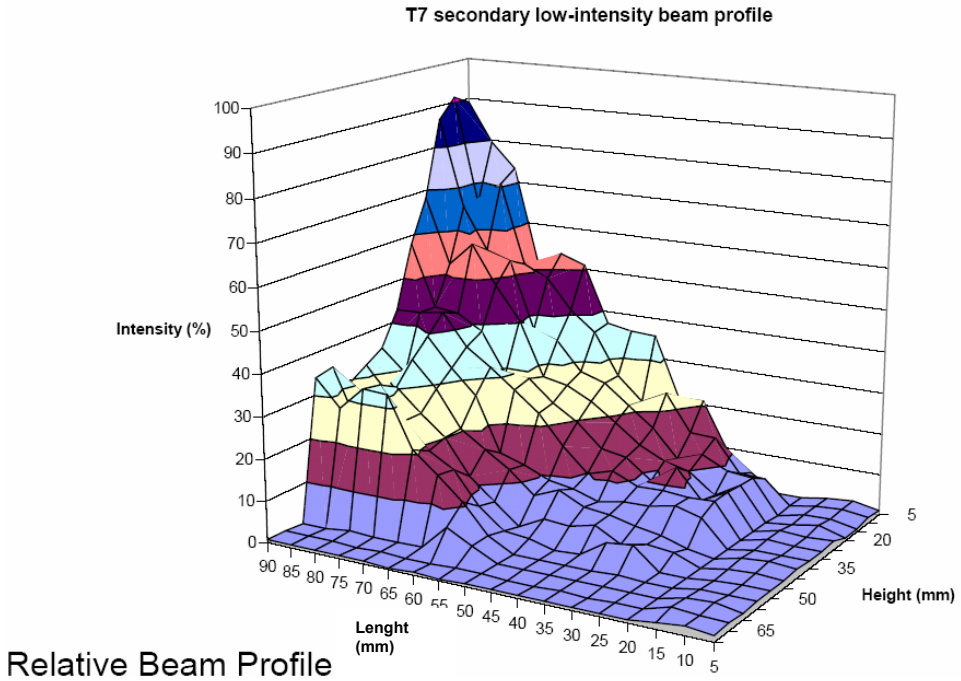

Fig. 10.7: Relative beam profile measured by the OSL dosimeters.

The dosimetry gave a fluence value of $5 \cdot 10^6$ particles per bunch over a spot of a 2 cm radius. The sensitive area of the OSL was partially outside the beam during this dosimetry.

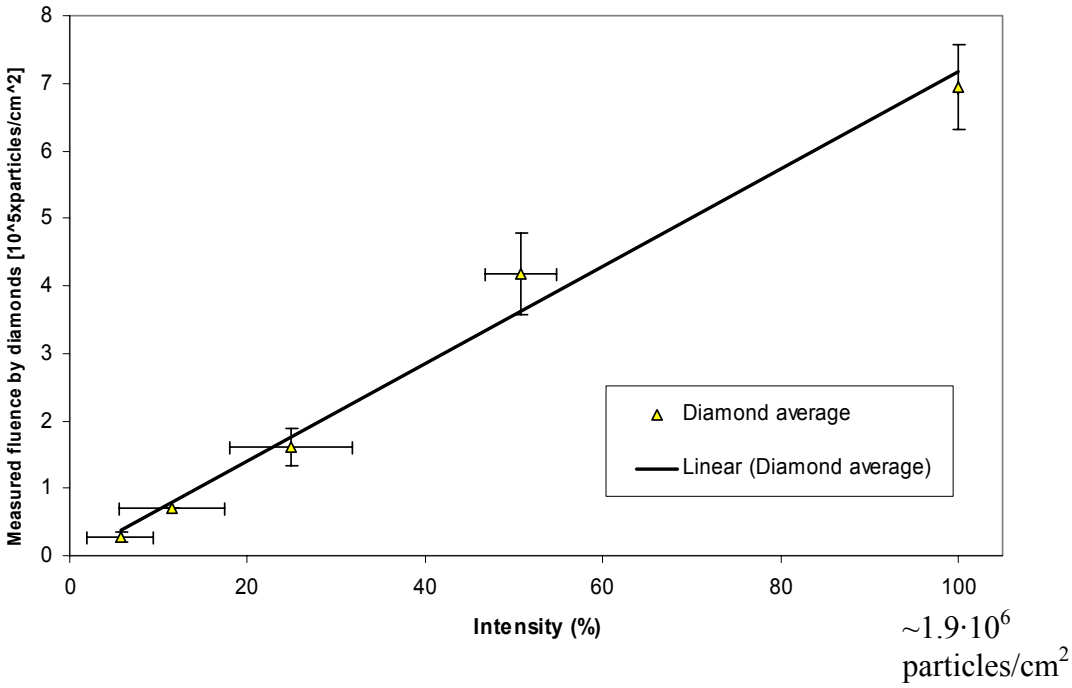

Figure 10.8: Average fluence measured by 2 diamonds against the beam intensity measured by 2 sets of scintillators.

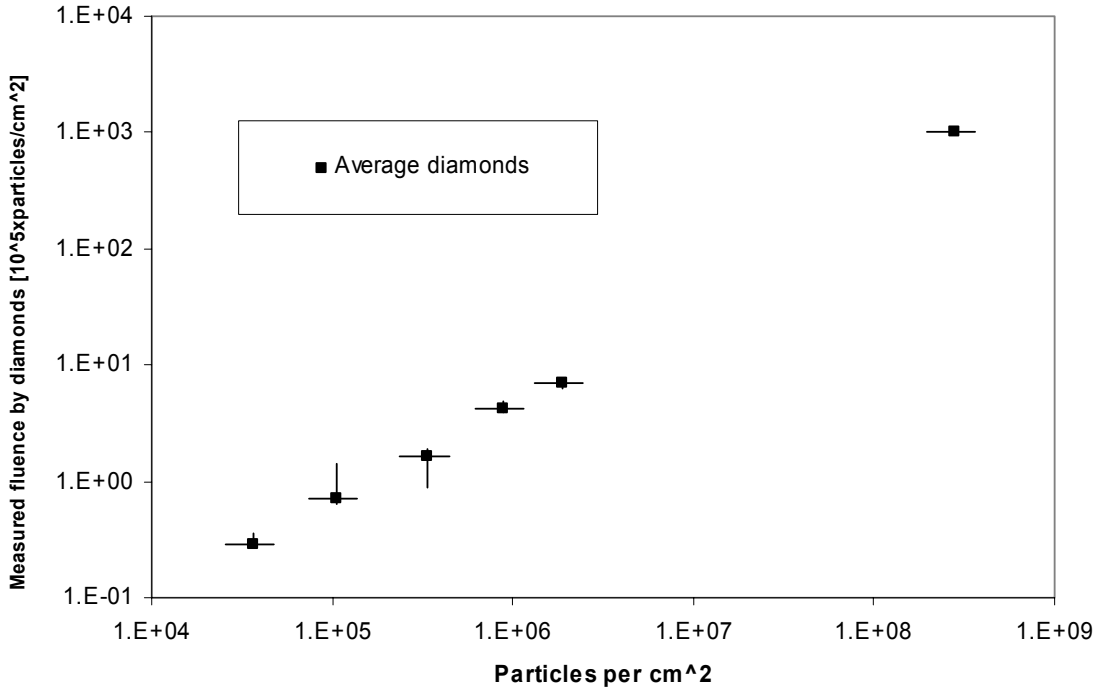

Figure 10.9: Average fluence measured by 2 diamonds against the beam intensity measured by other dosimetry sources.

Figure 10.8 shows the average readings from two diamond sensors versus the intensity of the beam measured by two different sets of scintillators. The scintillators measured a maximum fluence (corresponding to the 100% of intensity in the bottom axis of the plot in Figure 10.8) of ~$1.9 \cdot 10^6$ particles/cm^2. That is around a factor 2.5 higher than the fluence

measured by the diamonds. This 2.5 factor of difference can be explained as the beam that the scintillators saw was in slow extraction and the position along the beam axis was slightly different to that of the diamonds. However, the intensity distribution in slow or fast extraction is the same. The plot in Figure 10.9 adds the point measured at the high intensity test beam explained in Chapter 9.

10.3 Orientations of the sensors

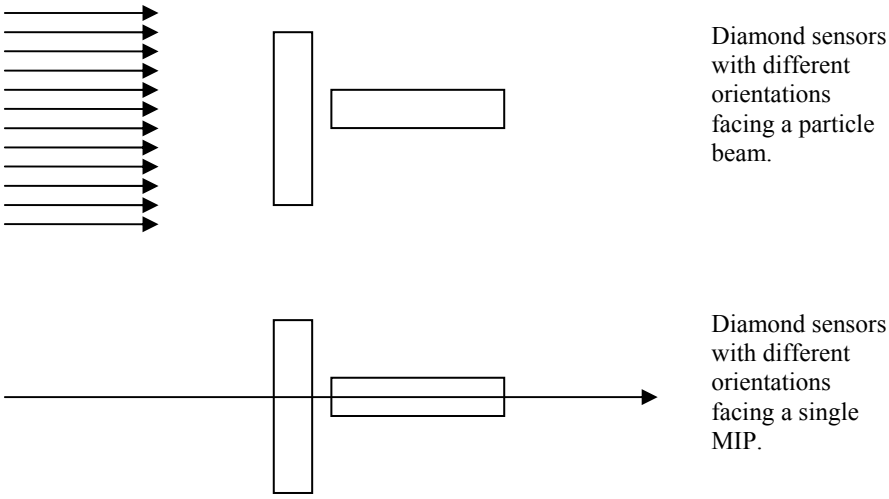

Fig. 10.10: Different orientations for the sensors.

The diamond sensors in the assembly could have two different orientations: perpendicular to the beam or parallel to the beam (see Figure 10.10). Intuitively one can think that in the case of a beam of particles traversing the whole diamond (upper figure), these particles will traverse the same sensor volume independently of the orientation. In the case of a single particle (MIP, during slow extraction) the orientation of the sensor is important. More electron-hole pairs are going to be created in the parallel orientation, because the particle traverses more material. Therefore, for detecting single MIPs, a parallel configuration should generate bigger signals.

In this test beam diamond sensors were oriented in these two ways and were placed under beams obtained by fast extraction or slow extraction; their response is studied and analyzed in this chapter.

10.4 Fast extraction

The objectives for the fast extraction are to test the response of the diamond sensors over a wide range of fluence and to see if there is any field dependence of the diamond response.

Figure 10.11 shows the diamond response to a double bunch spill of positive particles with momentum of 5 GeV/c. In this plot all the diamond sensors were at an electric field of 1.5 V/µm. At this field the collection distance for CDS116 is 150 µm, for CDS126 125 µm and for the set of CDS154 and CDS155 the joined collection distance is considered to be the sum of both, i.e. 430 µm. These last diamond sensors were parallel to the beam while the rest were perpendicular to it. The plot shows a larger peak from this set of diamonds due to the fact that the collection distance is around 3 times larger. As has been seen already in the test beam exposed on chapter 9, the bunch structure is clearly distinguishable: the bunch width of around 42 ns and the separation of around 262 ns can be clearly observed in Figure 10.11. To calculate the fluence equation (9.1) is used. This expression is only valid for fast extraction, as the width of the bunches dominated the time taken by the generated charges to traverse the diamond volume.

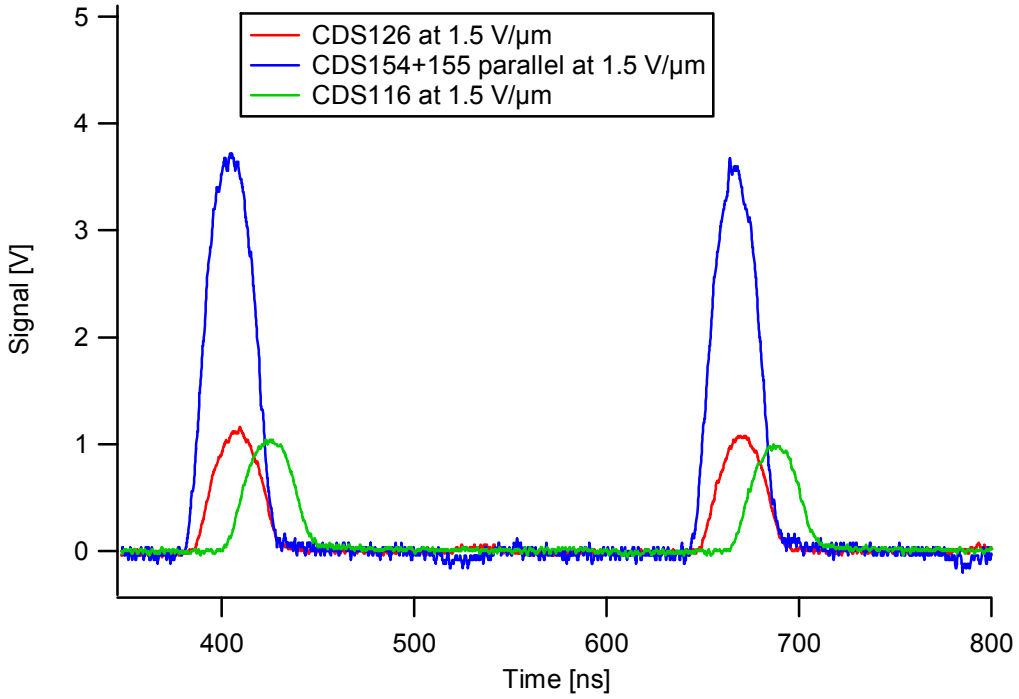

Fig. 10.11: Diamond response to a double bunch spill. The diamonds were at an electrical field of 1.5 V/µm.

The diamond sensors were biased at different fields (at 1.5 V/µm, 1 V/µm, 0.5 V/µm, 0.25 V/µm in both polarities) with the same type of beam. The response curves were integrated and the fluence seen by the sensors at different electric fields is shown in Figure 10.12. It can be seen a difference of fluence values of around 50% between the measures done at different electric field. This could be due to the variation in the beam bunch or be a dependence upon the electric field. Unfortunately, a sensor was not left always at the same

bias voltage value. That would have allowed to compare the readings from a diamond with a constant electric field on it with the readings of the rest of the sensors that were changing its bias. However, the readings at low electric fields are very different depending on the polarization of the bias (for the sensors in a positive field in Figure 10.12 the readings are higher than in the negative field) and this does not allow to conclude that there is a direct effect of the field applied to the diamond sensors. The difference of fluence readout between the sensors is around a 17%.

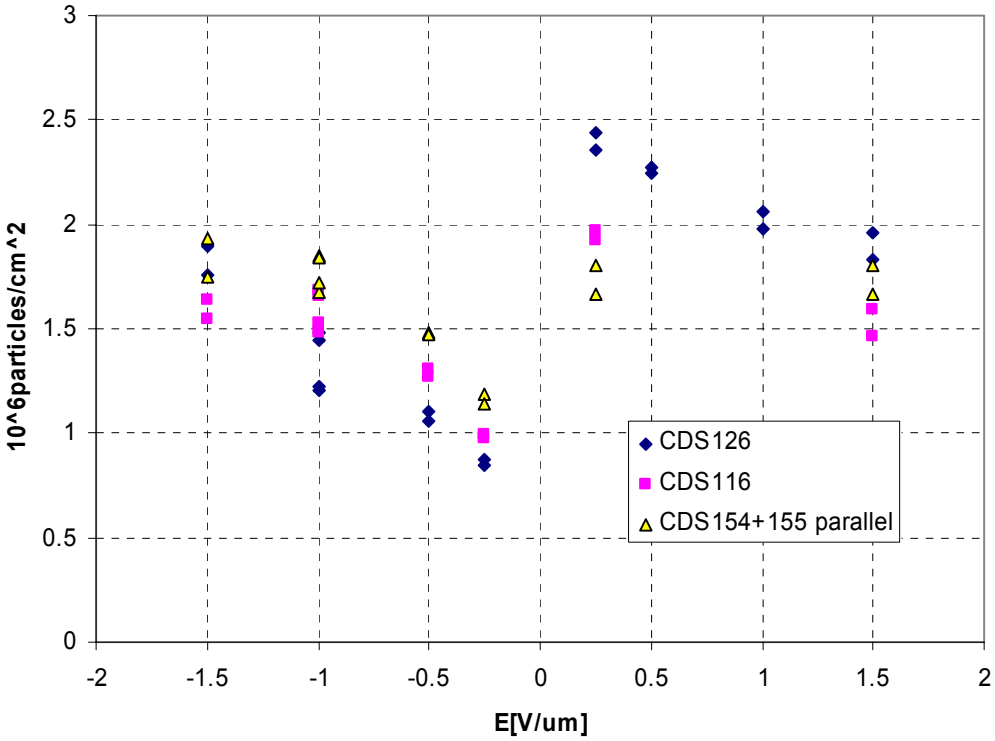

Fig. 10.12: Fluence measured with the diamonds at different electric fields.

Figure 10.13 shows the difference on the signal pulses from diamond CDS126 at different electric field. The width of the bunches and the separation between each of them can be clearly seen.

The orientation of the diamond sensors was changed for the shot shown in Figure 10.14. This time the sensor parallel to the beam was CDS126, and CDS116 and the set of CDS154 and CDS155 were perpendicular to it. Again, several shots, this time of 1 bunch per spill were taken by the sensors at different electric field each time. The plot in Figure 10.15 shows the fluence measured by the diamond sensors during these shots.

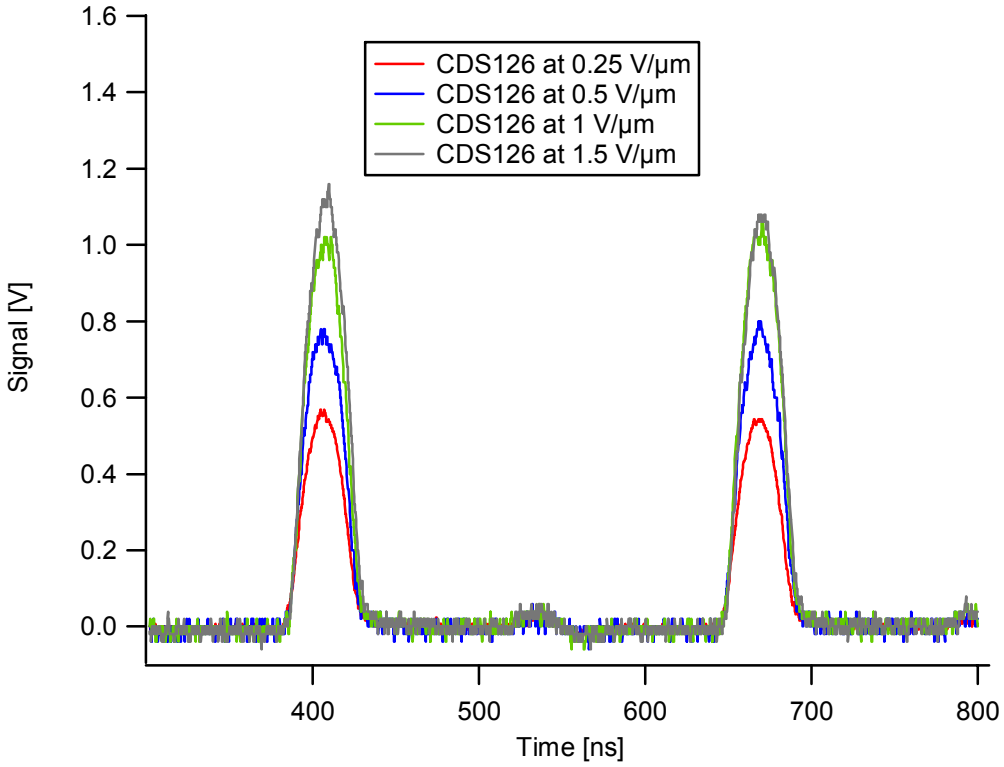

Fig. 10.13: CDS126 diamond response to a double bunch spill at different electric fields.

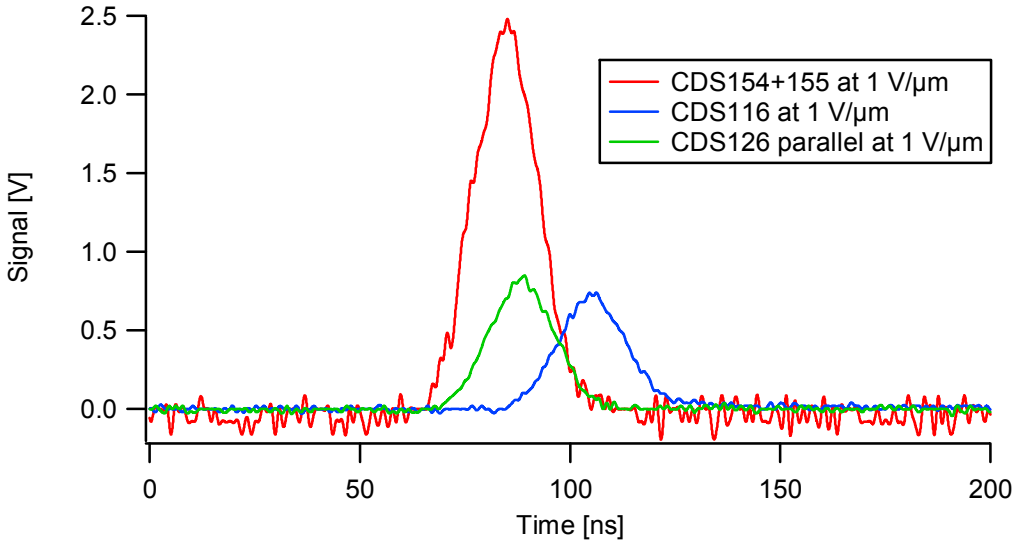

Fig. 10.14: Diamond response to a double bunch spill. The diamonds were at an electrical field of 1 V/µm.

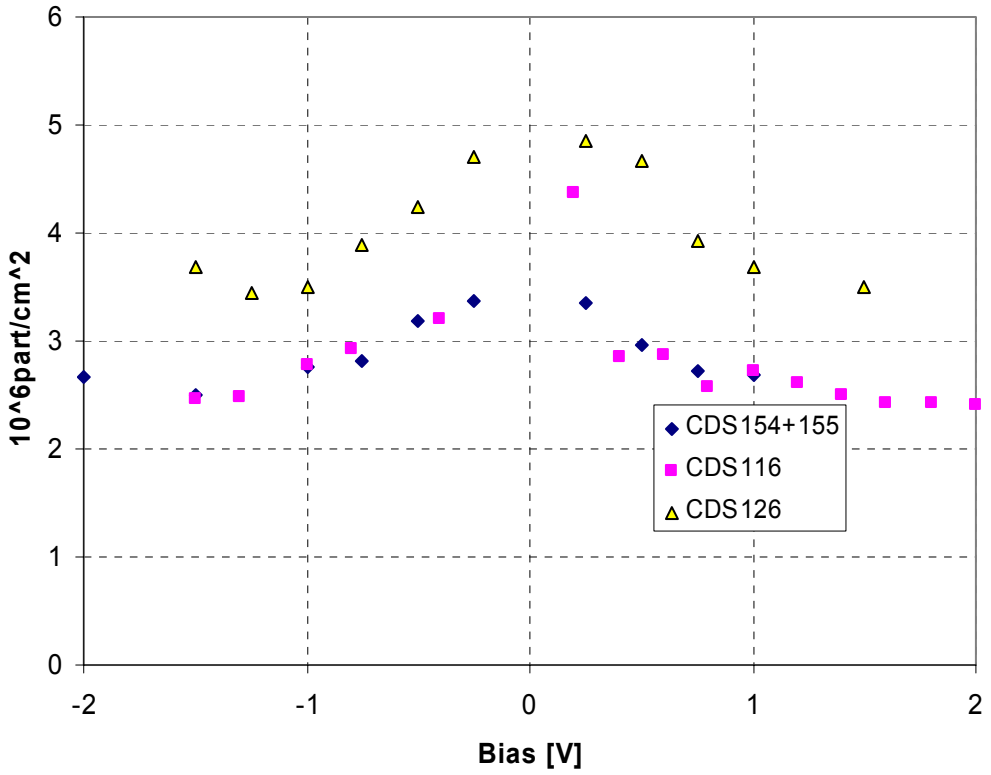

Fig. 10.15: Fluence measured with the diamonds at different electric fields. Diamond CDS126 was parallel to the beam while the rest were facing the beam perpendicularly.

Sensors CDS116 and the set of CDS154 and CDS155 showed a very good agreement on the fluence measured, both where perpendicular to the beam. Sensor CDS126 shows a higher fluence. This could be due to its parallel position respect to the beam. The number of electrons generated in the diamond was transformed into a fluence using the collection distance of each diamond and CDS126 clearly has generated more electrons than the rest of the sensors that were perpendicular to the beam. A possible explanation of this phenomenon could be that the particle beam is not homogeneous and that more particles per unit of surface hit the sensor which is parallel to the beam than the other sensors.

As Figure 10.15 shows the fluence measured is slightly higher when the sensors were biased at lower fields, this time in both polarities, contrary of what it is shown in Figure 10.12. Again, no clear conclusion can be drawn, but comparing the data of Figure 10.12 with the plots of Figure 10.15 it seems that the difference of measured fluence is due to fluence variations in the beam itself, and that the measurement would be independent of the electric field in the diamond, provided that the calibration of collection distance is properly done.

The fluence measurement was done again with a beam which intensity was halved. Figure 10.16 shows the results. CDS126 was still in parallel position and again shows higher signals than rest of the diamonds. CDS116 and the set of CDS154 and CDS155 agree again in the fluence measured, except in the points at lower electric fields. Note that the set CDS154 and CDS155 measured a very constant fluence, there is an 8% variation between the most extreme measures. Figure 10.16 shows a similar behaviour as Figure 10.12, but different to Figure 10.15.

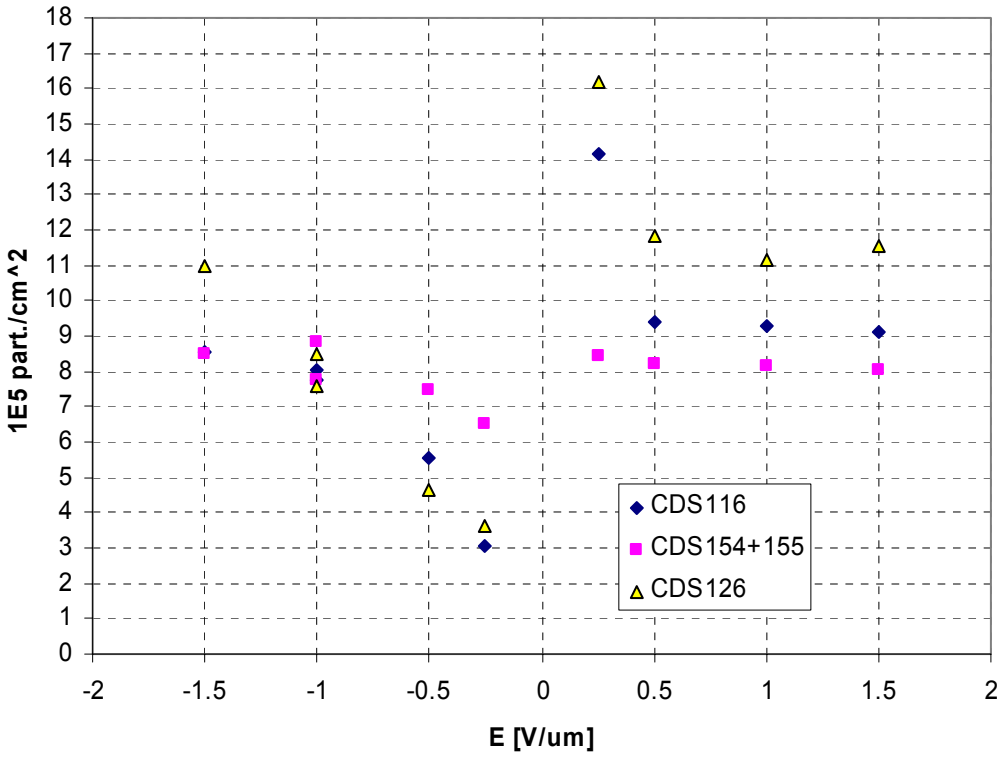

Fig. 10.16: Fluence measured with the diamonds at different electric fields. Diamond CDS126 was parallel to the beam while the rest were facing the beam perpendicularly. The beam fluence is halved respecto to the previous plots.

10.4.1 Conclusions

The diamond sensors were able to monitor fluence that ranged from 10^5 particles/cm^2 to 10^6 particles/cm^2, and the previous test beam (Chapter 9) showed that this range can be extended to 10^8 particles/cm^2.

There is not any reason to think that the measurement of fluence depends on the electric field, although no proof is given to demonstrate the contrary.

CDS126, when set in parallel orientation respect to the beam, gave more signal than expected. A possible explanation could be that the beam is not homogeneous and that CDS126 was in a region where the beam was more intense.

Diamonds in general showed a good agreement in the measured fluence. The difference of fluence measured by the diamond was always below a 20%. The diamond sensors were able to monitor fluences that ranged from 10^4 particles/cm^2 to 10^8 particles/cm^2 and showed a linear response within this range.

10.5 Slow extraction

The slow extraction beam was used to align the assembly onto the spot of the beam bunch. The objectives were to detect single MIPs with the diamond sensors.

The electric noise that the coaxial cable of 16 m added to the signal was of the order of 20 μV, the same order of magnitude as the signal that would generate a MIP in the diamond. Therefore current amplifiers close to the sensors, at 20 cm from them, were used for the readout.

The current signal that a MIP would generate in one sensor can be estimated using the following expression:

$$I(t) = F(t) \otimes \frac{v(E)}{d} Q_G \cdot e^{\frac{-t}{\tau}} \tag{10.1}$$

The expression (2) assumes that the lifetime τ is short in comparison to d/v, the time for a charge carrier to drift a distance d, with d the thickness of the detector and $v(E)$ the drift velocity for a given electrical field strength E. The amplifier response is parameterized by the response function $F(t)$. The amplifier response function has been approximated by a Butterworth band-pass filter model of third order with a lower cut-off frequency of 500 kHz and a upper cut-off frequency of 500 Mhz. The relative response of the amplifier model to a normalized current signal of form (2) with τ = 741 ps is shown in Figure 10.20. It is clearly visible that the bandwidth of the amplifier model is insufficient to map the exponential decay of the current signal. It should be noted that the shape is only dependent on the lifetime τ, while the amplitude is dependent on the electrical field strength by the factor $v(E)/d$ and the total produced charge Q_G and thus independent of the lifetime τ.

10.5.1 Diamond sensor perpendicular to the beam

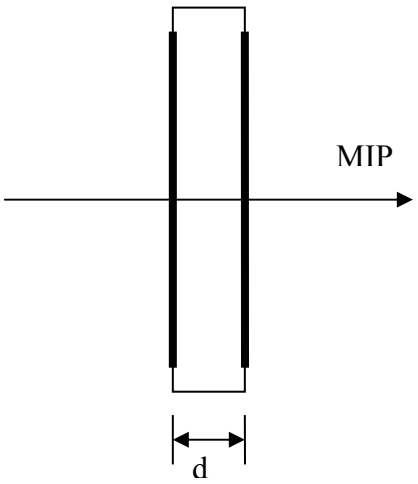

Fig. 10.17: Configuration with the metallizations of the diamond sensor perpendicular to the MIP trajectory.

The set of diamond sensors CDS154 and CDS155 was oriented with the metallizations perpendicular to the beam direction (see Figure 10.17). In the case shown in Figure 10.18, the average signal of the set made of CDS154 and CDS155 is 1113 μV, using an amplifier which provided an amplification of 10. Thus, dividing 1113 μV by 10 the value obtained for the

signal is of 111.3 µV. As there are two sensors (see Figure 10.2) this value has to be divided by two in order to get the contribution of each diamond, which is 55.65 µV. The electric noise after amplification has an average value of 338 µV. Therefore, the signal to noise ratio is ~3.

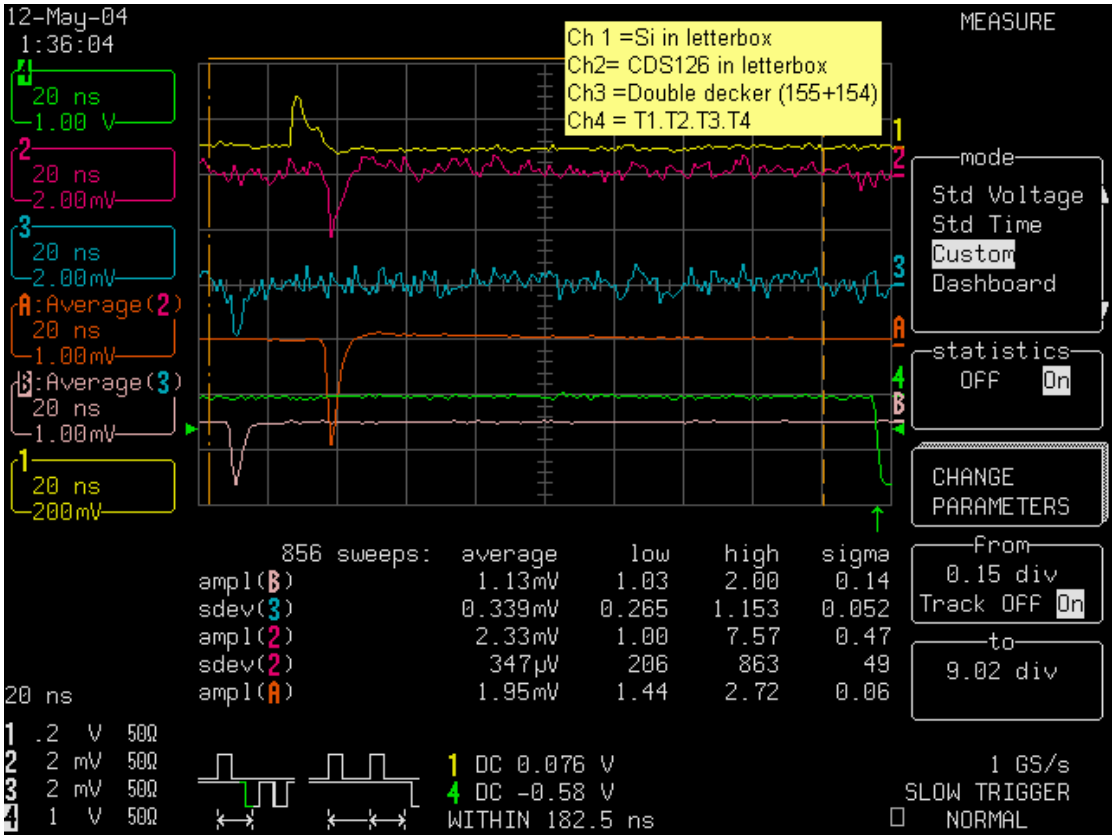

Fig. 10.18: Screen dump of the scope showing the signals from the sensors and its statistics.

10.5.2 Diamond sensor parallel to the beam

Fig. 10.19: Configuration with the metallizations of the diamond sensor parallel to the MIP trajectory. D is the maximum length of the metallization (in the case of a round metallization this distance would be the diameter).

The expected signal for diamond CDS126 was calculated with formula (2) with the assumption of the charge generating particle to be minimum ionizing and the lifetime to be an effective mobility weighted lifetime of electrons and holes. The diamond signal was recorded

at a field strength of 1 V/µm, the velocity *v(E)* was approximated to be 70% of the saturation velocity, which is typically obtained in the range of 10 V/µm. The value calculated for the amplitude is 8 mV, while the observed amplitude is about 15 mV. Within the uncertainties of the saturation speed and mobilities of electrons and holes the agreement is reasonable.

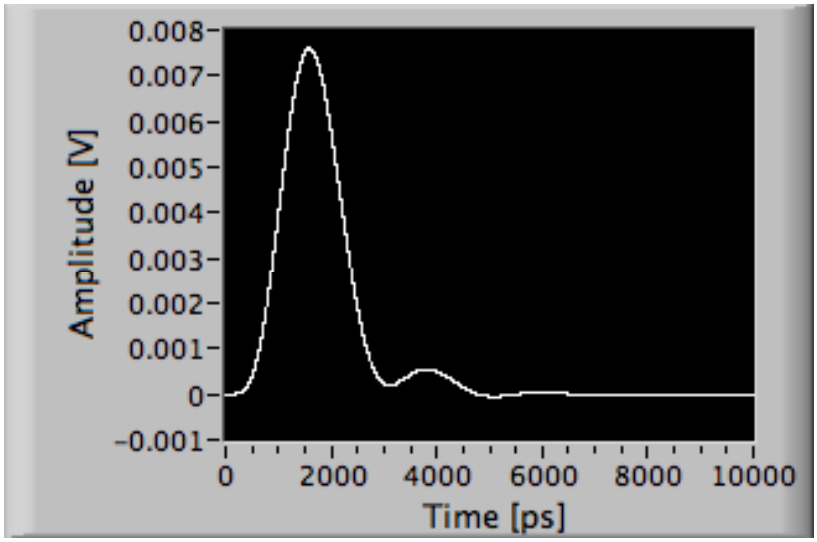

Figure 10.20: Response of the amplifier model described in the text with $\tau = 741$ ps.

The diamond was oriented parallel to the beam trajectory, therefore the particle traversed the whole length of the diamond sensor, see scheme in Figure 10.19.

Figure 10.21 shows a typical signal from a particle traversing the sensor after an amplification gain of 24 dB. Figure 10.22 shows the histrogram of several particle hits on the diamond sensor. The average signal sits around 16 mV (after amplification), that represents a factor 2 more from what the expected value calculated by expression (2).

Figure 10.21: Typical particle hit response on the diamond sensor. A gain of 24 dB is applied on the signal.

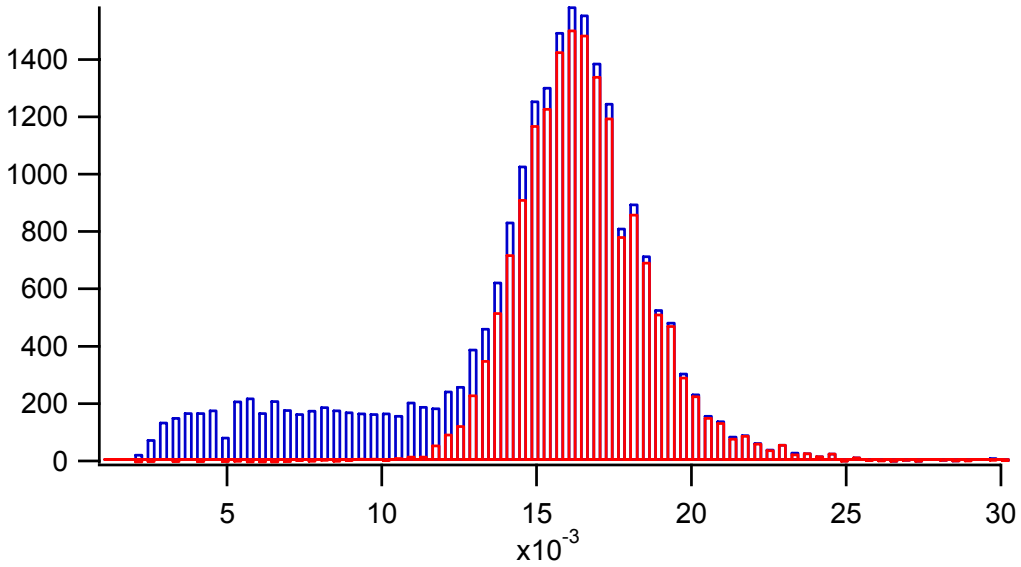

Figure 10.22: Histogram made after several particle hits in the diamond sensor. It can be seen that the average response sits around 16 mV (applying an amplification gain of 24 dB).

10.5.3 Conclusions

It has been shown that the diamond sensor is able to detect single MIP events when connected to an amplifier close to it (around 20 cm away). The signal to noise ratio in the case of the perpendicular orientation is around 3, and it is higher in the case of the parallel orientation, being bigger than 4.

The signal generated by a MIP was a factor 35 larger in the parallel orientation than in the perpendicular one. However, the particles that crossed the diamond in parallel orientation found different metallization lengths due to the round shape of CDS126 metallizations. A metallization in a square shape would be more advisable, therefore the signal generated by particles that traverse the diamond will be collected in more homogeneous length.

Expression (10.1) gives the expected signal after amplification from a MIP traversing the diamond volume. The expected signal is a factor 2 different from the signal obtained during the slow extraction test beams.

Conclusions and Outlook

Main conclusions

The possible accident scenarios and proton beam losses expected at the LHC make the development of a protection system to monitor the losses and radiation levels necessary. For the accelerator, the system developed is called the Beam Loss Monitors (BLM), while for the experimental areas the system developed is the Beam Condition Monitor (BCM). The BLM and BCM are complementary and must function continuously and be synchronized.

The BCM will give the information on the particle fluxes in positions close to the Interaction Points (IPs): this will serve to protect the subdetector systems close to the IPs and the beam pipe and to estimate the radiation dose level. It can be also used as beam diagnostic tool.

As shown in chapter 2, the harsh radiation environment in positions where the BCM sensors must be placed make the choice of CVD diamond the perfect candidate as the sensor for the BCM. The irradiation which has been performed shows that for proton fluences equivalent to the one experienced after 10 years of normal operation of the LHC close to the design positions for BCM sensors in CMS, the diamond sensor signals suffer from a signal degradation of 42%. Therefore, it has been proven that diamond can be used for this application as it still generates a signal after being irradiated with a fluence of more than $2 \cdot 10^{15}$ protons/cm^2.

The fast extraction test beams that have been performed demonstrate that CVD diamond is able to withstand intense beams. Diamond samples have been exposed to particle fluxes similar to an unsynchronized beam abort within the CMS experiment. Under such conditions, the diamond samples are found to respond and recover from consecutive high intensity beam bunches impacts. The diamond sensors were able to monitor fluences that ranged from 10^4 particles/cm^2 to 10^8 particles/cm^2 and showed a linear response within this range.

It has also been shown that the diamond sensor is able to detect single MIP events if they are connected to an amplifier close to it (around 20 cm away). The samples were tested in two different positions: with the metallizations being either perpendicular or parallel to the beam. The signal to noise ratio for the perpendicular orientation was around 3, and it is higher in the case of the parallel orientation, being more than 4. The signal generated by a MIP was a factor 25 larger in the parallel orientation than in the perpendicular one. A formula to calculate the maximum signal that a MIP would generate in a diamond sample in the parallel orientation was developed in chapter 10.

The observed high current generated in the diamond in conditions similar to an unsynchronized beam abort requires the implementation of a protection system for the BCM readout electronics.

The CVD diamond sensors were characterized with different measurement methods and test beams. The understanding of the response and performance of the diamond sensor has been advanced but there are still outstanding questions concerning its polarization behaviour.

Future outlook

Once the sensor has been characterized and understood one of the next steps in the development and construction of a BCM will be to choose and test the right amplifier for the readout system. That will be the most immediate step.

Further work concerning the readout system will be the configuration of an automatic (and fast) analysis system of the readout signals. As has been noted, this system will be constructed with FPGAs.

To calibrate correctly the threshold levels of the BCM a simulation of the number of protons lost due to a D1 (warm dipole) power failure and subsequently colliding with the experiment or with the TAS, as it is the narrowest aperture close to the experiment, should be made. This simulation will provide the contribution to the dose, in the positions where the BCM sensors sit, from the particle shower generated by the lost protons at every turn during the development of the accident.

Finally, a study for the final position of the BCM sensors, amplifiers and cabling inside the experimental volume is needed prior to the final installation in the experiment.

Appendix

Radiation monitoring with RadFET

The BCM in CMS forms a part of the so called Radiation Monitoring system. In this system, besides the BCM which provides a measurement of the beam condition and a beam abort signal, there will be a set of sensors to measure the radiation field in CMS. These sensors will not be located close to the IP as BCM sensors are but at larger radii.

This set of active sensors will be used to verify the radiation field simulations, correlate the BCM readings with the radiation field in the different sub-detectors [76], act as a long term radiation monitor in some critical locations and measure the radiation background in the experimental area together with the ionization chambers [77].

The different dosimetric technologies currently under test are: RadFET, OSL materials [78], *p-i-n* silicon diodes [79] and silicon Pad detectors [78]. In this chapter, the analysis of the response of different types of RadFET dosimeters which were irradiated under either a proton beam or a pion beam is presented.

A.1 Radiation-sensitive Field Effect Transistor (RadFET)

A FET (Field Effect Transistor) is a semiconductor device in which the internal current is controlled by an electric field. This current traverses a channel between two terminals, the *source* (S) and the *drain* (D), while the electric field is generated by a tension applied at the *gate* (G) terminal. In a MOSFET the gate is commonly isolated from the channel by silicon oxide (SiO_2) [80]. Figure A.1 shows a scheme of the MOSFET structure. The material is called n-MOS or p-MOS depending upon the material the channel is made of.

A RadFET dosimeter is a p-channel MOS transistor [81] used to measure ionizing dose via the build-up of charges in the oxide (SiO_2) layer of the device. The shift of the threshold voltage V_{Th} between the S and D of the transistor is proportional to the deposited dose when a constant current circulates through the device [82]. Figure A.2 shows the configuration of the circuit to measure the V_{Th} of the RadFET. The value of the current I_{DS} is given by the manufacturer of the device and its typical value ranges from 10 and 200 μA [83].

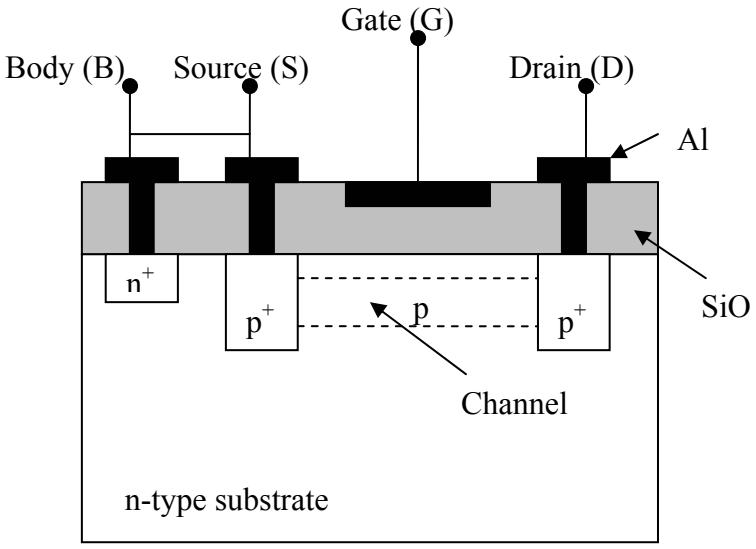

Fig. A.1: Scheme of a p-MOS.

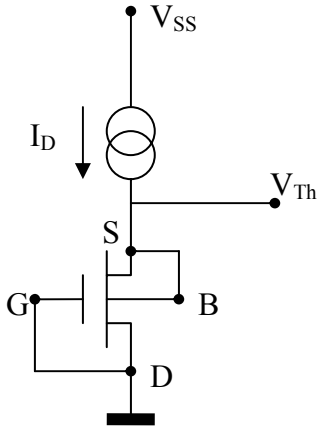

Fig. A.2: Circuit configuration to measure the RadFET.

The ionizing radiation traversing the RadFET will generate electron-hole pairs, which are separated by diffusion and by the electric field inside the oxide. While many electrons exit via the contacts, a proportion of holes will be trapped in the oxide layer. The field due to the trapped holes in the oxide induces a negative image charge in the silicon, resulting in a negative shift, ΔV_{Th}, in V_{Th}.

To calibrate a RadFET, the growth of ΔV_{Th} (i.e. the growth of the positive charge in the oxide) is plotted against the dose. The shape of the curve depends on the value of the voltage applied to the gate during exposure to radiation. The common modes of irradiation are "zero bias" or "passive mode" and "positive bias" or "active mode". In the "zero bias" condition the plot ΔV_{Th} vs dose is complex and not linear.

A.1.1 Annealing

RadFETs are integrating devices where the dosimetric information is kept even after every readout. Integrating dosimeters absorb radiation energy and trap a portion of it (converting it to a mixture of electrical charge and chemical energy). With time, a relaxation process takes place which affects the dosimetric information, i.e. decreases ΔV_{Th}. This process is called *annealing*.

The annealing depends on the absorbed dose, the temperature and the oxide characteristics [84]. When the absorbed dose increases more charges get trapped inside the oxide layer and the probability of recombination rises. This recombination is called *direct annealing*.

Moreover, with the increasing dose the number of free traps inside the oxide layer decreases, thus provoking a loss of sensitivity, i.e. ΔV_{Th} being smaller with the increment of dose. Moreover, the direct annealing generates a loss of signal that decreases ΔV_{Th} as well. Subsequently the dosimeter will arrive to an equilibrium between the rate of trapping and de-trapping where the RadFET will loose completely its sensitivity.

The annealing has to be corrected and taken into account to avoid the misunderstanding of the signal coming out of the device.

A.2 RadFET used on this study

RadFET from three different manufacturers were used during the pion and proton irradiations: National Microelectronics Research Center (NMRC), Radiation Experiments and Measurements (REM) and Thomson & Nielsen Electronics Ltd. (T&N).

A.2.1 National Microelectronics Research Center (NMRC)

This manufacturer provided one type of RadFET (ESAPMOS04 model). Four RadFETs were mounted in an integrated circuit of around 1 mm^2. All the devices have an oxide layer of 0.40 μm thickness. The substrate has a resistivity ranging from 2 to 5 Ωcm^2. Figure A.3 shows a board containing 12 integrated circuits of NMRC and REM RadFETs (four in each circuit).

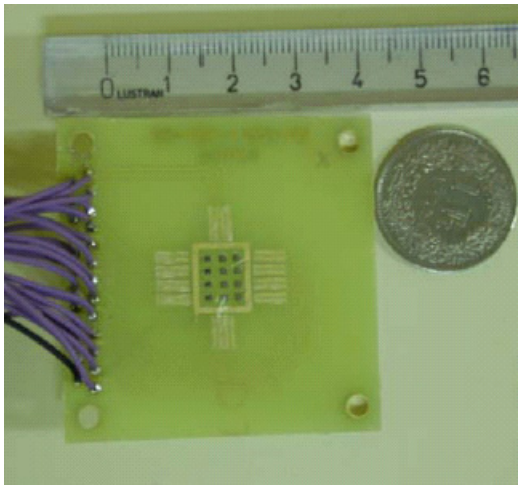

Fig. A.3: Board used for testing the RadFETs from REM and NMRC.

A.2.2 Radiation Experiments Measurement (REM)

The RadFETs provided by this manufacturer were mounted in an integrated circuit as for the NMRC RadFET. The oxide thickness layer of the RadFETs used in this study was of 0.13 μm. Its resistivity ranges between the same values as NMRC dosimeters.

A.2.3 Thomson & Nielsen (T&N)

This manufacturer put the integrated circuit with two RadFETs inside a package with eight pins. Three different types of dosimeters from T&N were tested: TN100P, TN250P and TN502P. Figure A.4 shows a picture with the three types of dosimeters on a board ready to be irradiated.

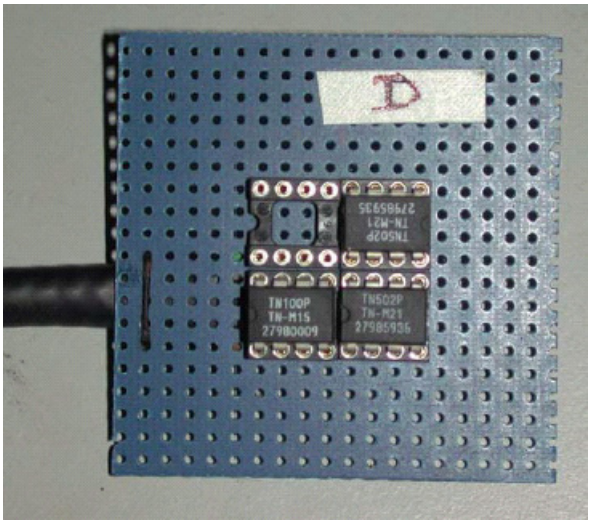

Fig. A.4: Board containing three TN type dosimeters.

The difference between the three different types of RadFET is its oxide layer thickness. For TN100P this thickness is 0.10 μm, while for TN250P and TN502P it is 0.25 μm and 0.50 μm respectively.

A.3 Pion irradiation

The different types of RadFET dosimeters mentioned above were irradiated with pions at the Paul Scherrer Institute (PSI) in the πE1 experimental area. The 590 MeV/c proton beam from the PSI cyclotron is used to generate pions with momenta ranging from 10 to 500 MeV/c. For the irradiation described here monoenergetic pions with momentum of 300 MeV/c were used. The pion flux was measured by a second emission chamber (SEC) counter inside the area [85]. This SEC gives an output which is proportional to the number of particles that traverse the counter.

The RadFET were posted perpendicularly to the beam line in an assembly shown in Figure A.5. This assembly was placed on a support (Figure A.6) located at the beam exit line.

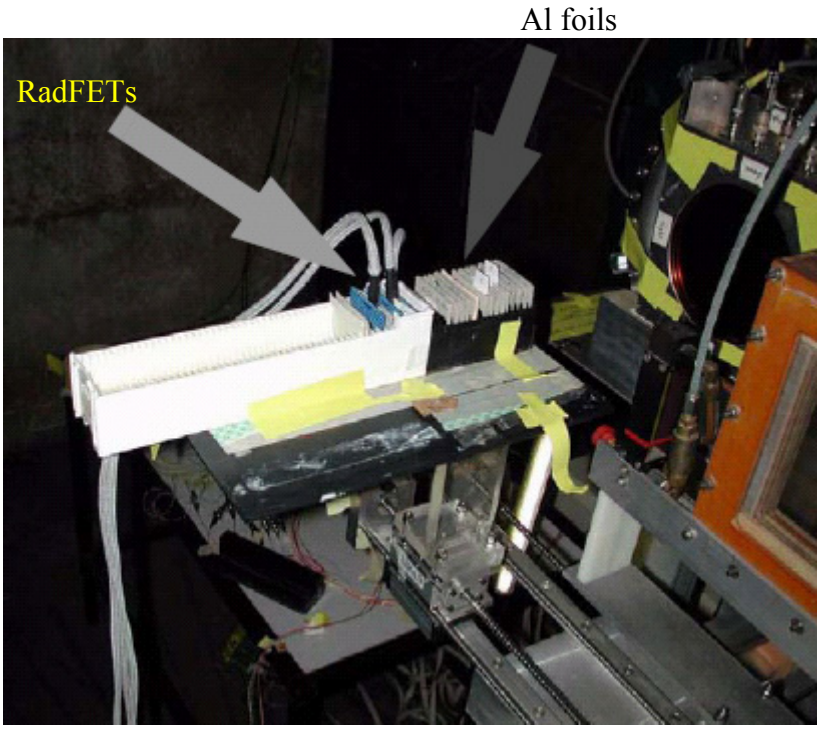

Fig. A.5: Assembly with RadFETs and, in front, aluminium foils used in the beam dosimetry.

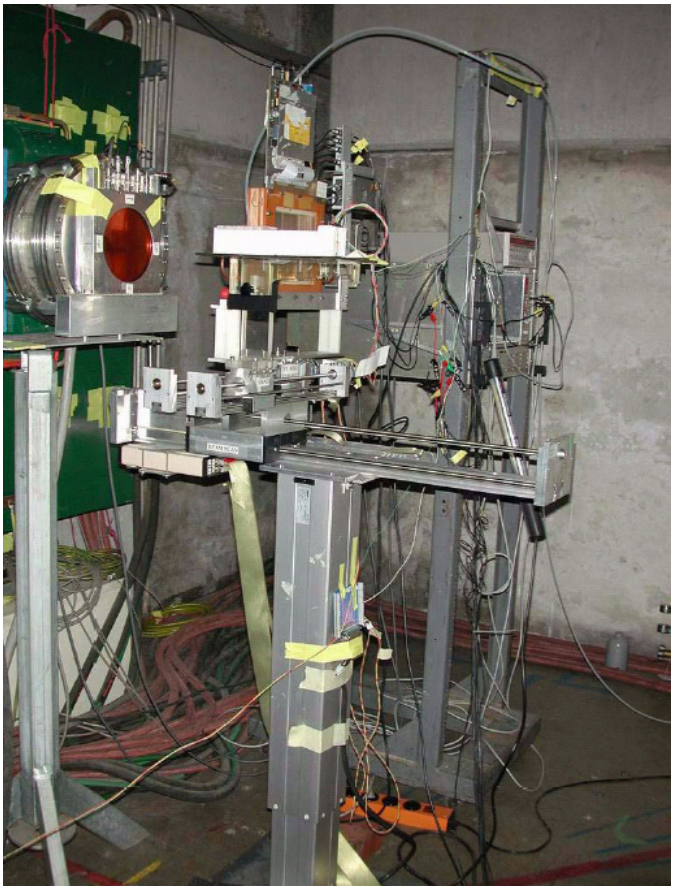

Fig. A.6: Support used to place the assembly in the beam line output.

The results shown for each type of dosimeter are its response, ΔV_{Th} vs the dose until the RadFET saturates and its calibration curve obtained by a fit to the response of the dosimeter. From the curves one can extract the response of the dosimeter to the dose deposited by the pions and the evolution of the sensitivity with the increment of dose. A RadFET saturates when its sensitivity it is close to zero, being the sensitivity the slope of the response curve or the derivative of the calibration curve.

A.3.1 NMRC

Two NMRC RadFETs were used and showed different behaviour. While one of the dosimeters saturated after a dose above 11800 Gy the other saturated earlier, at a dose of only 7150 Gy. Nevertheless, the calibration curves, which follow a power law, are similar. In Figure A.7, the readout from the RadFET (round dots), the calibration curve (blue line) and the fit expression within a certain dynamical range are shown.

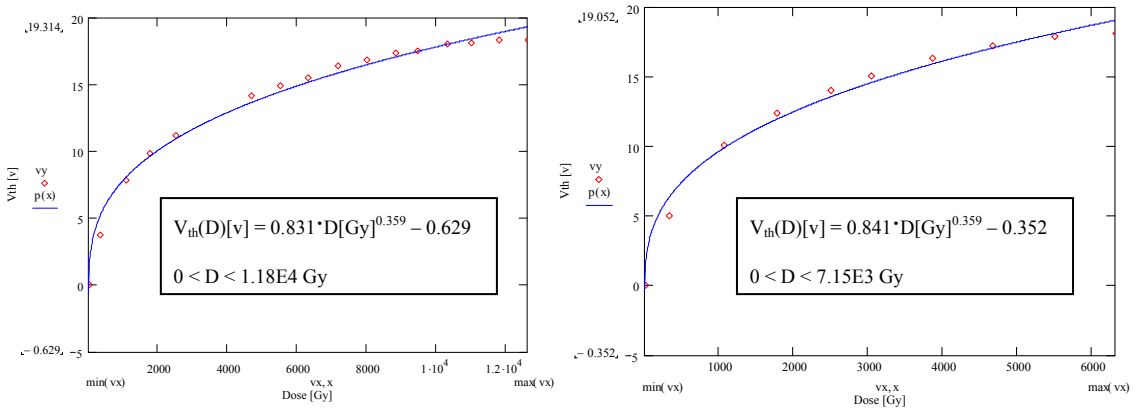

Fig. A.7: Response (round dots), calibration curve (blue line) and fit expression for two NMRC RadFET irradiated with pions.

The evolution of the sensitivity with the dose is shown in Figure A.8. Three different sensitivity regions can be distinguished. In the high sensitivity region, during the first moments of the irradiation, the sensitivity is around 6-7 mV/Gy. Then there is a zone where this sensitivity decreases down to 2-3 mV/Gy, to finally arrive to the last region, where the RadFET starts to be saturated, and the rate of trap filling is countered by the annealing rate. In this final region the sensitivity is around 1-1.5 mV/ Gy.

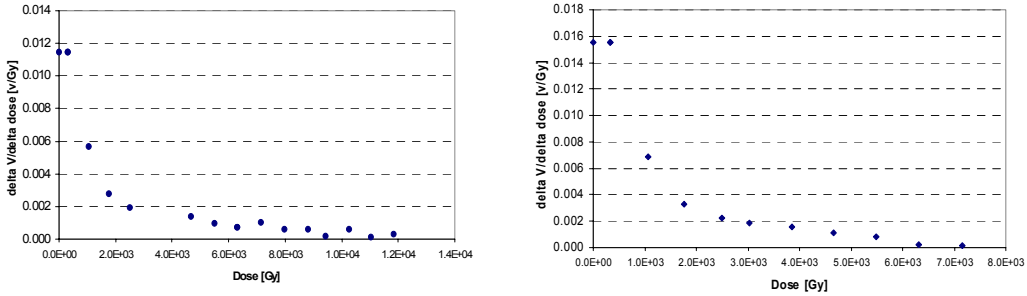

Fig. A.8: Sensitivity curves vs dose for two NMRC RadFET irradiated with pions.

A.3.2 REM

Three REM devices were irradiated. Figure A.9 shows the response of one of them together with the fit. For the REM RadFETs the fit of the response to a pion irradiation does not follow a power law. Figure A.9 shows the response curve.

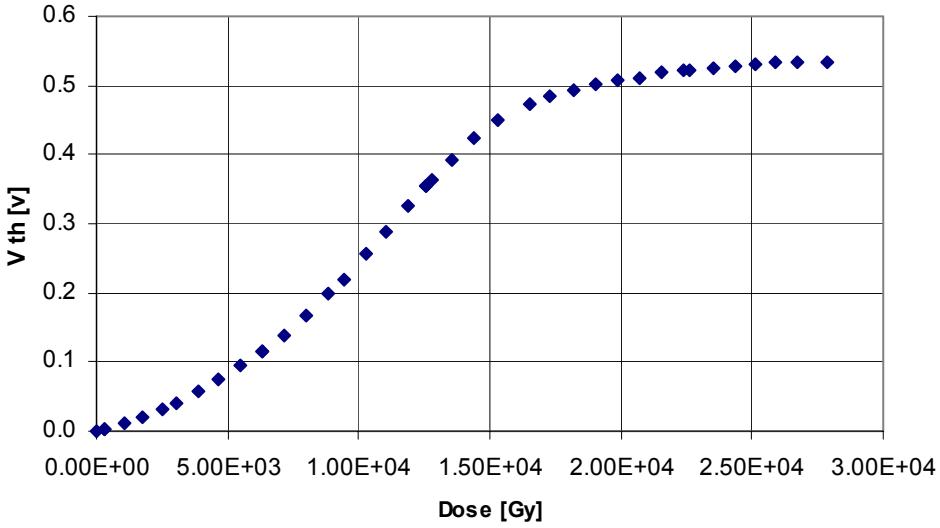

Fig. A.9: Response (diamonds), calibration curve (red line) and fit expression for a REM dosimeter.

A clear saturation of the devices cannot be observed. The plot range arrives up to 27800 Gy, which was the total dose obtained during the irradiation. The average sensitivity of this device is about $2 \cdot 10^{-5}$ V/Gy.

A.3.3 TN100P

There were two RadFET of the type TN100P. Again their dynamical range was different. One of the dosimeters did not reach saturation and gave a good response during the whole irradiation (Figure A.10 left). The other device broke after a dose of around 5500 Gy (Figure A.10 right).

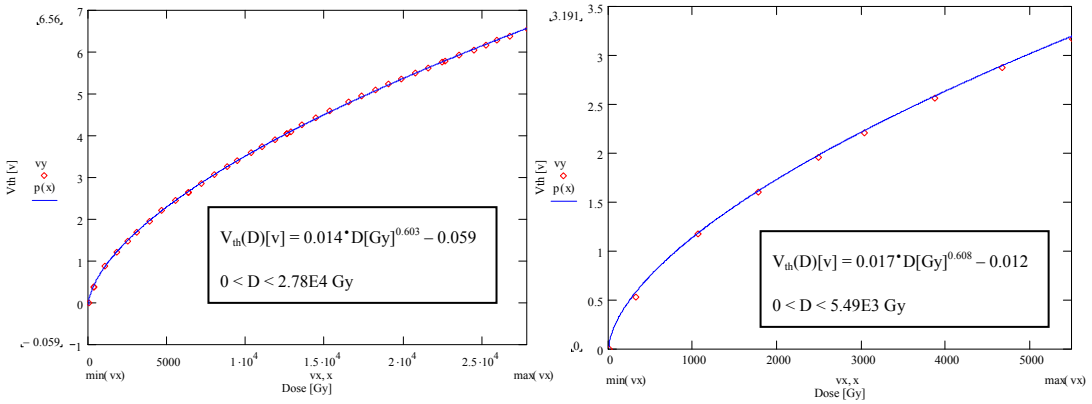

Fig. A.10: Response (round dots), calibration curve (blue line) and fit expression for two TN100P RadFET irradiated with pions.

The evolution of the sensitivity with the dose is shown in Figure A.11. Again, three different sensitivity regions can be differentiated. In the high sensitivity region the sensitivity is around 0.8-1.2 mV/Gy, then the sensitivity decreases down to 0.4-0.5 mV/Gy, to finally arrive to the last region (only the left plot in Figure A.11), where sensitivity stabilized around a value of 0.2 mV/ Gy.

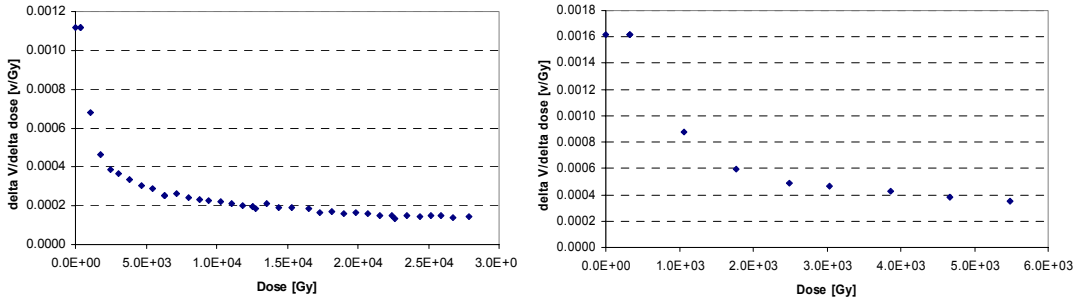

Fig. A.11: Sensitivity curves vs dose for two TN100P RadFET irradiated with pions.

A.3.4 TN250P

The results from two RadFETs of the type TN250P are shown in Figure A.12. For these two dosimeters the dynamical range is the same. The RadFET did not reach saturation after a dose of 27800 Gy. The fit curve is similar for both and it follows strictly the dosimeter response.

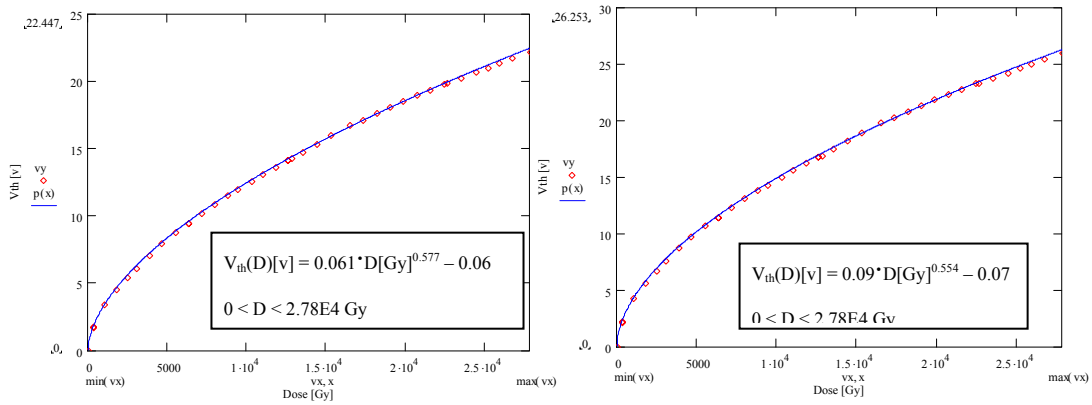

Fig. A.12: Response (round dots), calibration curve (blue line) and fit expression for two TN250P RadFET irradiated with pions.

The evolution of the sensitivity with the dose is shown in Figure A.13. And again, three different sensitivity regions can be differentiated. In the high sensitivity region the sensitivity is around 3.5 mV/Gy, then the sensitivity decreases down to 1.5 mV/Gy, to finally arrive to the last region, where the sensitivity stabilized around a value of 0.8 mV/ Gy.

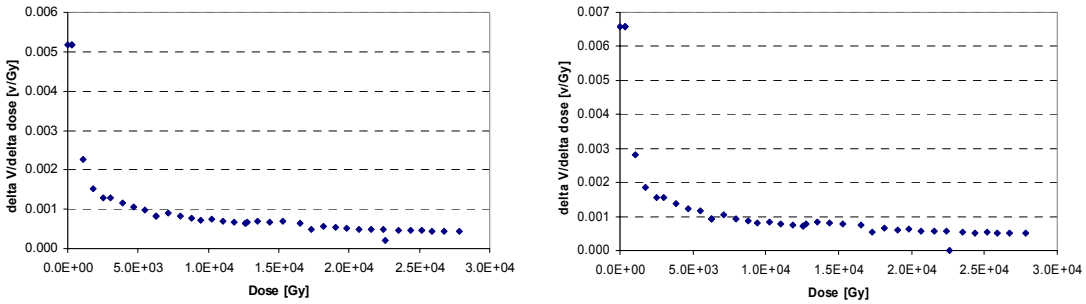

Fig. A.13: Sensitivity curves vs dose for two TN250P RadFET irradiated with pions.

A.3.5 TN502P

The two RadFETs type TN502P of T&N showed a higher sensitivity than the other T&N types but they exhibit a lower dynamical range (they have less oxide thickness). One of the dosimeters saturated at around 5500 Gy. The other did at around 3000 Gy. Figure A.14 shows the response together with the fit for both RadFETs. Figure A.15 shows the response of one of the TN502P RadFET during the whole irradiation where the moment when the RadFET stops working properly is clearly seen

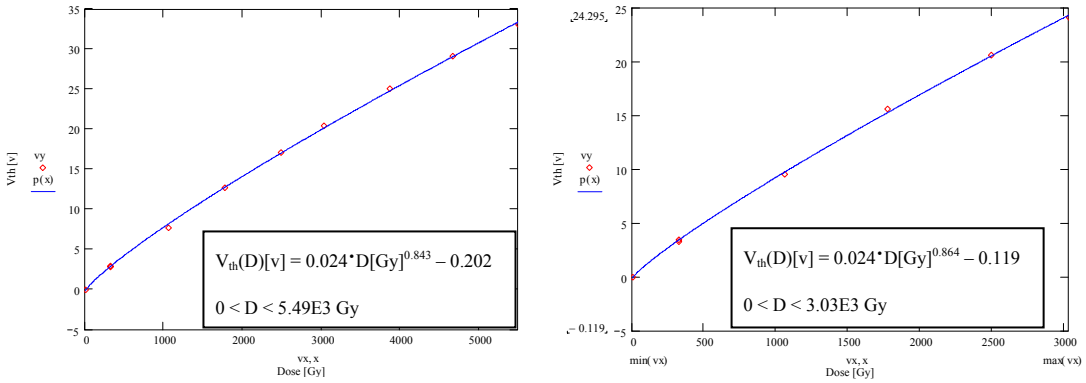

Fig. A.14: Response (round dots), fit curve (blue line) and fit expression for two TN502P RadFET irradiated with pions.

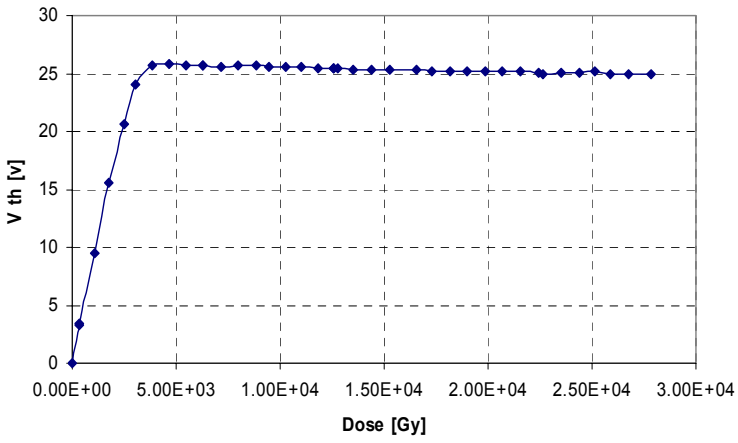

Fig. A.15: Response of one of the TN502P RadFET irradiated with pions.

Figure A.16 shows the evolution of the sensitivity with the dose for each dosimeter while they were still sensitive. The average sensitivity during the whole irradiation is around 6 mV/ Gy.

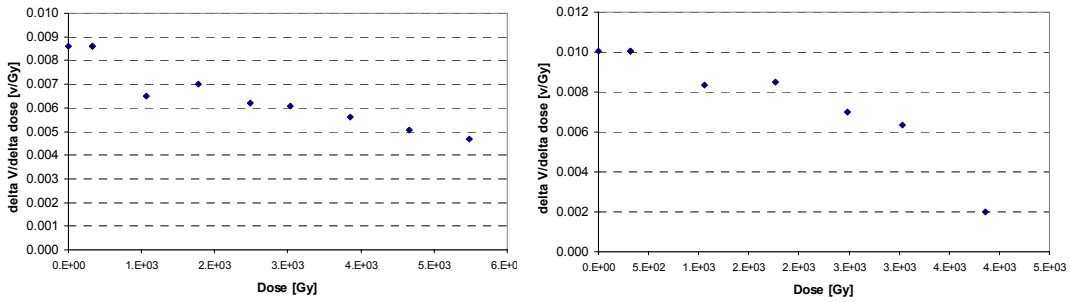

Fig. A.16: Sensitivity curves vs dose for two TN502P RadFET irradiated with pions.

A.4 Proton irradiation

The proton irradiation was performed at the PS irradiation facility, described in Chapter 8. The dosimeters were irradiated with 24 GeV/c protons up to a dose of 34900 Gy. Again, the RadFETs were facing perpendicularly the proton beam and were mounted on the shuttle as shown in Figure 8.4. The dose was monitored by Alanine foils.

The results for each type of dosimeter are ΔV_{Th} vs the dose deposited by the 24 GeV/c protons and the calibration curve.

A.4.1 NMRC

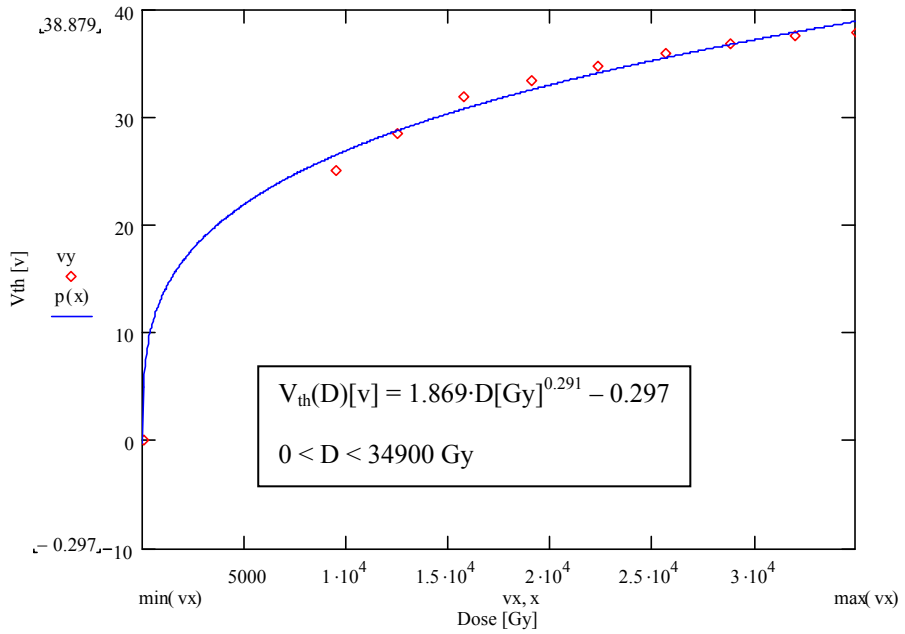

Fig. A.17: Response (round dots), calibration curve (blue line) and fit expression for a NMRC RadFET irradiated with protons.

Contrary to what was observed with the pions, the NMRC RadFETs did not reach saturation during this irradiation and was still working at a dose of 34900 Gy, while with the pion irradiation the dosimeters stopped working coherently at a dose of less than 12000 Gy. Figure A.17 shows the ΔV_{Th} vs the dose readout from the sensor and the fit curve, which is different from the fit curve for pions.

The evolution of the sensitivity with the dose is shown in Figure A.18. The three different sensitivity regions show sensitivities from 2.6 mV/Gy in the high sensitivity region, around 1.5 mV/Gy in the medium region and 0.5 mV/Gy in the low sensitivity zone.

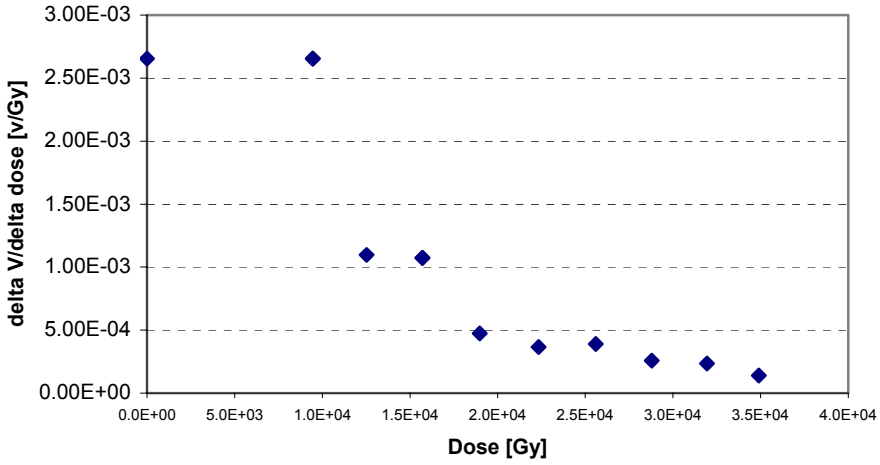

Fig. A.18: Sensitivity curve vs dose for a NMRC RadFET irradiated with protons.

A.4.2 REM

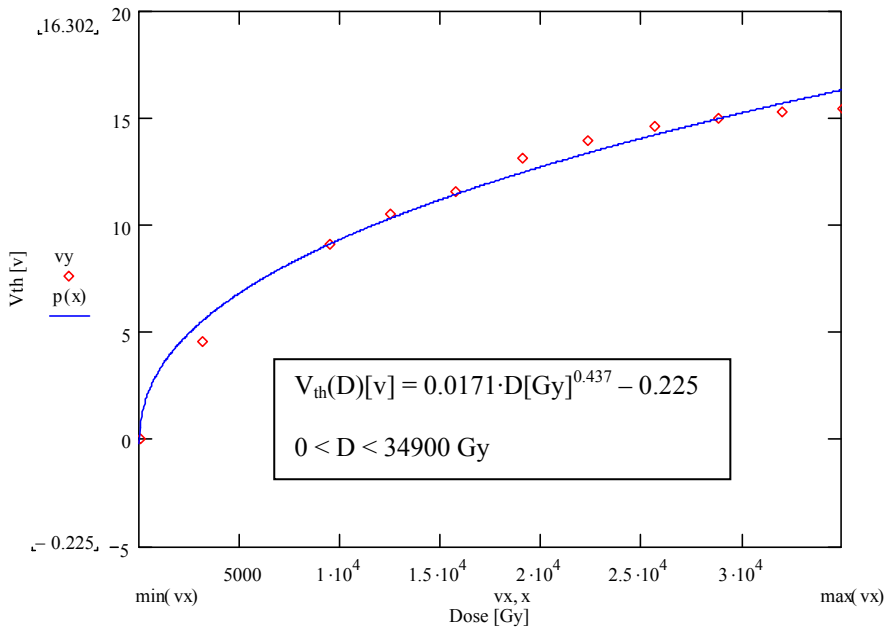

Fig. A.19: Response (round dots), calibration curve (blue line) and fit expression for a REM RadFET irradiated with protons.

The REM RadFET response to protons is very different in amplitude to the one obtained during the pion irradiation. This time the fit to the data readout follows the typical power law for this kind of dosimeters. Figure A.19 shows the response together with the power fit. The RadFET did not reach saturation after the 34900 Gy.

Figure A.20 shows the evolution of the sensitivity during the irradiation. The sensitivity decays from 1 mV/Gy to 0.2 mV/Gy, passing through a region whose sensitivity was about 0.6 mV/Gy.

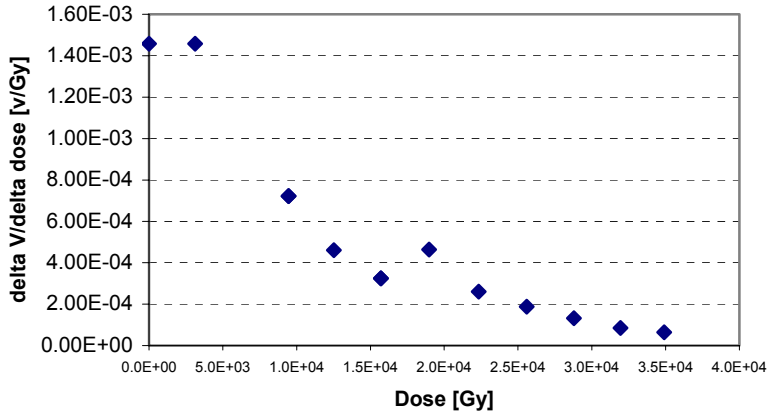

Fig. A.20: Sensitivity curve vs dose for a REM RadFET irradiated with protons.

A.4.3 TN100P

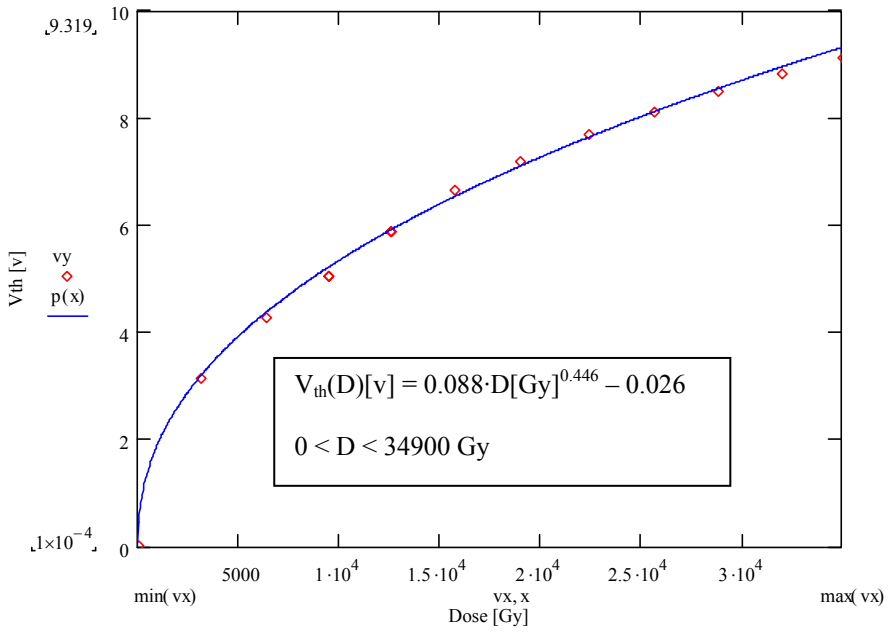

Fig. A.21: Average response (round dots), average calibration curve (blue line) and average fit expression from four TN100P RadFETs irradiated with protons.

Figure A.21 shows the average response of four TN100P RadFETs, the calibration curve and the fit expression for this average response. An average could be performed because of the great homogeneity of the response of these dosimeters. The TN100P did not saturate during the irradiation.

The evolution of the sensitivity, Figure A.22, shows a quick decrease after the first 5000 Gy of proton irradiation that is followed by a progressive, but slow, decrease of sensitivity. The final sensitivity is 0.2 mV/Gy, from a starting point of around 0.8 mV/Gy.

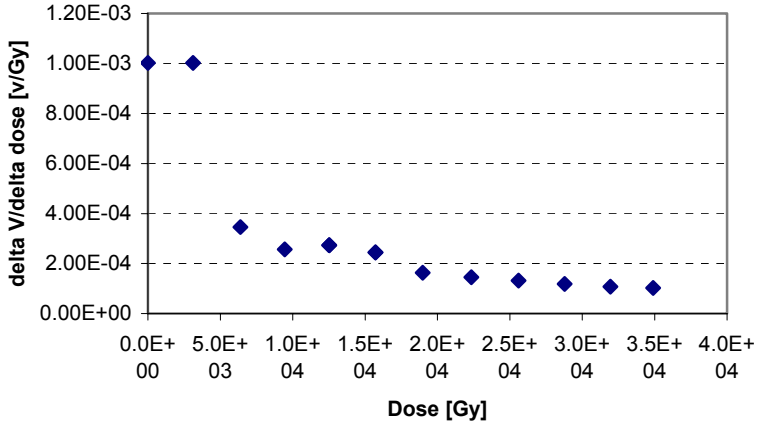

Fig. A.22: Sensitivity curve vs dose for the average response of four TN100P RadFETs irradiated with protons.

A.4.4 TN250P

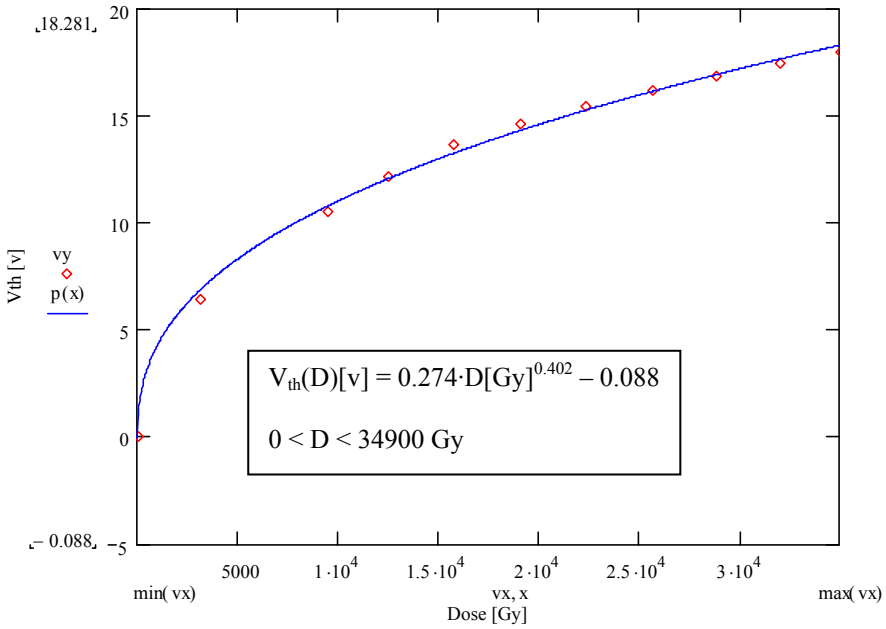

Fig. A.23: Average response (round dots), average calibration curve (blue line) and average fit expression from four TN250P RadFETs irradiated with protons.

The same averaging could be performed for the four TN250P dosimeters (Figure A.23). Again, the RadFETs did not reach saturation and remain sensitive all along the irradiation. As it is shown in Figure A.24, where a more progressive decay of sensitivity can be observed, compared to that observed for the TN100P. The average sensitivity in the first region of the curve is about 0.8 mV/Gy, decreasing to 0.4 mV/Gy and then to 0.3 mV/Gy.

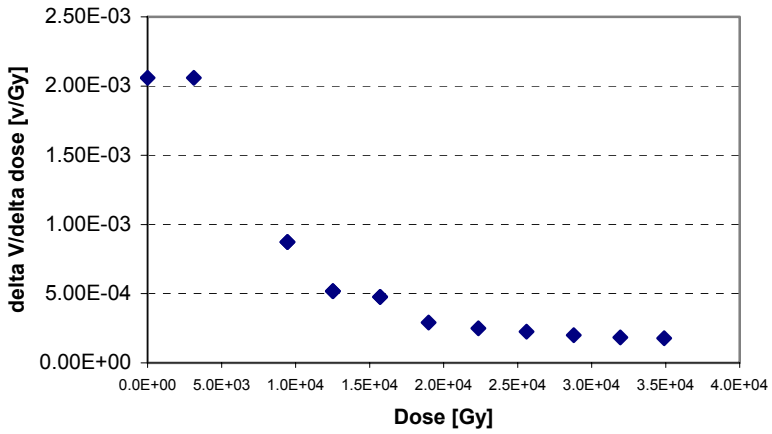

Fig. A.24: Sensitivity curve vs dose for the average response of four TN250P RadFETs irradiated with protons.

A.4.5 TN502P

The TN502P reached saturation after 12523 Gy. Figure A.25 show the response and the fit for this RadFET, which showed a good sensitivity, of about 3.68 mV/Gy, while it was functional. The dose needed to saturate the RadFET with protons is about 3 times higher than the one needed with pions.

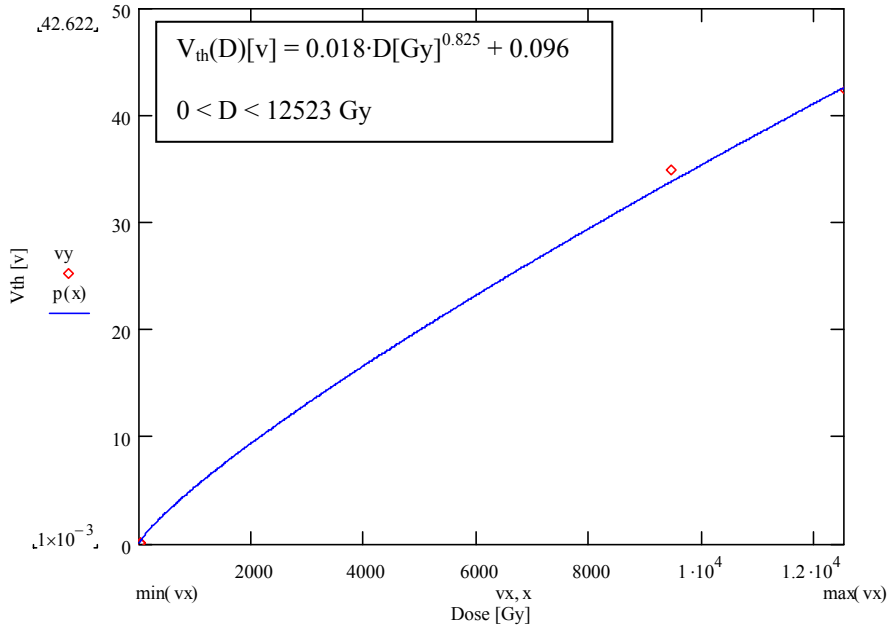

Fig. A.25: Response (round dots), fit curve (blue line) and calibration expression from a TN502P RadFET irradiated with protons.

Figure A.26 shows the whole readout from the TN502P during the irradiation with protons. The dose at which the RadFET starts to become saturated can be clearly observed.

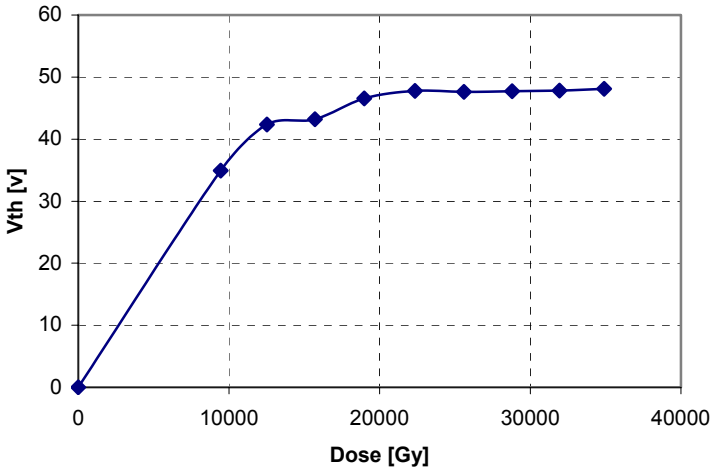

Fig. A.26: Response from a TN502P RadFET irradiated with protons.

A.5 Summary and Conclusions

	Pions	Protons	Sens. pions	Sens. protons
NMRC	Vth(D)[v] = 0.836·D[Gy]0.359 – 0.491 0 < D < 7000 Gy	Vth(D)[v] = 1.869·D[Gy]0.291 – 0.297 0 < D < 35000 Gy	From 7 mV/Gy To 1 mV/Gy	From 2.6 mV/Gy To 0.5 mV/Gy
REM	Not fitted to a power law 0 < D < 12000 Gy	Vth(D)[v] = 0.017·D[Gy]0.437 – 0. 225 0 < D < 35000 Gy	~0.02 mV/Gy	From 1 mV/Gy To 0.2 mV/Gy
TN100	Vth(D)[v] = 0.015·D[Gy]0.605 – 0.035 0 < D < 30000 Gy	Vth(D)[v] = 0.088·D[Gy]0.446 – 0.026 0 < D < 35000 Gy	From 1.2 mV/Gy To 0.2 mV/Gy	From 0.8 mV/Gy To 0.2 mV/Gy
TN250	Vth(D)[v] = 0.075·D[Gy]0.565 – 0.061 0 < D < 30000 Gy	Vth(D)[v] = 0.274·D[Gy]0.402 – 0.088 0 < D < 35000 Gy	From 4 mV/Gy To 0.5 mV/Gy	From 0.8 mV/Gy To 0.3 mV/Gy
TN502	Vth(D)[v] = 0.024·D[Gy]0.854 – 0.161 0 < D < 3000 Gy	Vth(D)[v] = 0.018·D[Gy]0.825 – 0.096 0 < D < 12000 Gy	~8-6 mV/Gy	~3.68 mV/Gy

Table A.1: Summary of the calibration expressions for pion and proton irradiation for each kind of RadFET and the sensitivities displayed.

Table A.1 shows a summary of the results obtained for the different types of RadFETs during the pion and the proton irradiations. The fit expression differs depending on the type of particles that were irradiated as the RadFET response depends on that factor. In this chapter a calibration for protons of 24 GeV/c and a different calibration for pions of 300 MeV/c are given.

For the implementation of this dosimetry technology in CMS, simulations of the type of radiation field (type and energy of the particles and their proportion) at each zone of the detector where RadFETs are going to be placed are important in order to recreate, in an irradiation test beam, the same (or similar) conditions that will allow the correct calibration of the dosimeters. It is also possible to calibrate them by using the dominant particles of the mixed field and take the differences into account for the evaluation of the error.

RadFETs have been irradiated up to doses of 35000 Gy (see Table 2.1 to compare with the doses per year in each subdetector system of CMS). They showed a quick decrease of the sensitivity during the first 5000 Gy. After that dose the RadFETs sensitivity decreases slowly and gradually. REM and TN100P, the devices with smaller oxide thickness layers, are less sensitive than the rest. Alternatively, TN502P showed a good initial sensitivity but much less radiation tolerance. It saturated after 3000 Gy, with pions, and after 12000 Gy, with the protons.

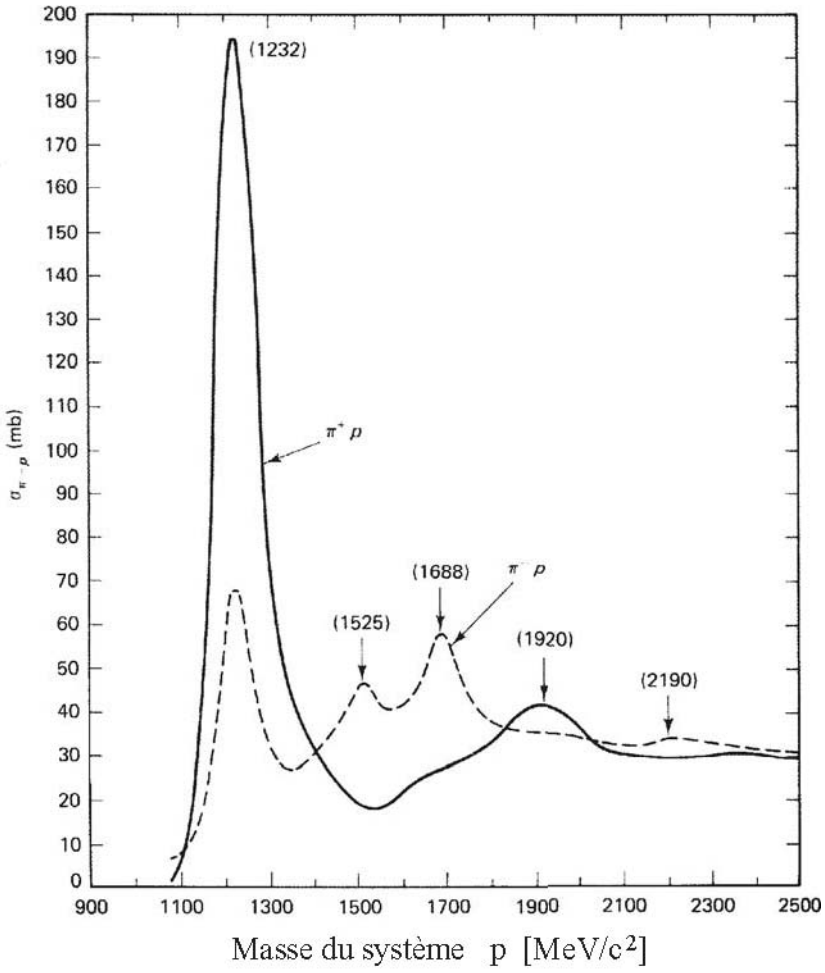

Fig. A.27: Evolution of the cross-section for the pion-proton collisions.

The 24 GeV/c proton are more ionizing than the 300 MeV/c pions which can be considered almost as MIPs. However, the dosimeters seem to saturate at earlier doses with the 300 MeV/c pions than with the 24 GeV/c protons. The reason why this happen could be because pions with the momentum used during the irradiation are in what is called the 33 resonance. Figure A.27 shows that the cross-section of the pion-proton collision (with the proton at rest) increases drastically for pions of 300 MeV/c. These pions will generate secondary particles, which are not detected by the SEC and therefore not counted for the dosimetry, which will give an extra ionization, and dose, to the dosimeter.

Bibliography

[1] P. Lefevre, et al. “The Large Hadron Collider: conceptual design”, CERN/AC/95-05. 1995.

[2] LHC Project Document LHC-PM-MS-0005, rev 1.4, April 2002.

[3] http://atlas.web.cern.ch/Atlas/Welcome.html

[4] Atlas Technical proposal, CERN/LHCC/94-43.

[5] CMS Technical proposal, CERN/LHCC/94-38.

[6] http://cmsinfo.cern.ch/Welcome.html/

[7] ALICE Technical proposal, CERN/LHCC/95-71.

[8] http://alice.web.cern.ch/Alice/AliceNew/

[9] LHCb Technical proposal, CERN/LHCC/98-4.

[10] http://lhcb.web.cern.ch/lhcb/

[11] John Womersley “The LHC Physics Program. FERMILAB-Conf-97/350. 1997.

[12] http://ab-div-op-sps.web.cern.ch/ab-div-op-sps/

[13] CMS. The Tracker System Project. Technical Design Report, CERN/LHCC 98-6, CMS TDR 5, 15 April 1998.

[14] CMS-Collaboration. “CMS Tracker TDR 5”, (1998). CERN/LHCC 98-6.

[15] ATLAS-Collaboration. “Inner Detector Technical Design Report”. CERN/LHCC/97-17

[16] LHCb-Collaboration. “LHCb Outer Tracker Technical Design Report”. CERN-LHCC-2001-024.

[17] LHCb Collaboration. “LHCb Inner Tracker Technical Design Report”. CERN-LHCC-2002-029.

[18] A. Vasilescu. **“**Overview on the radiation environment in ATLAS and CMS SCT and the irradiation facilities used for damage tests”. ROSE/TN/97-3.

[19] M. Huhtinen. “Radiation Environment Simulations for the CMS Detector”. CERN/CMS/TN/95-198. 1995.

[20] A. Fasso et al. *FLUKA92, Proc. Workshop on Simulating Accelerator Radiation Environments*. Santa Fe, USA, 1993.

[21] *Radiation Effects Course-Radiation Environment in experimental CMS Area*. http://lhc-radwg.web.cern.ch/LHC-radwg/

[22] A. Drozhdin et al. “Accelerator Related Background in the CMS detector at LHC”. CERN/CMS/TN/96-056. 1996.

[23] M. Glaser, M. Huhtinen, F. Lemeilleur, C. Leroy, P. Roy, M. Tavlet, "Radiation test facilities in the new PS East Hall at CERN", in Proc. IEEE RADECS 99, Fontevraud, France, Sept 13-17, 1999, pp. 136-141.

[24] C. Leroy et al. CERN ECP/93-12 (1993), *IV International Conference on Calorimetry in High Energy Physics*, La Biola, Isola d’Elba, Italy, 19-25 Sep. 1993.

[25] P. Aarnio, et al. *Nucl. Instr. and Meth.* A360 (1994) 521.

[26] S. Bates, et al. CERN ECP/95-03 (1995), *IV International Conference on Advanced Technology and Particle Physics,* Villa Olmo, Como, Italy, 3-7 Oct. 1994.

[27] R. Schmid et al. “Beam Loss Scenarios and Strategies for Machine Protection at the LHC”. LHC Project Report 665. 2003.

[28] A. Hilaire et al. “Beam Transfer to and injection onto the LHC”. EPAC’98, Stockholm, June 1998.

[29] http://lhc-new-homepage.web.cern.ch/lhc-new-homepage/

[30] R. Assmann et al. “Designing and Building a Collimation System for the High-Intensity LHC Beam”. PAC 2003, Portland, USA, May 2003.

[31] V. Kain et al. “Equipment Failure and Beam Losses in the LHC”. EPAC 2002, Paris, France, 2002.

[32] F. Sonnemann. “Resistive Transition and Protection of LHC Superconducting Cables and Magnets. Dissertation an der Reinisch-Westfälischen Technischen Hochschule Aachen. 2001.

[33] O. Brüning. “Mechanisms for Beam Losses and their Time Constants”. *Chamonix IX*. Jan. 1999.

[34] M. Huhtinen et. al. “Impact of the LHC beam abort kicker pre-fire on high luminosity insertion and CMS detector performance” *Proceedings of the 1999 Particle Accelerator Conference*, New York, pp 1231-1233.

[35] M. Huhtinen. “The radiation environment at the CMS experiment at the LHC”. Geneva, CERN, HU-SEFT-R-1996-14. 1996.

[36] DSS Working Group. “A Detector Safety System for the LHC Experiments”. Functional Requirements Document. CERN-JCOP-2002-012. 25 Apr. 2002.

[37] J.B. Jeanneret, H. Burkhardt. “Measurements of the Beam Losses in the LHC Rings”. LHC-BLM-ES-0001.00-rev1.1, 28.02.2003.

[38] http://itcobe.web.cern.ch/itcobe/Services/Pvss/

[39] J.B. Jeanneret et al. LHC Project Report 44, CERN, 1996.

[40] A. Arauzo-García et al. “LHC Beam Loss Monitors”. CERN-SL-2001-027-BI. 2001.

[41] E. Gschwendtner et al. “The Beam Loss Detection System of the LHC Ring”. EPAC 2002, Paris, France. 2002.

[42] http://www.slac.stanford.edu/BFROOT/

[43] O. Long et al. “The BaBar Silicon Vertex Tracker”. *Nucl. Instr. and Meth. in Physics Research* A 435 (1999) 25-33.

[44] G. Sciolla. “The BaBar Drift Chamber”. *Vienna Wire Chamber Conference* 1998.

[45] EMC homepage. http://www.slac.stanford.edu/BFROOT/www/Detector/Calorimeter/index.html

[46] PEP-II homepage. http://www.slac.stanford.edu/accel/pepii/home.html

[47] Belle homepage. http://belle.kek.jp/

[48] KEKB homepage. http://www-kekb.kek.jp/

[49] ZEUS homepage. http://www-zeus.desy.de/

[50] HERA homepage. http://www-hera-b.desy.de/

[51] E. Koffeman. “The construction of the ZEUS Micro Vertex Detector”. *Nucl. Instr and Meth.* A 473 (2001), 26

[52] *The European Physical Journal C. Review of Particle Physics*. Volume 15, Number 1-4, 2000.

[53] B. Rossi. “High Energy Particles”. Prentice-Hall, Inc., Englewood Cliffs, NJ, 1952.

[54] K.A. Ispirian, A.T. Margarian, and A.M. Zverev. *Nucl. Instr. Methods* 117, 125 (1974).

[55] W.H. Barkas and M.J. Berger. "Tables of Energy Losses and Ranges of Heavy Charged Particles". NASA-SP-3013 (1964).

[56] V.L. Highland, *Nucl. Instr. Methods* 129, 497 (1975).

[57] M.J. Berger and S.M. Seltzer. "Tables of Energy Losses and Ranges of Electrons and Positrons". NASA-SP-3012 (1964).

[58] P.J. Dean, C.D. Clark and P.V. Harris. "Intrinsic edge absorption in diamond". *Proc. Roy. Soc.* (London). A277:312. 1964.

[59] J.R. Chelikowsky and M.L. Cohen. "Nonlocal pseudopotential calculations for the electronic structure of eleven diamond and zinc-blende semiconductors". *Phys. Rev. B*. 13:556. 1976.

[60] L.S. Pan, S. Han and D.R. Kania. "Diamond: Electronic Properties and Applications". Page 241. *Kluwer Academic Publisher*. 1995.

[61] D.K. Ferry. "High-field transport in wide bandgap semiconductors". *Phys. Rev. B*. 1975.

[62] W. Shockley. *Czech. J. Phys. B*. 11:81. 1961.

[63] C. Canali et al. *Nucl. Instr. Methods*. 160:173. 1979.

[64] G. Cavalleri et al. *Nucl. Instr. Methods*. 92:137. 1971.

[65] R. Hofstadter. "Crystal counters". *Nucleonics*, page 2. 1949.

[66] L.S. Pan et al. "Particle and photoinduced conductivity in type IIa diamonds". *J. Appl. Phys*. 74(2):1086. 1993.

[67] Keithley Model 237-TRX-NG 3-Slot Triax to 3-Lug Triax Adapter (Guard Not Connected) PA-311 Rev. A.

[68] National Instruments. LabVIEW for Windows. Basic Course Manual. National Instruments Co. Austin. 1999.

[69] D. Meier. "CVD Diamond Sensors for Particle Detection and Tracking" PhD thesis, Universität Heidelberg. 1999.

[70] A. Oh et al. "Development of diamond films for particle detector applications". *Diamond and Related Materials*. 7:1553. 1998.

[71] M. Glaser, L. Durieu, F. Lemeilleur, M. Tavlet, C. Leroy, P. Roy. "New irradiation zones at the CERN-PS". *Nucl. Instr. Methods. in Phys. Research* A 426 (1999) 72-77.

[72] E. Borchi and m. Bruzzi. “Radiation Damage in Silicon Detectors”. *La Rivista del Nuovo Cimiento,* 17 (1994) 11.

[73] RG58 cables page. http://www.national-tech.com/catalog/rg58coaxialcables.htm

[74] Huber-Suhner homepage. http://www.hubersuhnerinc.com/co-ca-us/ca-us-index

[75] ^{R}MicroSim Pspice for Windows, 2nd ed, by Goody, Prentice-Hall, Upper Saddle River, N.J., ©1998.

[76] M. Huhtinen. “Proposal for a Radiation Monitoring System”. *3rd CMS Radiation Monitoring Meeting*, 2003. Available: http://cern.ch/lhc-expt-radmon

[77] D. Forkel-Wirth, D. Perrin, L. Scibile, G. Segura, F. Szoncso, P. Vojtyla. “Radiation Monitoring System for the Environment and Safety (RAMSES)-Functional Specificaton”. *LHC Project Document* LHC-P-ES-0003. 20 June 2003.

[78] F. Ravotti et al. “Conception of an Integrated Sensor for the Radiation Monitoring of the CMS Experiment at the Large Hadron Collider”. CERN-PH-EP/2004-004. 10 Feb. 2004.

[79] OSRAM BPW34F datasheet. Available: http://www.osram-os.com

[80] Cuniberti et al. “Elettronica (volume 2- componenti e tecniche circuitali)”. *Petrini Editore*. 1997.

[81] A.G. Holmes-Siedle, L. Adams. “Handbook of radiation effects”. Oxford University Press. 2002.

[82] B. Camanzi, A. G. Holmes-Siedle and A. K. McKemey. “The dose mapping system for the electromagnetic calorimeter of the BaBar experiment at SLAC”. *Nucl. Instr. Methods.* A 457, pp. 476-486. 2001.

[83] M. Bull. “Calibration and Temperature Characteristics of RadFET Dosimeters”. *Project for Bachelor of Science,* Brunel University. 1999.

[84] F. Ravotti. “Studio della risposta di dosimetri a stato solido da utilizzare per la misura dei campi di radiazione nell’esperimento CMS a LHC”. *Tesi di Laurea. Politecnico di Torino.* Oct. 2002.

[85] H. Ch. Walter et al. “PSI Accelerator Facilities Users’ Guide”. *Paul Scherrer Institut.* CH-5232 Villigen PSI. 1994 (2nd edition).

List of variables

A	atomic number of media atoms
A_0 , A_1 , A_2	polarization fit constants
B	magnetic field
B_0	initial magnetic field
β	velocity ($\beta=v/c$)
c	speed of light
d	diamond thickness
D	diameter
$D[Gy]$	Dose
δ_p	correction due to media polarization
δ	drift length; diamond collection distance
δ_e	drift distance for electrons
δ_h	drift distance for holes
δ_Q	collection distance
ΔE	average energy losses
ΔE^W	most probable energy losses
Δz	drift distance
e, q_e	electron charge
E	energy loss of a particle
$\vec{E}$	electrical field
E_C	critical energy
ε, ε_Q	collection efficiency
γ	gamma factor
h	Planck constant
I_p	average ionization potential
I	current
I_{DS}	current drain to source
$\vec{j}$	current density
l	magnet length
L	inductance
$L(\lambda_d)$	Landau distribution
λ	wavelength
λ_d	deviation from most probable energy losses
M	particle mass
m_e	electron mass
μ	carrier mobility
N_A	Avogadro number
p	particle momentum
p_t	transverse momentum
$P.Area$	peak area
q	charge
Q_C	induced charge
Q_G	primary ionization charge
r	bending radius
r_e	classical electron radius
R	resistance
R_C	cable resistance
ρ	densitiy
ρ_r	resistivity
ρ_e	number of electrons per µm that a MIP generates in diamond
σ	decay time constant for a quench
$\sigma_R(E)$	Rutherford cross-section
t_0	initial time
T_{cut}	energy at which photons have an absorption length of 500 µm
T_{max}	maximum kinetic energy which can be transferred to a free electron in a single collision
T_{upper}	minimal value between T_{cut} and T_{max}
τ	lifetime of the charge carrier
τ_d	decay time constant
τ_1, τ_2	polarization time fit constants
θ_0	rms of the distribution of θ_{plane} values
θ_{plane}	deflection angle projected into a two dimensional plane
Θ	deflection angle
U, V	bias voltage
v_p	particle velocity
v_e	electron drift velocity
v	carrier drift velocity
v_{sat}	saturated drift velocity
V_{th}	threshold voltage
W	average energy spent per electron release
x	thickness of the scattering medium
x_t	distance that a MIP traverses in diamond
X_0	radiation length
z	distance from the electrode
z_p	charge of the incoming particle in electron units
Z	charge of media atoms
ξ	parameter characterizing the width of the distribution

List of figures

List of tables

Acknowledgements

I would like to thank Dr. Minh-Tâm Tran for his support from the university during the development of my thesis at CERN and the wise corrections that helped to improve sensitively my work.

I must express my sincere gratitude to Dr. Emmanuel Tsesmelis for the opportunity he has given to me of doing my PhD at CERN and for his wise leadership during all these years.

I am much obliged to Dr. Alick Macpherson, without him this work would not have been possible.

Special thanks to Terry Pritchard for his fantastic work and his cool sense of humor, to work with him was always a pleasure.

I want also to thank Dr. Alexander Oh for helping me with the diamond measurements and their analysis. Dr. Peter Weilhammer, Dr. Harris Kagan and Dr. Eleni Berdermann for their great help on the understanding of CVD diamond material and the enlightening conversations during the measurements performed to CVD diamond samples. Thanks to Dr. Christoph Ilgner for his support during the measurements, to Dr. Stone, Dr. Worm and Dr. Gray for the nice time and good discussions during the test beams, to Federico Ravotti and Maurice Glaser for all the support provided to my thesis and for being so cool and to Mika Huhtinen for his great simulations of the worst case accident scenario.

I do not want to forget Dr. Paco Calviño who introduced me into CERN for the very first time, Dr. Carmelo D'Ambrosio and Dr. Olav Ullaland, who always had a helping hand for me, and Dr. Aurelio Bay and Erika Luthy of the LPHE in Lausanne.

My stage in Geneva would not have been as pleasant without my friends: MFCGyC Dr. Antonio, Boris, Esther, Alex, Iván, Juan, Mirko, Ricardo, Andrea, Frederique, Marco C, Marco L., Eva, Federico, Oscar, Alberto S., Alessandro M., Davide, Eli, Gemma, Tatiana, Julie, Stefano R., Andrés, Cristina, Arturo, Alessandro D., Rocío, Ubaldo, Christos, Elena, Francesco, Fabrizio, Giovanna, Mirco, Laura, Gianluca, Stefano P., Giuseppe, Sonia, Alberto, Georgina, Emanuele, Carmen and Ed, thanks to all of them.

Agradezco especialmente a mi madre, Mª Seny Hernando Rica, por su constante apoyo y fe ciega en mis posibilidades durante todos estos años, a mi hermano, Víctor Miguel, a mis tíos y primos maños y a mi abuela Carmen.

Gracias a mis amigos de universidad que vinieron a visitarme a Ginebra y con sus e-mails me han hecho sentir todos estos años parte del grupo. Quiero agradecer a mis amigos Roger, Bernat y Ramón por todos los buenos momentos y su amistad perenne, que vale un tesoro.

Y gracias a Ana María por su cariño, sus palabras, sus besos, sus visitas y su compañía que tanto han significado para mí durante todo este tiempo en Ginebra.